Universidade Federal de Minas Gerais
Instituto de Ciências Exatas - ICEx
Programa de Pós-Graduação em Química

Aline de Souza Bozzi

Decay Pathways and Dexter Energy Transfer: Computational Insights into the Photophysics of Ruthenium-Based Photosensitizers

Belo Horizonte

2025

UFMG/ICEX/DQ. 1.662
T. 757

Aline de Souza Bozzi

Decay Pathways and Dexter Energy Transfer: Computational Insights into the Photophysics of Ruthenium-Based Photosensitizers

Tese apresentada ao Departamento de Química do Instituto de Ciências Exatas da Universidade Federal de Minas Gerais, como requisito parcial para a obtenção do grau de Doutor em Ciências - Química.

Orientador : Prof. Dr. Willian Ricardo Rocha

Belo Horizonte
2025

Ficha Catalográfica

B662d
2025
T

Bozzi, Aline de Souza.
Decay pathways and Dexter energy transfer [manuscrito] : computational insights into the photophysics of ruthenium-based photosensitizers / Aline de Souza Bozzi. 2025.
190 f. : il., gráfs., tabs.

Orientador: Willian Ricardo Rocha.

Tese (doutorado) – Universidade Federal de Minas Gerais – Departamento de Química.
Bibliografia: f. 135-157.
Apêndices: f. 159-190.

1. Físico-química – Teses. 2. Biofísica – Teses. 3. Modelagem computacional – Teses. 4. Funcionais de densidade – Teses. 5. Fotoquimioterapia – Teses. 6. Rutênio – Teses. 7. Complexos metálicos de transição – Teses. 8. Câncer – Tratamento – Teses. 9. Energia – Transferência – Teses. I. Rocha, Willian Ricardo, Orientador. II. Título.

CDU 043

Elaborada por Márcia Cavalcanti Moreira – Bibliotecária – CRB6/3847.

UNIVERSIDADE FEDERAL DE MINAS GERAIS

UFMG
Programa de Pós-Graduação em Química
Departamento de Química - ICEx

química
pós-graduação-ufmg

"Decay Pathways And Dexter Energy Transfer: Computational Insights Into The Photophysics Of Ruthenium-based Photosensitizers"

Aline de Souza Bozzi

Tese aprovada pela banca examinadora constituída pelos Professores:

Prof. Willian Ricardo Rocha - Orientador
UFMG

Prof. Sylvio Roberto Accioly Canuto
USP

Prof. Josefredo Rodriguez Pliego Junior
UFSJ

Prof. Hélio Anderson Duarte
UFMG

Prof. Guilherme Ferreira de Lima
UFMG

Belo Horizonte, 27 de junho de 2025.

Documento assinado eletronicamente por **Josefredo Rodriguez Pliego Junior**, **Usuário Externo**, em 01/07/2025, às 11:47, conforme horário oficial de Brasília, com fundamento no art. 5º do Decreto nº 10.543, de 13 de novembro de 2020.

Documento assinado eletronicamente por **Sylvio Roberto Accioly Canuto**, **Usuário Externo**, em 01/07/2025, às 16:57, conforme horário oficial de Brasília, com fundamento no art. 5º do Decreto nº 10.543, de 13 de novembro de 2020.

Documento assinado eletronicamente por **Helio Anderson Duarte**, **Professor do Magistério Superior**, em 14/07/2025, às 10:40, conforme horário oficial de Brasília, com fundamento no art. 5º do Decreto nº 10.543, de 13 de novembro de 2020.

Documento assinado eletronicamente por **Guilherme Ferreira de Lima**, **Professor do Magistério Superior**, em 14/07/2025, às 13:59, conforme horário oficial de Brasília, com fundamento no art. 5º do Decreto nº 10.543, de 13 de novembro de 2020.

Documento assinado eletronicamente por **Willian Ricardo Rocha**, **Professor do Magistério Superior**, em 18/07/2025, às 10:40, conforme horário oficial de Brasília, com fundamento no art. 5º do Decreto nº 10.543, de 13 de novembro de 2020.

A autenticidade deste documento pode ser conferida no site https://sei.ufmg.br/sei/controlador_externo.php?acao=documento_conferir&id_orgao_acesso_externo=0, informando o código verificador **4340255** e o código CRC **59ADEA58**.

Acknowledgements

An old African proverb reminds us, "*It takes a village to raise a child.*" I believe this wisdom extends to many of life's great endeavors — including the journey of research, writing, and defending a doctorate. In that spirit, I wish to express my deepest gratitude to the "village" that made this achievement possible.

To my family, thank you for your unwavering support, boundless love, and steadfast belief in the power of education. You have always encouraged my choices and reminded me that learning is a compass for life.

To my second family — Lucas, my partner in every sense—words cannot faithfully capture my gratitude. Your presence has been my anchor, and your kindness, my constant. To Beatriz, my mother-in-law, thank you for embracing me as your own.

To my advisor, Prof. Willian Rocha, I am endlessly grateful for your guidance, patience, and friendship. Over nearly six years in your lab, you've shaped not only my research but also my growth as a scientist and person. Thank you for making this difficult journey much more bearable.

To my exchange advisor, Prof. David Beratan, thank you for welcoming me so warmly into your group and for your invaluable mentorship. Your generosity and insights made my time abroad both productive and unforgettable. I am also deeply thankful for your academic collaboration and encouragement.

To Prof. Rita Sebastião, thank you for your collaboration in this work, friendship, and enthusiasm.

To my colleagues in the $\langle e|Cs|Mo\rangle^{Lab}$, thank you for the lively discussions, shared struggles, and countless moments of laughter over coffee and beers. A special note to Sandy, whose curiosity and dedication made mentoring her a joy and a learning experience in itself.

To the Beratan Group, thank you for the stimulating exchanges and the camaraderie. My time with you profoundly enriched my perspective. I am especially grateful to Niven, Jon, Kiriko, and Hassan for their friendship and readiness to help. To Peng and Hassan, thank you for your collaboration — our debates pushed me to think more deeply and strive for greater rigor.

To my dear friends Ana, Nicolas, Philipe, and Diego, though distance and time have kept us apart more than I'd like, your friendship has been a steady comfort. I cherish the knowledge that you're always there.

To all the professors who have shaped my academic journey since my undergraduate years — thank you for sharing your knowledge and inspiring my path.

To UFMG and the Graduate Program in Chemistry, thank you for providing the environment and resources that made this journey possible.

Finally, to the Brazilian funding agencies, especially CAPES, I extend my sincere appreciation for the financial support that allowed me to come this far. Without it, none of this would have been within reach.

And God said: 'Let there be light';
and there was light.
And God saw that the light was good (...)
- Genesis, 1. 3-4

Resumo

A interação entre luz e matéria abre espaço para aplicações inovadoras em áreas como fotocatálise, células solares e fototerapias. Entre elas, a Terapia Fotodinâmica (TFD) tem ganhado destaque como tratamento promissor contra o câncer, sendo oficialmente incorporada ao Sistema Único de Saúde (SUS) em 2023. No entanto, seu avanço ainda depende do desenvolvimento de fotossensibilizadores (FSs) mais eficientes e da compreensão aprofundada de seus mecanismos de ação. Este trabalho contribui com esses objetivos ao desenvolver novos métodos computacionais para a modelagem de processos em estado excitados de sistemas complexos, com foco em complexos metálicos de transição. Um dos principais avanços foi a extensão da teoria de Marcus para o cálculo da constante de conversão interna (IC) para moléculas na região invertida, onde encontram-se grande parte dos FSs. Esse método conta com a incorporação de uma correção no termo da densidade de estados considerando interseções cônicas. Essa modificação, aplicada tanto à teoria de Marcus quanto à teoria de Marcus-Jortner-Levich, apresentou resultados satisfatórios para a determinação da constante de CI e tem sido aplicado em diversos estudos. Além disso, foi desenvolvido um modelo cinético capaz de mapear os processos de decaimento de estados excitados, incluindo canais secundários. Aplicado ao complexo $[Ru(bpz)_3]^{2+}$, o modelo reproduziu com sucesso resultados experimentais e revelou caminhos adicionais que explicam a labilidade desse composto. Esse trabalho também contribuiu com o entendimento da transferência de energia em sistemas supramoleculares, como na interação entre o complexo $[Ru(bpy)_3dppn]^{2+}$ e O_2. Foi proposta uma nova abordagem para modelar a Transferência de Energia Dexter (DET), com investigação sistemática das orientações relativas entre FS e O_2 para a identificação das coordenadas de reação para a DET. O modelo cinético, baseado na combinação de Teoria do Funcional da Densidade Restrita (CDFT) com a teoria de Marcus, permitiu o cálculo preciso das constantes de DET sem recorrer a métodos multirreferenciais, fator crucial para sistemas grandes. Em conjunto, os métodos desenvolvidos oferecem ferramentas escaláveis e transferíveis para o estudo da fotoquímica e da fotofísica de sistemas complexos, com especial aplicação na TFD.

PALAVRAS-CHAVE: **Terapia fotodinâmica; fotofísica; complexos de rutênio; transferência de energia por Dexter; DFT**.

Abstract

The interaction between light and matter opens pathways for groundbreaking applications in fields such as photocatalysis, solar energy, and phototherapies. Among them, Photodynamic Therapy (PDT) has emerged as a promising cancer treatment and was formally integrated into Brazil's public healthcare system (SUS) in 2023. However, its advancement still relies on the development of efficient photosensitizers (PSs) and a deeper understanding of their mechanisms of action. This work contributes to these goals by developing new computational strategies to model excited-state processes in complex systems, with a focus on transition-metal complexes. A central achievement of this work is the extension of Marcus' theory to the estimation of the internal conversion (IC) rate constant for molecules in the inverted region, where many PSs are located. By incorporating a correction on the density of states term through conical intersection considerations, a more accurate, computationally accessible method was proposed. This correction, applied to both Marcus and Marcus-Jortner-Levich theories, yields reliable IC rates and has already been employed in multiple works. Furthermore, a kinetic model was developed to map full excited-state decay pathways, including secondary deactivation channels critical for differentiating between Type I and Type II PDT mechanisms. When applied to the $[Ru(bpz)_3]^{2+}$ complex, the model successfully reproduced experimental behavior and unveiled thermally accessible pathways such as population of triplet metal-centered states, which explains the complex lability. This work also tackled the complexity of energy transfer in supramolecular systems, notably between $[Ru(bpy)_2dppn]^{2+}$ and O_2. A novel approach was introduced for modeling Dexter energy transfer (DET) by systematically scanning PS-O_2 orientations to identify the energy transfer reaction coordinate. The kinetic model, built using Constrained DFT (C-DFT) combined with Marcus' theory, enabled accurate rate constant calculations without resorting to computationally intensive multireference methods, crucial for large systems. Altogether, the methodologies developed here provide scalable and transferable tools for modeling the photophysics and photochemistry of complex systems, especially in PDT.

KEYWORDS: **Photodynamic therapy; photophysics; ruthenium complexes; Dexter energy transfer; DFT**.

List of Figures

List of Tables

Acronyms

BO Born-Oppenheimer. 28, 30, 39

CDFT Constrained Density Function Theory. 92–94, 96, 109, 118

CT Charge-Transfer. 89, 107, 109

DET Dexter Energy Transfer. , 25, 87–91, 93, 94, 108, 109, 119–122

DFT Density Functional Theory. 28, 29, 31–34, 59, 94, 109

EnT Energy Transfer. , 23–25, 83, 86–88, 90, 94, 96, 104, 108–110, 120–122

ET Electron Transfer. 23, 24, 82, 86

F Fluorescence. 36

FAC Full-Active-Space. 42, 43

FC Franck-Condon. 59–61, 70, 72, 74–76, 80

FCWD Franck-Condon Weighted Density. 41, 48, 51

FF Force-Field. 27

HAT Hydrogen Atom Transfer. 24

HK Hohenberg-Kohn. 33, 34

HR Huang-Rhys. 44, 46–48, 51, 54

IC Internal Conversion. , 24, 25, 36, 37, 40, 44, 45, 47, 52, 53, 61, 79

IL IntraLigand. 55, 56, 67–69, 100, 107, 108, 121

ISC Intersystem Crossing. 23, 24, 36, 37, 42, 58, 60, 61, 74–79, 102, 121

Acronyms

KS Kohn-Sham. 31, 32, 34, 35

LJ Lennard-Jones. 27

LLCT Ligand-to-Ligand Charge Transfer. 55, 67–69

LMCT Ligand-to-Metal Charge Transfer. 55, 68

LR Linear-Response. 35

LVC Linear Vibronic Coupling. 37

MC Metal-Centered. 55, 56, 68, 69, 101

MECI Minimum Energy Conical Intersection. 38, 44, 46, 49, 61

MJL Marcus-Jortner-Levich. 37, 38, 42, 44, 52–54, 60, 79

MLCT Metal-to-Ligand Charge Transfer. , 55, 56, 67–69, 71, 79, 99, 100, 105, 107, 121

NAC NonAdiabatic Coupling. 36, 44, 46

NACME NonAdiabatic Coupling Matrix Elements. 38

NTO Natural Transition Orbital. , 67–69, 105

PCET Proton-Coupled Electron Transfer. 24

PDT Photodynamic Therapy. 23–25, 81, 83–87, 89, 120, 122

PES Potential Energy Surface. , 36, 40, 44, 46, 58, 90, 94, 96, 109–118

Ph Phosphorescence. 36

PS Photosensitizer. , 23–26, 81–84, 86, 87, 94, 103–105, 107–109, 119, 121, 122

RG Runge-Gross. 33

ROS Reactive Oxygen Species. 81, 83

SF-TD-DFT Spin-Flip TD-DFT. 46, 61

SOC Spin-Orbit Coupling. 24, 36, 42, 58, 70, 74–76, 102, 122

TD-DFT Time-Dependent Density Functional Theory. 32, 33, 35, 60, 74

Acronyms

TS Transition State. 61

vdW van der Waals. 27

VR Vibrational Relaxation. 36, 74, 77, 79, 80

WFT WaveFunction Theory. 28, 29, 31, 32

ZORA Zeroth-Order Regular Approximation. 59, 95

Contents

Chapter 1

Introduction

Early photography faced a substantial limitation: silver bromide (AgBr) was especially sensitive to ultraviolet and blue light, causing blue objects to appear overly bright. In contrast, yellow and red objects appeared unnaturally dark. This changed in 1873 when German photographer and photochemist Hermann Wilhelm Vogel accidentally discovered that adding certain colored dyes to AgBr-based photographic emulsions extended their sensitivity to longer wavelengths of light [2]. His breakthrough enabled the production of black-and-white films capable of capturing the full visible spectrum. It later paved the way for color photography, which used stacked emulsion layers, each sensitive to different wavelengths [3]. Although silver halide photography has largely faded in the digital age, using dyes to absorb longer-wavelength light and to transfer electrons and energy remains crucial in modern applications [4].

In recent years, the number of light-sensitive molecules discovered has significantly increased. The scope of Photosensitizer (PS) types has stretched from organic dyes to porphyrin and derivatives, transition-metal complexes, crystals, and polymers, among others. Their miscellaneous applicability has also become more apparent, aiding technological breakthroughs and crowning a broad interest in many areas of chemistry, physics, and biological sciences. The vast applications encompass environmental science [5, 6], material science [7], photocatalytic processes [8–11], solar cells [12–15], Photodynamic Therapy (PDT) [16–20], and others [21]. To allow such broad applications, PSs must have a set of photophysical characteristics that promote them to interact in the excited state with other molecules through Energy Transfer (EnT), Electron Transfer (ET), and photochemical reactions or even undergo photoisomerization. Ideally, a PS should present a high excitation lifetime, guaranteeing that all the intermolecular photophysical and photochemical processes are enabled.

Closed-shell molecules constitute a large portion of the PS class. Taking a singlet PS in the ground state, one way of enabling longer excited state lifetimes is by enforcing the In-

tersystem Crossing (ISC) leading to the population of the triplet manifold ($^1PS \rightarrow {}^3PS$). That requires a small adiabatic energy difference and a large Spin-Orbit Coupling (SOC) between the singlet and the triplet excited states. Usually, molecules containing heavier atoms, such as transition-metal complexes, feature considerably high ISC rate constants due to large SOC. Furthermore, such complexes are also known for their rich excited-state photophysics, characterized by their collection of diverse transitions, in contrast to organic molecules whose transitions are mainly $n \rightarrow \pi^*$ and $\pi \rightarrow \pi^*$. Metal complexes of Pt(II), Pt(IV), Re(I), Os(II), Ir(IV), and Ru(II) are among the most investigated PSs for extensive applications. Therefore, understanding the photophysical properties that govern the excited-state dynamics of such systems is of fundamental interest. It also assists in the design of new compounds with tailored characteristics for specific usages.

Experimental determination of different deactivation mechanisms and photochemical interactions of PSs is a difficult task since it requires monitoring all species and intermediates generated throughout the photodynamic process using advanced spectroscopy techniques with temporal resolution at the picosecond scale. In addition, it has to consider that more than one mechanism can be involved in these systems. In this way, theoretical and computational studies are essential. They can contribute enormously on several fronts, such as (*i*) study of the dynamics of processes in the excited state, (*ii*) study of the photophysics of metal complexes and how it is affected by the solvent and medium, (*iii*) investigation of the mechanism of action of photoexcited metal complexes (ET, EnT, Proton-Coupled Electron Transfer (PCET), direct photo-oxidation, and Hydrogen Atom Transfer (HAT)) [22, 23].

In this work, we directed our efforts toward developing modeling methods for investigating and describing the several photophysical processes that occur in complex systems and applied them to Ruthenium(II)-based PSs. Because Ru(II)-polypyridyl complexes are primarily applied and tested as PSs in biological systems, *e.g.* PDT, we have also investigated their suitability for this end. Understanding photodynamic processes applied to biological systems, such as PDT, is just beginning, being a frontier area in chemistry, biology, medicine, and biochemistry. Even more recent is the contribution of computational studies, which demand more precise methods in electronic structure. In this sense, there are still many significant advances to be made, such as, for example, the investigation of the excited states of metal complexes and the application of more precise methods to describe biomolecules. Furthermore, the experimental challenges mentioned above culminate in a few research groups worldwide dedicating efforts to contribute to this subject.

In Chapter 3, we describe the development of a general method for calculating the Internal Conversion (IC) rate constant of molecules that belong to Marcus' inverted re-

gion by implementing a correction to the reorganization energy [24]. Due to the rigidity of Ru(II)-polypyridyl complexes, these compounds show minimal structure variations among the ground and excited states and are placed in the inverted region. Accordingly, this is a suitable method to determine the IC rate constant of such systems and has already been applied to some extent in other works [25–37]. This method has also been incorporated into our excitation decay kinetic model to describe the exciton dynamics and pathway deactivation channels of complex systems [38], described in Chapter 4. Furthermore, the general photophysics and suitability as PS for PDT of the $[Ru(bpz)_3]^{2+}$ (bpz = 2,2'-bipyrazyl) and $[Ru(bpy)_2dppn]^{2+}$ (bpy = 2,2'-bipyridine; dppn = benzo[*i*]-dipyrido[3,2-*a*:2',3'-*c*]phenazine) [39] complexes have been detailed in Chapters 4 and 5. Finally, a kinetic model for Dexter Energy Transfer (DET) has been applied to the investigation of the EnT reaction coordinates to generate singlet molecular oxygen from the $[Ru(bpy)_2dppn]^{2+}$ complex, a key species on PDT type II, which has been discussed in Chapter 5.

Chapter 2

Computational Methods

In computational modeling, mathematical tools and physical approximations are used to investigate the most varied molecular systems. It goes from atoms to macromolecules, applying molecular mechanics to *ab initio* quantum theory methods. Therefore, this chapter aims to provide an overview of the vast field of molecular modeling of complex systems, going from classical mechanics to quantum chemistry in a progressive way. The purpose here is not to derive all mathematical steps or to give a detailed description of theories but to provide some understanding of the methods applied to the investigation of the excited states of metal complexes, their kinetic decay, and their interaction with macromolecules.

2.1 Molecular Docking

An overview

Molecular docking is a computational method to predict the structure of a receptor-ligand complex, where the ligand is usually a small molecule and the receptor is a protein [40–42]. In general, docking simulations are used for two main purposes: correctly predicting the activity of ligands and accurately modeling the overall structure. In our work, the molecular docking methodology was applied to predict the Photosensitizer (PS) binding modes to a DNA model.

The molecular docking simulations start by posing the ligand into the active site. The algorithm can follow three different approaches: the complete rigid docking, which considers the lock and key model featuring both receptor and ligand with fixed bonds and angles; the rigid receptor and flexible ligand, which is the most used approach by the available docking programs; and the flexible docking, considering both macromolecule and ligand flexible with respect to their angles and dihedrals.

Furthermore, it is also important to consider the representation of the receptor and small molecules, whether they are atomic, surface, or grid [43]. The atomic representation is usually used in the final step (ranking) of the docking process, using a potential energy function. The surface-based docking is usually used for protein-protein interaction. The method is characterized by aligning surface points and minimizing the angle between the surface of opposing molecules [44]. The potential energy grid approach consists in storing the receptor's energy information at each point of the grid [45]. The simplest grid method accounts for two types of potential, the pairwise summation of Coulombic interactions and the Lennard-Jones (LJ) potential to describe the van der Waals (vdW) interactions. The terms are

$$U_{\text{ele}}(\mathbf{r}) = \sum_{i=1}^{N_{\text{A}}} \sum_{i=1}^{N_{\text{B}}} \frac{q_i q_j}{4\pi\varepsilon_0 \mathbf{r}_{ij}} \tag{2.1}$$

where N is the number of atoms in molecules A and B, q is the charge on each atom, ε_0 is the permittivity of free space, and $\mathbf{r}_{ij}$ is the distance between the atoms, and

$$U_{\text{vdW}}(r) = \sum_{i=1}^{N} \sum_{j=1}^{N} 4\epsilon \left[\left(\frac{\sigma_{ij}}{r_{ij}} \right)^{12} - \left(\frac{\sigma_{ij}}{r_{ij}} \right)^{6} \right] \tag{2.2}$$

being ϵ the energy depth of the potential and σ, the equilibrium distance between the atoms.

The molecular docking simulations also rely on algorithms for pose searching, considering the ligand flexibility. The main search methods are systematic methods (databases and conformational search), stochastic methods (Monte Carlo and genetic algorithm), and simulation methods (classical molecular dynamics) [46].

Scoring Functions

The molecular docking simulations are complemented by scoring functions. The scoring functions are designed to evaluate the interactions between receptor and ligand in the poses predicted by the docking algorithm. In order to be computationally cheap, the scoring functions usually make simplifications in the evaluation of the models, leading to low accuracy for some phenomena. One of the limitations of most scoring functions is that they do not focus on entropy but rather only on the enthalpic aspects of the binding interactions [47, 48]. The scoring functions can be divided into three groups: the Force-Field (FF), the empirical, and the knowledge-based.

The FF-based scoring functions usually account for two energies: the receptor-ligand interaction and the ligand internal energy. The protein is considered rigid and, therefore, presents only one conformation, and the receptor internal energy is omitted from

the calculations. The non-bonding terms are described by the Equations 2.1 and 2.2. Some recent formulations of FF-based scoring functions include a torsional entropy and a protein-ligand hydrogen bond terms [40].

The empirical scoring functions, as the name suggests, are constructed based on parameters determined experimentally. Therefore, these scoring functions fit experimental data and are built upon the idea that the binding energy is a summation of uncorrelated terms. This type of scoring function is somewhat simple; however, it depends on the availability of experimental data. The empirical scoring functions can include terms other than enthalpy, such as entropic penalties on bond flexibility due to binding [40].

And finally, the knowledge-based scoring functions are also built upon experimental data, however, focused on structure rather than the binding energies. The scoring function accounts for atomic interaction-pair potentials to model the receptor-ligand complex [40].

2.2 Density Functional Theory

Before entering into the Density Functional Theory (DFT) description, it is essential to establish some quantum mechanics foundations under the light of the WaveFunction Theory (WFT).

2.2.1 Elementary quantum mechanics

In quantum mechanics, all the information about a system is contained in the system's wavefunction $\Psi(\mathbf{r}, t)$. In the WFT, the wavefunction can be obtained from the Schrödinger equation given by [49–51],

$$i\hbar \frac{\partial \Psi(\mathbf{r}, t)}{\partial t} = \mathcal{H}\Psi(\mathbf{r}, t) \tag{2.3}$$

where $\hbar$ and $\mathcal{H}$ are the reduced Planck's constant and the Hamiltonian operator, respectively. The Hamiltonian operator delivers the total energy, E, of the system and, hence, is built upon the kinetic (T) and potential ($V(\mathbf{r}, t)$) energies, the latter varying depending on the system. Therefore, the Hamiltonian operator can be written as

$$\mathcal{H} = -\frac{\hbar}{2m}\nabla^2 + \mathcal{V}(\mathbf{r}, t) \tag{2.4}$$

where ∇^2 is the Laplacian operator $\left(\frac{\partial^2}{\partial x^2} + \frac{\partial^2}{\partial y^2} + \frac{\partial^2}{\partial z^2}\right)$, and m is the particle mass. Hence, for a system containing M nuclei and N electrons, we can construct the non-relativistic time-independent Hamiltonian for the Born-Oppenheimer (BO) approximation in atomic units as follows [50]

$$\mathcal{H}_{\mathrm{BO}} = -\sum_{i}^{N}\frac{1}{2}\nabla_i^2 - \sum_{i}^{N}\sum_{A}^{M}\frac{Z_A}{\mathbf{r}_{iA}} + \sum_{i}^{N}\sum_{j>i}^{N}\frac{1}{\mathbf{r}_{ij}} + \sum_{A}^{M}\sum_{B>A}^{M}\frac{Z_A Z_B}{\mathbf{R}_{AB}} \tag{2.5}$$

where i and j represent the electrons and A and B, the nuclei. In the same way, $\mathbf{r}_i$ and $\mathbf{R}_A$ are the coordinates for the i-th electron and A-th nucleus, respectively, and Z is the atomic number. The terms of Equation 2.5 are the electronic kinetic energy operator, the electron-nucleus attraction potential operator or external potential, the electron-electron repulsion potential operator, and the nuclear repulsion potential operator.

By the separation of variables method [49], the general solution for the wavefunction $\Psi(\mathbf{r}, t)$ given by Equation 2.3 can be written as

$$\Psi(\mathbf{r}, t) = \psi(\mathbf{r}) \exp\left(-it\frac{E}{\hbar}\right) \tag{2.6}$$

and $\psi(\mathbf{r})$ is the time-independent wavefunction. Therefore, the $\mathcal{H}_{\mathrm{BO}}$ operator (Equation 2.5) will act upon the spatial part of the wavefunction, $\psi(\mathbf{r})$, and the total ground state energy will be given by

$$E_0 = \int \psi^*\left(\mathbf{r}_1, \mathbf{r}_2, \ldots, \mathbf{r}_N\right)\ \mathcal{H}_{\mathrm{BO}}\ \psi\left(\mathbf{r}_1, \mathbf{r}_2, \ldots, \mathbf{r}_N\right)\ \mathrm{d}r_2\ \mathrm{d}r_3\ \ldots\ \mathrm{d}r_N = \langle\psi\,|\mathcal{H}_{\mathrm{BO}}|\,\psi\rangle \tag{2.7}$$

2.2.2 DFT foundations

The intrinsic philosophy of DFT is to determine the energy of a molecular system through a physical *observable*, in this case, the electronic density, $\rho(\mathbf{r})$. In this approach, for a system composed of N electrons, the electronic density depends only upon the three spatial coordinates ($\mathbf{r}$) rather than $3N$ spatial and N spin coordinates, as for the WFT formalism [51–53]. Therefore, $\rho(\mathbf{r})$ integrated over all space gives the total number of electrons

$$N = \int \rho\left(\mathbf{r}\right)\mathrm{d}\mathbf{r} \tag{2.8}$$

moreover, the electronic density can be expressed as

$$\rho(\mathbf{r}) = N\int\ldots\int \psi^*\left(\mathbf{r}_1, \mathbf{r}_2, \ldots, \mathbf{r}_N\right)\ \psi\left(\mathbf{r}_1, \mathbf{r}_2, \ldots, \mathbf{r}_N\right)\ \mathrm{d}\mathbf{r}_1\ \mathrm{d}\mathbf{r}_2\ \ldots\ \mathrm{d}\mathbf{r}_N \tag{2.9}$$

where $\psi(\mathbf{r}_1, \mathbf{r}_2, \ldots, \mathbf{r}_N)$ represents the solution for the ground state Hamiltonian $\mathcal{H}_{\mathrm{BO}}$.

The Hohenberg-Kohn Theorems

Recalling the BO approximation (Equation 2.5), the $\mathcal{H}_{\text{BO}}$ is uniquely given by the number of electrons and the potential created by the nuclei, V_{ne}. Therefore, the electronic density, the wave function, and the ground-state energy will be determined only by these quantities.

This can be proven by assuming the existence of two distinct external potentials, V_{ext} and V'_{ext} satisfying the same ground-state electronic density $\rho_0(\mathbf{r})$. Hence, two Hamiltonian operators arise naturally, $\mathcal{H}$ and $\mathcal{H}'$, with two wavefunctions, Ψ_0 and Ψ'_0, for the ground-state. The variational principle states that the expectation value of a Hamiltonian a applied to a wavefunction b must be higher than the ground-state energy of a. Therefore, using Ψ'_0 as an approximated wavefunction for the operator $\mathcal{H}$ [54]

$$\langle \Psi'_0 | \mathcal{H} | \Psi'_0 \rangle > E_0 \tag{2.10}$$

and rewriting this expression

$$\langle \Psi'_0 | \mathcal{H}' | \Psi'_0 \rangle + \langle \Psi'_0 | \mathcal{H} - \mathcal{H}' | \Psi'_0 \rangle > E_0 \tag{2.11}$$

$$E'_0 + \langle \Psi'_0 | V_{\text{ext}} - V'_{\text{ext}} | \Psi'_0 \rangle > E_0 \tag{2.12}$$

$$E'_0 + \int \rho_0 (\mathbf{r}) \left(V_{\text{ext}} - V'_{\text{ext}} \right) \, \mathrm{d}r > E_0 \tag{2.13}$$

undergoing the same path for a wavefunction Ψ_0 and a Hamiltonian $\mathcal{H}'$ and summing them up, one gets

$$E'_0 + E_0 > E'_0 + E_0 \tag{2.14}$$

which makes the assumption incorrect. Therefore, for the ground state, there can be only one electronic density and correspondent nuclear potential. Hence, it is proven that the energy is a functional of the electronic density.

Making further use of the variational principle, taking an approximated electronic density, ρ', the energy given will be higher than the exact ground-state energy

$$E_0[\rho'] \geq E_0[\rho] \tag{2.15}$$

The energy functional, $E[\rho]$, can be split into three parts: the kinetic energy, $T[\rho]$, the electron-nucleus interaction, $V_{\text{ne}}[\rho]$, and the electron-electron repulsion, $V_{\text{ee}}[\rho]$. Taking into account the Hartree-Fock energy, the electron-electron repulsion can be further divided

into two other parts: the Coulomb, $J[\rho]$, and the exchange, $V_{\text{ex}}[\rho]$. The functionals $V_{\text{ne}}[\rho]$ and $J[\rho]$ are given by

$$\mathcal{V}_{\text{ne}}\left[\rho\right] = \sum\nolimits_{A} \frac{Z_A\ \rho\left(\mathbf{r}\right)}{\left|\mathbf{R}_A - \mathbf{r}\right|}\ \mathrm{d}\mathbf{r} \tag{2.16}$$

$$\mathcal{J}\left[\rho\right] = \frac{1}{2}\int \frac{\rho\left(\mathbf{r}\right)\rho'\left(\mathbf{r}\right)}{\left|\mathbf{r} - \mathbf{r}'\right|}\ \mathrm{d}\mathbf{r}\ \mathrm{d}\mathbf{r}' \tag{2.17}$$

The Kohn-Sham Formalism

The WFT difficulty relies on the electron-electron interaction, which is treated in the DFT with the Kohn-Sham (KS) formalism [55]. The key is to start with a fictitious system of non-interacting electrons that have the same ground-state energy as a real interacting system. Then, the kinetic energy is divided into two terms: an exact one and a correction [51, 52]. The exact solution for the Schrödinger equation is given by the Slater determinant orbitals ϕ_i, and the exact kinetic energy is

$$\mathcal{T}_0 = \sum_{i}^{N} \left\langle \phi_i \left| -\frac{1}{2}\nabla^2 \right| \phi_i \right\rangle \tag{2.18}$$

For interacting electrons (real system), the $\mathcal{T}_0$ is an approximation that requires a correction, and the density for a Slater wavefunction is,

$$\rho\left(\mathbf{r}\right) = \sum_{1}^{N} \left|\phi_i\left(\mathbf{r}\right)\right|^2 \tag{2.19}$$

The residual kinetic energy is included in the exchange-correlation energy, $E_{\text{xc}}[\rho]$ and the DFT energy can be written as,

$$E_{\text{DFT}}\left[\rho\right] = T_0\left[\rho\right] + V_{\text{ne}}\left[\rho\right] + J\left[\rho\right] + E_{\text{xc}}\left[\rho\right] \tag{2.20}$$

The problem here is to find the adequate term of exchange-correlation energy. One way is to use the Lagrange method,

$$L\left[\rho\right] = E_{\text{DFT}}\left[\rho\right] - \sum_{ij}^{N} \lambda_{ij}\left[\langle\phi_i|\phi_j\rangle - \delta_{ij}\right] \tag{2.21}$$

where λ_{ij} is the Lagrange multiplier and δ_{ij}, the Kronecker delta. The equation above will generate a set of one-electron operator, h_{KS}. Therefore,

$$h_{\text{KS}}\ \phi_i = \sum_{ij}^{N} \lambda_{ij}\phi_j \tag{2.22}$$

$$h_{\mathrm{KS}} = -\frac{1}{2}\nabla^2 + \mathcal{V}_{\mathrm{eff}} \tag{2.23}$$

$$\mathcal{V}_{\mathrm{eff}}\left(\mathbf{r}\right) = \mathcal{V}_{\mathrm{ne}}\left(\mathbf{r}\right) + \int \frac{\rho'\left(\mathbf{r}\right)}{|\mathbf{r}-\mathbf{r}'|}\, \mathrm{d}\mathbf{r}' + \mathcal{V}_{\mathrm{xc}}\left(\mathbf{r}\right) \tag{2.24}$$

we see that the effective potential, V_{eff} is given by the Coulomb potential, the interaction electron-nucleus, and a so-called functional derivative, V_{xc}. The set of orbitals produced through the Lagrangian multiplier culminates in the pseudoeigenvalue equations known as KS equations,

$$h_{\mathrm{KS}}\ \phi_i = \varepsilon_i\ \phi_i \tag{2.25}$$

Therefore, the KS equations are not exact, and the exchange-correlation term needs to be constructed systematically. In this sense, there are many approximations to determine it, *i.e.*, the Local Density Approximation (LDA), Generalized Gradient Approximation (GGA), and hybrid functionals, among others [51].

2.3 Time-Dependent Density Functional Theory (TDDFT)

The Time-Dependent Density Functional Theory (TD-DFT) is an extension of DFT. It is usually applied to describe the properties and phenomena of many-body systems and their dynamics due to a time-dependent external potential [56, 57]. The foundations of TD-DFT, similar to DFT, lie in demonstrating its equivalence to the description of the time-dependent WFT and deriving the fictitious potential for a non-interacting system that describes the density of an interacting system.

Recalling the time-dependent Schrödinger Equation (2.3) acting upon a system of N interacting particles, where the total Hamiltonian is

$$\mathcal{H}(t) = \mathcal{T} + \mathcal{V}(t) + \mathcal{W} \tag{2.26}$$

where $\mathcal{T}$ is the kinetic-energy operator, and the potential has been divided into the particle-particle interaction operator, $\mathcal{W}$, and the time-dependent external potential, $\mathcal{V}(\mathbf{r}, t)$,

$$\mathcal{V}(t) = \sum_{j=1}^{N} v(\mathbf{r}_j, t) \tag{2.27}$$

$v(\mathbf{r}_j, t)$ propagates the initial state, $\Psi(t_0) \equiv \Psi_0$ in a time interval $[t_0, t_1]$. If, initially, the

system is in its ground state, the time-dependent external potential applied to the system at time t_0 can be rewritten as,

$$v(\mathbf{r},t) = v_0(\mathbf{r}) + v_1(\mathbf{r},t)\theta(t-t_0) \tag{2.28}$$

where $\theta(t-t_0)$ is the Heaviside function, used to enforce the external potential to act only when $t = t_0$ [56].

2.3.1 The Runge-Gross Theorem

The Runge-Gross (RG) Theorem [58] sets the formal foundations of the TD-DFT approach and is equivalent to the Hohenberg-Kohn (HK) theorem for DFT. As stated above, the Schrödinger equation produces a time-dependent wavefunction $\Psi(t)$ for a given Ψ_0. It means that the time-dependent potential determines the system's dynamics. To construct a valid TD-DFT picture, the time-dependent density, $\rho(\mathbf{r},t)$, has to determine the dynamics of the system. Hence, there must be a unique correspondence between time-dependent densities and potentials, which is established by the RG theorem, that can be stated as follows [56–58]:

Runge-Gross Theorem

"Two densitites, $\rho(\mathbf{r},t)$ and $\rho'(\mathbf{r},t)$, evolving from a common initial many-body state, Ψ_0, under the influence of two different potentials $v(\mathbf{r},t)$ and $v'(\mathbf{r},t) \neq v(\mathbf{r},t)+c(t)$ (...), will start to become different infinitesimally later than t_0. Therefore, there is a one-to-one correspondence between densities and potentials for any fixed initial many-body state." [56]

The theorem implies that the time-dependent density is a univocal functional of the potential, and the opposite is also true: the external potential is a unique functional of the time-dependent density. This indicates that the many-body Hamiltonian, $\mathcal{H}(t)$, and, therefore, the many-body wavefunction $\Psi(t)$ are functional of $\rho(\mathbf{r},t)$ as well [56],

$$v(\mathbf{r},t) = v[\rho,\Psi_0](\mathbf{r},t) \Rightarrow \mathcal{H}(t) = \mathcal{H}[\rho,\Psi_0](t) \Rightarrow \Psi(t) = \Psi[\rho,\Psi_0](t) \tag{2.29}$$

As a consequence, any given physical observables, $O(t)$, become functionals of the density:

$$O(t) = \langle\Psi[\rho,\Psi_0]|\mathcal{O}(t)|\Psi[\rho,\Psi_0]\rangle = O[\rho,\Psi_0](t) \tag{2.30}$$

Formally, the RG theorem provides fundamental support for TD-DFT.

2.3.2 The time-dependent Kohn-Sham equation

The van Leeuwen theorem [59] states, in a simple manner, that the time-dependent density $\rho(\mathbf{r},t)$ of an interacting system, evolving from an initial state, Ψ_0, can be reproduced by a non-interacting system under the influence of the time-dependent potential $v(\mathbf{r},t)$. This non-interacting system evolves under the effective potential,

$$v_s[\rho,\Psi_0,\Phi_0](\mathbf{r},t) \tag{2.31}$$

where Φ_0 is the initial state of the non-interacting system. In many cases, the system is initially in the ground state at the initial time t_0 and begins to evolve after the perturbation of an external potential (recall Equation 2.28). For these cases, the HK theorem of DFT applies to the initial state, simplifying the effective potential to become a density functional only, $v_s[\rho](\mathbf{r},t)$.

The initial non-interacting wavefunction Φ_0 is a single Slater determinant constructed of N KS orbitals $\phi_j^0(\mathbf{r})$, arising from the self-consistent solution of the KS equation,

$$\left[-\frac{\nabla^2}{2}+v_{\mathrm{s}}^0\left[\rho_0\right](\mathbf{r})\right]\phi_j^0(\mathbf{r})=\varepsilon_j\ \phi_j^0\left(\mathbf{r}\right) \tag{2.32}$$

where the ground-state density is

$$\rho_0(\mathbf{r})=\sum_{j=1}^{N}|\phi_j^0(\mathbf{r})|^2 \tag{2.33}$$

and the static KS effective potential is

$$v_{\mathrm{s}}^0\left[\rho_0\right](\mathbf{r})=v_0\left(\mathbf{r}\right)+\int \mathrm{d}^3r'\frac{\rho_0\left(\mathbf{r}'\right)}{|\mathbf{r}-\mathbf{r}'|}+v_{\mathrm{xc}}^0\left[\rho_0\right](\mathbf{r}) \tag{2.34}$$

After the initial time t_0, the time-dependent potential acts upon the system, leading the density to

$$\rho\left(\mathbf{r},t\right)=\sum_{j=1}^{N}\left|\phi_j^{\mathrm{KS}}\left(\mathbf{r},t\right)\right|^2 \tag{2.35}$$

where the orbitals $\phi_j^{\mathrm{KS}}\left(\mathbf{r},t\right)$ arise from the time-dependent KS equation,

$$\left[-\frac{\nabla^2}{2}+v_{\mathrm{s}}\left[\rho\right](\mathbf{r},t)\right]\phi_j^{\mathrm{KS}}\left(\mathbf{r},t\right)=i\ \frac{\partial}{\partial t}\ \phi_j^{\mathrm{KS}}\left(\mathbf{r},t\right) \tag{2.36}$$

where the initial condition is given by $\phi_j^{\mathrm{KS}}\left(\mathbf{r},t\right)=\phi_j^0\left(\mathbf{r},t\right)$.

Therefore, only the single-particle orbitals initially occupied are time-propagated upon the resolution of Equation 2.36. The effective potential is given by,

$$v_{\mathrm{s}}\left[\rho\right]\left(\mathbf{r},t\right)=v\left(\mathbf{r},t\right)+\int\mathrm{d}^{3}r'\frac{\rho\left(\mathbf{r}',t\right)}{\left|\mathbf{r}-\mathbf{r}'\right|}+v_{\mathrm{xc}}\left[\rho\right]\left(\mathbf{r},t\right) \tag{2.37}$$

In principle, the time-dependent KS formalism leads to the exact time-dependent density of the n-electron system evolving in the external potential, starting from the ground state [56, 57].

2.3.3 Linear-Response Theory

The full resolution of the time-dependent KS scheme is rather costly and often unnecessary, especially when the system does not deviate significantly from the ground state. The Linear-Response (LR) theory is primarily employed whenever a weak perturbation is considered and is largely used in spectroscopy [56, 57].

In the TD-DFT context, the external perturbation is a scalar potential, $v_1(\mathbf{r},t)$, that starts affecting the system at the time t_0. The Hamiltonian is then,

$$\mathcal{H}_1\left(t\right)=\int\mathrm{d}^{3}r'v_1\left(\mathbf{r}',t\right)\varrho\left(\mathbf{r}'\right) \tag{2.38}$$

where $\mathbf{r}'$ is the electron position in space at the time t' when the perturbation is applied, and ϱ is the electron density operator. The system will then respond to this external perturbation that can be represented in terms of a Taylor expansion,

$$\rho(\mathbf{r},t)-\rho_0(\mathbf{r},t)=\rho_1(\mathbf{r},t)+\rho_2(\mathbf{r},t)+...+\rho_n(\mathbf{r},t) \tag{2.39}$$

where $\rho_0(\mathbf{r},t)$ is the ground-state electron density, $\rho_1(\mathbf{r},t)$ is the first-order response (linear response), $\rho_2(\mathbf{r},t)$ is the second-order response, and so on. The linear response of the density is given by,

$$\rho\left(\mathbf{r},t\right)=\int_{-\infty}^{+\infty}\mathrm{d}t'\int\mathrm{d}^{3}r'\chi_{mn}\left(\mathbf{r},\mathbf{r}',t-t'\right)v_1\left(\mathbf{r}',t'\right) \tag{2.40}$$

where the density-density response function is defined as,

$$\chi_{mn}\left(\mathbf{r},\mathbf{r}',t-t'\right)=-i\theta\left(t-t'\right)\left\langle\Psi_0\left|\left[\varrho\left(\mathbf{r},t-t'\right),\varrho\left(\mathbf{r}'\right)\right]\right|\Psi_0\right\rangle \tag{2.41}$$

The linear response to different external perturbations can be treated as the sum of perturbations $v_1(\mathbf{r}',t)\rho(\mathbf{r}')$, which gives a retarded density response at all $\mathbf{r}$ [56, 57].

Chapter 3

Internal Conversion Rate Constant Calculation Using the One-Effective Mode Marcus-Jortner-Levich Theory

3.1 Introduction

Upon irradiation with a suitable wavelength, a given molecule is excited to higher electronic states, and once there, the deactivation to low-lying energy states begins. Excited-state decay mechanisms involve a handful of competing events where two intramolecular deactivation channels are possible: radiative and nonradiative decays, as illustrated in Figure (3.1). The radiative pathway can occur through Fluorescence (F) for a transition between two states of the same spin multiplicity, or through Phosphorescence (Ph), for transitions between states with a distinct spin multiplicity. Assuming a closed shell ground state, Kasha's rule [60, 61] says that fluorescence always originates from the lowest-energy singlet state ($S_1 \rightarrow S_0$), and phosphorescence originates from the lowest-energy triplet state ($T_1 \rightarrow S_0$). However, there are examples of violation of this rule in what is called anti-Kasha transitions [62, 63]. On the other hand, the nonradiative deactivation process can occur via Vibrational Relaxation (VR), in which the system geometry relaxes within the same electronic Potential Energy Surface (PES); Internal Conversion (IC) that, like fluorescence, also happens between states with the same spin multiplicity, while the radiationless decay for different spin states is given through Intersystem Crossing (ISC) processes. The IC process occurs due to NonAdiabatic Coupling (NAC) between the states involved in the transition, while the ISC occurs due to Spin-Orbit Coupling (SOC) [64, 65]. Nevertheless, in all cases, the probability of the transition also depends greatly on the energy gap between the states involved.

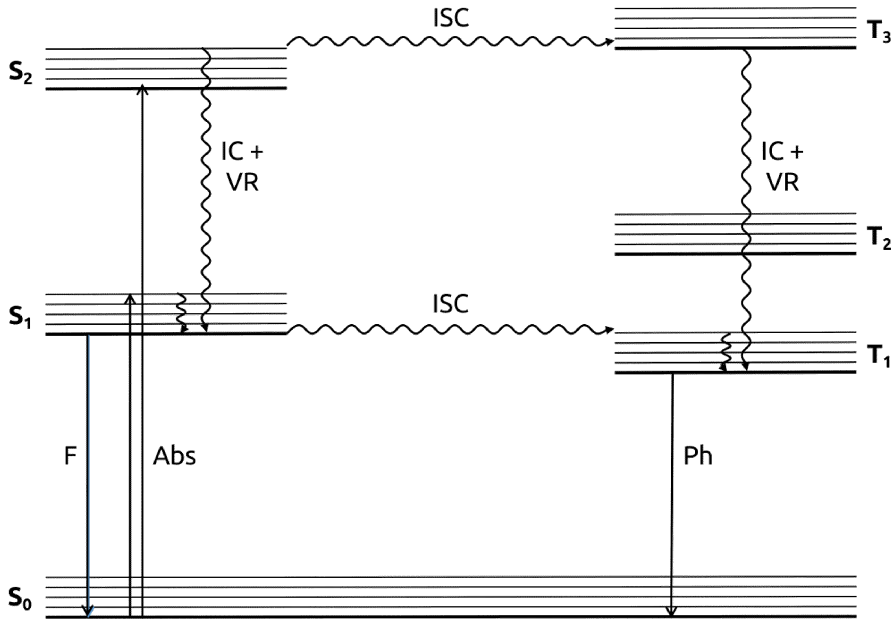

Figure 3.1: Schematic representation of a Jablonski diagram, where Abs is absorption, F is fluorescence, Ph is phosphorescence, IC is internal conversion, ISC is intersystem crossing, and VR is vibrational relaxation. Singlet states are represented by S_n, and triplet states are represented by T_n. The solid arrows indicate radiative processes, while the wavy arrows indicate non-radiative processes.

The experimental determination of nonradiative rate constants, k_{nr}, is a difficult task [66, 67]. For a small concentration of molecules, the k_{nr} can be approximated by summing the IC and the ISC rate constants, k_{IC} and k_{ISC}, respectively, and can be estimated based on the radiative quantum yields (ϕ_F and ϕ_{Ph}) and the total radiative rate constant, k_r [68]. The radiative and nonradiative rate constants can also be estimated by *ab initio* calculations [64]. The most popular method for computing radiationless decay rate constants is based on the Fermi Golden Rule, which treats the transition as a time-dependent perturbation [65]. Many authors have applied this method to determine ISC [69–72] and IC [73–75] rate constants. However, the IC rate calculation process is laborious, and several strategies have been implemented, most relying on fitting experimental parameters or on empirical constant values for sets of similar molecules [76–78], others applying the Linear Vibronic Coupling (LVC) model [79, 80].

In this chapter, we show that it is possible to use the one-effective mode Marcus-Jortner-Levich (MJL) theory for electron transfer [81] to calculate IC rate constants. We also compared the results with calculations using the semi-classical Marcus' theory [82–85], a simplified version of the former. Both theories are derived from the Fermi Golden Rule, and, despite its simplicity, Marcus' theory has been applied to ISC rate constant

calculations, yielding good results [69, 70, 86, 87]. It is known that Marcus' theory for electron transfer underestimates rate constants values for molecules within the inverted region, *i.e.*, molecules where the energy difference, $|\Delta G|$, is greater than the reorganization energy, and the MJL theory overcomes this issue by accounting for the vibronic coupling between the states involved in the transition through a correction to the density of states factor [88, 89]. However, the original reorganization energy calculation does not lead to k_{IC} values that agree with the experimentally determined ones. Hence, we propose bypassing this issue by using the Minimum Energy Conical Intersection (MECI) between the two transitional states and calculating the reorganization energy at this geometry. This approach assumes the existence of a MECI between the two states and that the mechanism for radiationless deactivation will be given by a change in geometry in the form $S_1 \rightarrow \mathrm{MECI} \rightarrow S_0$ going through an activation energy barrier for which no tunneling effects are accounted. Furthermore, the NonAdiabatic Coupling Matrix Elements (NACME) are also computed at the MECI geometry since, at this point, the NACME presents its maximum value. Nonetheless, considering that the states are only weakly coupled, and therefore, the Fermi Golden Rule can be applied, the nonadiabatic coupling calculated at the S_1 geometry does not significantly change the final rate constant. The procedure is a more direct and cheaper way to compute the internal conversion between two states of inverted-region molecules, giving good results compared with experimental values.

3.2 Light Absorption

Considering the simplest model of interaction between light and matter, where a single molecule absorbs one photon and is promoted to the excited states, the energy change in the molecule must relate to the frequency of light through the Bohr equation

$$h\nu = E_f - E_i \tag{3.1}$$

where E_f and E_i are the energy of the excited state, Ψ_f, and the ground state, Ψ_i, respectively [90]. Light absorption can be understood in terms of the time-dependent perturbation theory [65, 90] when considering the electromagnetic field interacting with a molecule. The oscillating magnetic field can be neglected compared to the electric-dipole contribution to this phenomenon in most cases. A molecule in an initial stationary state is subjected to the Schrödinger Equation 2.3. When exposed to the perturbation of light, the electric component of the light induces oscillating forces on the charged particles of the system. Therefore, the initial Hamiltonian, $\mathcal{H}_0$, no longer describes the total energy of the system and is replaced by $\mathcal{H}_0 + \mathcal{H}'$, where $\mathcal{H}'$ is the perturbation operator that accounts for the radiation interaction [64]. The eigenfunctions will be different from the

initial wavefunction, Ψ_i, and will now be functions of time. Hence,

$$(\mathcal{H}_0 + \mathcal{H}')\Psi(\mathbf{r}, t) = E\Psi(\mathbf{r}, t) \tag{3.2}$$

The new wavefunctions can be expanded in terms of the unperturbed system,

$$\Psi(\mathbf{r}, t) = \sum a_i(t)\Psi_i \tag{3.3}$$

The mixing of the ground state wave function with other states' wavefunctions can be interpreted as the initial state evolving into other states. If the perturbation is turned off at a given time t, there is a probability that the system will be at a certain final state, Ψ_f. This probability is given by the square of the coefficient $[a_f(t)^2]$, which is proportional to $\langle\Psi_i|\hat{\mu}|\Psi_f\rangle$, *i.e.* the transition moment, and $\hat{\mu}$ is the dipole-moment operator given as $e\sum \mathbf{r}_j$, where e is the electronic charge and $\mathbf{r}_j$ is the distance between the j-th electron to the center of the positive charge of the system, as

$$[a_f(t)]^2 = \frac{8\pi^3}{3h^2}\langle\Psi_i|\hat{\mu}|\Psi_f\rangle^2\rho(\nu_{if})t \tag{3.4}$$

where h is the Planck's constant, $\rho(\nu_{if})$ is the radiation density at the frequency ν_{if} corresponding to the transition, and t is the time.

Recalling the Born-Oppenheimer (BO) approximation (Equation (2.5)), light absorption occurs on a much shorter time scale, making the electron excitation much faster than the nuclear motion. Thus, the wavefunction can be separated into an electronic wavefunction, ψ, and a nuclear (vibrational) wavefunction, θ. As the dipole-moment operator is considered to be independent of the nuclear coordinates (Condon principle), it operates only on the electronic part,

$$\mu = \int \psi_i^* \ \hat{\mu} \ \psi_f \ \mathrm{d}\tau_e \int \theta_i \ \theta_f \ \mathrm{d}\tau_N \tag{3.5}$$

The electronic wavefunction can be further factorized into the product of one-electron wavefunctions, ϕ, and the corresponding spin function, S. The transition moment becomes,

$$\mu = \int \phi_i^* \ \hat{\mu} \ \phi_f \ \mathrm{d}\tau_e \int S_i^* \ S_f \ \mathrm{d}\tau_e \int \theta_i \ \theta_f \ \mathrm{d}\tau_N \tag{3.6}$$

where the first term is the *electronic transition moment*, the second term is the spin overlap integral, and the last term is the overlap integral of the initial and final wavefunctions for nuclear vibration [90].

3.3 Radiationless Decay Theory

Upon absorption of light, the probability, P, of a radiationless transition from an initial, $|i\rangle$, to a final, $|f\rangle$, state weakly coupled can be described by a first-order time-dependent perturbation theory as [64, 65]

$$P = \frac{2\pi\tau}{\hbar} \langle i \left| \mathcal{H}_{if} \right| f \rangle^2 \rho(E) \tag{3.7}$$

where τ is time, $\hbar$ is the reduced Planck's constant, $\mathcal{H}_{if}$ is the matrix element of the coupling operator between the two states, and $\rho(E)$ is the density of states per unit of energy. The total transition probability is a linear function of time and, therefore, can be conveniently written as a rate constant

$$k = \frac{P}{\tau} = \frac{2\pi}{\hbar} \langle i | \mathcal{H}_{if} | f \rangle^2 \rho(E) \tag{3.8}$$

Equation (3.8), vastly known as the *Fermi golden rule* [91], is built upon the assumptions (i) that $\tau \gg [(2\pi\hbar)/(E_f - E_i)]$; and (ii) that both $\mathcal{H}_{if}$ and $\rho(E_f)$ have a weak dependence towards the final state. For the IC process, the interaction between initial and final states is ruled by the kinetic energy operator, $\mathcal{T}$, which, under the harmonic approximation, is expressed by [64]

$$\mathcal{T} = -\sum_j \frac{\hbar\omega_j}{2} \frac{\partial^2}{\partial Q_j} \tag{3.9}$$

where ω_j and Q_j are the frequency and the dimensionless coordinates associated with the normal mode j, respectively. For the vibronic representation under the adiabatic approximation, the interaction between the initial and final states is given by

$$H_{im,fn} = -\left\langle \psi_j^{(f)} \prod_{j=1}^{N} \phi_j^{(fn)} \left| -\sum\nolimits_j \frac{\hbar\omega_j}{2} \frac{\partial^2}{\partial Q_j} \right| \psi_j^{(i)} \prod_{j=1}^{N} \phi_j^{(im)} \right\rangle \tag{3.10}$$

Here, the vibronic state is divided into electronic and vibrational contributions. The $\psi_j^{(f)}$ represents the final electronic state wavefunction at Q_j, while $\prod_{j=1}^{N} \phi_j^{(fn)}$ is the final state vibrational function, which is given as the product of all N vibrational modes, at Q_j with n occupation number for a harmonic PES approximation. The same is applicable to the initial state. By dismissing high-order terms for the interaction operator, one gets

$$H_{im,fn} = -\sum\nolimits_j \hbar\omega_j \left\langle \psi_j^{(f)} \left| \frac{\partial}{\partial Q_j} \right| \psi_j^{(i)} \right\rangle \left\langle \phi_j^{(fn)} \left| \frac{\partial}{\partial Q_j} \right| \phi_j^{(im)} \right\rangle \prod_{\substack{k=1 \\ k\neq j}}^{N} \left\langle \phi_k^{(fn)} | \phi_k^{(im)} \right\rangle \tag{3.11}$$

where $\hbar\omega_j \left\langle \psi_j^{(f)} \middle| \frac{\partial}{\partial Q_j} \middle| \psi_j^{(i)} \right\rangle$ is the electronic nonadiabatic coupling (NAC) between the initial and final states for the normal mode j. It has been demonstrated that assuming $m = 0$ is a good approximation for low temperatures [76] and that the other two integrals can be calculated analytically, showing dependence only on n, yielding

$$|\langle \phi_j^{(fn)} | \frac{\partial}{\partial Q_j} | \phi_j^{(i0)} \rangle|^2 = \frac{1}{2n!}(n - S_j)^2 S_j^{n-1} \exp(-S_j) \tag{3.12}$$

$$|\langle \phi_k^{(fn)} | \phi_k^{(i0)} \rangle|^2 = \exp(-S_k) \frac{S_k^n}{n!} \tag{3.13}$$

where S_j is the Huang-Rhys factor computed over each normal mode j and can be calculated by projecting the reaction coordinate vectors onto the normal mode coordinate displacement vectors [92, 93]. Equation (3.13) is usually recognized as the Franck-Condon (FC) factor. Under these approaches, equation (3.8) for the rate constant can be rewritten as

$$k = \frac{2\pi}{\hbar} \sum_n \left| \sum_j \mathrm{NAC}_j \left\langle \phi_j^{(fn)} \middle| \frac{\partial}{\partial Q_j} \middle| \phi_j^{(i0)} \right\rangle \prod_{\substack{k=1 \\ k \neq j}}^{N} \left\langle \phi_k^{(fn)} | \phi_k^{(i0)} \right\rangle \right|^2 \rho(E) \tag{3.14}$$

A valid assumption is to consider that the modes inducing the transition (*i.e.*, NAC $\neq$ 0) and the ones accepting the electronic energy ($S_j \neq 0$) are not the same [76, 94]. In this case, equation (3.12) does not vanish only for $n = 1$ and contributes with 1/2. Also, the density of states is calculated over the energy difference between the two electronic states and corrected by the vibrational levels in the so-called energy-shifted Franck-Condon Weighted Density (FCWD) [76]. The rate equation then becomes

$$k = \frac{\pi}{\hbar} \sum_{\substack{j \\ \mathrm{NAC}_j \neq 0}} |\mathrm{NAC}_j|^2 \sum_n \left| \prod_{\substack{k=1 \\ S_k \neq 0}}^{N} \left\langle \phi_k^{(fn)} | \phi_k^{(i0)} \right\rangle \right|^2 \rho\left(E_f - E_i + \sum_k n\hbar\omega_k \right) \tag{3.15}$$

Note that, according to equation (3.15), the rate constant is obtained as a summation over all normal modes of the molecule, which imposes limitations for large systems. An alternative procedure would be to perform the calculation only on the normal modes leading to appreciable vibronic coupling, but we usually do not know this information *a priori*.

Another approach to computing the rate constant for radiationless deactivation involving two electronic states is to borrow concepts from the Marcus electron transfer theory. Marcus considered that the vibronic transition scale is considerably smaller than any

other vibronic energy scale and, within this semiclassical limit, equation (3.8) is obtained as [82–85]

$$k_{T,\text{Marcus}} = \frac{2\pi}{\hbar}|\mathcal{H}_{if}|^2 \frac{1}{\sqrt{4\pi\lambda_\text{M} k_\text{B} T}} \exp\left(\frac{-(\Delta G^\circ + \lambda_\text{M})^2}{4\lambda_\text{M} k_\text{B} T}\right) \tag{3.16}$$

where k_B is the Boltzmann's constant, λ_M is the reorganization energy, and ΔG° is the adiabatic energy difference between the relaxed structure of the initial and final electronic states calculated as shown in Figure (3.2). The reorganization energy, λ_M, is the energy required to relax the structure and the environment upon electron transfer and is computed as the energy difference between the final electronic state in its equilibrium geometry and in the equilibrium geometry of the initial state. Equation (3.16) is largely applied to electron transfer problems [86, 95–98], but has also been extended to ISC rate constant calculations [69, 70, 86], where the coupling matrix element is derived from the SOC.

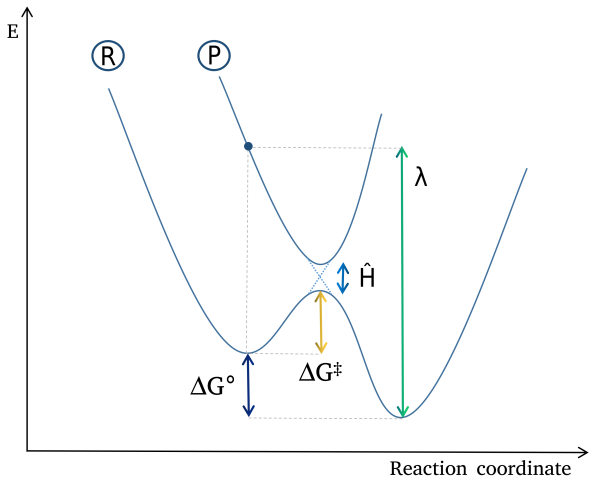

Figure 3.2: Representation of the reactant and product adiabatic surfaces and the avoided crossing between them, where $\hat{H}$ is the nonadiabatic coupling, ΔG° is the adiabatic energy difference, $\Delta G^\ddagger$ is the activation energy, and λ_M is the inner-sphere reorganization energy.
Reprinted with permission from J. Chem. Theory Comput. 2023, 19, 8, 2316–2326 [24].
Copyright (2023) American Chemical Society.

Usually, the simplified version (equation (3.16)) underestimates the transition rate constant for molecules belonging to the Marcus' inverted region, which is characterized by $-\Delta G^\circ > \lambda_\text{M}$ (Figure 3.3 C) [88, 89].

The MJL Full-Active-Space (FAC) theory still considers the semiclassical form for the rate constant. However, it overcomes the deviation from experimental values for the inverted region by accounting for the vibronic coupling between the states, still under the harmonic approximation, and by separating the total reorganization energy into λ_V

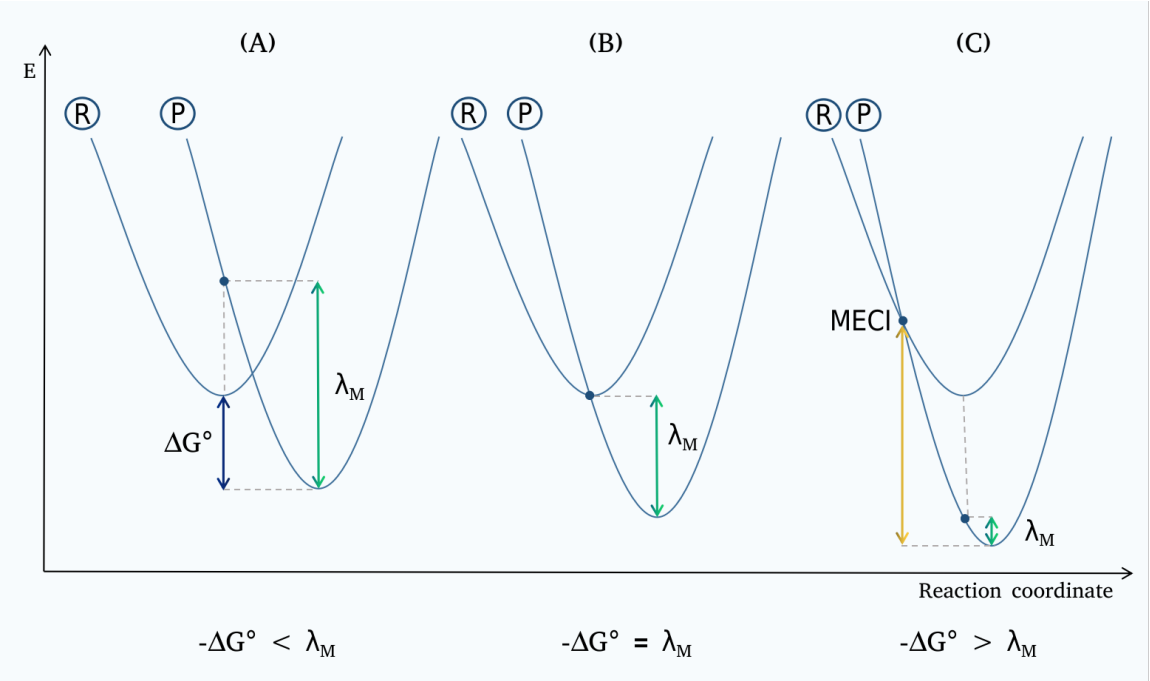

Figure 3.3: Reorganization energy for different Marcus regions, where ΔG° is the adiabatic energy difference, λ_M is the inner-sphere reorganization energy, and MECI is the Minimum Energy Conical Intersection. (A) represents the normal region, where $-\Delta G^\circ < \lambda_\mathrm{M}$; (B), the region where $-\Delta G^\circ = \lambda_\mathrm{M}$; and (C), the inverted region, where $-\Delta G^\circ > \lambda_\mathrm{M}$.

(inner-sphere) and λ_S (outer-sphere) [81].

$$k_{T,MJL,FAS} = \frac{\pi}{\hbar}|\mathrm{NAC}|^2 \frac{1}{\sqrt{4\pi\lambda_S k_\mathrm{B} T}} \exp\left(\sum_{j=1}^{N} - S_j\right) \sum_{n_1=0}^{\infty} \cdots \sum_{n_2=0}^{\infty} \cdots \sum_{n_N=0}^{\infty} \times \left(\prod_{j=1}^{N} \left(\frac{S_j^{n_j}}{n_j!}\right) \exp\left(\frac{-(\Delta G^\circ + \lambda_S + \sum_{j=1}^{N} n_j \hbar\omega_j)^2}{4\lambda_S k_\mathrm{B} T}\right)\right) \tag{3.17}$$

The similarities between equations (3.17) and (3.15) are apparent. Computing the FAC-based equation is, however, considerably time-consuming as the summations go over the vibrational quantum number, n_j, of each vibrational mode, j, and, therefore, its computational cost increases drastically for larger molecules. Nonetheless, it has been demonstrated by Closs *et al.* that approximating the FAC theory by a one-effective mode yields good results [99, 100]. In fact, many authors have been using this approach in miscellaneous problems involving charge transfer and photoinduced processes [101–103]. Therefore, the one-effective mode equation reads

$$k_{T,\mathrm{MJL,eff}} = \frac{\pi}{\hbar}|\mathrm{NAC}|^2 \frac{1}{\sqrt{4\pi\lambda_\mathrm{M} k_\mathrm{B} T}} \sum_{n=0}^{\infty} \exp(-S)\frac{S^n}{n!} \exp\left(\frac{-(\Delta G^\circ + \lambda_\mathrm{M} + n\hbar\omega_\mathrm{eff})^2}{4\lambda_\mathrm{M} k_\mathrm{B} T}\right) \quad (3.18)$$

where S is the summation over all S_j and ω_eff is calculated based on the Huang-Rhys (HR) factors as,

$$\omega_\mathrm{eff} = \frac{\sum_{j=1}^{N} S_j \omega_j}{\sum_{j=1}^{N} S_j} \quad (3.19)$$

In this work, we show that, by extending the Fermi golden rule under the one-effective mode MJL approximation, it is possible to calculate the IC rate constants in good agreement with previous theoretical works and experimental data. Furthermore, we also demonstrate that to do so, the reorganization energy has to be calculated regarding the minimum energy conical intersection involving the initial and final states (Figure 3.3 C). The reorganization energy calculated regarding the MECI geometry imposes a correction to the whole density of states factor rather than just the reorganization energy itself, and so equation (3.18) is rewritten as,

$$k_\mathrm{IC} = \frac{\pi}{\hbar}|\mathrm{NAC}|^2 \frac{1}{\sqrt{4\pi\lambda_\mathrm{MECI} k_\mathrm{B} T}} \sum_{n=0}^{\infty} \exp(-S)\frac{S^n}{n!} \exp\left(\frac{-(\Delta G^\circ + \lambda_\mathrm{MECI} + n\hbar\omega_\mathrm{eff})^2}{4\lambda_\mathrm{MECI} k_\mathrm{B} T}\right) \quad (3.20)$$

here, only the inner-sphere reorganization energy is calculated, which is given as the difference between the minimum energy conical intersection energy and the minimum PES energy of the final state, and the NAC is computed at the MECI geometry.

3.4 Computational Details

In order to test the validity of this approach, we considered the molecules illustrated in Figure (3.4). The set of molecules includes Benzophenone, Naphthalene, Psolarene, Dibenzoxalene, 1-Aminonaphthalene (1AN), 1-Dimethylamino-4-cyanonaphthalene (14DMCN), and *Tris*(2,2'-bipyridine)ruthenium(II). Besides having their photophysics largely described by both experimental and theoretical works [64, 73, 76, 78, 104–108], their shared characteristic is the aromatic moiety, which carries an expressive rigidity when compared to others. This rigidity is responsible for the small change in geometry between different states PES, culminating in a small reorganization energy, λ_M. Therefore, these molecules are grouped in the Marcus inverted region. The main electronic transition for the set of organic molecules involves the first singlet excited state ($S_1 \rightarrow S_0$), which is

essentially $\pi \rightarrow \pi^*$ in nature and, therefore, these two states were chosen for the internal conversion study reported here. It is worth mentioning that, however, Benzophenone is an exception to this, and its photophysics can also proceed involving the $n \rightarrow \pi^*$ state or even through a three-state quasi-degeneracy region involving both singlet and triplet manifolds [73]. In our calculations, the transition is represented by both $n \rightarrow \pi^*/\pi \rightarrow \pi^*$ meaning major and minor contributions, respectively. For the $[Ru(bpy)_3]^{2+}$, the S_1 state is MLCT (metal-ligand charge transfer) in nature. The first triplet excited state of the molecules was also investigated.

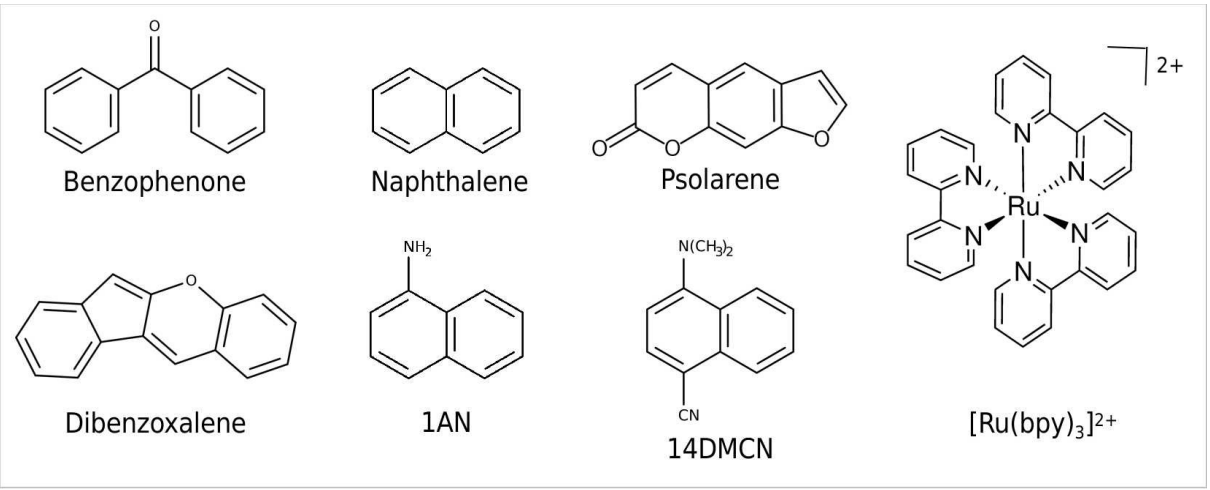

Figure 3.4: The set of Marcus inverted region molecules for the IC rate constant calculation in this work. The molecules are: Benzophenone, Naphthalene, Psolarene, Dibenzoxalene, 1-Aminonaphthalene (1AN), 1-Dimethylamino-4-cyanonaphthalene (14DMCN), and Tris(2,2'-bipyridine)ruthenium(II).
Reprinted with permission from J. Chem. Theory Comput. 2023, 19, 8, 2316–2326 [24].
Copyright (2023) American Chemical Society.

Full unconstrained geometry optimizations and frequency calculations for states S_0, S_1, and T_1 for all molecules were carried out using the ORCA-5.0.3 software [109, 110]. Density Functional Theory (DFT), both time-dependent and independent, was used with the hybrid functional B3LYP [111]. The Ahlrichs full-electron def2-TZVP(-f) basis set [112] was used for all atoms, and the calculations included the Grimme's D3 dispersion correction [113] with the Becke-Johnson (BJ) damping [114]. Coulomb integrals were sped up by RI approximation [115] using def2/J as an auxiliary basis set [116]. The Tamm-Dancoff approximation (TDA) [117] was used to calculate the excited state. The conductor-like polarizable continuum model (C-PCM) [118] was used to perform all calculations for the $[Ru(bpy)_3]^{2+}$ complex to simulate water solvation. For this case Linear response (LR-CPCM) formalism [119] was used for both geometry optimization and excitation energies within the equilibrium and nonequilibrium regimes, respectively. The properties of the organic molecules were calculated in the gas phase. The free energies,

ΔG°, of all molecules, were calculated as shown in Figure (3.2), as the adiabatic energy difference between the equilibrium geometries of S_0 and S_1 states.

The classical Marcus reorganization energies, λ_M, were calculated in order to check whether the molecules were grouped in the Marcus inverted region. Single point energy calculations were performed for the S_0 state at the S_1 equilibrium geometry ($S_0@S_1$) at B3LYP/def2-TZVP(-f) level of theory. Then, λ_M was determined as the energy difference in the S_0 PES at S_1 and S_0 equilibrium geometries, given as

$$\lambda_M = S_0@S_1 - S_0@S_0 \tag{3.21}$$

which considers only the inner-sphere contribution [120–123].

The minimum energy conical intersection reorganization energies, λ_{MECI}, proposed in this work, were calculated as follows,

$$\lambda_{MECI} = E_{MECI} - S_0@S_0 \tag{3.22}$$

where E_{MECI} is the energy computed at the minimum energy conical intersection geometry between the S_0 and S_1 states. The idea is that, when computing the reorganization energy at this point of maximum nonadiabatic coupling, a correction to the whole density of states factor (equation 3.20) is imposed, rather than just on the reorganization energy itself. This reorganization energy can be viewed as the energy necessary to relax the structure to the final S_0 state from the minimum energy conical intersection point. Although TDDFT can be used to determine the minimum energy conical intersection between two PES, it might predict the wrong dimensionality for the intersection space. In this case, the Spin-Flip TD-DFT (SF-TD-DFT) [124] method is advised, which uses the T_1 state as the reference state, and calculates both the S_0 and S_1 as excited states. The method of the gradient projection (GP) [125] was used to find the MECI point. Once the MECI geometries and the λ_{MECI} were determined, the NAC was calculated between the ground state and the first singlet excited state [126] at the MECI geometry for each molecule.

To determine the HR factor for each molecule, we used the Dushin code [93]. To do so, we calculated the S_0 and S_1 normal mode frequencies at their respective equilibrium geometries at B3LYP/6-31G* level of theory for the organic molecules and the bpy ligand of the complex, while the Ru was treated with LANL2DZ and the pseudo-potential [127] using the Gaussian09 software [128].

The k_{IC} was computed using a FORTRAN95-built code. Although it is a very simple and straightforward calculation, we are open to sharing the code with the community. It is printed in the Appendix B under section B.1.2, or it can be downloaded at https://ecsmolab.qui.ufmg.br/index.php/download/programa-kic/ for a more

complete usage description.

3.5 Results and discussion

Free Energies and Frequencies

The free energies of all molecules were calculated as the adiabatic energy difference between the equilibrium geometries of the S_0 and S_1 states and are shown in Table (3.1). As expected, the ΔG° values are negative, indicating an exergonic process, considering that the initial states are higher in energy than the final states. Table (3.1) also shows the Marcus reorganization energy values calculated using equation (3.21), which are considerably lower than their corresponding free energy moduli. This indicates that the molecules are, in fact, located at the Marcus inverted region.

Table 3.1: Calculated adiabatic difference between S_0 and S_1, ΔG°, in eV, and reorganization energy, λ_M, in eV, for each molecule.

Molecule	ΔG° (eV)	λ_M (eV)
Benzophenone	−3.295	0.395
Naphthalene	−4.375	0.104
Dibenzoxalene	−2.095	0.555
Psolarene	−3.477	0.460
1AN	−3.656	0.321
14DMCN	−2.909	0.639
$[Ru(bpy)_3]^{2+}$	−2.303	0.198

Huang-Rhys Factor and Effective Frequency

The total HR factors and effective frequencies for the set of molecules are shown in Table (3.2). The effective frequency has an expressive dependence on the HR factor, as demonstrated in equation (3.19), and only values of $S_j \geq 0.03$ were considered representative, as discussed before by Chaudhuri and coworkers [88], meaning these are the normal modes that contribute most to the transition by accepting the electronic energy, especially for molecules of the Marcus inverted region.
The effective frequencies range from 1539.6 cm^{-1} to 137.4 cm^{-1}, which is far from the characteristic frequencies of C−H bond displacements for organic molecules, suggested to be responsible for the radiationless deactivation of the excited states [106, 129–131].

Besides the HR factor and the effective frequency, the occupation number also reflects on the IC rate constant. Small values of S_j are associated with a major contribution from $n = 0$, while larger values of S_j have more contributions from other excited vibrational

Table 3.2: The calculated Huang-Rhys (HR) factors and effective frequencies, $\tilde{\omega}_{\text{eff}}$, in cm^{-1} for each molecule.

Molecule	HR Factor	$\tilde{\omega}_{\text{eff}}$ (cm^{-1})
Benzophenone	2.296	1539.6
Naphthalene	0.828	844.9
Dibenzoxalene	5.155	540.9
Psolarene	4.764	502.3
1AN	4.197	284.2
14DMCN	55.531	137.4
$[Ru(bpy)_3]^{2+}$	2.769	314.5

levels. This tendency can be observed in Figure (3.5), which shows the convergence of the FCWD factor as a function of n. All molecules but 14DMCN show full convergence at $n < 15$, which agrees with a small total HR factor (< 6), naphthalene being the molecule with the lowest HR factor and the fastest convergence. On the other hand, 14DMCN converged for $n > 65$, showing an expressively high HR factor of 55.531.

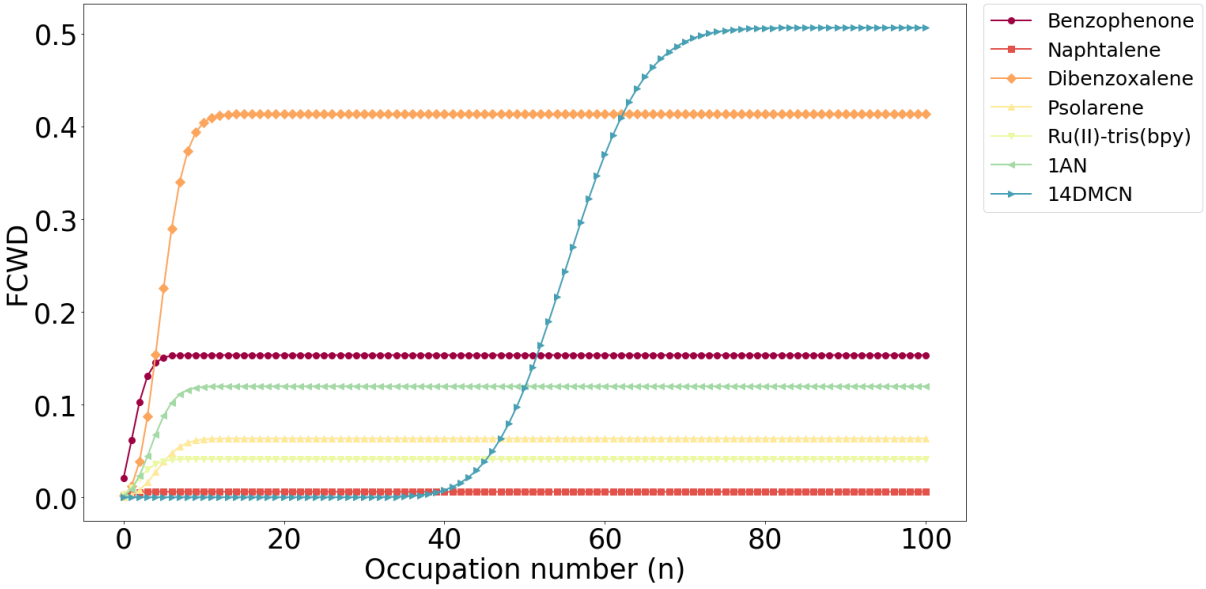

Figure 3.5: Convergence of the Franck-Condon Weighted Density (FCWD) given as a function of the vibrational quantum number, n.

Minimum Energy Conical Intersection, Reorganization Energy, and Nonadiabatic Couplings

The Marcus inverted region is majorly composed of molecules containing rigid moieties. Hence, their equilibrium geometries for ground and excited states are virtually the same, showing minimal differences. Consequently, the classical reorganization energy can be considerably lower than the free energy, and the density of states can be compromised. Instead, by considering that the transition will follow the mechanism $S_1 \rightarrow$ MECI $\rightarrow S_0$ and will not deactivate by tunneling, the density of states can be corrected by using the minimum energy conical intersection point between the two states involved in the transition. As shown in Figure (3.6), the ground and first excited singlet states present almost identical equilibrium geometries. The only molecule showing worth-mentioning change is 14DMCN, for which the S_1 geometry presents a tilt on the amine group compared to the S_0 geometry. Contrasting, the MECIs present significant changes in their geometries. Interestingly, these changes show minor contributions from C−H bond stretching, meaning other normal modes can induce the decay.

For benzophenone, it has been previously demonstrated a small difference in the C=O bond length, and the angle between the two aromatic rings for states S_0 and S_1 (1.23 Å and 50°; 1.32 Å and 40°, respectively) [73], which was reproduced in our calculations (1.219 Å and 55.28°; 1.315 Å and 40.23°, respectively), while the minimum energy conical intersection geometry shows C=O bond length of 1.627 Å and dihedral angle between the rings of 0.112°. The C=O bond stretching occurs for normal modes between 1282.7 cm^{-1} and 1612.6 cm^{-1}, a frequency range that comprises the effective frequency calculated for this molecule, suggesting these are the modes most contributing to the internal conversion.

Naphthalene, 1AN, and 14DMCN share the same framework composed of two rings forming an aromatic moiety and, therefore, present similar distortions for the minimum energy conical intersection geometry. The change is observed as a torsion of the ring possessing substituent groups for 1AN and 14DMCN. Such a difference is not noticed between the equilibrium geometry of states S_0 and S_1 of the molecules. Although geometry distortions are similar, each molecule's effective frequency differs significantly. Nonetheless, all the effective frequencies correspond to normal modes where hydrogens or the CN group, for the 14DMCN, bounce off of the ring plane, implying a distortion on that ring. The frequency values differ due to different groups binding to the framework, which will affect bond strength and length.

For dibenzoxalene, a molecule even more rigid, the conformational change towards the minimum energy conical intersection appears as bond length stretching, which occurs at the five-membered ring, where the minimum energy conical intersection geometry shows a C−C bond length of 1.575 Å neighboring the oxygen-containing ring. For the S_0 and

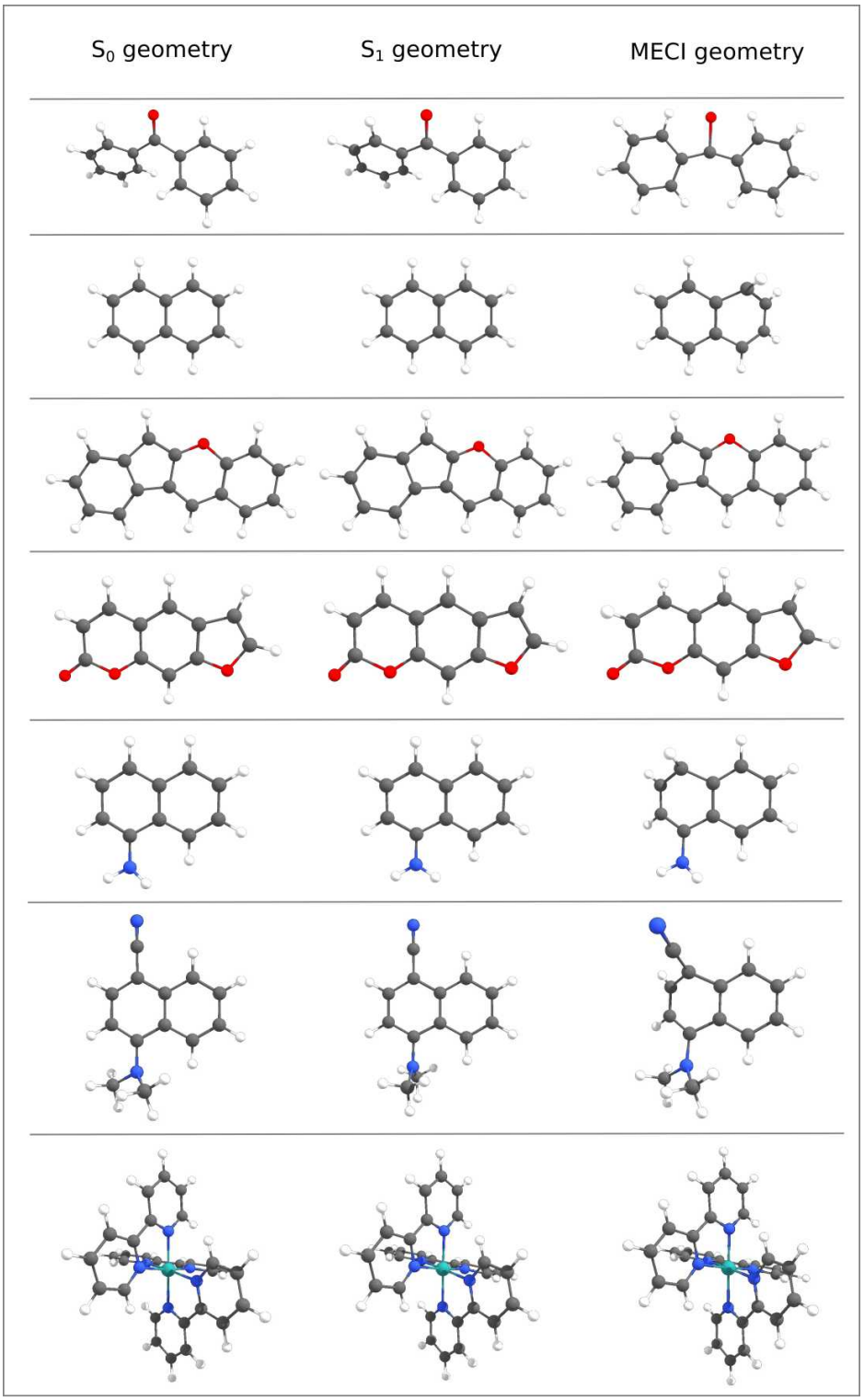

Figure 3.6: Equilibrium geometries of states S_0 and S_1 and minimum energy conical intersection geometry of benzophenone, naphthalene, dibenzoxalene, psoralene, 1AN, 14DMCN, and $[Ru(bpy)_3]^{2+}$, respectively.
Reprinted with permission from J. Chem. Theory Comput. 2023, 19, 8, 2316–2326 [24].

the S_1 states, the same bond has lengths of 1.354 Å and 1.438 Å, respectively. The effective frequency of 540.9 cm^{-1} for this molecule corresponds to angular distortions of the five-membered ring; however, the referenced bond stretching occurs at 1641.8 cm^{-1}.

Although psoralene also possesses a rigid framework like dibenzoxalene, its minimum energy conical intersection geometry shows an off-plane distortion where the two hydrogens of the lactone ring form a dihedral angle of 85.31°. Such distortion is partially given by a normal mode at 535.3 cm^{-1}, which is considerably close to the calculated effective frequency.

The $[Ru(bpy)_3]^{2+}$ is a more complex molecule containing a metal center. Nevertheless, besides its complexity, the bipyridine ligand is aromatic, a characteristic of all molecules presented here. This feature allocates this metal complex at the inverted region and shows very restricted changes, being the most pronounced effect a small twist on the ligands, which are no longer with their rings aligned. Such distortion is seen in several normal modes, all below 730 cm^{-1}, where some are below, and others are above the effective frequency calculated (314.5 cm^{-1}).

Table (3.3) shows the corrected reorganization energy calculated regarding the minimum energy conical intersection point for each molecule. The λ_{MECI} energy is up to ten times greater than the classical reorganization energy, being closer to the free energy values. However, it is not responsible for correcting the FCWD factor alone, as the density of states is also corrected by the HR factor and the introduction of an effective frequency. The effect will be clearer in the next section.

Table 3.3: The calculated corrected reorganization energy, λ_{MECI}, in eV and the nonadiabatic coupling, |NAC|, in cm^{-1} for each molecule.

Molecule	λ_{MECI} (eV)	|NAC| (cm^{-1})
Benzophenone	4.189	0.40
Naphthalene	3.099	0.46
Dibenzoxalene	1.707	2.06
Psolarene	2.621	0.88
1AN	2.868	0.63
14DMCN	2.503	0.66
$[Ru(bpy)_3]^{2+}$	3.348	1.00

It is also interesting to note that even though the nonadiabatic couplings between the S_1 and S_0 states were calculated at the minimum energy conical intersection geometries, the coupling values were low, indicating that the states are weakly coupled, and the Fermi Golden Rule is applicable.

Internal Conversion Rate Constant

Table (3.4) shows the experimental IC rate constants for the set of molecules. It also shows k_{IC} calculated in previous works, and the results calculated using the one-effective mode MJL and the classical Marcus equation, using the λ_{MECI}. At first glance, it is noticeable that the IC rate constants calculated by the one-effective mode MJL theory are consistent and agree with the experimental values, with few discrepancies. Furthermore, the semi-classical Marcus equation also yielded good results but presented a larger deviation from experimental values.

Table 3.4: Experimentally determined internal conversion rate constants, k_{IC}^{exp}, in s^{-1} and calculated internal conversion rate constants, k_{IC}^{calc}, in s^{-1} for each molecule.

Molecule	$\log(k_{IC}^{exp}/s^{-1})$	$\log(k_{IC}^{calc}/s^{-1})^a$	$\log(k_{IC}^{calc}/s^{-1})^b$	$\log(k_{IC}^{calc}/s^{-1})^c$
Benzophenone	< 7 [64, 104]	6.55 [73]	6.50	7.20
Naphthalene	5.30 [106, 132]	-4.21 [76]	5.27	5.91
Dibenzoxalene	11.89 [76]	9.66 [76]	8.54	8.53
Psolarene	-	5.70 [106]	6.89	7.27
1AN	6.30 [107]	7.39 [78]	6.87	7.37
14DMCN	8.55 [107]	10.92 [78]	7.57	8.06
$[Ru(bpy)_3]^{2+}$	6.12 [108]	-	6.76	7.07

[a] Calculated in other works; [b] Calculated in this work using the one-effective mode MJL theory. [c] Calculated in this work using the classical Marcus theory.

Although all molecules but $[Ru(bpy)_3]^{2+}$ were calculated using gas-phase, the agreement with experimentally determined values varied. Benzophenone and naphthalene presented the closest results between the experimentally determined and the calculated through one-effective mode MJL k_{IC}. The experimental results for benzophenone were obtained in liquid paraffin [104]. However, Marazzi and coworkers demonstrated that the solvent nature does not affect the qualitative and semiquantitative optical properties of this molecule [133], which has been confirmed by Shizu and Kaji [73]. For naphthalene, the experimental k_{IC} was estimated by Valiev *et al.* using the experimental fluorescence lifetime and quantum yield values [106, 132]. Although the experiments were performed in cyclohexane, the theoretical constant value calculated in gas-phase also agrees with it, suggesting that the solvent does not play an important role in the photophysics of the molecule. In fact, both the cyclohexane and liquid paraffin are apolar solvents and are expected to interact with the medium weakly.

On the other hand, dibenzoxalene is the molecule that presented the worst agreement between the experiments and the calculations. However, it is interesting mentioning that the value presented in Table (3.4) refers to the total experimental nonradiative rate constant, k_{nr}, which accounts for both k_{IC} and k_{ISC}, as previously mentioned. In this case,

it is expected for the k_{IC} to be lower than the total nonradiative constant. Furthermore, Valiev *et al.* calculations also predicted a considerably lower internal conversion rate constant [106], suggesting our estimations are consistent. Besides, it is possible that the dibenzoxalene photophysical properties are more dependent on the solvent nature, even though the experiments were reported to be performed in cyclohexane.

The dependence on the solvent nature is well illustrated for the 1AN and 14DMCN molecules, and the reported experimental rate constants in Table (3.4) refer to acetonitrile as the solvent. However, the authors also reported rate constants determined in hexane and diethyl ether, resulting in different k_{IC} values. For 1AN and 14DMCN the $\log(k_{IC})$ in hexane were 7.14 s^{-1} and 11.24 s^{-1}, respectively, while in diethyl ether the values were 7.04 s^{-1} and 9.72 s^{-1}, respectively [107]. While our calculations performed in gas-phase are closer to the experimental values performed in acetonitrile, the calculated values by Kohn *et al.* [78], also presented in Table (3.4), are considerably higher, especially for 14DMCN, which agrees with experimental values performed on hexane by Suzuki *et al.* [107]. Nonetheless, their work does not mention whether the calculations considered any solvation method.

The estimated IC rate constant of psoralene was higher than the one previously calculated by Valiev *et al.* [106]. The authors made systematic comparisons with other coumarins [134] and evaluated the consistency of their methods based on experimental fluorescence and quantum yields. The solvation methods were not explicitly mentioned.

As for the dibenzoxalene, the $[Ru(bpy)_3]^{2+}$ experimentally determined rate constant was also given in terms of the total nonradiative decay in water [108]. Although our calculations used implicit solvation to simulate the environment, the k_{IC} value was higher than the experimental k_{nr} for both methods. Ruthenium complexes with nitrogen-containing conjugated ligands are known for their high performance as photosensitizers [23], which are characterized by a strong spin-orbit coupling between excited singlet-triplet states, which is translated into high k_{ISC}. It suggests that even though the k_{IC} calculated for this compound is close to the k_{nr}, the methods hereby used overestimates the rate constant value.

As an overall result, the classical Marcus theory predicted higher rate constants compared to the one-effective mode MJL, which is the opposite of expected since the MJL proposition was to avoid underestimations for the inverted region. However, it is wise to keep in mind that these formulations were originally proposed for electron-transfer problems.

3.6 Conclusions

In this work, we have applied the classical Marcus theory and the one-effective mode MJL theory for electron transfer to calculate the internal conversion rate constant of $S_1 \rightarrow S_0$ deactivation of a set of molecules of the inverted region. To do so, we incorporated a correction to the density of states by using the minimum energy conical intersection energies to determine the new reorganization energy. In general, both theories yielded good results that are in agreement with the experimental rate constants of each molecule, although the Marcus theory presented a higher overestimation for k_{IC}. Besides, the results were comparable to previously calculated rate constants computed with a handful of methods already described.

These results showed that the use of minimum energy conical intersection energies on the reorganization energy is a good estimation to correct the density of states. Furthermore, the HR factor and the effective frequencies also contributed to refining the corrections. It was seen that each molecule has a unique effective frequency that corresponds to a combination of normal modes that not necessarily matches the X−H bond stretching, as previously suggested.

Chapter 4

Excited-State Decay Mechanism of Complex Systems: A Kinetic Model

4.1 Introduction

The photoexcitation of compounds such as dyes, porphyrins, and metal complexes unlocks a set of possibilities for new physical and chemical processes that are otherwise inaccessible, enabling advances in many different areas of physics, chemistry, biological sciences, and engineering [5–7, 9–19, 21, 39, 64, 69, 87, 135–137]. Consequently, elucidating the photophysical processes that dictate the dynamics of excited states in these systems is of paramount significance, allowing the design of photoactive species to target specific features.

As mentioned in Chapter 3, the experimental determination of rate constants is usually given in terms of the total radiative and nonradiative rate constants, k_{r} and k_{nr}, respectively, which are calculated with quantum yields and luminescence lifetimes [66–68]. In this sense, it is hard to have a detailed photophysical profile of a given system. On the other hand, theoretical investigation of the excited-state dynamics of a system is held under the light of nonadiabatic excited-state molecular dynamics calculations [138], which offer a handful of different approaches but are not computationally cost-effective for systems containing more than a few atoms, especially when transition metal atoms are included.

When dealing with transition-metal complexes, the nature of the transitions and excited states are more vast than those of organic compounds. While the latter is mainly composed of $\pi \rightarrow \pi^*$ and $n \rightarrow \pi^*$, the former can be Metal-to-Ligand Charge Transfer (MLCT), Ligand-to-Metal Charge Transfer (LMCT), local excitation or IntraLigand (IL), Metal-Centered (MC), and Ligand-to-Ligand Charge Transfer (LLCT), as shown in Figure 4.1.

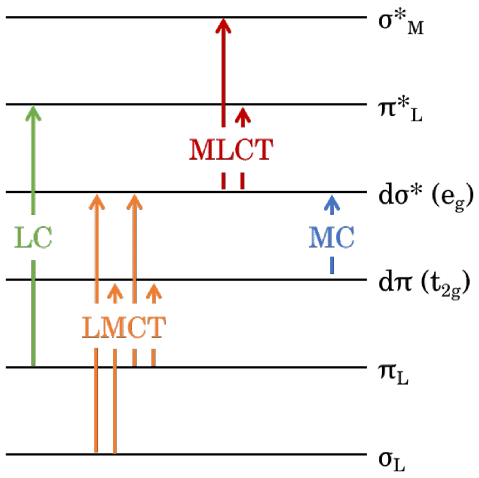

Figure 4.1: Main electronic transitions on transition metal complexes: MLCT (Metal-to-Ligand Charge Transfer), LMCT (Ligand-to-Metal Charge Transfer), IL (IntraLigand) or LC (Ligand Centered), and MC (Metal-Centered).

Ruthenium complexes featuring polypyridyl ligands have been widely studied and are very well described in many works [1, 64, 69, 139–144]. A remarkable characteristic of such compounds is their MLCT transitions in the singlet and triplet manifolds. A second important transition is of IL nature, occurring more often for heteroleptic complexes with extended conjugation [39, 140, 142, 145]. For homoleptic complexes, specially formed with ligands such as tap (1,4,5,8-tetraazaphenanthrene), bpy (2,2'-bipyridine), phen (1,10-phenantroline), and bpz (2,2'-bipyrazyl), additional thermally-activated MC transitions are also observed, adding another deactivation channel to the decay pathway.

In this chapter, the dynamics of an excited-state decay of a fairly large and complex system are described in detail through the calculation of the radiative and nonradiative rate constants of all photophysical processes of a collection of crucial low-lying excited states at their respective Franck-Condon region. After determining all the rate constants, the excited-state decay over time is modeled using a first-order kinetic model. The excited-state population evolution shows not only the major deactivation channel but also all the secondary states that contribute to the decay pathway and maps the alternative channels that can lead to side photochemical products. As an example, we have chosen the complex $[Ru(bpz)_3]^{2+}$, illustrated in Figure 4.2. This complex has been extensively studied both experimental and theoretically in many works [142–144, 146, 147] and serves as a guide to our findings. It will be demonstrated that calculating the rate constants and applying the kinetic model offers a computationally cheaper, but still accurate, way to investigate more complex and larger systems that are of interest to broad applications involving photoinduced processes, widening the understanding of such compounds and directing to specific chemical and structural properties tuning.

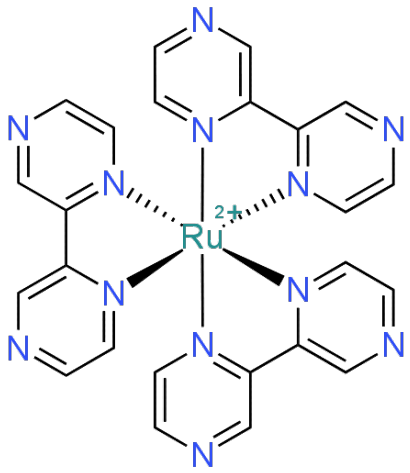

Figure 4.2: The $[Ru(bpz)_3]^{2+}$ complex structure (bpz = 2,2'-bipyrazyl).
Reprinted with permission from Phys. Chem. Chem. Phys., 2025, 27, 9806-9816 [38].
Copyright (2025) Royal Society of Chemistry.

4.2 Radiative Decay

In Chapter 3, the radiationless decay was discussed as a competing deactivation process upon light absorption from a low-energy to a high-energy state of a given system. As mentioned, other deactivation channels are also present, such as vibrational relaxation and radiative decay (fluorescence and phosphorescence). These processes combined describe the photophysics of a system and open the possibility of a kinetic description of the phenomenon.

The radiative decay rate constant for a spontaneous emission from an initial excited state, i, to a final ground state, f, is given by a first-order kinetic process as

$$\frac{dN_i}{dt} = -N_f A_{if} \tag{4.1}$$

where N_i is the population of the initial state, N_f is the population of the final state, and A_{if} is the Einstein Coefficient [148, 149]. A_{if} can be calculated according to

$$A_{if} = \frac{(E_f - E_i)^3}{3\varepsilon_0 \pi \hbar^4 c^3} |\mu_{if}|^2 \tag{4.2}$$

where E_f is the energy of the final state, E_i is the energy of the initial state, ε_0 is the electrical permittivity of free space, $\hbar$ is the reduced Planck constant, c is the speed of light in vacuum, and μ_{if} is the transition electric dipole moment calculated as $\langle S_f|\mu|S_1\rangle @ S_f$ at the S_1 geometry.

4.3 The Kinetic Model

As discussed so far, two unimolecular processes, *i.e.*, the radiative and the radiationless decays, and photochemical reactions compete for the deactivation of any molecule in the excited state. Therefore, the rate constants of such processes and the kinetics of the competition are paramount in determining the photophysics and the reaction pathways of any excited system. Figure 4.3 illustrates the possible deactivation channels a given system or molecule can undergo.

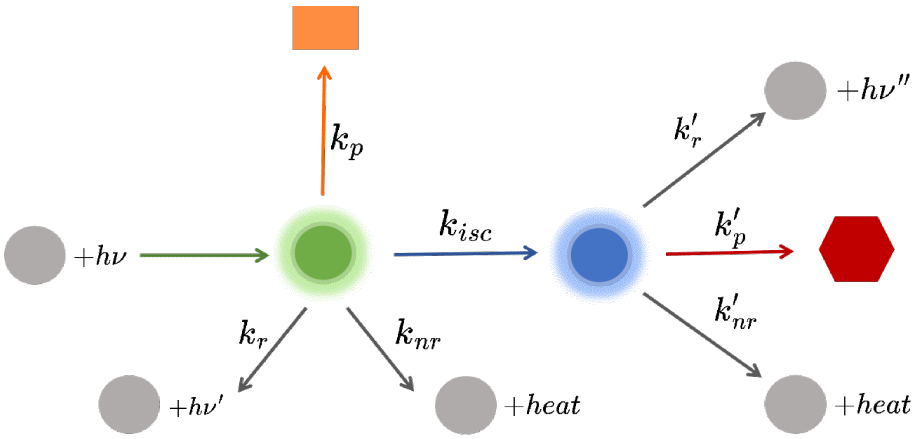

Figure 4.3: Schematic representation of the possible deactivation processes of a given molecule yielding different decay pathways. The rate constants are generally represented by k, while the text in subscript determines the phenomenon, where r is radiative, nr is nonradiative, p is product, and isc is intersystem crossing.

The excited state will decay following a first-order kinetics, with a lifetime τ. The probability of each process is related to its rate constant. Because radiationless decay from a high-energy to a low-energy state with the same spin multiplicity is faster, usually the emitting state is the lowest excited state (Kasha's rule) [60]. However, compounds featuring heavier atoms, such as transition metals, benefit from the Spin-Orbit Coupling (SOC) effect that enables Intersystem Crossing (ISC), unlocking new pathways and photochemical products [64, 90].

In this sense, we propose mapping the dynamics of an exciton by solving the set of coupled differential equations dependent on the evolution time arising from every possible decay event at a strategic given Potential Energy Surface (PES) point. To do so, the decay rate constants of all possible events at the equilibrium geometry of each important state have been calculated. The general first-order kinetic equation is

$$\begin{aligned}\frac{d[\mathrm{M@N}](t)}{dt} = -(k^{\mathrm{N}}_{\mathrm{M}\to\mathrm{T}_1} + \ldots + k^{\mathrm{N}}_{\mathrm{M}\to\mathrm{T}_n} + k^{\mathrm{N}}_{\mathrm{M}\to\mathrm{S}_0} + \ldots + k^{\mathrm{N}}_{\mathrm{M}\to\mathrm{S}_n} + k^{\mathrm{N}}_{\mathrm{F/Ph}} + \\ k_{\mathrm{vr}})[\mathrm{M@N}](t) + k^{\mathrm{N}}_{\mathrm{T}_1\to\mathrm{M}}[\mathrm{T}_1\mathrm{@N}](t) + \ldots + k^{\mathrm{N}}_{\mathrm{T}_n\to\mathrm{M}}[\mathrm{T}_n\mathrm{@N}](t) \\ + k^{\mathrm{N}}_{\mathrm{S}_0\to\mathrm{M}}[\mathrm{S}_0\mathrm{@N}](t) + \ldots + k^{\mathrm{N}}_{\mathrm{S}_n\to\mathrm{M}}[\mathrm{S}_n\mathrm{@N}](t)\end{aligned} \tag{4.3}$$

where the notation herein used follows that $[\mathrm{M@N}](t)$ is the population concentration of state M at the Franck-Condon (FC) region of state N at a given time t, and $k^{\mathrm{N}}_{\mathrm{M}} \to \mathrm{S}$ is the rate constant for the transition $\mathrm{M} \to \mathrm{S}$ (subscript) at the FC region of state N (superscript).

4.4 Computational Details

Density Functional Theory (DFT), both time-dependent and independent, was used with the hybrid functional B3LYP [150] to perform the full unconstrained geometry optimizations and frequency calculations for the ground state (S_0), the first singlet excited state (S_1), the first two triplet excited states (T_1 and T_2), the first triplet excited state metal-centered (^{3}MC), and the transition state (TS) using the ORCA-5.0.3 software [110, 151]. The SCF convergence accuracy was set to 10^{-8} E_h in the total energy and 10^{-6} in the density. The Ahlrichs full-electron def2-TZVP basis set [112] was employed for all atoms, and the calculations included the Grimme D3 dispersion correction [152] with Becke-Johnson (BJ) damping [153]. RI approximation [154] using def2/J as an auxiliary basis set [116] was used to speed up Coulomb integrals. The conductor-like polarizable continuum model (C-PCM) [118] was utilized to simulate the water solvation. Scalar relativistic corrections were treated using the zeroth-order regular approximation Zeroth-Order Regular Approximation (ZORA) [155, 156]. The simulated electronic spectra for 75 roots in the S_0 and S_1 Franck-Condon regions were calculated to determine the number of low-energy triplet states and the nature of the transitions.

After a careful analysis, it was determined that S_0, S_1, T_1, and T_2 were the essential states involved in the deactivation pathway of the system. Therefore, the four regions were established based on their minimum-energy geometry, and the photophysical rate constants for all competing events involving all possible transitions within these states were computed at these four regions.

Following the notation established in equation 4.3, the methods discussed in the previous chapters alongside the radiation decay description in section 4.2 are herein rewritten in the kinetic model notation for further clarification of the approximations made. The fluorescence and phosphorescence rate constants were computed assuming a first-order

kinetic process obeying Kasha's rules [60, 61],

$$\frac{d\mathrm{M}_i^{\mathrm{N}}}{dt} = -\mathrm{M}_f^{\mathrm{N}} A_{if}^{\mathrm{N}} \tag{4.4}$$

where A_{if}^{N} is the Einstein's coefficient, i is the initial state, f is the final ground state, and N is the FC region of state N. The Einstein's coefficient is given by [148, 149],

$$A_{if}^{\mathrm{N}} = \frac{(E_f - E_i)^3}{3\varepsilon_0 \pi \hbar^4 c^3} |\mu_{if}@\mathrm{N}|^2 \eta^2 \tag{4.5}$$

where E_f and E_i are the energy of the final and initial states, respectively, computed at their respective geometries, ε_0 is the electrical permittivity of free space, c is the speed of light in vacuum, η is the refractive index of the solvent, $\hbar$ is the reduced Planck constant, and $\mu_{if}@\mathrm{N}$ is the transition electric dipole moment calculated as $\langle f|\mu|i\rangle$ at a given N geometry, representative of the FC region of state N. The phosphorescence rate constants were calculated using the average value of $|\mu_{if}@\mathrm{N}|^2$ for $\mathrm{MS} = -1, 0, +1$.

The ISC rate constants were calculated using Fermi's Golden Rule as follows [64, 91],

$$k_{\mathrm{S}_1 \to \mathrm{T}_m}^{\mathrm{N}} = \frac{2\pi}{\hbar} \langle \mathrm{S}_1 | \mathcal{H}_{\mathrm{SOC}}^{\mathrm{N}} | \mathrm{T}_m \rangle^2 \rho(E) \tag{4.6}$$

where the $\mathcal{H}_{\mathrm{SOC}}^{\mathrm{N}}$ is the spin-orbit coupling between the excited singlet and triplet states at the FC region of state N, calculated from Time-Dependent Density Functional Theory (TD-DFT) by using quasi-degenerate perturbation theory [157] and computed at the B3LYP level with the full-electron zora-tzvp basis, and $\rho(E)$ is the Franck-Condon density of state computed using the semi-classical Marcus theory [82–85], and given as,

$$\rho_{FC} = \frac{1}{\sqrt{4\pi\lambda_{\mathrm{M}} k_{\mathrm{B}} T}} \exp\left(\frac{-(\Delta E + \lambda_{\mathrm{M}})^2}{4\lambda_{\mathrm{M}} k_{\mathrm{B}} T}\right) \tag{4.7}$$

where ΔE was calculated as the adiabatic energy difference between the states involved in the transition, $\mathrm{k_B}$ is the Boltzmann constant, T is the temperature (set to 298.15 K for all calculations), and λ_{M} is the Marcus reorganization energy calculated as,

$$\lambda_{\mathrm{M}} = \mathrm{T}_m@\mathrm{S}_1 - \mathrm{T}_m@\mathrm{T}_m \tag{4.8}$$

In this case, λ_{M} was determined considering only the inner-sphere contribution [120–123].

The internal conversion rate constant for the $\mathrm{S}_1 \to \mathrm{S}_0$ and $\mathrm{T}_2 \to \mathrm{T}_1$ transitions were calculated using the one-effective mode Marcus-Jortner-Levich (MJL) theory (described in Chapter 3) [24], using the conical intersection reorganization energies, λ_{MECI}, as following,

$$k_{IC}^{\mathrm{N}} = \frac{\pi}{\hbar}|\mathrm{NAC@N}|^2 \frac{1}{\sqrt{4\pi\lambda_{\mathrm{MECI}}k_{\mathrm{B}}T}} \sum_{n=0}^{\infty} \exp(-S)\frac{S^n}{n!} \times \exp\left(\frac{-(\Delta G^{\circ} + \lambda_{\mathrm{MECI}} + n\hbar\omega_{eff})^2}{4\lambda_{\mathrm{MECI}}k_{\mathrm{B}}T}\right) \tag{4.9}$$

where S is the summation over all S_j, which is the Huang-Rhys factor computed over each normal mode j, n is the vibrational quantum number, ω_{eff} is the effective frequency determined as $\omega_{eff} = \sum_{j=1}^{\mathrm{N}} S_j\omega_j / \sum_{j=1}^{\mathrm{N}} S_j$, and the corrected reorganization energy was calculated as

$$\lambda_{\mathrm{MECI}} = E_{\mathrm{MECI}} - \mathrm{M}_f\mathrm{@M}_f \tag{4.10}$$

where E_{MECI} is the energy computed at the conical intersection between the S_0 and S_1 for $S_1 \rightarrow S_0$ and T_2 and T_1 for $T_2 \rightarrow T_1$, and M_f is the final state, *i.e.*, S_0 and T_1, respectively. The gradient projection (GP) [125] was used to find the Minimum Energy Conical Intersection (MECI) point using the Spin-Flip TD-DFT (SF-TD-DFT) [124] method. The HR factor was calculated using the Dushin code [93]. Because the Dushin code is not implemented for ORCA, the S_0, S_1, T_1, and T_2 normal mode frequencies at their respective equilibrium geometries were calculated at B3LYP/6-31G* level of theory for the ligands while the Ru was treated with LANL2DZ and the pseudo-potential [127] using the Gaussian09 software [128]. The final k_{IC}^{N} was computed using the method mentioned in Chapter 3 [24].

The photophysical constants calculated using the methods mentioned above are energy downhill, leading to the deactivation of the excited state of the system. However, for completeness, it is important to consider the uphill energy constants when solving the set of kinetic equations. For the radiationless constants, *i.e.*, Internal Conversion (IC) and ISC, the uphill rate constants were computed using the following equation,

$$k_{up}^{\mathrm{N}} = k_{down}^{\mathrm{N}} \times \exp\left(\frac{-\Delta E_{FC}}{k_{\mathrm{B}}T}\right) \tag{4.11}$$

which has previously been used in the same sense [73], where the ΔE_{FC} is the energy difference between the involved states at the FC region of state N.

The transitions between T_1 and ^{3}MC are thermally activated through a Transition State (TS) and the rate constants for these processes were calculated using the Eyring equation [158],

$$k_{M\rightarrow N} = \kappa\frac{k_{\mathrm{B}}T}{h}\exp\left(\frac{-\Delta G^{\ddagger}}{RT}\right) \tag{4.12}$$

where κ is the transmission coefficient, h is the Planck constant, R is the gas constant, and $\Delta G^{\ddagger}$ is the activation energy barrier regarding the initial state of the transition.

With all photophysical rate constants calculated, the eighteen ordinary differential coupled kinetic equations solved are detailed below.

$$\begin{aligned}\frac{d[\mathrm{S_1@S_0}](t)}{dt} = &-(k^{\mathrm{S_0}}_{\mathrm{S_1}\rightarrow\mathrm{T_1}} + k^{\mathrm{S_0}}_{\mathrm{S_1}\rightarrow\mathrm{T_2}} + k^{\mathrm{S_0}}_{\mathrm{S_1}\rightarrow\mathrm{S_0}} + k^{\mathrm{S_0}}_{F} + k_{\mathrm{S_1,GR}})[\mathrm{S_1@S_0}](t) \\ &+ k^{\mathrm{S_0}}_{\mathrm{T_1}\rightarrow\mathrm{S_1}}[\mathrm{T_1@S_0}](t) + k^{\mathrm{S_0}}_{\mathrm{T_2}\rightarrow\mathrm{S_1}}[\mathrm{T_2@S_0}](t)\end{aligned} \tag{4.13}$$

$$\begin{aligned}\frac{d[\mathrm{T_1@S_0}](t)}{dt} = &-(k^{\mathrm{S_0}}_{\mathrm{T_1}\rightarrow\mathrm{S_1}} + k^{\mathrm{S_0}}_{\mathrm{T_1}\rightarrow\mathrm{T_2}} + k^{\mathrm{S_0}}_{\mathrm{T_1}\rightarrow\mathrm{S_0}} + k^{\mathrm{S_0}}_{P} + k_{\mathrm{T_1,GR}})[\mathrm{T_1@S_0}](t) \\ &+ k^{\mathrm{S_0}}_{\mathrm{S_1}\rightarrow\mathrm{T_1}}[\mathrm{S_1@S_0}](t) + k^{\mathrm{S_0}}_{\mathrm{T_2}\rightarrow\mathrm{T_1}}[\mathrm{T_2@S_0}](t)\end{aligned} \tag{4.14}$$

$$\begin{aligned}\frac{d[\mathrm{T_2@S_0}](t)}{dt} = &-(k^{\mathrm{S_0}}_{\mathrm{T_2}\rightarrow\mathrm{S_1}} + k^{\mathrm{S_0}}_{\mathrm{T_2}\rightarrow\mathrm{T_1}} + k_{\mathrm{T_2,GR}})[\mathrm{T_2@S_0}](t) + k^{\mathrm{S_0}}_{\mathrm{S_1}\rightarrow\mathrm{T_2}}[\mathrm{S_1@S_0}](t) \\ &+ k^{\mathrm{S_0}}_{\mathrm{T_1}\rightarrow\mathrm{T_2}}[\mathrm{T_1@S_0}](t)\end{aligned} \tag{4.15}$$

$$\begin{aligned}\frac{d[\mathrm{S_0@S_0}](t)}{dt} = &(k^{\mathrm{S_0}}_{\mathrm{S_1}\rightarrow\mathrm{S_0}} + k^{\mathrm{S_0}}_{F})[\mathrm{S_1@S_0}](t) + (k^{\mathrm{S_0}}_{\mathrm{T_1}\rightarrow\mathrm{S_0}} + k^{\mathrm{S_0}}_{P})[\mathrm{T_1@S_0}](t) \\ &+ \{[\mathrm{S_0@S_1}](t) + [\mathrm{S_0@T_1}](t) + [\mathrm{S_0@T_2}](t) + [\mathrm{S_0@^3MC}]\}k_{\mathrm{S_0,GR}}\end{aligned} \tag{4.16}$$

$$\begin{aligned}\frac{d[\mathrm{S_1@S_1}](t)}{dt} = &-(k^{\mathrm{S_1}}_{\mathrm{S_1}\rightarrow\mathrm{T_1}} + k^{\mathrm{S_1}}_{\mathrm{S_1}\rightarrow\mathrm{T_2}} + k^{\mathrm{S_1}}_{\mathrm{S_1}\rightarrow\mathrm{S_0}} + k^{\mathrm{S_1}}_{F})[\mathrm{S_1@S_1}](t) + \\ &k^{\mathrm{S_1}}_{\mathrm{T_1}\rightarrow\mathrm{S_1}}[\mathrm{T_1@S_1}](t) + k^{\mathrm{S_1}}_{\mathrm{T_2}\rightarrow\mathrm{S_1}}[\mathrm{T_2@S_1}](t) + \{[\mathrm{S_1@S_0}](t) + \\ &[\mathrm{S_1@T_1}](t) + [\mathrm{S_1@T_2}](t)\}k_{\mathrm{S_1,GR}}\end{aligned} \tag{4.17}$$

$$\begin{aligned}\frac{d[\mathrm{T_1@S_1}](t)}{dt} = &-(k^{\mathrm{S_1}}_{\mathrm{T_1}\rightarrow\mathrm{S_1}} + k^{\mathrm{S_1}}_{\mathrm{T_1}\rightarrow\mathrm{T_2}} + k^{\mathrm{S_1}}_{\mathrm{T_1}\rightarrow\mathrm{S_0}} + k^{\mathrm{S_1}}_{P} + k_{\mathrm{T_1,GR}})[\mathrm{T_1@S_1}](t) \\ &+ k^{\mathrm{S_1}}_{\mathrm{S_1}\rightarrow\mathrm{T_1}}[\mathrm{S_1@S_1}](t) + k^{\mathrm{S_1}}_{\mathrm{T_2}\rightarrow\mathrm{T_1}}[\mathrm{T_2@S_1}](t)\end{aligned} \tag{4.18}$$

$$\begin{aligned}\frac{d[\mathrm{T_2@S_1}](t)}{dt} = &-(k^{\mathrm{S_1}}_{\mathrm{T_2}\rightarrow\mathrm{S_1}} + k^{\mathrm{S_1}}_{\mathrm{T_2}\rightarrow\mathrm{T_1}} + k_{\mathrm{T_2,GR}})[\mathrm{T_2@S_1}](t) + k^{\mathrm{S_1}}_{\mathrm{S_1}\rightarrow\mathrm{T_2}}[\mathrm{S_1@S_1}](t) \\ &+ k^{\mathrm{S_1}}_{\mathrm{T_1}\rightarrow\mathrm{T_2}}[\mathrm{T_1@S_1}](t)\end{aligned} \tag{4.19}$$

$$\frac{d[\mathrm{S_0@S_1}](t)}{dt} = -k_{\mathrm{S_0,GR}}[\mathrm{S_0@S_1}](t) + (k^{\mathrm{S_1}}_{\mathrm{S_1\rightarrow S_0}} + k^{\mathrm{S_1}}_{F})[\mathrm{S_1@S_1}](t) + (k^{\mathrm{S_1}}_{\mathrm{T_1\rightarrow S_0}} + k^{\mathrm{S_1}}_{p})[\mathrm{T_1@S_1}](t) \tag{4.20}$$

$$\frac{d[\mathrm{S_1@T_1}](t)}{dt} = -(k^{\mathrm{T_1}}_{\mathrm{S_1\rightarrow T_1}} + k^{\mathrm{T_1}}_{\mathrm{S_1\rightarrow T_2}} + k^{\mathrm{T_1}}_{\mathrm{S_1\rightarrow S_0}} + k^{\mathrm{T_1}}_{F} + k_{\mathrm{S_1,GR}})[\mathrm{S_1@T_1}](t) + k^{\mathrm{T_1}}_{\mathrm{T_1\rightarrow S_1}}[\mathrm{T_1@T_1}](t) + k^{\mathrm{T_1}}_{\mathrm{T_2\rightarrow S_1}}[\mathrm{T_2@T_1}](t) \tag{4.21}$$

$$\frac{d[\mathrm{T_1@T_1}](t)}{dt} = -(k^{\mathrm{T_1}}_{\mathrm{T_1\rightarrow S_1}} + k^{\mathrm{T_1}}_{\mathrm{T_1\rightarrow T_2}} + k^{\mathrm{T_1}}_{\mathrm{T_1\rightarrow S_0}} + k^{\mathrm{T_1}}_{\mathrm{T_1\rightarrow {}^3MC}} + k^{\mathrm{T_1}}_{P})[\mathrm{T_1@T_1}](t) + k^{\mathrm{^3MC}}_{\mathrm{^3MC\rightarrow T_1}}[^3\mathrm{MC}](t) + k^{\mathrm{T_1}}_{\mathrm{S_1\rightarrow T_1}}[\mathrm{S_1@T_1}](t) + k^{\mathrm{T_1}}_{\mathrm{T_2\rightarrow T_1}}[\mathrm{T_2@T_1}](t) + \{[\mathrm{T_1@S_0}](t) + [\mathrm{T_1@S_1}](t) + [\mathrm{T_1@T_2}](t)\}k_{\mathrm{T_1,GR}} \tag{4.22}$$

$$\frac{d[\mathrm{T_2@T_1}](t)}{dt} = -(k^{\mathrm{T_1}}_{\mathrm{T_2\rightarrow S_1}} + k^{\mathrm{T_1}}_{\mathrm{T_2\rightarrow T_1}} + k_{\mathrm{T_2,GR}})[\mathrm{T_2@T_1}](t) + k^{\mathrm{T_1}}_{\mathrm{S_1\rightarrow T_2}}[\mathrm{S_1@T_1}](t) + k^{\mathrm{T_1}}_{\mathrm{T_1\rightarrow T_2}}[\mathrm{T_1@T_1}](t) \tag{4.23}$$

$$\frac{d[\mathrm{S_0@T_1}](t)}{dt} = -k_{\mathrm{S_0,GR}}[\mathrm{S_0@T_1}](t) + (k^{\mathrm{T_1}}_{\mathrm{S_1\rightarrow S_0}} + k^{\mathrm{T_1}}_{F})[\mathrm{S_1@T_1}](t) + (k^{\mathrm{T_1}}_{\mathrm{T_1\rightarrow S_0}} + k^{\mathrm{T_1}}_{p})[\mathrm{T_1@T_1}](t) \tag{4.24}$$

$$\frac{d[\mathrm{S_1@T_2}](t)}{dt} = -(k^{\mathrm{T_2}}_{\mathrm{S_1\rightarrow T_1}} + k^{\mathrm{T_2}}_{\mathrm{S_1\rightarrow T_2}} + k^{\mathrm{T_2}}_{\mathrm{S_1\rightarrow S_0}} + k^{\mathrm{T_2}}_{F} + k_{\mathrm{S_1,GR}})[\mathrm{S_1@T_2}](t) + k^{\mathrm{T_2}}_{\mathrm{T_1\rightarrow S_1}}[\mathrm{T_1@T_2}](t) + k^{\mathrm{T_2}}_{\mathrm{T_2\rightarrow S_1}}[\mathrm{T_2@T_2}](t) \tag{4.25}$$

$$\frac{d[\mathrm{T_1@T_2}](t)}{dt} = -(k^{\mathrm{T_2}}_{\mathrm{T_1\rightarrow S_1}} + k^{\mathrm{T_2}}_{\mathrm{T_1\rightarrow T_2}} + k^{\mathrm{T_2}}_{\mathrm{T_1\rightarrow S_0}} + k^{\mathrm{T_2}}_{P} + k_{\mathrm{T_1,GR}})[\mathrm{T_1@T_2}](t) + k^{\mathrm{T_2}}_{\mathrm{S_1\rightarrow T_1}}[\mathrm{S_1@T_2}](t) + k^{\mathrm{T_2}}_{\mathrm{T_2\rightarrow T_1}}[\mathrm{T_2@T_2}](t) \tag{4.26}$$

$$\frac{d[\mathrm{T_2@T_2}](t)}{dt} = -(k^{\mathrm{T_2}}_{\mathrm{T_2\rightarrow S_1}} + k^{\mathrm{T_2}}_{\mathrm{T_2\rightarrow T_1}})[\mathrm{T_2@T_2}](t) + k^{\mathrm{T_2}}_{\mathrm{S_1\rightarrow T_2}}[\mathrm{S_1@T_2}](t) + k^{\mathrm{T_2}}_{\mathrm{T_1\rightarrow T_2}}[\mathrm{T_1@T_2}](t) + \{[\mathrm{T_2@S_0}](t) + [\mathrm{T_2@S_1}](t) + [\mathrm{T_2@T_1}](t)\}k_{\mathrm{T_2,GR}} \tag{4.27}$$

$$\frac{d[S_0@T_2](t)}{dt} = -k_{S_0,GR}[S_0@T_2](t) + (k^{T_2}_{S_1\rightarrow S_0} + k^{T_2}_F)[S_1@T_2](t) + (k^{T_2}_{T_1\rightarrow S_0} + k^{T_2}_p)[T_1@T_2](t) \tag{4.28}$$

$$\frac{d[^3MC](t)}{dt} = -(k^{^3MC}_{^3MC\rightarrow T_1} + k^{^3MC}_P)[^3MC](t) + k^{T_1}_{T_1\rightarrow ^3MC}[T_1@T_1] \tag{4.29}$$

$$\frac{d[S_0@^3MC](t)}{dt} = -k_{S_0,GR}[S_0@^3MC](t) + k^{^3MC}_p[^3MC](t) \tag{4.30}$$

The set of equations was represented in a matricial system, and matrix exponential was computed using a scaling and squaring algorithm with a Pade approximation in a homemade code developed in MATLAB.

4.5 Results and Discussion

4.5.1 Structural parameters

One of the main features to distinguish between different electronic states of a molecule is the change in some structural parameters and properties, such as bond distances, angles, dihedrals, dipole moments, and so on. Figure 4.4 shows the general structure and geometry of the $[Ru(bpz)_3]^{2+}$ complex. Its metal center and coordinating atoms are emphasized for didactic purposes.

Table 4.1: Structural parameters for the ground and the low excited electronic states of $[Ru(bpz)_3]^{2+}$ with implicit water solvation. Bond distances are given in Å, and the electric dipole moments are given in a.u..

Parameter	S_0	S_1	T_1	T_2	^3MC
Ru–N1	2.080	2.097	2.045	2.113	2.083
Ru–N3	2.078	2.082	2.042	2.082	2.083
Ru–N5	2.082	2.073	2.086	2.058	2.450
Ru–N7	2.081	2.071	2.103	2.057	2.137
Ru–N9	2.080	2.083	2.101	2.082	2.136
Ru–N11	2.078	2.098	2.083	2.112	2.473
∠ N1–Ru–N5	96.4	96.9	96.3	94.3	94.3
∠ N1–Ru–N9	96.3	100.2	96.4	95.4	98.3
μ(D)	0.032	3.715	2.583	3.419	0.713

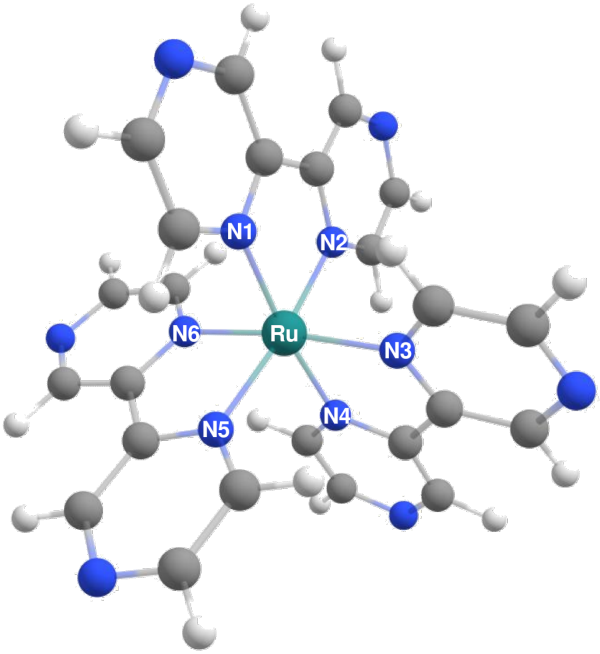

Figure 4.4: $[Ru(bpz)_3]^{2+}$ complex structure with labels in the main atoms.

Taking Figure 4.4 as a reference, table 4.1 shows the structural changes between the ground and some low excited states regarding bond distance, angle, and electric dipole moment. The bond distances between the metal center and the coordinating nitrogen atoms suffer small variations, except for the ^{3}MC state. While there is no pattern in the stretching or shrinking of bonds, their overall change alongside the varying angles between different ligands demonstrates that the complex undergoes torsions in geometry depending on the state. The S_1 excited state shows the highest distortion in angles, which is implied to be a consequence of a change in its electronic density distribution. In fact, the electric dipole moment of this specific state is also the highest. On the other hand, the metal-centered triplet state presents the longest bond lengths for the two axial bonds, expressing a Janh-Teller effect that has been observed in many similar systems [147, 159]. In general, the excited states are expected to have a different charge separation and electronic distribution due to the electrons occupying more energetic orbitals. However, polypyridyl ligands are bidentate and π-conjugated systems, which intrinsically show a rigidity associated with them. This rigidity has been observed in other theoretical studies featuring Ru-based polypyridyl complexes [69]. The structures of the optimized states are shown below, with their respective spin-contamination (Figure 4.5).

4.5.2 Photophysics

The nature of the first five transitions for the singlet and triplet manifolds at the ground-state equilibrium geometry was evaluated using the Theodore package [160] and

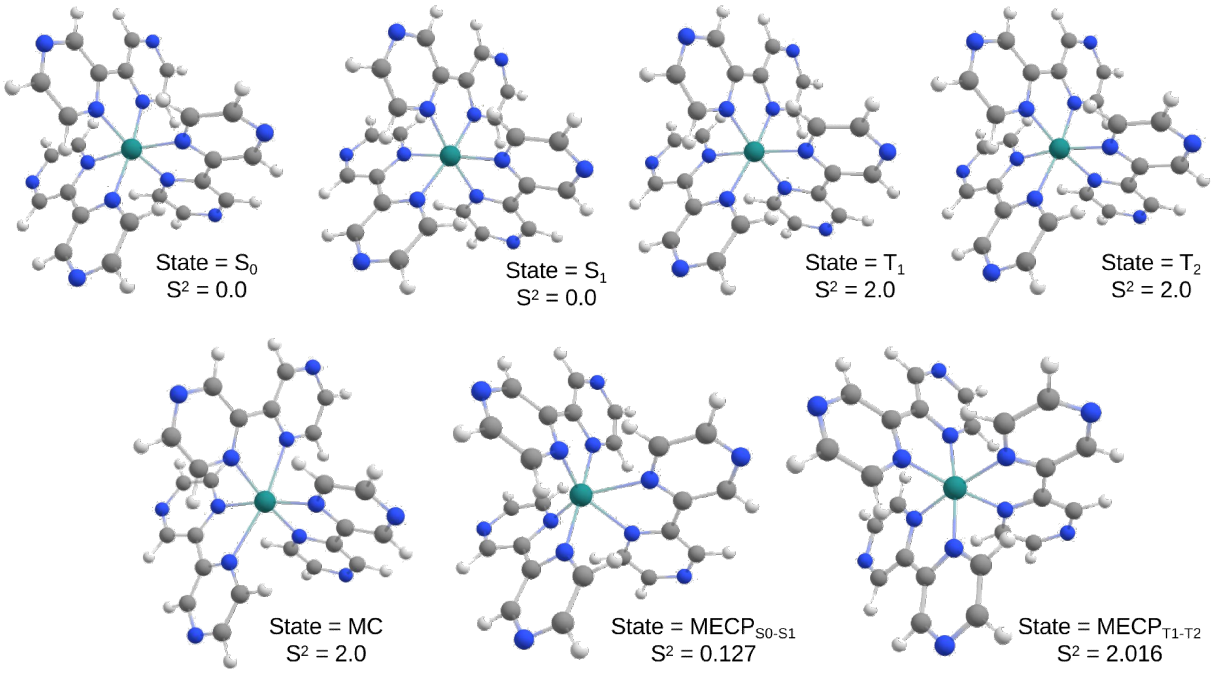

Figure 4.5: Structures of the optimized states and crossing points along with their spin-contamination.

is shown in Figure 4.6.

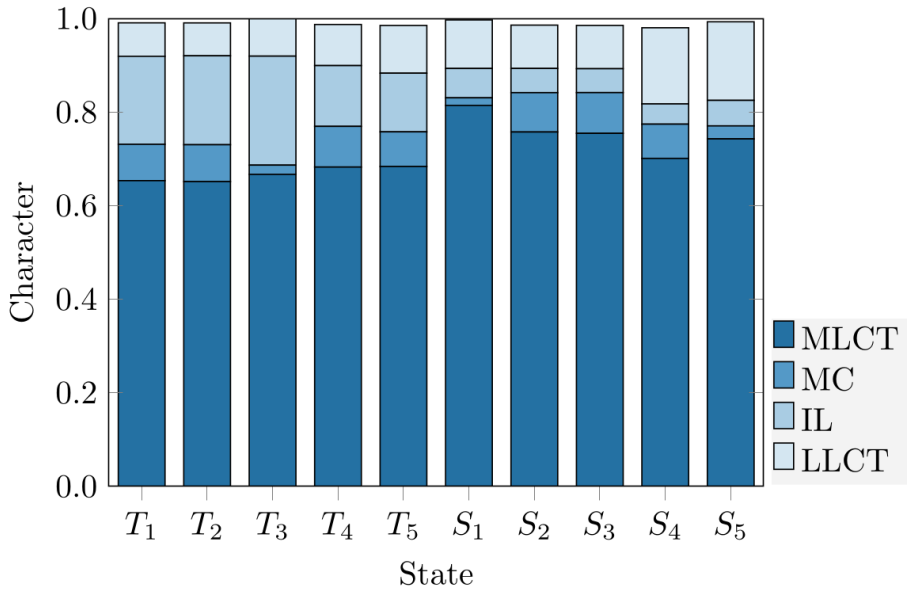

Figure 4.6: Character contributions to the first five transitions of the triplet and singlet manifold, respectively, at the ground-state Franck-Condon region of the $[Ru(bpz)_3]^{2+}$ complex. The transitions are divided into Metal-to-Ligand Charge Transfer (MLCT), Ligand-to-Metal Charge Transfer (LMCT), IntraLigand (IL), Metal-Centered (MC), and Ligand-to-Ligand Charge Transfer (LLCT).

All transitions have shown a dominant MLCT character higher than 60%, indicating that this complex follows the trend observed for ruthenium complexes with polypyridyl ligands. The secondary character, however, differs for the singlet and triplet manifolds. While the IL character is the second most relevant contribution for triplet states, the LLCT character is more relevant for the singlet states. This result implies that the singlet manifold has a stronger charge-transfer character (CT) than the triplet states, for which the local excitation plays a more relevant role.

A thorough evaluation of the simulated electronic absorption spectrum of the $[Ru(bpz)_3]^{2+}$ complex with implicit water solvation has also confirmed these results. The simulated electronic absorption spectrum of the Ru-bpz complex with implicit water solvation is shown in Figure 4.7, and the attributions regarding the nature of the transitions of the main absorption bands are shown in Table 4.2, as well as the excited state and its associated energy, wavelength, and oscillator strength.

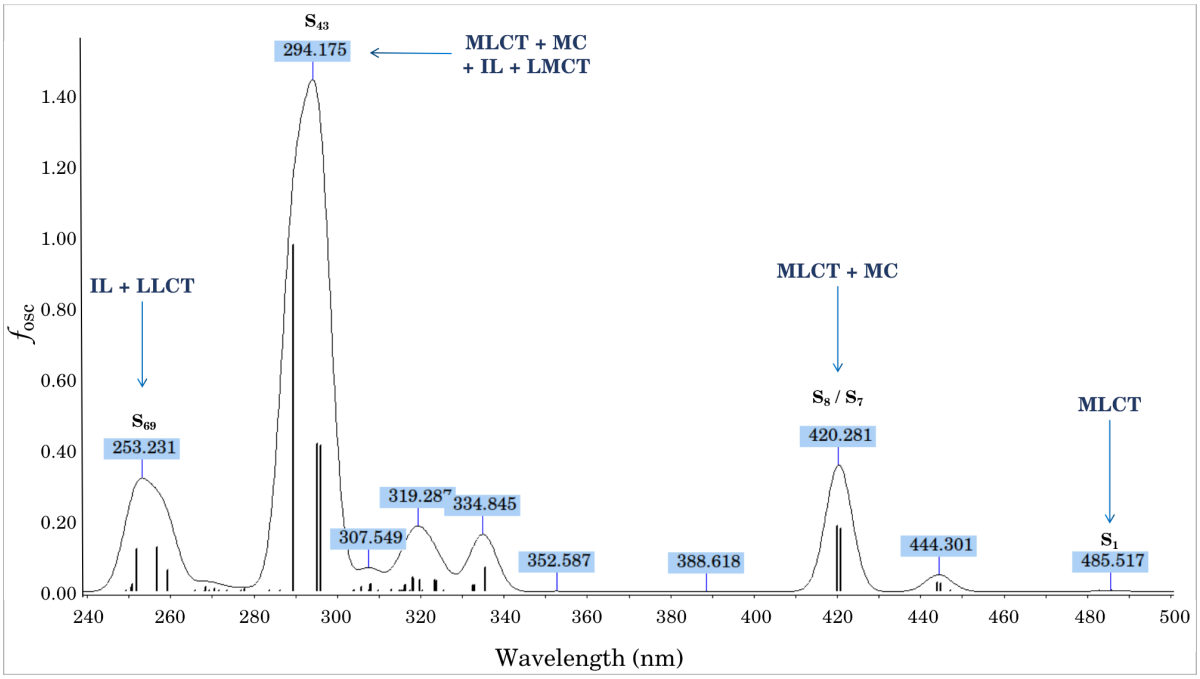

Figure 4.7: The calculated electronic absorption spectrum of the $[Ru(bpz)_3]^{2+}$ complex. The transition nature of the main bands is indicated, where MLCT (Metal-to-Ligand Charge Transfer), LMCT (Ligand-to-Metal Charge Transfer), IL (IntraLigand) and MC (Metal-Centered).

The lowest energy band observed in the spectrum occurs at 484.06 nm and the $S_0 \rightarrow S_1$ transition occurs at 484.4 nm, showing that the band features the lowest state, corresponding to a S_1 state 2.560 eV higher in energy regarding the ground-state. The Natural Transition Orbital (NTO) involved in this particular transition are d_{Ru} and π^*_{bpz}, characterizing an MLCT transition. However, the oscillator strength is 0.0028, which is

Table 4.2: Attribution of state, energy, E, in eV, absorption wavelength, λ, in nm, oscillator strength, f_{osc}, and nature of the transition of the main absorption bands of the spectrum of the $[Ru(bpz)_3]^{2+}$ complex.

State	E(eV)	λ(nm)	f_{osc}	Attribution
1	2.560	484.4	0.002798	MLCT($d_{Ru} \rightarrow \pi^*_{bpz}$)
7	2.976	416.6	0.130621	MLCT($d_{Ru} \rightarrow \pi^*_{bpz}$) + MC($d_{Ru} \rightarrow d_{Ru}$)
8	2.982	415.6	0.137872	MLCT($d_{Ru} \rightarrow \pi^*_{bpz}$) + MC($d_{Ru} \rightarrow d_{Ru}$)
11	3.717	333.6	0.054447	MLCT($d_{Ru} \rightarrow \pi^*_{bpz}$)
12	2.718	333.5	0.055120	MLCT($d_{Ru} \rightarrow \pi^*_{bpz}$)
43	4.270	290.4	0.728992	MC($d_{Ru} \rightarrow d_{Ru}$) + MLCT($d_{Ru} \rightarrow \pi^*_{bpz}$) + IL($\pi_{bpz} \rightarrow \pi^*_{bpz}$) + LMCT($\pi_{bpz} \rightarrow d_{Ru}$)
69	4.827	256.8	0.090769	IL + LLCT($\pi_{bpz} \rightarrow \pi^*_{bpz}$)

All values were obtained at the b3lyp/def2-TZVP level.

considerably low, affecting the intensity of the band. Therefore, although the first excited state is important to be considered in photophysics studies, it is not always detected in experimental measurements. Usually, the bright states of metal complexes are of higher energy.

The next prominent band occurs at 416.12 nm and features the $S_0 \rightarrow S_7$ and $S_0 \rightarrow S_8$ transitions that are at 416.6 and 415.6 nm, respectively. These transitions are also MLCT in nature but their intensities are considerably higher compared to the $S_0 \rightarrow S_1$ transition, with oscillator strength of approximately 0.13. The NTOs involved in the transition $S_0 \rightarrow S_8$ show a contribution of an MC transition besides the main MLCT transition. The absorption bands at 333.02 nm and 317.36 nm are less intense than the former, with an oscillator strength of approximately 0.05 and MLCT nature of transition, showing that this type of transition rules the photophysics of the ru-bpz complex. The most intense absorption band is at 290.83 nm and its most prominent contribution comes from the $S_0 \rightarrow S_{43}$ transition, which is 4.270 eV higher than the ground-state in energy. Because this transition has such high energy, its nature is a mixture of many different charge-transfers. The major contributions are of MLCT and MC nature, but it also has IL and LMCT transitions adding to it. The high intensity comes from a somewhat higher oscillator strength of 0.729. The last absorption band encompasses mainly the states S_{69}, S_{71}, and S_{72}, which are 4.9 eV higher in energy than the ground state, corresponding to a wavelength of 256.8 nm and with an oscillator strength of approximately 0.09. Such transitions are not in the visible wavelength range. The orbitals suggest that the transitions are of the IL and LLCT natures which account for 95.5% of the contribution.

These results agree with the experimental data previously published. [147] reported the first experimental results on electronic absorption spectra of the $[Ru(bpz)_3]^{2+}$ complex. They verified that contrary to the $[Fe(bpz)_3]^{2+}$ complex, the Ru-based complex was stable in an aqueous solution, beginning the interest in investigating complexes featuring the bpz as a ligand. However, the authors performed the electronic absorption spectrum acquisition in ethanol. They observed two main absorption bands in 296 nm and 443 nm, which they attributed to n $\rightarrow \pi^*$ and $\pi \rightarrow \pi^*$ IL transitions and $d_{Ru} \rightarrow \pi^*$ MLCT, respectively. It was also reported that the room temperature emission of this complex occurred from its MLCT state, being centered at 603 nm [147]. A more recent work revisited this complex and performed the same measurements in acetonitrile and water [144]. Although the solvents differ in their physicochemical properties, they barely shift the absorption bands. The main bands reported are at 235 nm (LLCT), 265 nm and 292 nm (LLCT, MLCT, IL, and MC), 340 nm (MLCT), 409 nm (MLCT), and 440 nm (MLCT) in acetonitrile. In water, the main bands are at 238 nm, 294 nm, 411 nm, and 441 nm, but no attributions regarding the nature of the transition were mentioned. Figure 4.8 shows the NTOs involved in the main transitions of the singlet and triplet manifold that are studied in this work and play an important role in the excited state deactivation dynamics.

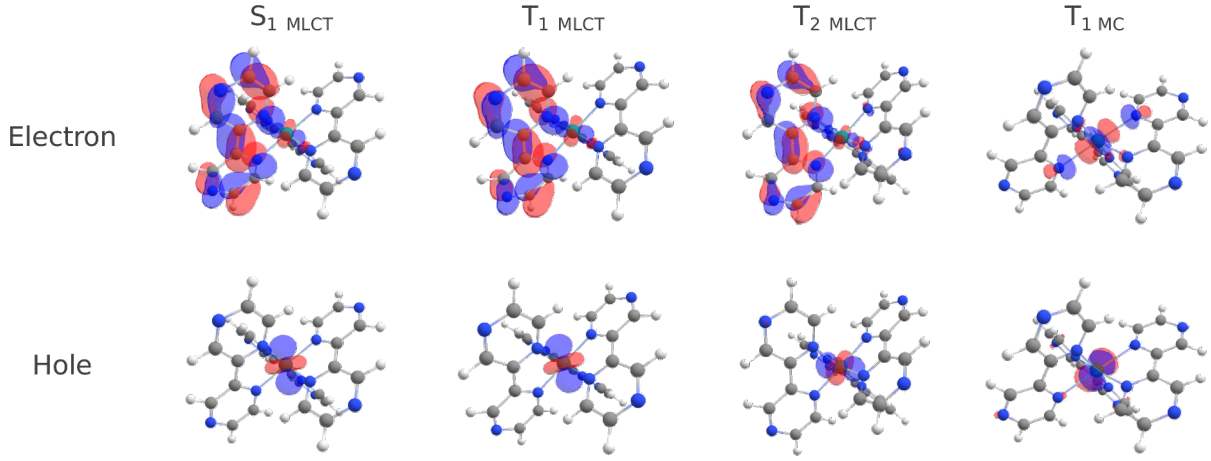

Figure 4.8: Natural Transition Orbitals (NTOs) involved in the main transition of the S_1, T_1, T_2, and ^{3}MC states.

The emissions encountered are at 611 nm and 604 nm in water and acetonitrile, respectively, which agree with the emission previously reported in ethanol by [147]. The calculated emission in water implicit solvation is 567.7 nm as shown in table 4.3. This result is below the emission values reported previously for various solvents.

Table 4.3 also gathers the parameters involved in the fluorescence decay, *i.e.*, the

Table 4.3: Calculated parameters involved in the fluorescence decay for the $[Ru(bpz)_3]^{2+}$ complex. ΔE is the energy difference between S_1 and S_0 given in eV, λ_{em} is the emission frequency in nm, f_{osc} is the oscillator strength of the transition, μ^2 is the electric transition dipole moment in a.u.^{2}, and k_f is the fluorescence rate constant in s^{-1}.

Parameters	
ΔE (eV)	2.393
λ_{em} (nm)	567.7
f_{osc}	0.0001
μ^2 ($S_1 \rightarrow S_0$)	0.003
k_f (s^{-1})	3.88×10^4

adiabatic difference between the S_0 and S_1, the oscillator strength of the transition, and the transition electric dipole moment. The fluorescence rate constant was calculated using equation 4.5 and predicted a value of 3.887×10^4 s^{-1}, being lower than the experimentally determined radiative decay rate constant of 7.44×10^4 s^{-1} in water and 6.37×10^4 s^{-1} in acetonitrile [144]. However, the total radiative decay rate constant accounts for both fluorescence and phosphorescence. Therefore, considering that the phosphorescence rate constant calculated was 737 s^{-1} the total radiative decay rate constant was estimated to be 3.96×10^4 s^{-1}.

This long phosphorescence lifetime of approximately 1.3 ms is enabled by a high intersystem crossing rate constant from the S_1 to the two lowest triplet states T_1 and T_2, as shown in table 4.4. In the FC region of the S_1 state, there are two triplet states of lower energy, and the T_2 state is almost degenerate with the S_1. They also present a pronounced SOC constant, which alongside the small energy gap, is favoring the crossing pathway.

Table 4.4: Calculated parameters involved in the intersystem crossing transition for the $[Ru(bpz)_3]^{2+}$ complex. SOC is the Spin-Orbit Coupling between the S_1 and T_n states given in cm^{-1}, ΔE_{ST} is the energy difference between the states involved in the transition given in eV, λ_M is the reorganization energy in eV, and k_{ISC} is the intersystem crossing rate constant in s^{-1}.

State	SOC (cm^{-1})S_1/T_n	ΔE_{ST} (eV)	λ_M(eV)	k_{ISC}(s^{-1})
T_1	63.85	-0.301	0.086	5.40×10^5
T_2	438.30	-0.012	0.053	1.37×10^{14}

The d-d metal-centered transitions are believed to be the states responsible for the complexes' liability, culminating in ligand exchange in the biological medium [108, 136, 144, 146]. Hernández-Castillo and co-workers have shown that ^{3}MC states are determining when it comes to the luminescence of Ru-based complexes with polypyridyl ligands

[159, 161], and have thoroughly studied these systems providing theoretical insights on these metal-centered states. Hence, the triplet metal-centered (^{3}MC) state is paramount in understanding the complete photophysics of the system and can provide fundamental insights about the subsequent photochemical reactions. Therefore, for completeness, we have also investigated the formation of the ^{3}MC state and have calculated the rate constants involved in this alternative channel.

As experimentally reported for $[Ru(bpy)_3]^{2+}$ by van Houten and Watts [162], and later on applied to other complexes [142, 144], the nonradiative deactivation process for the triplet state is dominated by the transition to the ^{3}MC state, which is widely dependent on the temperature. In the absence of a quenching, the ^{3}MLCT decay is described by,

$$\tau_{MLCT}^{-1} = k_{\mathrm{r}} + k_{\mathrm{nr,vib}}(T) + k_{MC}(T) \tag{4.31}$$

$$\tau_{MLCT}^{-1} = k_{\mathrm{r}} + k_{\mathrm{nr,vib}}(T) + k'_{MC} \exp\left(\frac{-\Delta E_{MC}}{RT}\right) \tag{4.32}$$

where k_r is the total radiative rate constant, $k_{nr,vib}$ is the vibrational nonradiative rate constant and has a dependence on the temperature, and k'_{MC} is an Arrhenius-type pre-exponential factor of the kinetic constant for the ^{3}MLCT $\rightarrow$ ^{3}MC internal conversion [163].

The prevailing framework for understanding the photophysics in this context suggests that the temperature sensitivity of τ_{MLCT}^{-1} arises from an activated transition, facilitating the crossing between the MLCT state and the d-d state and the overall kinetic of this process is,

$$\mathrm{MLCT} \underset{k_{\mathrm{b}}}{\overset{k_{\mathrm{a}}}{\rightleftharpoons}} \mathrm{MC} \tag{4.33}$$

$$\mathrm{MC} \xrightarrow{\mathrm{kc}} \mathrm{S_0 \text{ and photoproducts}} \tag{4.34}$$

$$k' = \frac{k_a k_c}{k_b + k_c} \tag{4.35}$$

where k' is equal to the third term of equation 4.32. Two cases can arise from this process depending on the system: i) the irreversible transition, where $k_b \ll k_c$ and $k' \approx k_b$; and ii) the equilibrium regime, where $k_b \gg k_c$ and $k' \approx k_c(k_b/k_a)$.

By fitting experimental data of luminescence lifetimes as a function of temperature, collected in acetonitrile, to equation 4.31, Kajouj and coworkers[144] suggested that the

transition ^{3}MLCT $\rightarrow$ ^{3}MC is irreversible. By using the Arrhenius equation, they have found an activation energy, E_a, of 3800 cm^{-1}, equivalent to a 10.8 kcal.mol^{-1} energy barrier, and a pre-exponential factor of 5.67×10^{13} s^{-1}, which they have used to calculate the ^{3}MLCT $\rightarrow$ ^{3}MC rate constant of 1.33×10^6 s^{-1} with an estimated error of 20% [144].

Figure 4.9 shows the free-energy profile of the thermal activation of the $T_1 \rightarrow {}^3$MC transition calculated in this work. We have computed an electronic energy barrier of 10.03 kcal.mol^{-1}, which is a value compatible with the activation energy calculated by Kajouj and coworkers [144]. However, because we have applied the Eyring equation [158] in our calculations to compute the rate constants involved in this side decay channel, we have instead used the Gibbs free energy of activation, $\Delta G^{\ddagger}$.

In transition state theory [164], the Eyring equation is used to describe the rate constant of a reaction (equation 4.12) [158]. However, instead of modeling the temperature dependence of reaction rate phenomenologically, the Eyring equation models individual elementary steps of a reaction. Although Arrhenius and Eyring's models resemble each other, the Eyring equation fundamentally describes the kinetics of individual steps within a reaction mechanism. A significant distinction is that the Eyring equation utilizes $\Delta G^{\ddagger}$ to characterize the TS rather than E_a as in the Arrhenius equation. It is important to recognize that $\Delta G^{\ddagger}$ encloses both entropic and enthalpic contributions, whereas, in the Arrhenius framework, the entropic factor is incorporated into the pre-exponential factor. Consequently, for multistep processes, one cannot directly equate the predictions of the two models. However, they should yield similar results for a one-step process, which is the case of the $T_1 \rightarrow {}^3$MC transition.

Assuming a transmission coefficient, κ, equals to 1, the calculated rate constants for the transitions involving the ^{3}MC states are $k_a = 5.81 \times 10^7$ s^{-1} and $k_b = 2.80 \times 10^{10}$ s^{-1}. The phosphorescence decay ^{3}MC $\rightarrow$ S_0 is $k_c = 279.96$ s^{-1}, also computed using the average of μ^2 for MS $= -1, 0, +1$, and is smaller than the phosphorescence constants calculated for ^{3}MLCT $\rightarrow$ S_0 at the four different FC regions. The values of k_a, k_b, and k_c calculated indicate that the equilibrium is favored over the irreversible process, as stated before.

The excited-state energies and the calculation of the radiative and nonradiative decay rate constants can be seen in Figure 4.10. The results suggest that although the internal conversion presents an elevated rate constant, the intersystem crossing is highly probable. The overall photophysics of this Ru-bpz complex is favoring access to the triplet states with long excited-state lifetimes, which are requirements for a good PS, considering the photochemical reactions follow from this point on.

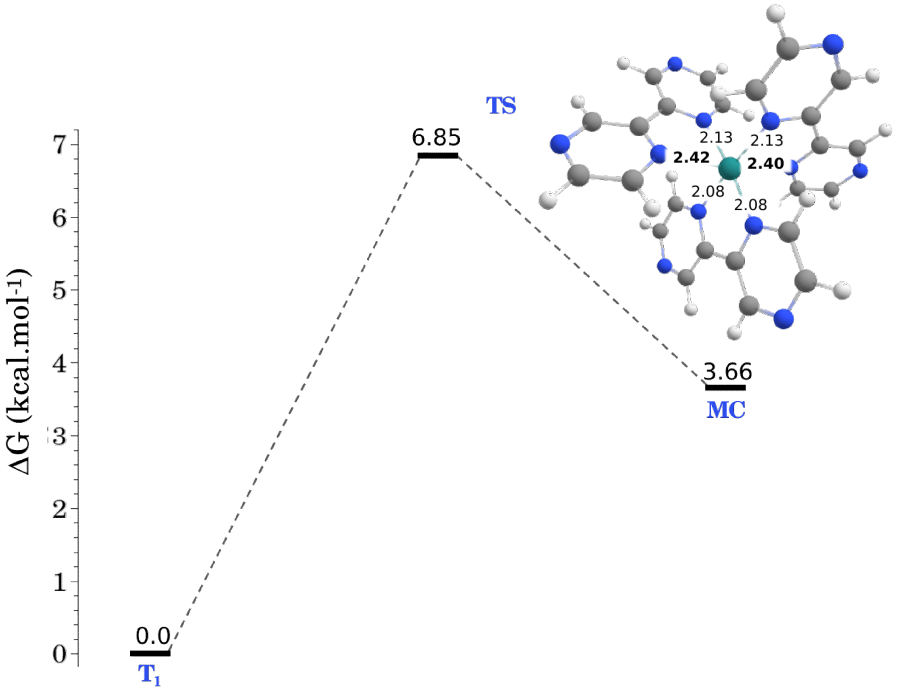

Figure 4.9: Free-energy diagram of the thermal activation leading to the population of the ^{3}MC state from T_1. Energies are given in kcal.mol^{-1}, and T_1 is set as the reference. Reprinted with permission from Phys. Chem. Chem. Phys., 2025, 27, 9806-9816 [38]. Copyright (2025) Royal Society of Chemistry.

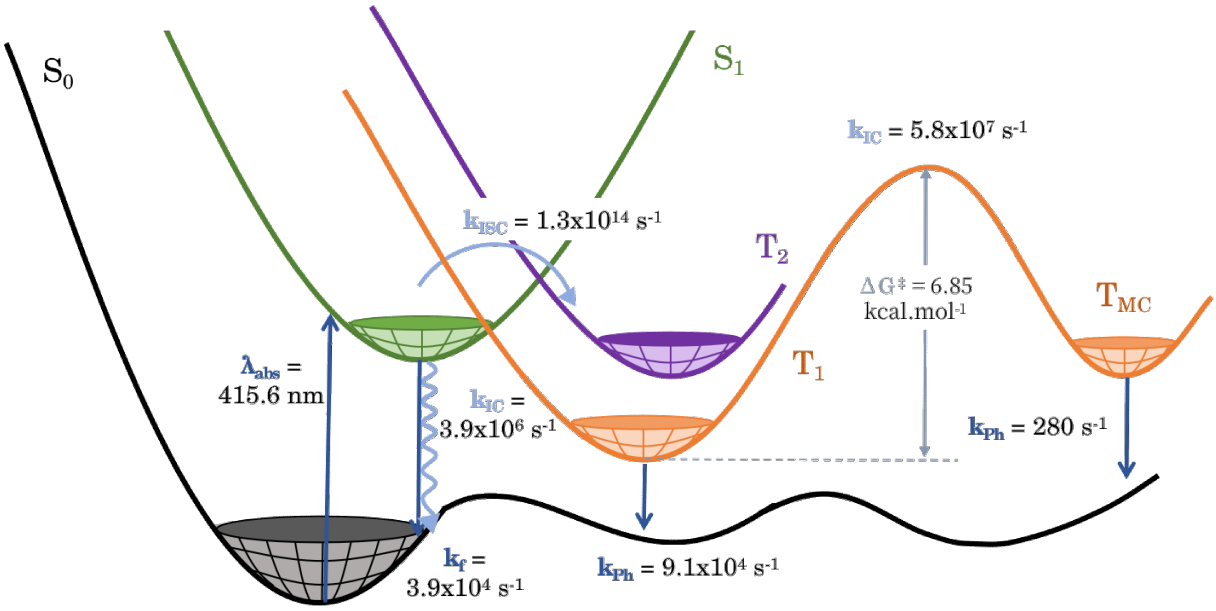

Figure 4.10: Energy diagram and deactivation rate constants calculated for the $[Ru(bpz)_3]^{2+}$ complex. The rate constants are generally represented by k, while the text in subscript determines the phenomenon, where f is the fluorescence, Ph is the phosphorescence, ISC is the intersystem crossing, and IC is the internal conversion.

4.5.3 Kinetics

When irradiated with a suitable wavelength radiation, a photosensitive compound is vertically excited to high-energy electronic states under the adiabatic approximation. Considering that the system obeys Kasha's rule, nonradiative transitions will govern the deactivation process of the excited state until it reaches the first excited state. On the other hand, radiation absorption can also lead directly to the population of the first excited state, especially for organic compounds, where the first excited state is usually bright. Nonetheless, considering a closed-shell system, the S_1 state is often the key point where the essential processes that can culminate in photochemical reactions important for a handful of applications will happen. The $[Ru(bpz)_3]^{2+}$ complex studied here is one example of a photosensitizer that undergoes a number of different processes coming from the S_1 state depending on the system conditions. Therefore, we assume the S_1 state to be the starting point at the FC region of the ground state ($S_1@S_0$), with a population equal to 1 at time 0 s. A second valid assumption is to consider only the triplet states equal to or lower in energy regarding the S_1 state. This approximation assumes that the downhill pathway is considerably faster (has a higher rate constant) than the uphill transition, which would require a gain of energy to occur and would lead to a negligible population.

The analysis of the absorption spectra at the S_0 and S_1 FC regions revealed two important triplet states below the S_1 (Figure 4.11). A third triplet state also appears almost degenerate with S_1 at the S_0 geometry. Still, it is not considered a relevant deactivation channel due to its low SOC of 6.17 cm^{-1} for the $S_1 \rightarrow T_3$ transition, being approximately ten times lower than the SOC calculated for the $S_1 \rightarrow T_2$ transition in the same region, culminating in an ISC constant of 4.4×10^3 s^{-1}. Considering all the processes that can occur from this point, we shall see that all the other possible decay channels are faster, with Vibrational Relaxation (VR) and ISC for $S_1 \rightarrow T_2@S_0$ on the picoseconds scale, making $T_3@S_0$ a negligible state. Therefore, four states are considered relevant for the decay pathway of the PS: singlet states S_0 and S_1, and triplet states T_1 and T_2. The structures of all states involved in the calculation are presented in the Supporting Information (Figure S1). Furthermore, information on spin contamination is also included, considering this can be an issue when using TD-DFT and spin-flip TD-DFT methods. The ordination of the states at each of the four FC regions can be seen in Figure 4.11.

Besides the low-lying T_3 at the S_0 minimum energy geometry, the first two singlet excited states are almost degenerate in energy, being approximately 2.6 eV higher than the ground state. These two features are not observed for other geometries, being a characteristic of the S_0 FC region. The S_1 and T_1 regions are similar in the excited state energies ordination. Only the first triplet excited state is below the S_1, while the second

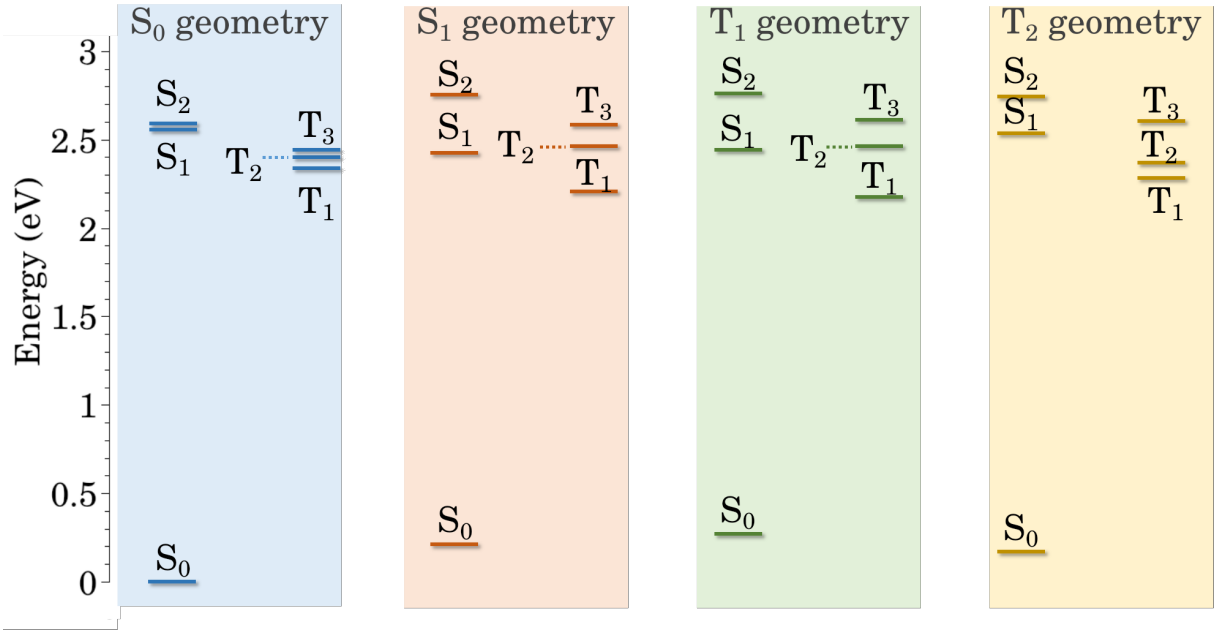

Figure 4.11: Ordination of states at each given Franck-Condon region. The S_0@S_0 energy is the reference state for being the ground state at its minimum energy geometry. Reprinted with permission from Phys. Chem. Chem. Phys., 2025, 27, 9806-9816 [38]. Copyright (2025) Royal Society of Chemistry.

triplet excited state is almost degenerate with it. Moving on to the T_2 FC region, both T_1 and T_2 are below the S_1 state. The second singlet excited state is always above the T_3 for all geometries.

Although the energy difference between two states is critical to determining the decay pathway, it does not rule it alone. According to Fermi's Golden Rule [91], the transition probabilities expressed as rate constants also depend on the coupling between the two states involved in the transition. For radiative deactivations, this dependence is given in terms of the transition electric dipole moments. Table 4.5 gathers these rate constants estimated at the four different FC regions.

It is interesting to observe that in all regions, the ISC is highly favorable, especially for the $S_1 \rightarrow T_2$ transition, with the largest rate constant being at the S_1 FC region, which also shows the strongest spin-orbit couplings. This corroborates previous results showing that the triplet manifold is populated, given that the decay pathway will likely lead to this surface crossing [144]. The ISC rate constant for $S_1 \rightarrow T_1$ is considerably lower than for $S_1 \rightarrow T_2$ in all regions, and it competes with fluorescence and internal conversion for $S_1 \rightarrow S_0$. The SOC for this process is considerably smaller, especially at the S_1, T_1, and T_2 regions. The backward processes, *i.e.*, the energy uphill rate constants, were calculated using equation 4.11 and showed large values for the $T_2 \rightarrow S_1$ process. This result can be interpreted in terms of the energy difference between these two states, which are 0.18

Table 4.5: Computed decay rate constants for various Franck-Condon regions, given in s^{-1}. Values in parenthesis are Spin-Orbit Coupling for intersystem crossing and Nonadiabatic Coupling for internal conversion processes, given in cm^{-1}, and μ^2 for fluorescence and phosphoresce, given in a.u.^{2}

	S_0 geometry	S_1 geometry	T_1 geometry	T_2 geometry
		Radiative Decay		
$S_1 \rightarrow S_0$	5.67×10^5 (0.039)	3.89×10^4 (0.003)	1.96×10^4 (0.001)	5.03×10^4 (0.003)
$T_1 \rightarrow S_0$ [a]	3.58×10^3 (0.0003)	6.06×10^4 (0.006)	9.14×10^4 (0.008)	8.11×10^4 (0.007)
		Nonradiative Decay (Intersystem Crossing)		
$S_1 \rightarrow T_1$	1.75×10^5 (36.3)	5.40×10^5 (63.8)	5.81×10^5 (66.2)	9.32×10^5 (83.9)
$T_1 \rightarrow S_1$	131	130	18.5	59.9
$S_1 \rightarrow T_2$	2.78×10^{12} (62.4)	1.37×10^{14} (438.3)	1.35×10^{14} (435.6)	1.16×10^{14} (402.7)
$T_2 \rightarrow S_1$	2.62×10^9	2.68×10^{13}	6.99×10^{13}	2.47×10^{11}
		Nonradiative Decay (Internal Conversion)		
$S_1 \rightarrow S_0$	1.93×10^6 (0.44)	2.18×10^6 (0.46)	2.57×10^6 (0.50)	2.11×10^6 (0.46)
$S_0 \rightarrow S_1$	1.41×10^{-37}	2.63×10^{-31}	1.22×10^{-30}	8.71×10^{-34}
$T_2 \rightarrow T_1$	2.73×10^{11} (28.8)	2.17×10^8 (0.81)	2.75×10^8 (0.91)	4.49×10^9 (3.69)
$T_1 \rightarrow T_2$	2.16×10^{11}	1.02×10^4	4.52×10^3	1.35×10^8

[a] Rate constants and μ^2 values are given as the average values for MS = +1,0,-1. All values were obtained at the b3lyp/def2-TZVP level and included water solvation effects through C-PCM.

eV at S_0, 0.04 eV at S_1, 0.02 eV at T_1, and 0.16 eV at T_2. Such slight variations can be easily overcome by thermal fluctuations, considering that the states are near degenerate, making the uphill transition extremely accessible. However, this is not true for the uphill $T_1 \rightarrow S_1$ transition. Although the uphill energy difference is not quite expressive, the downhill path already has small ISC values due to the small SOC, as mentioned above. Hence, the uphill $T_1 \rightarrow S_1$ transition has rate constants of the order of 10^2 s^{-1} for the singlet FC regions and 10^1 s^{-1} for the triplet FC regions.

According to Sun and Hoffman [142], the total radiative rate constant for the $[Ru(bpz)_3]^{2+}$ complex is 6.8×10^4 s^{-1} in water, corroborating our estimations for fluorescence and phosphorescence constants, also calculated in implicit water solvation. Interestingly, the fluorescence rate constant at the ground state geometry had the highest value among them, with a transition electric dipole moment ten times greater than for the other three regions. On the other hand, the average transition electric dipole moment, μ^2, and k_{Ph} at the T_1 FC region were the largest, which is the geometry where phosphorescence is expected to be the most favorable.

With all calculated constants, we have solved the set of eighteen first-order kinetic equations to analyze the time evolution of the S_0, S_1, T_1, T_2, and ^{3}MC states and determine the possible deactivation channels. As discussed before, our starting point was to consider $S_1@S_0$ as the initial state at the initial geometry, in which the population was set to one at time $t = 0$ s. All other states had populations equal to 0 at time $t = 0$ s. Furthermore, we worked with a closed system so that the sum of all populations at any given simulation time was always one. In a geometry different from the minimum-energy geometry, vibrational relaxation within the same electronic state is usually one of the most competing decay events. This rate constant, k_{vr}, is typically of the order of picoseconds [73, 165], and, therefore, was set to 1×10^{12} s^{-1} in our simulation. Figure 4.12 shows the time evolution of the states in three different time scales.

In Figure 4.12-a, the time range goes up to 5 ps with a propagation step of 0.1 ps. The initial $S_1@S_0$ state immediately starts to decrease, drastically reaching zero within 2 ps. The $S_1 \rightarrow T_2@S_0$ transition rate constant is 2.78×10^{12}, competing with VR from $S_1@S_0$ to $S_1@S_1$, and is the first population rising before 1 ps. It is noteworthy that, even though these two processes are of the same order, the $S_1@S_1$ population does not increase significantly, reaching approximately 0.5% of the population that rapidly decays before 1 ps (Appendix B, Figure B.6). Although it may seem odd due to the high k_{vr} value, the $T_2@S_1$ state is readily populated before 1 ps with a rate constant of the order of 10^{14} s^{-1} for the $S_1 \rightarrow T_2@S_1$ transition, implying that all the vibrational relaxation forming $S_1@S_1$ is nearly instantly converted into $T_2@S_1$ through ISC. Following the time evolution, $T_2@S_0$ starts to decay through ISC and VR after reaching a peak of approximately 40% of the total population, giving rise to a small population of $T_1@S_0$ that completely fades away before 5 ps, and an increasing population of $T_2@T_2$ that achieve 80% of the total population within the picoseconds time scale. It is also noticeable a $T_1@T_1$ population rise that comes from VR of $T_1@S_0$ and $T_1@T_2$ (Appendix B, figures B.3, B.4, and B.5) and from ISC of $T_2 \rightarrow T_1@S_0$. In Figure 4.12-b, the same propagation step is used, but the time range goes up to 10^{-10} seconds, and the events detailed in Figure 4.12-a are no longer visible. It is interesting to note that the population of $T_2@T_2$ increases by 80% within picoseconds but has a very fast decay as well, approaching 10% of the total population before 5×10^{-10} s. The $T_1@T_1$ population dominates this time range, approaching 90% of the total population due to VR of $T_1@T_2$ state, which is a result of the ISC from $T_2@T_2$. $T_1@T_1$ reaches a maximum population by nanoseconds (Appendix B, Figure B.2). Its decrease starts at the microsecond time scale (Appendix B, Figure B.1), in perfect agreement with luminescence lifetime experiments acquired in acetonitrile in a temperature range of 275 to 300 K [144]. In the milliseconds timescale (Figure 4.12-c), the $T_1@T_1$ population has dominated the decay pathway, and it is responsible for the

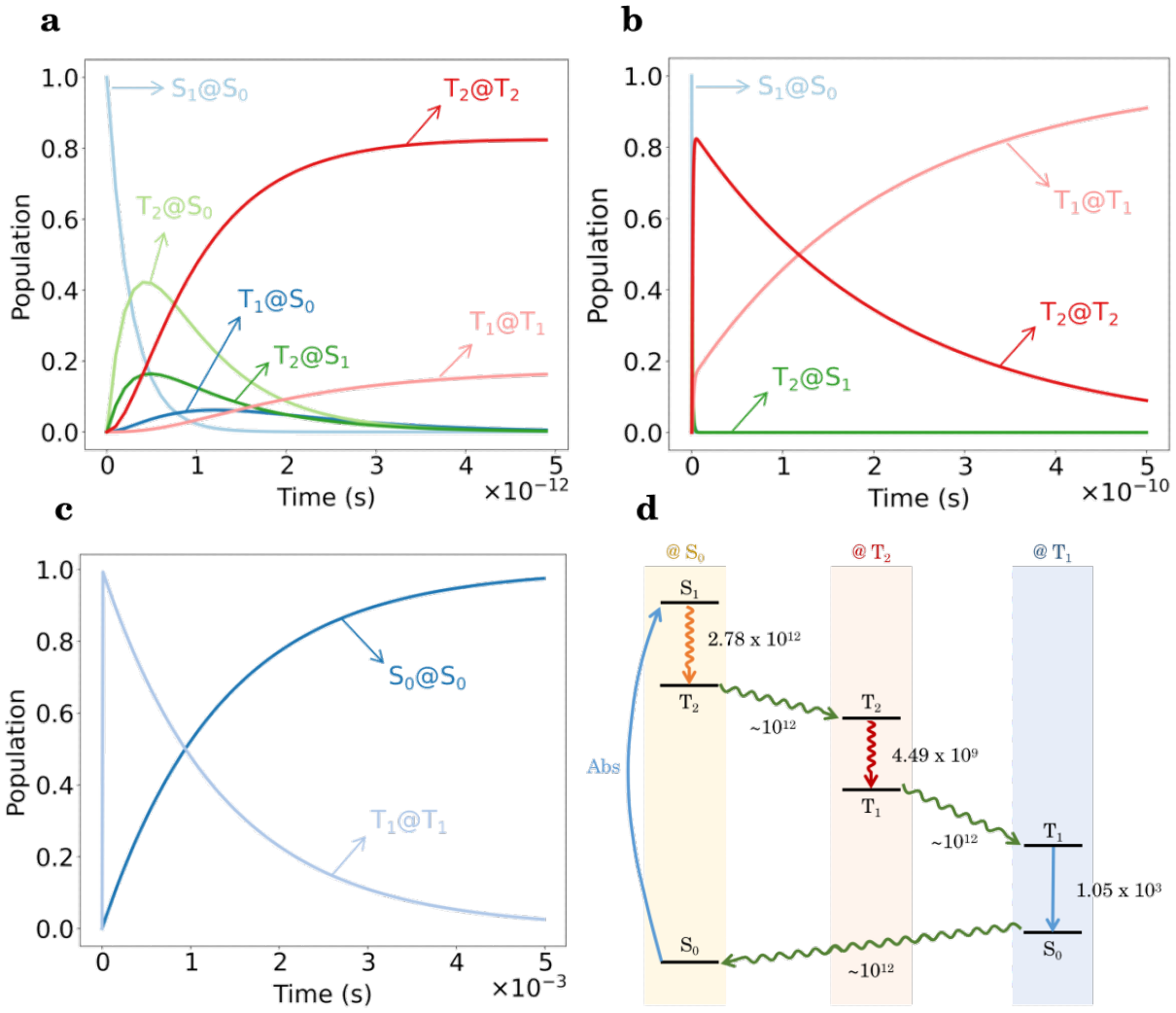

Figure 4.12: Evolution of states' population over time solved using the proposed first-order kinetic model and the rate constants calculated. (a) Time range from 0 to 5 ps using a propagation step of 10^{-13}; (b) Time range from 0 to 5×10^{-10} s using a propagation step of 10^{-13}; (c) Time range from 0 to 5 ms using a propagation step of 10^{-5}; (d) Deactivation channel proposed using the calculated decay rate constants and solved kinetic model. Solid arrows represent radiative decays, and wavy arrows represent radiationless decays. The vibrational relaxation is set to 10^{12} s^{-1}.

Adapted with permission from [38]. Copyright (2025) Royal Society of Chemistry.

primary deactivation channel that feeds the ground state population. $S_0@T_1$ is readily relaxed into $S_0@S_0$, achieving maximum population and turning the complex completely deactivated. The population of the triplet manifold is not only observed in experimental works [144, 146], but has also been reported through a theoretical investigation on the decay dynamics of this system using Trajectory Surface-Hopping Dynamics for Ru-based polypyridyl complexes [159, 161, 166]. They have demonstrated that the triplet manifold for $[Ru(bpy)_3]^{2+}$ complex is populated within 26 fs, due to an ISC from high-lying singlets.

They also observed a competing IC event that would lead to the lowest singlet state with a minor population, which could also cross to the triplet states in a subsequent ISC process, corroborating the ISC process observed in this work from S_1 on the scale of picoseconds.

Although not explicitly shown as a deactivation channel, the ^{3}MC state is one of the deactivation possibilities for $T_1@T_1$, and acquires a maximum population of 0.2% by 1 ns (Appendix B, Figure B.2). However, the phosphorescence is not favored, and the $S_0@MC$ population has a negligible value peak of the order of 10^{-13}. This result is also in agreement with experimental findings [142] that suggest that the luminescent excited states of $[Ru(L)_3]^{2+}$ complexes are MLCT. Furthermore, Sun and coworkers [142] also observed that at lower temperatures, the temperature-independent MLCT $\rightarrow S_0$ is dominant, and that the overall decay is faster in polar solvents that can better stabilize CT states, which are dominated by larger dipole moments, while at higher temperatures, the temperature-dependent MLCT $\rightarrow$ MC transition is dominant, and the overall decay is slower. The states $S_1@T_1$, $S_1@T_2$, and $T_2@T_1$ are not populated at any time of the simulation. Hence, the proposed deactivation channel is illustrated in Figure 4.12-d.

Considering a VR rate constant of 10^{12} s^{-1}, the estimated decay pathway was $S_1@S_0 \rightarrow T_2@S_0 \rightarrow T_2@T_2 \rightarrow T_1@T_2 \rightarrow T_1@T_1 \rightarrow S_0@T_1 \rightarrow S_0@S_0$. This deactivation channel is not the only possibility but reflects the most probable pathway. It agrees with previous experimental results that suggest that the decay of ruthenium-based complexes featuring polypyridyl ligands are highly prone to ISC crossing to populate the triplet manifold and that their excited state lifetime is usually on the microseconds timescale.

The overall results obtained upon the implementation of this method are satisfactory when compared to experimental results, as mentioned above. The key point of the kinetic model is to obtain reasonable and trustworthy results with a cheaper computational methodology for complex systems. However, it is essential to understand the limitations of the method and the approximations herein applied. The semi-classical Marcus equation [82–85] has been used to calculate rate constants in many works [24, 69, 73], considering it derives from Fermi's golden rule [64, 91]. In Marcus' expression, the perturbation operator that activates the electronic transitions is substituted by the electronic coupling between the states involved in the transition. However, it should be noted that its applicability is limited to cases where states are weakly coupled (coupling smaller than k_bT). These assumptions invalidate this approach for transitions that occur via nuclear tunneling [73]. Furthermore, the application of the one-effective mode MJL theory developed in our group [24] should be used for molecules in the inverted region ($\lambda_M < \Delta G$), where the minimum energy crossing point correction in the density of states is needed. Finally, the kinetic model is faster than non-adiabatic molecular dynamics and holistically provides similar results; however, its limitations lie in the number of states investigated. It is crucial to

correctly identify the critical states contributing to the overall photo-decay prior to the simulation. Moreover, this study does not rule out the existence of other intermediate states and does not account for multi-excitation processes.

4.6 Conclusions

In this work, we have used the time-dependent density function theory in conjunction with a first-order kinetic model as an alternative to investigate the excited state dynamics of complex systems. This approach was applied to the $[Ru(bpz)_3]^{2+}$ complex, in which five electronic states (S_0, S_1, T_1, T_2, and ^3MC) were selected, leading to eighteen coupled kinetic equations. The rate constants were computed for each process using the formalism of Fermi's golden rule, Marcus' theory, and Einstein's coefficients. According to the decay rate constants and the population dynamics over time, the k_{ISC} for the $S_1 \rightarrow T_2$ is of the same order as the k_{vr} and, therefore, are competing events. In this case, we considered the crossing to occur preferably over the VR. However, should the VR occur first, the k_{ISC} for $S_1 \rightarrow T_2$ at the S_1 geometry is approximately 10^{14} s^{-1}, leading to the crossing then, and the overall result is similar. Once in the T_2 excited state at the S_0 FC region, the VR is the most probable event, relaxing the structure to the T_2 FC region. Once in the triplet spin state, the internal conversion to the lowest triplet state is favored over the direct crossing to the ground state. After VR to the T_1 FC region, the phosphorescence occurs. At this point, the phosphorescence rate constant is low, meaning the triplet electronic configuration has a long lifetime, as observed for $T_1@T_1$ that started deactivating around 1 μs. The proposed path agrees with the overall photophysical patterns observed by many different experimental works. These results are a clear indication that the kinetic model herein proposed to study the dynamics of the excited states of the $[Ru(bpz)_3]^{2+}$ complex, allied with Marcus' equation and Einstein's coefficient, is a powerful and effective method to evaluate medium-sized and complex systems.

Chapter 5

Dexter Energy Transfer: $^1O_2$ Generation through $[Ru(bpy)_2dppn]^{2+}$ photoexcitation

5.1 Introduction

Photodynamic Therapy (PDT) applied to cancer is a treatment strategy that has as its principle the use of a compound, the Photosensitizer (PS), that is photoactivated through the incidence of radiation of a specific wavelength, which will imply cytotoxicity to cancer cells through the generation of Reactive Oxygen Species (ROS) (Figure 5.1) [167]. In most cases, the PS is given intravenously to the patient and, as such, will be distributed non-specifically throughout the body. After the incubation time, referred to as the drug-light interval, which can vary from 5 minutes to 24 hours, the PS is mainly accumulated in the cancerous region. At this stage, the incidence of light is made through a laser ensuring the generation of cytotoxic species [167–170].

Light penetration and propagation on the skin depend on the type of tissue, light properties, exposure period, and the medium. For instance, molecules like water or biological chromophores such as melanin will influence the process. Therefore, light permeability for most tissues is optimum for the spectral range of 620nm - 850 nm, which is known as the phototherapeutic window (Figure 5.2), and the penetration can be up to 200% compared to other ranges of smaller wavelengths [23, 169].

After irradiating PS compounds with radiation of the appropriate wavelength, they are excited to higher-energy electronic states. From this, some phenomena of physical and chemical nature must occur, as seen in Figure 5.3 through the Jablonski diagram adapted for PDT [167]. Once in the excited state, the PS undergoes energy decay processes until it

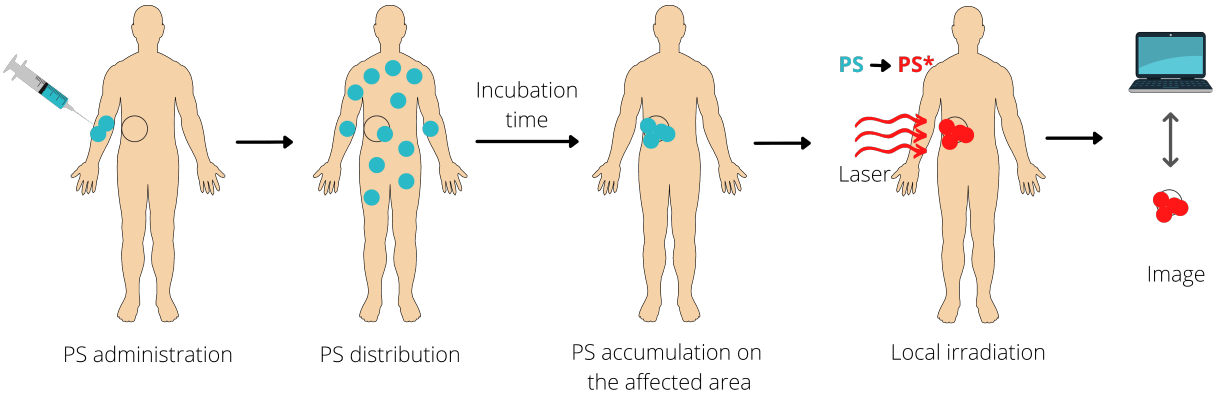

Figure 5.1: The principle of Photodynamic Therapy (PDT). The PS is administered and distributed throughout the patient's body. After an incubation time, the PS is accumulated on the affected area and is ready to be irradiated with a laser of optimum wavelength.

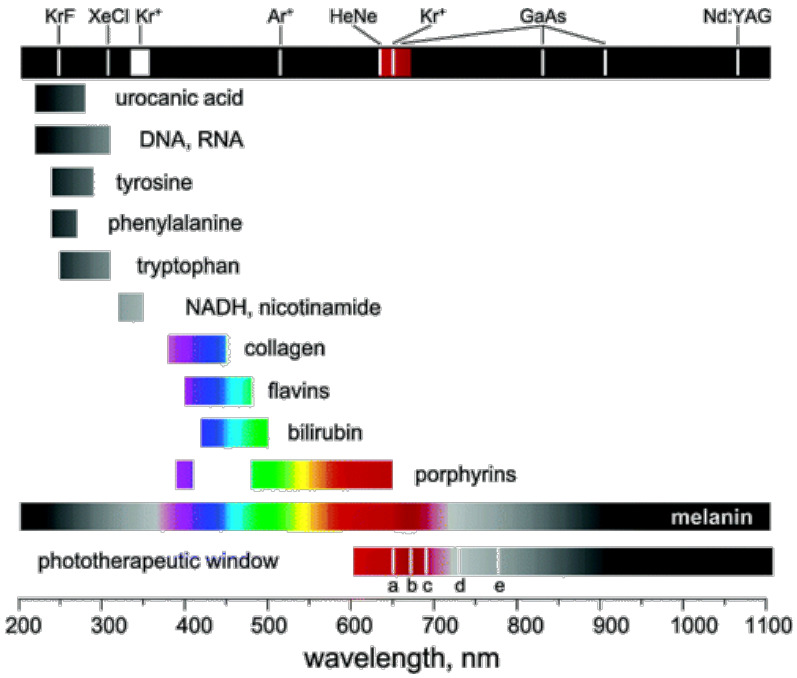

Figure 5.2: Phototherapeutic window and biological chromophores with their wavelength of absorption.
Reprinted with permission from Chemical Reviews, 2005, 6, 2647–2694 [23]. Copyright 2023 American Chemical Society.

returns to its ground state. These possible processes are fluorescence, phosphorescence, vibrational relaxation, internal conversion, and intersystem crossing. The latter leads to the triplet state population of the photosensitizer, which has a longer lifetime as an intrinsic characteristic, reaching the microsecond scale. This condition is ideal for photochemical mechanisms to occur, such as Type I and Type II, as also illustrated in Figure 5.3. The Type I mechanism is recognized by its Electron Transfer (ET), between the photosensi-

tizer and a molecule in the medium, leading to radical and ionic species, mainly oxygen, referred to as ROS. These species, in turn, react with DNA, causing cellular death. On the other hand, the Type II mechanism is characterized by Energy Transfer (EnT), between the photosensitizer and an oxygen molecule, $^3O_2$, resulting in the deactivation of the PS excited state and the generation of singlet oxygen molecules, $^1O_2$, in the medium. The $^1O_2$ species also has high cytotoxicity to the cancer cell [23, 167, 170]. In more recent studies, some PSs were suggested to interact directly with the DNA by intercalation between two nucleic acid pairs undergoing an ET mechanism, having a preference for interacting with the guanosine monophosphate [171–174].

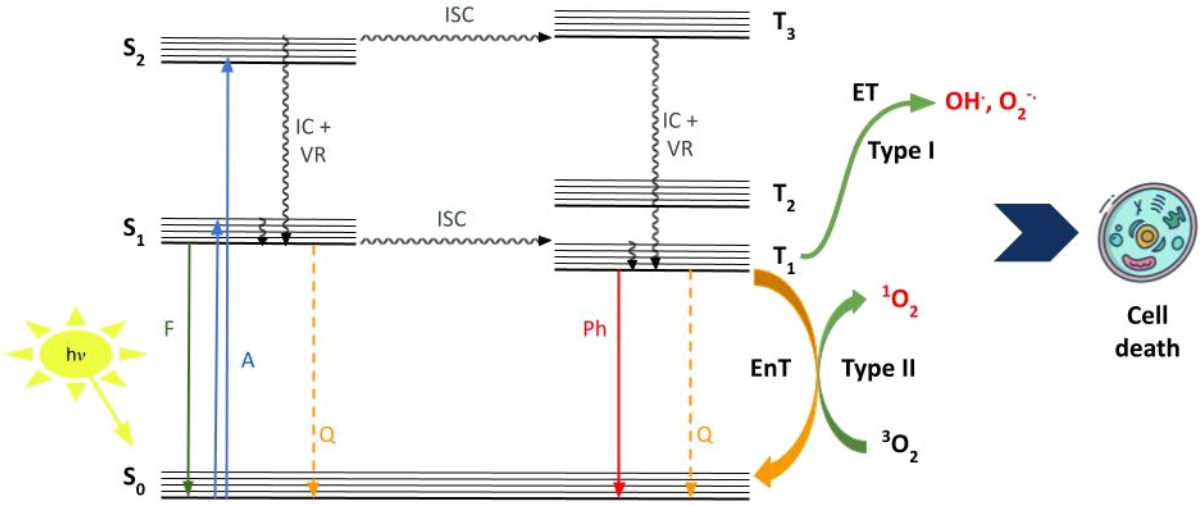

Figure 5.3: Jablonski diagram and photochemical processes involved in the Photodynamic Therapy. The photophysical processes are A (absorption), F (fluorescence), Ph (phosphorescence), IC (internal conversion), VR (vibrational relaxation), ISC (intersystem crossing), and Q (quenching). At the same time, the photochemical reactions are ET (electron transfer) and EnT (energy transfer).

In this way, it is possible to perceive that the PS has a central importance in PDT, and its careful design can lead to tuning specific features to favor one mechanism over another. A suitable PS is desired to have a set of fundamental properties, such as being easy to synthesize and presenting high chemical purity, being inactive and nontoxic in the dark, being stable under physiological conditions, intensely absorbing in the phototherapeutic window but showing low absorption for other wavelengths, having a long excited-state lifetime to enable either PDT mechanisms, among other features [23, 163, 175, 176].

The most studied potential PSs are porphyrins and their derivatives [168], and the so-called first-generation photosensitizers are based on modified hematoporphyrins [23]. However, their weak absorption in the phototherapeutic window led to subsequent development of the second (porphyrins with systematic modifications with substituents at the pyrrole rings) and third (PS moieties linked to biomolecules) generations [177]. Currently,

the PSs under investigation belong to different groups as porphyrins, chlorins, phthalocyanines, and others. The first approved PS to be commercialized is the Photofrin®, a Haematoporphyrin derivatived, and is indicated for treating cervical, endobronchial, gastric, and brain tumours [168, 169]. Table 5.1 gathers some of the clinically approved PSs used nowadays, however, there are others not listed, and many being tested in other clinical phases. PDT has been incorporated into the Brazilian Public Health System (SUS) as a treatment for skin cancer in 2023, and is offered entirely free of charge.

Table 5.1: Aproved photosensitizers for malignant diseases.

PS	Commercial Name	Indications	Activation wavelength
Haematoporphyrin, porfimer sodium	Photofrin®	Cervical, endobronchial, gastric, and brain tumours	630 nm
BPD-MA	Verteporfin	Basel-cell carcinoma	689 nm
m-THPC	Foscan®	Head and neck tumours	652 nm
5-ALA	Levulan®	Basal-cell carcinoma, head and neck, and gynaecological tumours	635 nm

Hypoxia and tissue penetration are among the challenges for PDT and, therefore, require attention to PS next generations design. Besides the porphyrin group, metal complexes also show a prominent perspective as PSs, taking into consideration that they can meet the properties desired for a successful PS.

Transition metal complexes have been used in medicine with diverse applications. For instance, for enzyme inhibition, drug release, labeling proteins, and contrast MRI agents, among others. Cisplatin (cis-diamminedichloroplatinum(II)), as an example, is used in almost 50% of cancer treatments [178, 179]. The success of coordination complexes and organometallics is due to their d-block properties, such as a range of coordination numbers, oxidation states, and geometries, and their susceptibility to change upon metal-ligand choice, which can be designed to alter reactivity, charge, acidity, redox-potentials, and so on. The photophysical properties of these metal complexes can also be tuned following the same logic, which explains the interest in employing them for photobiological demands [178]. The variety of transitions possible and a usually long excited-state lifetime for metal complexes enable their ability to undergo both PDT mechanisms. Recent studies suggested that d-block metal complexes are also able to intercalate with DNA and, therefore, have one more mechanism of action by directly interacting with the target [171–174].

Alongside platinum-based complexes, ruthenium(II) complexes are considered to form a potential new generation of anticancer drugs due to some photophysical and medicinal

properties, such as (*i*) being effective against some cisplatin-resistant cells (*ii*) having a higher selectivity for cancer cells (*iii*) being able to mimic iron in binding to biological macromolecules, (*iv*) having long excited-states lifetime, good quantum-yield, affordable synthesis, good stability, luminescence in room temperature, and good Stokes shifts, and (*v*) acting as good electron and energy transfer agents [171, 180–183].

The interest in ruthenium complexes started with NAMI-A (imidazolium dimethylsulfoxidetetrachlororuthenate(III)), discovered to have antimetastatic properties, and KP1019 (indazolium trans-tetrachlorobis(1*H*-indazole)ruthenate(III), which entered the clinical trials. Polypyridyl ruthenium(II) complexes also started to show promising results by exerting activities against tumor cells, and TLD1433 ($[Ru(dmb)_2(IP\text{-}TT)]^{2+}$, where dmb = 4,4'-dimethyl-2,2'-bipyridine and IP-TT = 2-(2',2":5",2"'-terthiophene)-imidazo[4,5-*f*][1,10] phenanthroline) became the first Ru-based complex to enter a human clinical trial, proposed for the treatment of bladder cancer [184]. Other Ru(II)-polypyridyl complexes have also shown promising results, such as the largely studied dppz-based ones and their light-switch effect [185–190].

The most studied metal complexes as potential photosensitizers used in photodynamic therapy are those characterized by the metals Pt(II), Pt(IV), Re(I), Os(II), Ir(IV), and Ru(II). Among these, Ru(II) accompanied by polypyridine ligands are the most investigated, as they present a set of fundamental properties for this application [170, 191–194]. These properties are long excited-state lifetimes (especially triplets), a propensity to charge and energy transfers, luminescence in solution at room temperature, significant Stokes shifts, affordable synthesis, and chemical and photochemical stability. Ru(II) complexes can interact with DNA through various mechanisms, such as covalent bonding, electrostatic interaction, interaction at the surface of DNA clefts, and intercalation between base pairs. The types of interaction between a given complex and the target molecule depend directly on the nature of the ligands so that a minor modification of these structures can lead to different mechanisms of action.

However, the determination of the different mechanisms of both PS-DNA and photochemical interactions is a difficult task since it requires monitoring all species and intermediates generated throughout the photodynamic process. In addition, it has to be considered that more than one mechanism can be involved in these systems. In this way, theoretical and computational studies are essential. Understanding photodynamic processes applied to biological systems, such as PDT, is just beginning, being a frontier area in chemistry, biology, medicine, and biochemistry. Even more recent is the contribution of computational studies, which demand more precise methods in electronic structure. In this sense, there are still many significant advances to be made, such as, for instance, the investigation of the excited states of metal complexes and the application of more precise

methods to describe biomolecules. Furthermore, the experimental challenges mentioned above culminate in a few research groups worldwide dedicating efforts to contribute to this subject.

Due to the outstanding photophysical and photochemical properties of Ru(II)-dppz complexes, other analog ligands gained attention. This is the case of the dppn ligand (dppn = benzo[*i*]-dipyrido[3,2-*a*:2',3'-*c*]phenazine), which has been investigated combined with a handful of other ligands, demonstrating its suitability as a PS [141, 145, 195, 196]. Especially, the $[Ru(bpy)_2dppn]^{2+}$ complex (bpy = 2,2'-bipyridine) has demonstrated to be able to generate $^1O_2$ [1, 142]. Furthermore, the same complex has also been demonstrated to oxidize guanine nucleobases and derivatives and to photocleave DNA upon intercalation in a so-called dual-channel reaction (Figure 5.4) [23, 142, 146, 178]. However, in contrast to other polypyridyl-based complexes, the $[Ru(bpy)_2dppn]^{2+}$ lacks some insights into its photophysical rate constants. Furthermore, additional analysis of its interactions with DNA fragments might help better understand the mechanisms of action of this PS.

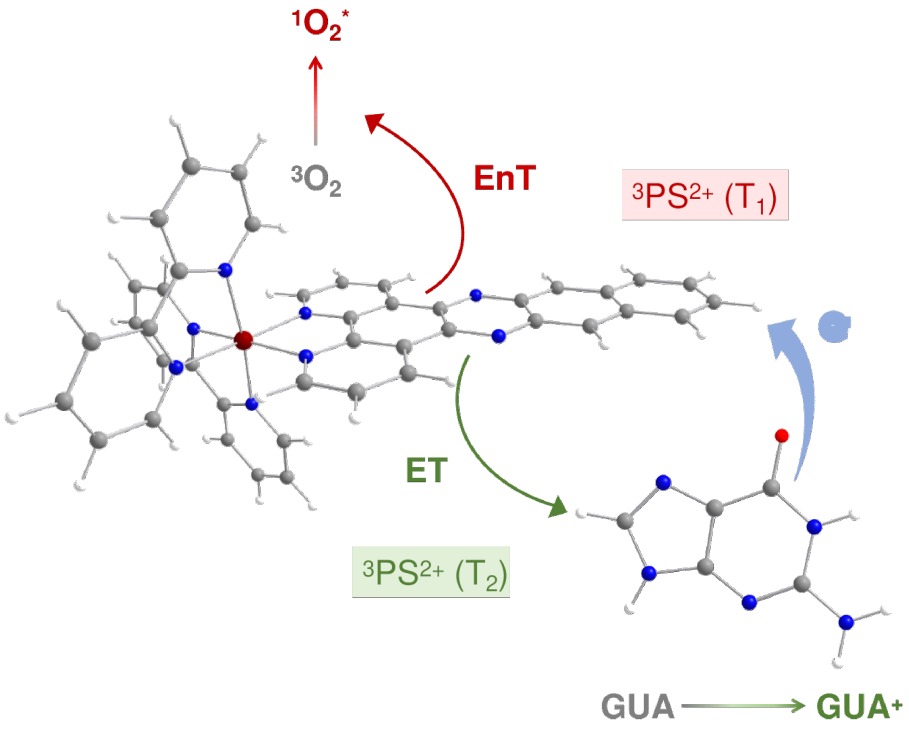

Figure 5.4: Dual-channel reaction of the $[Ru(bpy)_2dppn]^{2+}$ complex as a photosensitizer. EnT refers to energy transfer, ET refers to electron transfer, and GUA refers to the molecule guanine.

Besides mapping the photophysics of PSs and understanding their properties to design better molecules, it is also crucial to understand the EnT and ET processes that lead to the two main mechanisms of PDT. Most experimental works have been focusing on developing and testing new phototherapeutic agents [89, 141, 142, 144, 146, 147], usually reporting

whether the PS under study is capable of generating singlet oxygen. Although very useful, this information does not provide many insights into the nature of this process. Some computational works have also addressed this problem from a more thermodynamical perspective [39, 69, 70] also aiming to report the suitability of PSs for PDT Types I and II. However, modeling EnT in supramolecular excited systems is a challenging task because two main issues arise: (*i*) understanding which energy transfer mechanism is dominant and (*ii*) the reaction coordinate for the energy being transferred.

Hence, in the first part of this chapter, we investigated the excited state rate constants quantitatively. Also, we demonstrate that molecular oxygen sensitization is thermodynamically favorable. Finally, we also show that intercalation with DNA does not significantly shift the absorption bands on the electronic spectrum, but it changes the nature of the transitions. In the second part, we have put together different kinetic models to describe the Dexter Energy Transfer (DET), responsible for the Type II mechanism of PDT to generate singlet oxygen molecules.

5.2 Energy Transfer

5.2.1 An overview

Excited-state EnT is one of the competing processes of deactivating a system. It involves a donor (D), which is the species in the excited state that will transfer its excess energy, and the acceptor (A), which will receive the energy, in a process that can be illustrated as $D + h\nu \rightarrow D^* + A \rightarrow D + A^*$ [90]. EnT can occur through both radiative and nonradiative mechanisms.

The radiative mechanism, also known as the *trivial mechanism*, occurs when the donor (D^*) is deactivated through a radiative process emitting a photon, which is then absorbed by the acceptor (A). This process is not dependent on the distance between D^* and A and does not affect the excited state lifetime of the donor; however, it depends on the spectral overlap between the two species involved, the concentration of the acceptor, and the optical path of the photon through the system [90].

The radiationless mechanism can be understood in terms of the *Fermi Golden Rule*. It can be approximated as an isoenergetic nonradiative deactivation between two localized electronic states $D^*.A \rightarrow D.A^*$, where the electronic coupling, $\mathcal{H}_{el}$, will govern the transfer alongside the Franck-Condon Weighted Density (FCWD). The FCWD can be expressed through either a classical or quantum mechanical fashion [90]. The classical approach would arise from Marcus theory, which is the general approach for weakly coupled systems [82, 84, 85, 197]. From the quantum mechanical approach, the FCWD is calculated through the vibrational overlap integrals. It can also be estimated through the overlap

integral between the donor emission spectrum and the acceptor absorption spectrum, as illustrated in Figure 5.5.

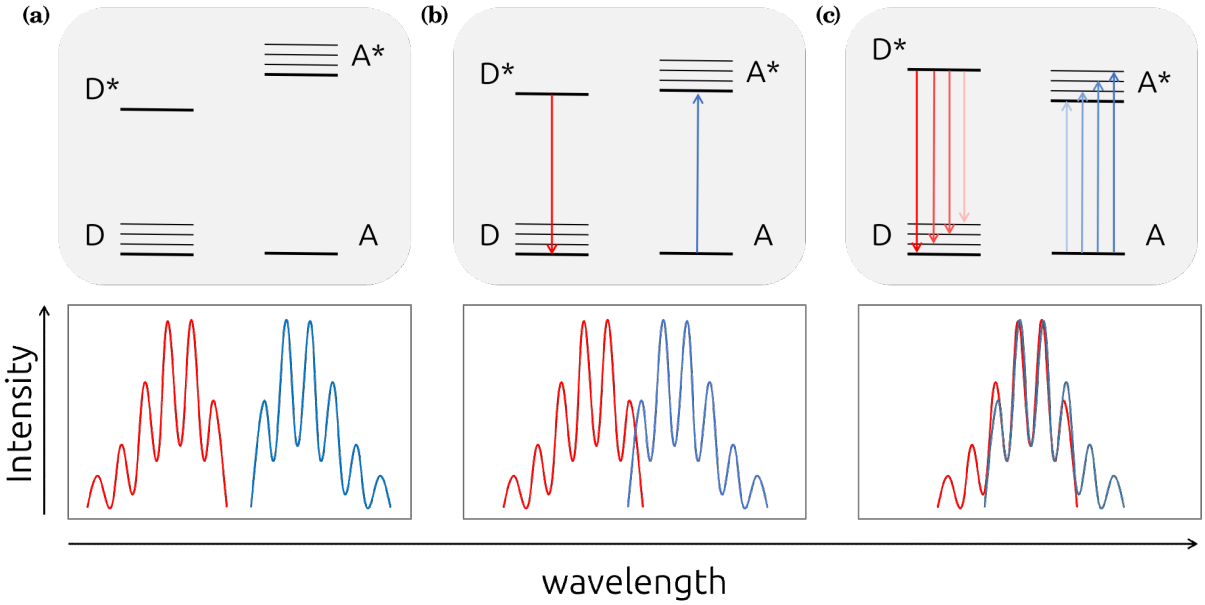

Figure 5.5: Illustrative energy level diagram of donor (D) and acceptor (A) (top), and spectral overlap between donor emission (red line) and acceptor absorption (blue) for cases: (a) $E(D^*) < E(A^*)$; (b) $E(D^*) = E(A^*)$; and (c) $E(D^*) > E(A^*)$.

In Figure 5.5 (a), $E(D^*) < E(A^*)$ and, therefore, FCWD is negligible and the transfer does not occur. In (b), the FCWD term is small, and the energy rate transfer will be low. Finally, in (c), the FCWD will greatly favor a high energy transfer rate constant.

The electronic operator, $\mathcal{H}_{el}$, depends on the HOMO and LUMO energies of the donor and the acceptor. This term can be further divided into two additive factors, the *coulombic*, $\mathcal{H}_c$, and the *exchange*, $\mathcal{H}_e$, operators. Therefore, the non-radiative mechanism can also be divided into two different mechanisms. The Coulombic mechanism, also known as *Förster resonance energy transfer* (FRET) [198], is a long-range mechanism that does not involve direct contact between donor and acceptor, usually occurring from 1 to 10 nm. This process involves a dipole-dipole coupling between the two species, making the FRET efficiency dependent on the magnitude of the oscillator strength, the relative orientation between donor and acceptor, and the overlap between the emission spectrum of D^* and the absorption spectrum of A [90, 199]. On the other hand, the exchange mechanism, also known as *DET* [200], is short-ranged (≤ 1 nm) and requires the molecules to overlap wavefunctions. In this case, the exchange electronic coupling governs the energy transfer instead of the dipole-dipole interaction. Hence, the oscillator strength does not affect the overall transfer rate constant.

As stated before, the $[Ru(bpy)_2dppn]^{2+}$ complex can undergo EnT to generate singlet

oxygen species in the PDT context. In the next section, more focus will be dedicated to discussing the DET mechanism and methods for modeling this phenomenon.

5.2.2 Dexter Energy Transfer: The exchange mechanism

The exchange mechanism can be perceived as a double electron transfer process, split into two-electron and one-electron interactions. The two-electron interaction is the concerted exchange between donor and acceptor, yielding a direct excitation transfer ($D^* + A \rightarrow D + A^*$). In this double exchange, the electron on the SOMO of the donor is transferred to the LUMO of the acceptor, and an electron is transferred back from the acceptor's HOMO to the donor's HOMO. On the one-electron interaction, there are two Charge-Transfer (CT) processes in sequence. The mechanism through CT occurs with the donor transferring the electron from the LUMO to the acceptor, followed by the reception of an electron to the HOMO hole ($D^* + A \rightarrow D^+ + A^- \rightarrow D + A^*$). The hole transfer mechanism occurs when the hole on the donor's HOMO is transferred to the acceptor, followed by the electron transfer from the LUMO ($D^* + A \rightarrow D^- + A^+ \rightarrow D + A^*$). Although the two-electron and one-electron interaction mechanisms lead to the same net result, the one-electron mechanism involves a CT intermediate. It is noteworthy that in all mechanisms, the entity being transferred is the electron, and referring to *hole transfer* is rather a perspective. Figure 5.6 illustrates the three DET mechanisms [90, 201].

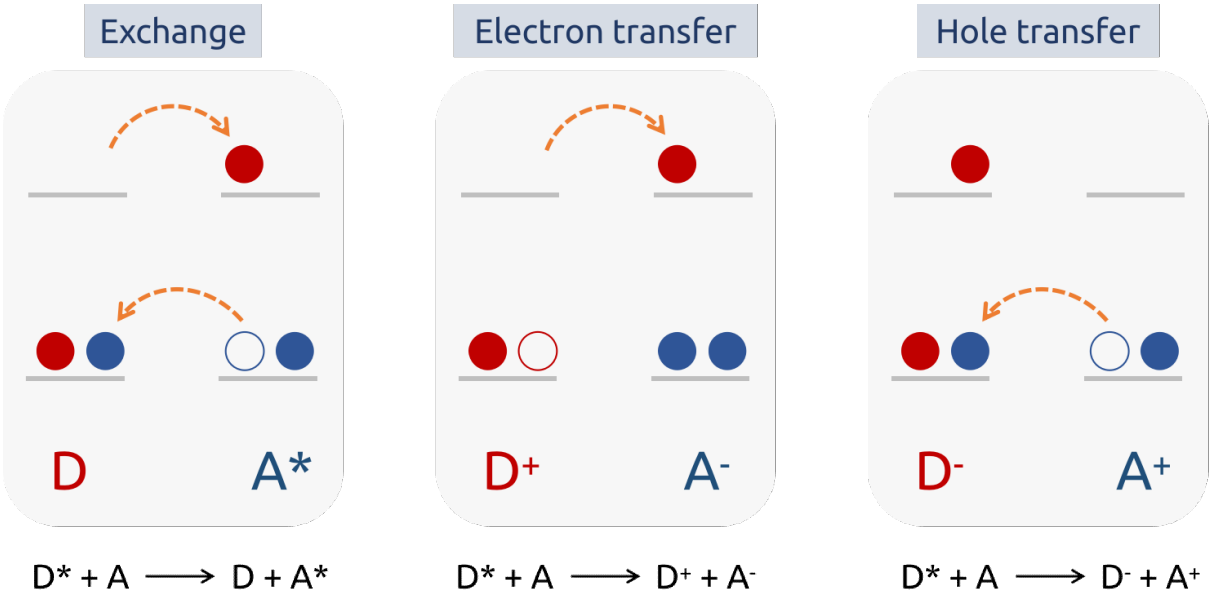

Figure 5.6: The Dexter energy transfer mechanism can be divided into the exchange transfer, the electron transfer followed by hole transfer, or the hole transfer followed by electron transfer.

Because the exchange mechanism is a double electron transfer problem with an energy

transfer net result, Marcus' theory for electron transfer [82–85] can be applied to the DET phenomenon, and can be expressed as,

$$k_{el} = \nu_N \kappa_{el} \exp\left(\frac{\Delta G^{\ddagger}}{RT}\right) \tag{5.1}$$

where ν_N is the average nuclear frequency factor, κ_{el} is the electronic transmission coefficient, $\Delta G^{\ddagger}$ is the activation energy, R is the gas constant, and T is the temperature. The quadratic term represented in the Marcus formulation of equation 3.16 is due to approximating the Potential Energy Surface (PES) as a parabolic potential for both reactants and products in the reaction coordinate. Making reference to Figure 3.2, κ_{el} $(0 < \kappa_{el} < 1)$ is connected to the probability of a crossing at the intersection region of the two PES involved, and is given as,

$$\kappa_{el} = \frac{2[1 - \exp(-\nu_{el}/2\nu_N)]}{2 - \exp(-\nu_{el}/2\nu_N)} \tag{5.2}$$

where

$$\nu_{el} = \frac{\langle 2\Psi_{D^*.A}|\mathcal{H}_{el}|\Psi_{D.A^*}\rangle^2}{h}\sqrt{\frac{\pi^3}{\lambda RT}} \tag{5.3}$$

if the matrix element for the electronic coupling between the two states is large, then $\nu_{el} \gg \nu_N$ and $\kappa_{el} = 1$. In this case, the system is in the adiabatic limit. If $\nu_{el} \ll \nu_N$, then $\kappa_{el} = \nu_{el}/\nu_N$ and the system is in the nonadiabatic limit, and k_{el} is dependent on $\mathcal{H}_{el}^2$ [90]. The electronic factor is dependent on the distance between the species involved in the EnT,

$$H_{el} = \langle 2\Psi_{D^*.A}|\mathcal{H}_{el}|\Psi_{D.A^*}\rangle = H_{el}(0)\exp\left[\frac{-\beta_{el}}{2}(r_{DA} - r_0)\right] \tag{5.4}$$

where $H_{el}(0)$ is the interaction at contact distance, r_0, r_{DA} is a given distance between donor and acceptor, and β_{el} is an attenuation factor. At contact, the exponential term is 1, and the interaction is simply $H_{el}(0)$.

5.2.3 Dexter Energy Transfer Modeling

Because DET is a distance-dependent process, the coupling between the two states involved in the energy transfer will be paramount in determining the rate constant. H_{el} arise from the interactions between $|D^*A\rangle$ and $|DA^*\rangle$, which are diabatic states that represent the localized excitation on each molecule (for supramolecular systems), or part of the molecule (for intramolecular EnT) [201–204]. Qualitatively, a diabatic state conserves its electronic characteristics regardless of the nuclear configuration. In contrast, an adia-

batic state is always an eigenvalue of the Born-Oppenheimer Hamiltonian, $\mathcal{H}_{BO}$, and will have its electronic character coupled to the nuclear motion [205]. For instance, Figure 5.7 illustrates both adiabatic and diabatic states for the NaCl dissociation. The solid red and blue curves represent the ionic and covalent diabatic states, respectively. Both states maintain their electronic character regardless of the distance between the Na and Cl atoms. Meanwhile, the two dashed lines are adiabatic states, which present an ionic-like character for short distances but a covalent-like one for larger distances, minimizing the system energy. The adiabatic picture is usually employed in chemical reaction descriptions (Minimum energy path (MEP), Transition state theory (TST)), excited state dynamics, and spectroscopy, among others [205]. On the other hand, the diabatic description is used when a localized character is invoked (Marcus electron transfer, vibronic transitions) and for a qualitative chemical understanding of molecular bonding. DET also relies on the diabatic representation given the excitation energy, whether in the donor or the acceptor, has a localized character to it.

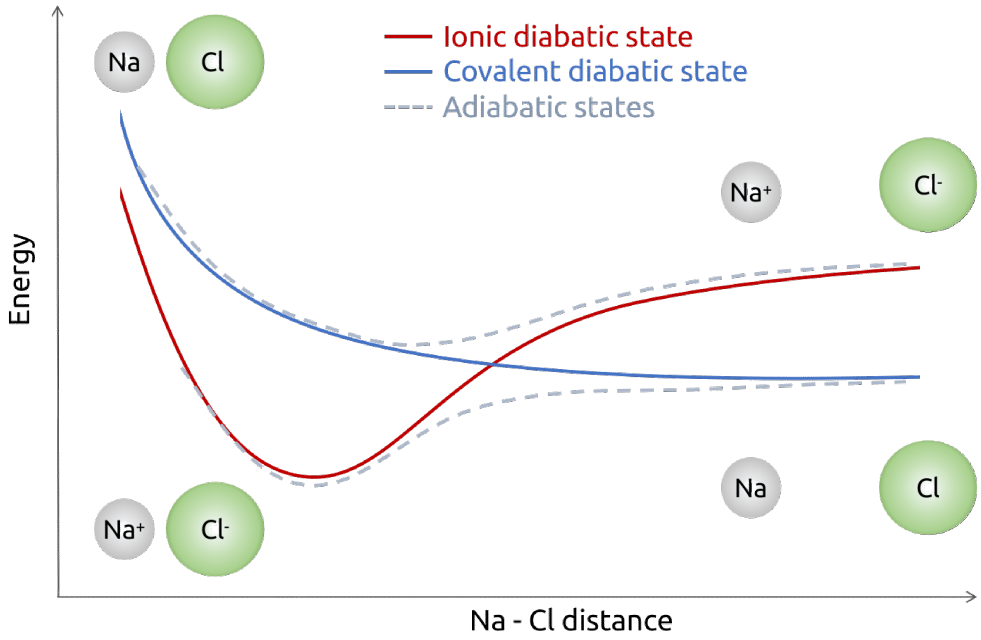

Figure 5.7: Scheme of dissociation of NaCl in terms of the adiabatic (dashed lines) and diabatic (solid lines) states.

Modeling DET systems has been a challenge due to its many particularities. Besides the two-particle and one-particle mechanisms already discussed, a DET process can be mediated by a bridge (DBA), giving rise to a handful of other mechanisms [201]. In this sense, many different approaches have been employed to model intramolecular and supramolecular DET [201–204, 206], but all based on concentrating the efforts towards determining the diabatic states and coupling, either through diabatization methods or direct calculation of the diabats.

The diabatization can be achieved by rotation of the adiabatic states. The transformation can be represented in the following form [204],

$$\begin{bmatrix} \epsilon_i & H_{if} \\ H_{if} & \epsilon_f \end{bmatrix} \begin{bmatrix} c_{i\pm} \\ c_{f\pm} \end{bmatrix} = \epsilon_\pm \begin{bmatrix} 1 & S_{if} \\ S_{if} & 1 \end{bmatrix} \begin{bmatrix} c_{i\pm} \\ c_{f\pm} \end{bmatrix} \tag{5.5}$$

where $\epsilon_{i,f}$ are the diabatic state energies, H_{if} is the diabatic coupling, $c_{i,f}$ are the eigenvector coefficients from which the rotations angle can be obtained, $\epsilon_\pm$ are the adiabatic state energies, and S_{if} are the diabatic state overlap. The diabatic states obtained from this approach are not orthogonal, and further orthogonalization is required, yielding:

$$V_{if} = \frac{H_{if} - S_{if}(\epsilon_i + \epsilon_f)/2}{1 - S_{if}^2} \tag{5.6}$$

If the system has some intrinsic symmetry, such as identical molecules, then $\epsilon_i = \epsilon_f$, and the coupling can be reduced to $V_{if} = (\epsilon_- - \epsilon_+)/2$, which is known as the *splitting method* [204, 205]. The general expression for obtaining the coupling is

$$V_{if} = \frac{\sqrt{(\epsilon_i - \epsilon_+)(\epsilon_f - \epsilon_+)} + S_{if}(\epsilon_+ - (\epsilon_i + \epsilon_f)/2)}{1 - S_{if}^2} \tag{5.7}$$

where S_{if} can be obtained from directly calculating the overlap between the diabatic states involved. Alternatively, it is possible to directly calculate the diabatic coupling using diabatic states. Calculating diabatic states usually involves multireference methods, which can be computationally challenging for large and complex systems. An interesting alternative is applying the Constrained Density Function Theory (CDFT) approach and calculating the diabats as ground states of an alternative potential. This method is applied in this work and is briefed in the next session.

Constrained DFT

CDFT [204, 205, 207] is a method to obtain diabatic states where the ground state of a system is constructed based on determined constraints on the density. The constraints can be chosen based on a number of observables, *e.g.*, charge distribution, dipole moment, and spin state. The constraints are implemented during the Self-Consistent Field (SCF) optimization through the introduction of a Lagrange multiplier, V_c

$$W[\rho, V_c] = E[\rho] + V_c \left(\sum_\sigma^{\alpha,\beta} \int d\mathbf{r}\ w_c^\sigma(\mathbf{r}) \rho^\sigma(\mathbf{r}) - N_c) \right) \tag{5.8}$$

where w_c^σ

is the weight function that determines the constraint and is usually chosen to be

Becke's partitioning scheme [208], N_c is the constraint, and $E[\rho]$ is the electronic energy being minimized [204, 205]. By setting $w_c^\alpha \neq w_c^\beta$, spin constraints can be defined under the unrestricted formalism. In a Kohn-Sham (KS) framework, the stationary condition ($\partial W/\partial V_c = 0$) gives rise to the modified Schrödinger equation,

$$\left(-\frac{1}{2}\nabla^2 + \int \frac{\rho(\mathbf{r}')}{|\mathbf{r}-\mathbf{r}'|}d\mathbf{r}' + v_{xc}(\mathbf{r}) + V_c w_c(\mathbf{r})\right)\psi_i(\mathbf{r}) = \epsilon_i\psi_i(\mathbf{r}) \tag{5.9}$$

where v_{xc} is the exchange-correlation potential and ψ_i are the KS orbitals, and the adi-tional $V_c w_c(\mathbf{r})$ introduces the extra potential from the constraints. In this approach, the diabatic states are given as adiabatic ground states of a modified potential. The direct calculation of the diabatic coupling is now straightforward and benefits from not requiring a wavefunction derivative as the nonadiabatic coupling. However, the CDFT approach requires evaluating one and two-electron matrix elements. An approximation to compute the coupling is, then, necessary to avoid the two-body problem. Taking each diabat (i) as an eigenstate of the Hamiltonian in the alternative potential ($V_c w_c(\mathbf{r})$), then

$$\mathcal{H} + V_i\hat{w}_i|\psi_i\rangle \equiv \mathcal{H}_i|\psi_i\rangle = F_i|\psi_i\rangle \equiv (E_i + V_i N_i)|\psi_i\rangle \quad \forall i \tag{5.10}$$

where E_i are the diabatic energy, V_i is the Lagrange multiplier, and N_i is the specified constraint. This allows the diabatic coupling to be written as:

$$\langle\psi_i|\mathcal{H}|\psi_f\rangle = \frac{1}{2}\langle\psi_i|\mathcal{H}_i - V_i\hat{w}_i + \mathcal{H}_f - V_f\hat{w}_f|\psi_f\rangle = \frac{F_i+F_f}{2}\langle\psi_i|\psi_f\rangle - \frac{1}{2}\langle\psi_i|V_i\hat{w}_i + V_f\hat{w}_f|\psi_f\rangle \tag{5.11}$$

where the coupling dependence on the KS orbitals is to a zero- and one-body problem. Therefore, the coupling depends on the overlap between the two states (first state) and the weight function imposing the constrained potential (second term) [204, 205, 207].

A kinetic Model

Besides choosing a suitable computational method, the kinetic modeling of a DET supramolecular system also impacts the final results. A handful of strategies for modeling energy transfer have been employed to calculate rate constants [203, 204, 206]. However, most strategies have been applied to symmetric systems (facilitating the use of the splitting method for coupling calculation) or conveniently small systems. In this work, we deal with a fairly large photosensitizer, the $[Ru(bpy)_2dppn]^{2+}$ complex, which undergoes DET to generate singlet molecular oxygen.

As discussed, Marcus' theory equation (3.16) for electron transfer can also be extended to determine the DET rate constant. From earlier discussions, we have established that

Marcus' equation is mainly dependent on the coupling between the states involved (V_{if}), the adiabatic energy difference of quadratic-like PES (ΔG), and the reorganization energy (λ_M). In our approach, a coordinate $\mathbf{D}_{if}$ establishing the intermolecular distance between the molecular oxygen and the PS was defined, and the diabatic surfaces of the states involved in the EnT were calculated using the CDFT method. The initial state is composed of two species in the triplet state yielding a singlet state, herein referred to as ^{1}(TT), and the final state is composed of two singlet species yielding a singlet system, herein referred to as ^{1}(SS). The diabatic coupling was calculated from them using CDFT-CI, as described above, at the crossing point, CP, between the two diabats. The intramolecular coordinates ($\mathbf{R}$) of both molecules were not set as a variable in this model. The role of intra and intermolecular coordinates have been investigated by Bai and Barbatti in their *Divide-to-Conquer* model [206], and it has been demonstrated that the intermolecular coordinate connecting the two molecules plays a major role, reinforcing that the orbital overlap is crucial for the transfer. However, it is advised not to neglect $\mathbf{R}$ for floppy molecules. In this case, the PS belongs to the Marcus inverted region with intrinsic rigidity. Following the frozen $\mathbf{R}$ coordinates, ΔG does not vary for different sets of $\mathbf{D}_{if}$. It is determined as the energy difference between the two diabatic states at the asymptotic limit. The asymptotic limit of the diabats determines the non-interacting system. In other words, at the asymptotic limit, the energy E_{D^*A} becomes $E_{D^*} + E_A$, and E_{DA^*} becomes $E_D + E_{A^*}$. Finally, the reorganization energy, λ_M, was determined as the summation of the independent reorganization energy of each molecule, $\lambda_M = \lambda_D + \lambda_A$.

The kinetic model constructed provides a simple but effective way of determining the DET rate constant, giving space to a bigger issue: the EnT reaction coordinate, $\mathbf{D}_{if}$. Because this is a large system, it is hard to predict which orientation between the PS and O_2 yields the largest coupling, leading to the largest rate constant, or even determining a single orientation capable of representing the phenomenon. Hence, to further investigate this matter, we computed the two diabatic state PES and their coupling at the crossing point (CP) for a set of 15 different orientations, aiming to understand the crucial spatial factors that lead to effective energy transfer for complex DA pairs.

5.3 Computational Details

Full unconstrained geometry optimizations and frequency calculations for states S_0, S_1, S_2, T_1, T_2, and T_3 were carried out using the ORCA-5.0.3 software [110, 151]. Density Functional Theory (DFT), both time-dependent and independent, was used with the hybrid functional B3LYP [150]. The Ahlrichs def2-TZVP(-f) basis set [112] was used for all atoms, and the calculations included the Grimme's D3 dispersion correction [152]

with Becke-Johnson (BJ) damping [153]. Coulomb integrals were sped up by RICOSX approximation [154] using def2/J as an auxiliary basis set [116]. The Tamm-Dancoff approximation (TDA) [117] was used to calculate the excited state. The conductor-like polarizable continuum model (C-PCM) [118] was used to simulate water solvation. Scalar relativistic corrections were treated by the Zeroth-Order Regular Approximation (ZORA) formalism [155, 156]. The simulated electronic spectra for 70 roots in the S_0 and S_1 Franck-Condon regions were calculated to determine the number of low-energy triplet states and the nature of the transitions.

The photophysics investigation followed the same methodology described in section 4.4 of Chapter 4 applied to the $[Ru(bpz)_3]^{2+}$ complex; therefore, it has not been herein described to avoid redundancy.

To compute the $\Delta_r G^\circ$ for the photoreactions with the guanosine monophosphate (GMP) and the molecular oxygen, all the species involved were optimized with frequencies at the same level of theory described above, using the C-PCM model for water implicit solvation.

Molecular dockings were performed using a double-stranded DNA d(ATGCAT)2 (structure resolved by x-ray [139]) obtained from the Protein Data Bank under the PDB ID4JD8. The file has the coordinates of the two strands, A and B, and both enantiomers of *rac*-$[Ru(phen)_2dppz]^{2+}$ acting as intercalators (phen = phenanthroline; dppz = dipyridophenazine). The system had the intercalators, water molecules, and ions removed. Hydrogen atoms were added to the structure. The molecular docking simulations were carried out with the MetalDock program [209], using a grid of radius of 20 Å from the center of the DNA (coordinates $x = -12.9; y = 11.8; z = -11.0$). Since the DNA model used is 34 Ålong, the whole DNA fragment is involved in the docking. All remaining parameters regarding ligand flexibility were kept as default.

Redocking simulations were performed for both enantiomers, Δ-$[Ru(tmp)_2dppz)]^{2+}$ and Λ-$[Ru(tmp)_2dppz)]^{2+}$, to validate the docking protocol and evaluate its suitability to be used for the Δ-$[Ru(bpy)_2dppn)]^{2+}$ complex. Docking of the Δ-$[Ru(bpy)_2dppn)]^{2+}$ complex was carried out following the same protocol, and 100 poses were generated. The best pose was selected and used in all subsequent electronic structure calculations. Given that the system was too large for this investigation, the macro-molecule was truncated, leaving two base pairs above and two below the intercalating complex, resulting in a d(ATGC)2 DNA fragment, featuring the TG/CA step. Hydrogen atoms were manually added to complete the valence. The system was submitted to electronic absorption spectrum calculation using the B3LYP [150] functional and def2-TZVP(-f) [112] basis set under implicit water solvation with C-PCM [118].

Dexter Energy Transfer

The optimized structure of the T_1 state of the $[Ru(bpy)_2dppn]^{2+}$ complex has been chosen for the EnT study. Unconstrained geometry optimization and frequency calculations of the ground electronic state structure of O_2 ($^3\Sigma_g^-$) were performed using unrestricted Kohn-Sham, UKS, with B3LYP-D3(BJ)/def2-TZVP level of theory. To investigate the energy transfer reaction coordinate, 15 different orientations for the O_2 molecule approaching the dppn ligand were defined, where the distance between the species varied from 2 to 4 Å with a step of 0.1 Å, totaling 21 points for each orientation (Figure 5.8).

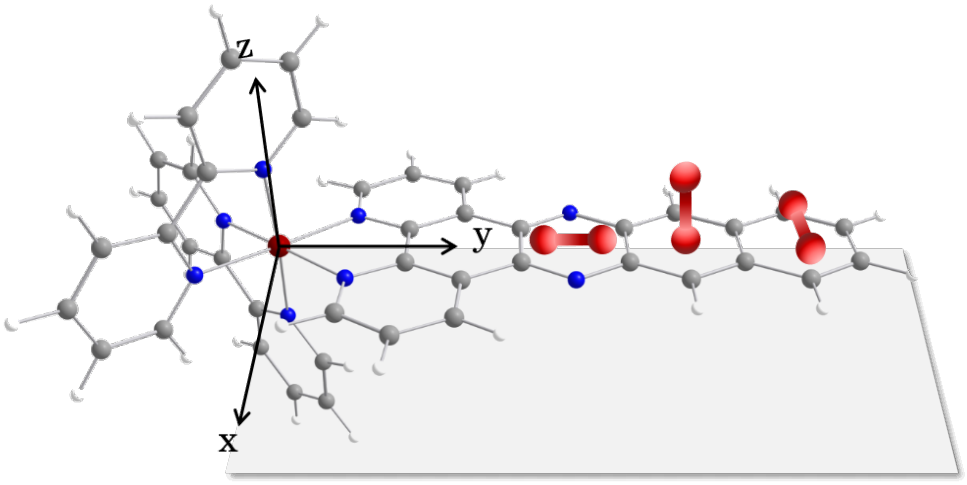

Figure 5.8: Schematic representation of the reaction coordinate modeling and orientations adopted for the oxygen molecule approaching the dppn ligand.

UKS B3LYP-D3(BJ)/def2-TZVP single-point calculations were initially carried out on the system quintet PES, ^{5}(TT), formed by both species in their lowest triplet electronic state. The energy asymptotic limit of all different orientations was then determined to be at 3.5 Å distance, where starting at 3.0 Å, the energy difference among the poses can already be considered very small. The energy asymptotic limit was tested by comparing different orientations among the ^{1}(SS) and ^{1}(TT) states, confirming the distance of 3.5 Å. The crossing point distances between the two singlet electronic states, ^{1}SS and ^{1}TT, were also investigated and determined to occur before 3.0 Å. Therefore, considering the large volume of different orientations, the distance span of the study was truncated at 3.0 Å to speed up the calculations, reducing from 21 to 11 points. Single point calculation using CDFT with CAM-B3LYP/def2-TZVP level of theory of the 11 points for the 15 orientations for state ^{1}(SS), followed by the diabatic coupling calculations between states ^{1}(SS) and ^{1}(TT) at the crossing points were performed. The CDFT single-point calculations and diabatic couplings were performed using the Q-Chem 5 software. The EnT rate constant, k_{EnT}, was determined for all orientations using Marcus' equation (3.16). The ΔG

was defined as the asymptotic limit difference between the two singlet electronic states, and the reorganization energy was determined as the summation of the reorganization energy of both isolated species.

5.4 Results and Discussion

5.4.1 Photophysics and Photochemical Reactions

Structural parameters

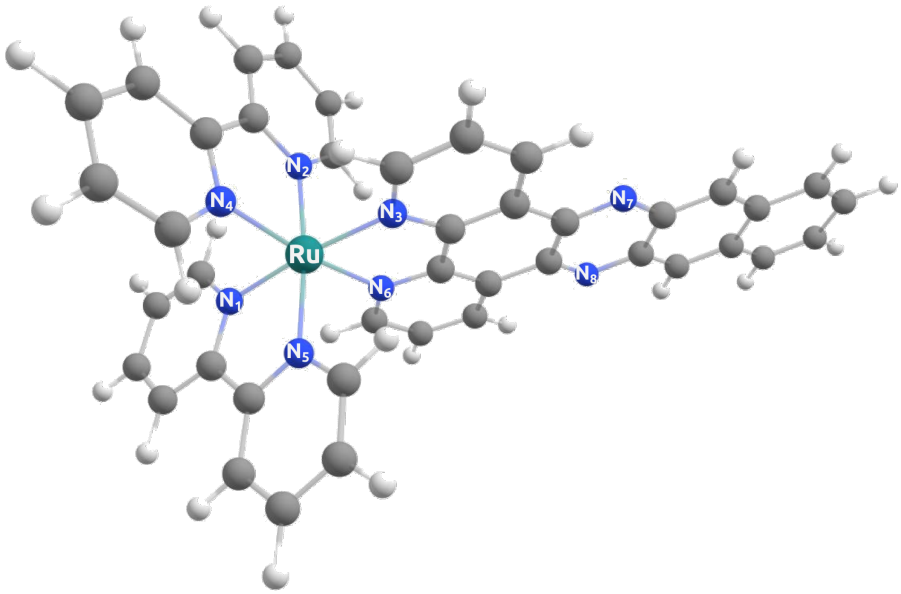

Figure 5.9: $[Ru(bpy)_2dppn]^{2+}$ complex structure with labels in the main atoms. Adapted with permission from Chemistry – An Asian Journal, 19(22), 11 2024 [39]. Copyright (2024) Wiley-VCH GmbH.

Figure 5.9 shows the general structure and geometry of the $[Ru(bpy)_2dppn]^{2+}$ complex. Its metal center and nitrogen atoms are emphasized for reference. Table 5.2 gathers structural parameters related to bond distance and angles regarding the ruthenium and the coordinating nitrogen atoms, and electric dipole moments for the ground state and some singlet and triplet excited states. As discussed before for the Ru-bpz complex, the polypyridyl groups are a rigid moiety and undergo small changes in bond length and angles. Nonetheless, the S_1, T_2, and T_3 excited states show considering bond stretch between the metal center and the coordinating atoms. These states are also associated with a much larger electric dipole moment. Interestingly, the S_2 and T_1 excited states presented a smaller transition electric dipole moment compared to the ground state. In general, the transition electric dipole moment is a direct indication of the charge distribution on a molecule. When it comes to different electronic states of the same molecule,

this can be an indication of the nature of the transitions, which will be discussed in the next topic. Furthermore, there was no significant torsion associated with the different electronic states, indicating that the overall geometry was kept still while the changes were concentrated in the bond distances. Figure 5.10 gathers the structures of the main states investigated and their respective spin-contamination.

Table 5.2: Structural parameters for the ground and the low excited electronic states of $[Ru(bpy)_2dppn]^{2+}$ with implicit water solvation. Bond distances are given in Å, and the transition electric dipole moments are given in a.u..

Parameter	S_0	S_1	S_2	T_1	T_2	T_3
Ru–N1	2.068	2.074	2.068	2.068	2.077	2.094
Ru–N2	2.076	2.071	2.071	2.072	2.073	2.068
Ru–N3	2.081	2.082	2.082	2.081	2.076	2.071
Ru–N4	2.071	2.074	2.070	2.070	2.078	2.093
Ru–N5	2.072	2.073	2.072	2.071	2.073	2.067
Ru–N6	2.080	2.084	2.083	2.081	20.77	2.071
∠ N1–Ru–N2	97.0	98.7	97.1	97.0	98.9	94.8
∠ N1–Ru–N6	96.5	97.4	96.2	96.2	96.9	94.8
μ(D)	7.129	18.105	2.418	4.827	17.423	17.131

Level of theory: B3LYP-D3(BJ)/Def2-TZVP(-f) under water solvation.

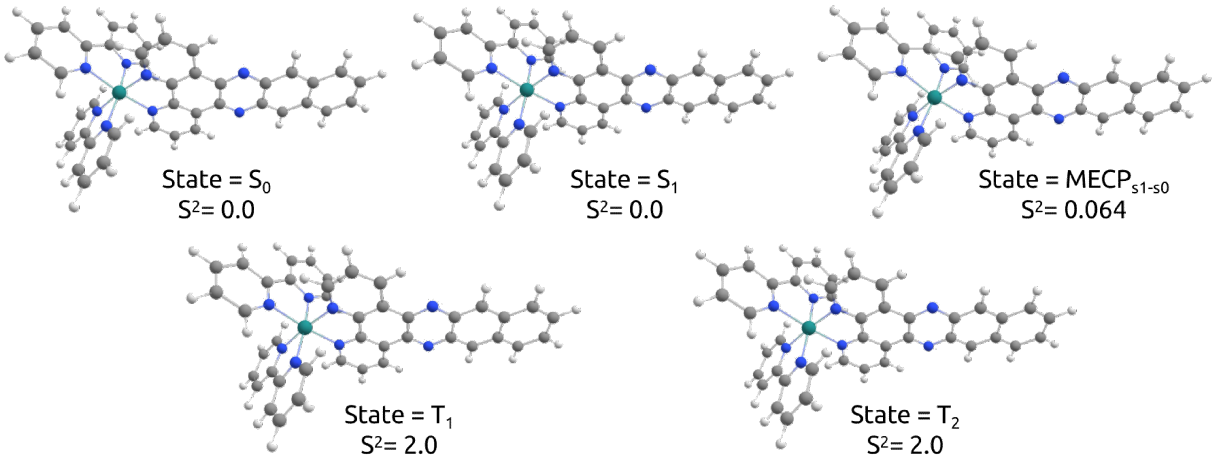

Figure 5.10: Structures of the optimized states and crossing points along with their spin-contamination.

Photophysics

Unveiling the photophysics of a photosensitizer plays an important role in its usage and gives us a glimpse of its photochemical prospects. In that sense, the first step is identifying the main electronic transitions and calculating the photophysical rate constants. The

simulated electronic absorption spectrum in implicit water solvation of $[Ru(bpy)_2dppn]^{2+}$ was evaluated, and the attribution regarding the nature of the transitions of the main absorption bands is shown in Table 5.3. The natural transition orbitals involved in the main transitions are illustrated in Figure 5.11.

Table 5.3: Attribution of state, energy, E, in eV, absorption wavelength, λ, in nm, oscillator strength, f_{osc}, and nature of the transition of the main absorption bands of the spectrum of the $[Ru(bpy)_2dppn]^{2+}$ complex. Values are computed at the B3LYP/def2-TZVP(-f), D3BJ, and including water solvation. Experimental values [1] are written in bold and their molecular absorptivity in parenthesis are given in 10^{-3} $M^{-1}cm^{-1}$.

State	E(eV)	λ(nm)	f_{osc}	Attribution
1	2.20	562.8	0.002	MLCT($d_{Ru} \rightarrow \pi^*_{dppn}$)
11	2.89	428.4	0.236	MLCT($d_{Ru} \rightarrow \pi^*_{dppn}$) + MLCT($d_{Ru} \rightarrow \pi^*_{bpy}$)
	2.79	**443 (11.9)**		
12	2.92	423.9	0.181	MLCT($d_{Ru} \rightarrow \pi^*_{bpy}$)
	3.00	**412 (16.6)**		
20	3.34	371.2	0.118	MLCT($d_{Ru} \rightarrow \pi^*_{dppn}$) + MLCT($d_{Ru} \rightarrow \pi^*_{bpy}$)
29	3.77	328.2	1.754	IL($\pi_{dppn} \rightarrow \pi^*_{dppn}$) + MLCT($d_{Ru} \rightarrow \pi^*_{bpy}$)
31	3.82	324.1	0.134	MLCT($d_{Ru} \rightarrow \pi^*_{bpy}$)
	3.85	**322 (55.2)**		
61	4.52	274.0	0.431	IL($\pi_{dppn} \rightarrow \pi^*_{dppn} + \pi^*_{bpy}$) + IL($\pi_{bpy} \rightarrow \pi^*_{bpy}$)
	4.35	**285 (57.1)**		

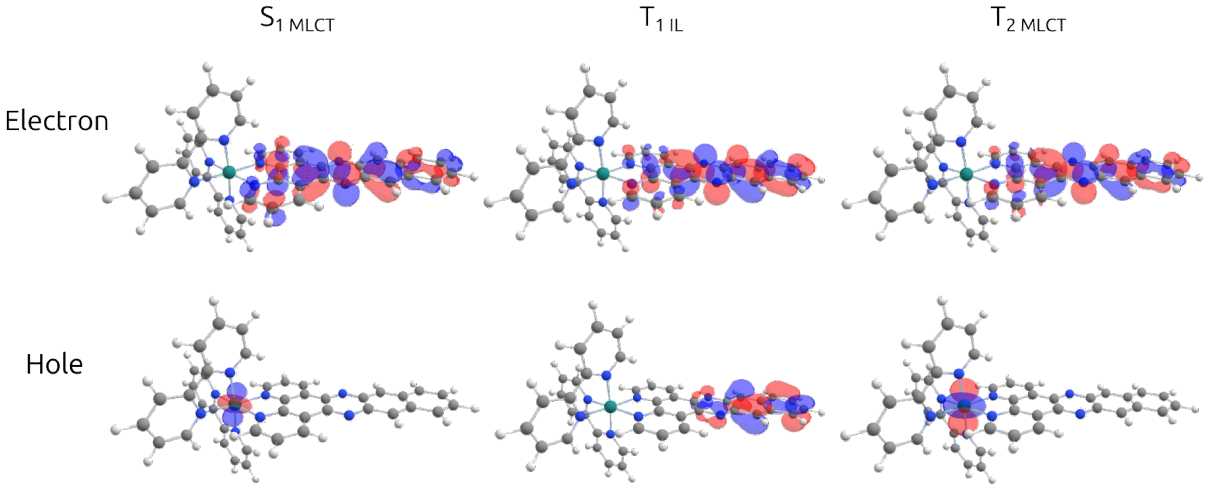

Figure 5.11: Natural transition orbitals, NTO, involved in the main Metal-to-Ligand Charge Transfer (MLCT) electronic transitions.

Experimental results [1, 196] have demonstrated that the Ru-dppn complex presents

two well-defined bands, a bright-state below 350 nm assigned to be an intraligand transition within the dppn ligand ($^1\pi\pi^*$) and a broad manifold accounting for several overlapped transitions assigned to be Ru-dppn and Ru-bpy ^{1}MLCT. In acetonitrile, the main transitions of the experimental spectrum are at 286 nm, 323 nm, 338 nm, 387 nm, 409 nm, and 443 nm, while for the experimental spectrum in water, the peaks are at 285 nm, 322 nm, 412 nm, and 443 nm [142]. The calculations reproduced the main absorption peaks (table 5.3). The lowest energy absorption band, corresponding to the S_0-S_1 transition, is centered at 562.8 nm, which is not observed in experimental spectra and can be considered a dark state. The calculated oscillator strength, f_{osc}, is 0.0021, corresponding to a very weak absorption intensity, corroborating the experimental results. The bright state band is a manifold of a handful of transitions, with the S_{29} being the most intense, with the absorption peak at 328.2 nm and f_{osc} of 1.7545, very close to the values reported for experimental spectra both in acetonitrile and water. Other transitions also contribute to the band, as the S_{31} illustrated in Figure 5.11. This transition is mainly ^{1}MLCT involving the bpy ligand, while the S_{29} also features IntraLigand (IL) charge transfer within dppn these transitions are illustrated in Figure 5.11.

Previous works have demonstrated that the lowest singlet excited state is a Ru-dppn ^{1}MLCT, while subsequent singlet excited states can have a mixture of Ru-dppn and Ru-bpy ^{1}MLCT. According to Peña et. al. [196], although the first singlet excited states are MLCT, the HOMO is a π-orbital originating from the dppn ligand, and the HOMO-1 is metal-centered, and they are reported to differ by 0.002 eV. However, we have observed an exchange between HOMO and HOMO-1 with the metal-centered orbitals as the frontier orbitals and an energy difference of 0.0004 eV between HOMO and HOMO-1 (Figure 5.12). Nonetheless, based on the energy differences, the interchange of orbitals is expected to happen due to their quasi-degeneracy and, if considered carefully, does not alter the overall interpretation of the photophysical properties.

On the other hand, the first triplet excited state is ^{3}IL ($^3\pi\pi^*$) in nature and is estimated to be 1.65 eV above the ground state, which agrees with previous calculations [196] and experimental results [1, 142, 178] that has determined the first triplet excited state of being approximately 1.5 eV above the GS. Analysis of the nature of transitions shows that the first triplet state has 96% contributions from the HOMO-1 $\rightarrow$ LUMO. This result is associated with the more π-extended character of the dppn ligand when compared to other similar ligands, placing the $^3\pi\pi^*$ state lower than MLCT states [178]. The second excited triplet state, T_2, is a ^{3}MLCT from the metal center to the dppn corresponding to 96% contributions. As discussed, the T_1 state is characterized by only an IL transition within dppn. In contrast, the other triplet states have a mixture of different transitions with MLCT having the major contribution. The singlet manifold follows a similar pattern,

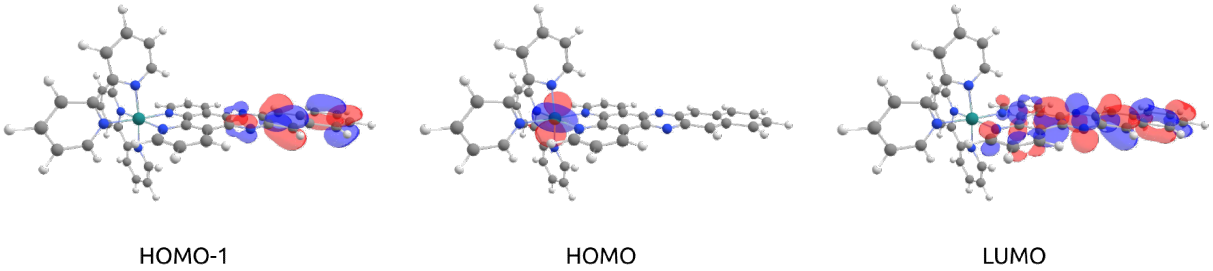

Figure 5.12: Natural transition orbitals associated with HOMO-1, HOMO, and LUMO, respectively, for the isolated $[Ru(bpy)_2dppn]^{2+}$ complex. The HOMO-1 are π-ortbitals centered at the benzo-phenazine portion of the dppn ligand, the HOMO is a d-orbital, and the LUMO orbitals are π^* spread all over the dppn ligand.

except for state S_4 that is constructed over a solely Metal-Centered (MC) contribution.

The calculated emission from the S_1 was 635.7 nm, corresponding to red light in the electromagnetic spectrum. Other parameters associated with the emission and fluorescence are listed in Table 5.4, *i.e.*, the adiabatic energy difference between the ground and the first singlet excited states, the intensity of the transition given in terms of the oscillator strength, the transition electric dipole moment, and the fluorescence rate constant calculated using the Einstein's coefficient (equation 4.5). The latter was predicted to be 6.235×10^5 s^{-1}, which is low for a fluorescence constant but comparable to other ruthenium complexes with polypyridyl ligands [69, 178]. In addition, the results show that the main route for deactivation of the S_1 state to the ground state is through internal conversion, with a computed rate constant (k_{IC}) of 7.4×10^7 s^{-1}, as shown in Figure 5.13.

Table 5.4: Calculated parameters involved in the fluorescence decay for the $[Ru(bpy)_2dppn]^{2+}$ complex. ΔE is the energy difference between S_1 and S_0 given in eV, λ_{em} is the emission frequency in nm, f_{osc} is the oscillator strength of the transition, μ^2 is the electric transition dipole moment in a.u.^{2}, and k_f is the fluorescence rate constant in s^{-1}.

Parameters	
ΔE (eV)	2.07
λ_{em} (nm)	635.7
f_{osc}	0.003
μ^2 ($S_1 \rightarrow S_0$) (a.u.)^2	0.066
k_f (s^{-1})	6.2×10^5

A low fluorescence rate constant enables other photophysical phenomena to occur, leading to different excited-state deactivation channels. For instance, the intersystem crossing is governed by the adiabatic energy difference and the spin-orbit coupling, as can

be interpreted from equation 3.8. A small ΔE_{ST} and high Spin-Orbit Coupling (SOC) values will lead to more significant rate constants [64]. As shown in Table 5.5, the Intersystem Crossing (ISC) rate constant between the S_1 and T_2 is 1.02×10^{10} s^{-1}, even though the SOC value is low for the coupling of these two states at the S_1 geometry, indicating that this electronic state will most likely participate in the deactivation channel. The SOC calculated between the S_1 and T_1 states is approximately six times smaller than the SOC for T_2 and S_1, and although the energy difference of 0.673 eV is small, this crossing rate is virtually zero. If the first triplet state is populated during the deactivation pathway, it is assumably due to internal conversion from other triplet states. Contrastingly, the coupling between the S_1 and T_3 states is 426.99 cm^{-1}, being the highest. The adiabatic energy difference is also low enough for the transition, even though the third triplet state is 0.11 eV higher in energy than the S_1. The rate constant for this ISC is 7.75×10^{12} and governs the whole ISC process. On the other hand, spin-orbit coupling calculations performed at the T_1 geometry showed that the T_1-S_0 coupling is nearly zero due to an absent transition electric dipole moment, indicating that a deactivation through phosphorescence is highly unlikely to happen. These results agree with previous ISC processes reported to occur in less than 1 ps for populating T_2 and T_3 states. Furthermore, according to Sun *et al.* [142], the radiative decay from triplet states originates from higher triplet excited

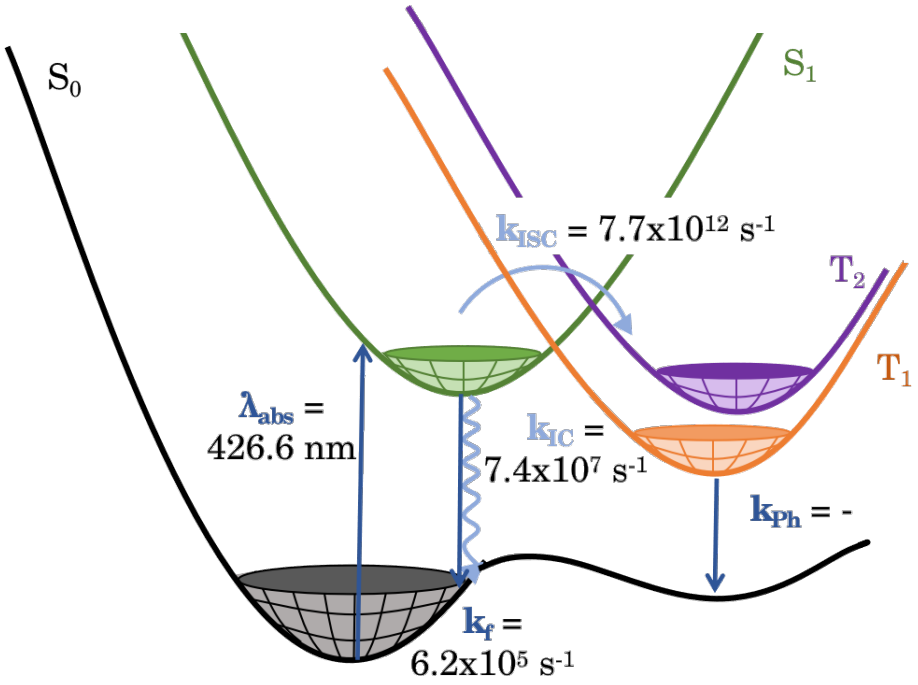

Figure 5.13: Energy diagram and computed rate constants for the photophysics of the $[Ru(bpy)_2dppn]^{2+}$ complex. The rate constants are generally represented by k, while the text in subscript determines the phenomenon, where f is the fluorescence, Ph is the phosphorescence, ISC is the intersystem crossing, and IC is the internal conversion.

states instead of the T_1, going against Kasha's rules. Figure 5.13 shows the overall energy diagram for the $[Ru(bpy)_2dppn]^{2+}$ complex, summarizing the photophysical processes and the rate constants computed.

Table 5.5: Calculated parameters involved in the intersystem crossing transition for the $[Ru(bpy)_2dppn]^{2+}$ complex. SOC is the Spin-Orbit Coupling between the S_1 and T_n states given in cm^{-1}, ΔE_{ST} is the energy difference between the states involved in the transition given in eV, λ_M is the reorganization energy in eV, and k_{ISC} is the intersystem crossing rate constant in s^{-1}.

State	SOC $(cm^{-1})S_1/T_n$	ΔE_{ST} (eV)	λ_M(eV)	ρ_{FC}	$k_{ISC}(s^{-1})$
T_1	2.66	0.67	0.17	-	-
T_2	12.23	0.02	0.001	0.46	1.02×10^{10}
T_3	426.99	0.11	0.08	0.07	7.75×10^{12}

Reactivity

The ability to undergo intersystem crossing and populate the triplet excited-state manifold with high lifetimes is the gateway to the photoreactivity of PSs. Considering that the photophysical processes will lead to decay to the lowest triplet excited state, T_1, electron and energy transfers are possible photochemical mechanisms for the interaction between the PS and some species of the medium. We investigated the photoreactions between the first triplet excited state, herein referred to as $^3PS^{2+}$, and the molecular oxygen as well as the direct interaction with the DNA through the guanine nucleobase. Here, we considered the guanosine-5'-monophosphate nucleotide doubly deprotonated, $^1GMP^{2-}$, as the most abundant species at physiological pH [210]. The computed reaction free energies ($\Delta_r G^\circ$) for these reactions are quoted in Table 5.6. Reactions 1–3 are of the electron transfer type, where the PS acts as an electron donor in 1 and 2, and an electron acceptor in 3, leading to doublet PS species in the oxidized or reduced forms, and reactions 4 and 5 are of the Type II mechanism, *i.e.*, energy transfer, leading to the complete deactivation of the PS to its ground state.

Among the three ET reactions calculated for the Ru-dppn complex, only the oxidation of the GMP molecule, leading to a $^2PS^{\bullet+}$ species, is predicted to be favorable, with a free energy value of approximately -7.9 $kcal.mol^{-1}$. Guanine has a redox potential of 1.29 V, the easiest nucleobase to oxidize. In fact, damage at the 5'-G of 5'-GG-3' sites is considered a fingerprint of an electron transfer process [146]. It has been proposed that the ^{3}MLCT state of this complex, which corresponds to the second triplet excited state, is highly reactive and is probably responsible for the oxidation of guanine when acting as an intercalator, culminating in a dual-channel mechanism [142]. We observe that the

Table 5.6: Calculated $\Delta_r G^\circ$ for several reactions the activated PS can undergo in biological medium.

	Reaction	$\Delta_r G^\circ$ (kcal.mol^{-1})
1	$^3PS^{2+}(T_1) + {}^3O_2 \rightarrow {}^2PS^{\bullet 3+} + {}^2O_2^{\bullet -}$	22.441
2	$^3PS^{2+}(T_1) + {}^1GMP^{2-} \rightarrow {}^2PS^{\bullet 3+} + {}^2GMP^{\bullet 3-}$	66.228
3	$^3PS^{2+}(T_1) + {}^1GMP^{2-} \rightarrow {}^2PS^{\bullet +} + {}^2GMP^{\bullet -}$	−7.897
4	$^3PS^{2+}(T_1) + {}^1GMP^{2-} \rightarrow PS^{2+}(S_0) + {}^3GMP^{2-}$	31.235
5	$^3PS^{2+}(T_1) + {}^3O_2 \rightarrow PS^{2+}(S_0) + {}^1O_2$	−8.333

Level of theory: B3LYP/def2-TZVP(-f) under water solvation. $\Delta_r G^\circ$ calculated in water implicit solvation; GMP = guanosine monophosphate; PS = $[Ru(bpz)_3]^{2+}$.

first triplet excited state also has enough energy to photooxidize this nucleotide. As for the O_2, the electron affinity, EA, was calculated to be -3.41 kcal.mol^{-1} and agrees with other calculations that have predicted values between -3.1 and -3.4 kcal.mol^{-1} [211, 212]. Nonetheless, reducing the oxygen molecule is not favorable for this complex.

On the other hand, only the photosensitization of the molecular oxygen is thermodynamically favorable for the EnT photoreactions with the free energy of -8.33 kcal.mol^{-1}. The ground state of molecular oxygen is a triplet state, while the first two excited states are two non-degenerate singlet states, $^1\Delta$g and $^1\Sigma_g^+$, with the former being the lowest in energy and featuring two electrons paired in the same orbital. The EnT calculation regarding the lowest singlet excited state was carried out using the widely known first singlet excitation energy of oxygen ($^1\Delta$g) of 0.98 eV [213]. Additionally, the GMP molecule is unlikely to undergo EnT with the PS. Sun et. al. [142] have demonstrated that this complex can photocleave the DNA through the combined action of guanine oxidation and $^1O_2$ generation, which we observed to be thermodynamically feasible.

Interaction with DNA

Besides acting through Types I and II mechanisms with molecules of the medium, some PSs have also been reported to interact with the DNA directly [214]. The interaction modes may vary, and the PS can be classified as an intercalator when it binds non-covalently between two base pairs of nucleic acids, as a groove-binder when it interacts through either the major or the minor grooves of the DNA, or it can be covalently anchored to the DNA. The $[Ru(bpy)_2dppn]^{2+}$ complex has been experimentally verified to interact directly with the DNA besides acting as a Type II photosensitizer. As discussed, Sun et al. suggested that this Ru-dppn complex could oxidize guanine nucleobases [142]. Furthermore, an increase in the relative viscosity of DNA solutions was observed in the presence of this PS, which indicates that intercalation is the preferable interaction mode.

In order to evaluate the effects of the intercalation on the main transitions of the complex, we performed molecular docking simulations using a DNA fragment co-crystallized with Δ and Λ enantiomers of $[Ru(tmp)_2dppz]^{2+}$, which is very similar complex to the one studied in this work. Furthermore, the DNA fragment features intercalation sites containing guanine nucleobases, which also serves our purpose in this context. Figure 5.14 shows the best poses from the docking of the Δ-$[Ru(bpy)_2dppn)]^{2+}$ complex (green) and the redocking of the Δ-$[Ru(tmp)_2dppz)]^{2+}$ complex (orange) using the DNA fragment $d(ATGCAT)_2$ crystalized and published under the PDB ID 4JD8 by Hall and coworkers [139]. The crystallized DNA fragment features a pair of enantiomers, Λ-$[Ru(phen)_2dppz]^{2+}$ and Δ-$[Ru(phen)_2dppz]^{2+}$. Each enantiomer of this complex binds to a TG/CA step through the minor groove and shows a different orientation. While the Λ complex is oriented perpendicular to the base pairs, the Δ complex shows a more angled orientation [139]. The redocking of Δ-$[Ru(phen)_2dppz]^{2+}$ shows 100% of intercalation at the Δ cavity, while the redocking of Λ-$[Ru(phen)_2dppz]^{2+}$ reveals only 21% of intercalation at the Λ cavity. The Δ-$[Ru(bpy)2dppn)]^{2+}$ docking exhibited all poses intercalating at the Δ site with the angled orientation, agreeing with experimental results that suggested it interacts as an intercalator and with the redocking results for the Δ-$[Ru(phen)_2dppz]^{2+}$.

The intercalating binding mode allows a maximized interaction between the PS and the DNA base pairs, as seen in Figure 5.14. The four aligned aromatic rings of the dppn ligand interact with all nucleobases of the TG/CA step through $\pi-\pi$ stacking interaction. Because the reactive state of the Ru-dppn complex is a $^3\pi\pi^*$ centered at the dppn ligand, the direct interaction of this portion of the complex with the guanine nucleobase can favor the reaction to occur.

The best pose for the Ru-complex from the docking simulation was chosen to proceed with electronic structure calculations. For this, the DNA sequence was truncated, yielding a d(ATGC)2 fragment containing the TG/CA step where the Ru-dppn complex intercalates.

Figure 5.15 shows the Natural Transition Orbitals (NTOs) involved in the first electronic transition. The transition involves the HOMO and LUMO orbitals of the system and is classified as an MLCT transition from a d-orbital of the Ru(II) atom to π^*-orbital of the dppn ligand. Although the HOMO and LUMO natures of the system follow the same pattern compared to the isolated complex, the energy difference between HOMO and HOMO-1 increased to approximately 0.07 eV, indicating that the interactions between the nucleobases with the dppn ligand help to stabilize the π-orbitals of this ligand. However, the energy difference between the two states is still low enough to consider them degenerate.

The attributions to the main band of the calculated absorption spectra for the op-

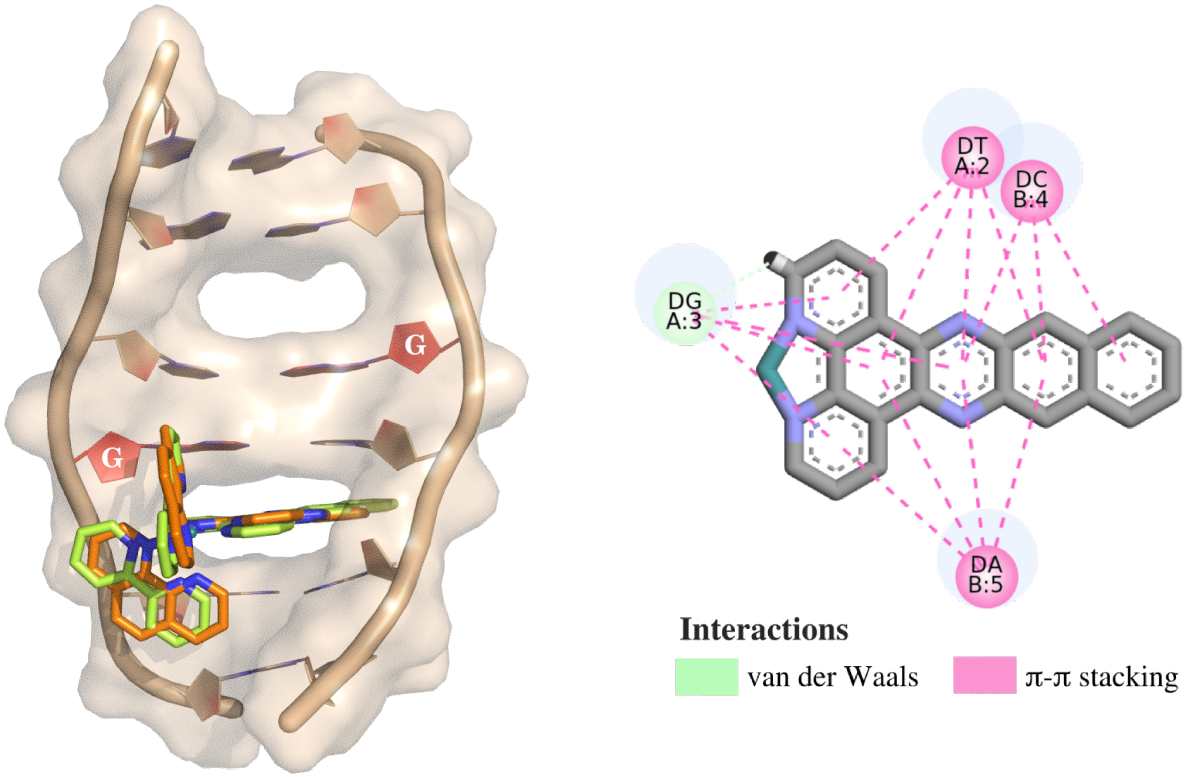

Figure 5.14: Redocking of Δ-$[Ru(tmp)_2dppz)]^{2+}$ in orange and docking of Δ-$[Ru(bpy)_2dppn)]^{2+}$ in green; and interactions between the DNA TG/CA step and the dppn ligand of Δ-$[Ru(bpy)_2dppn)]^{2+}$ complex. The labels on the nucleobases describe the position on the DNA strand; for instance, DG A:3 refers to the deoxyguanine on strand A at position 3.

timized geometry are shown in Table 5.7. The first transition ($S_1 \rightarrow S_0$) calculated for the system composed of the Ru-complex and the four based-pairs of the DNA fragment shows a small red-shift of approximately 14 nm, which is not an expressive change. The transitions corresponding to states 15 and 16 are comparable, in terms of wavelength, to the ones of states 11 and 12 for the isolated complex. While the latter are 428.4 nm and 423.9 nm, respectively, the former are 432.6 nm and 429.7 nm, respectively. The oscillator strengths are also comparable with a slight decrease for the system. However, the transitions feature an additional contribution from a charge transfer from the guanine of the TG/CA step to the dppn ligand, indicating the propensity of this nucleobase to be oxidized, as discussed by Gicquel et al. [146].

Another interesting transition to highlight is the one corresponding to the bright state, *i.e.*, the state 59 of the system. This transition occurs at 326.6 nm, with an oscillator strength of 0.340, while the bright state of the isolated complex, state 29, occurs at 328.2 nm, with an oscillator strength of 1.754, which is more than five times greater,

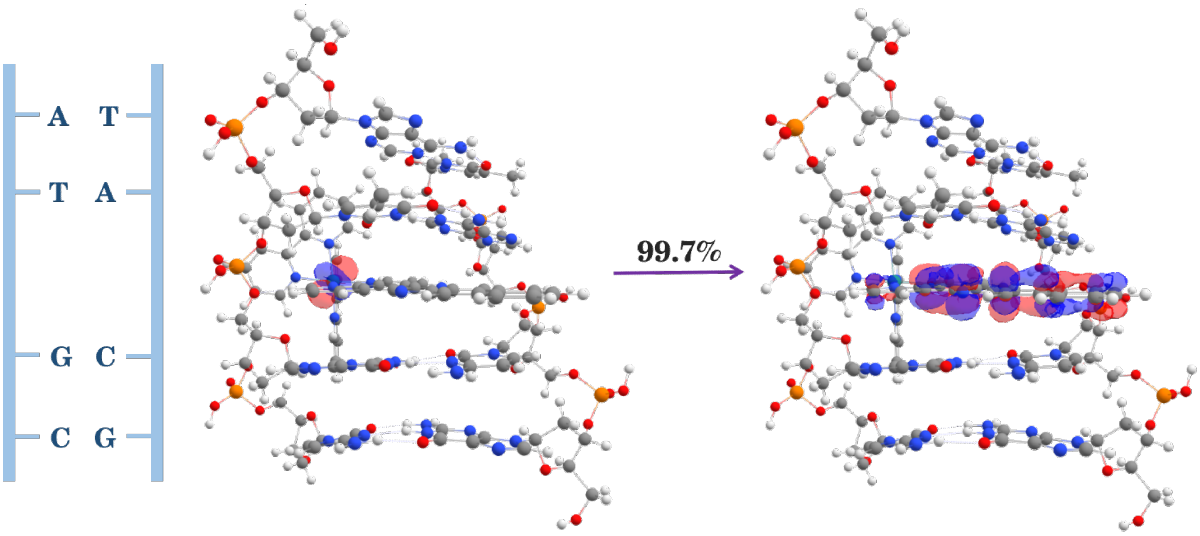

Figure 5.15: The natural transition orbitals, NTO, involved in the transition from the S_0 state to the S_1 state computed at the docking geometry.
Adapted with permission from Chemistry – An Asian Journal, 19(22), 11 2024 [39].

indicating that the intercalation and, consequently, the interactions between the PS and the macromolecule affect the intensity of the bands observed in the spectrum. Moreover, the nature of the transition is also different. Although the IL transition within the dppn ligand is still present, the MLCT($d_{Ru} \rightarrow \pi^*_{bpy}$) is absent. Furthermore, a CT transition from the guanine of the TG/CA step is present, leading the contributions (approximately 48%) to this state. Nonetheless, the main bands did not suffer any significant wavelength shift but had a significant decrease in intensity.

Table 5.7: Attribution of state, energy, E, in eV, absorption wavelength, λ, in nm, oscillator strength, f_{osc}, and nature of the transition of the main absorption bands of the spectrum of the $[Ru(bpy)_2dppn]^{2+}$ complex intercalated to the d(ACGT)2 DNA fragment.

State	E(eV)	λ(nm)	f_{osc}	Attribution
1	2.15	576.3	0.001	MLCT($d_{Ru} \rightarrow \pi^*_{dppn}$)
15	2.86	432.6	0.179	MLCT($d_{Ru} \rightarrow \pi^*_{dppn}$) + CT($\pi_G \rightarrow \pi^*_{dppn}$) + MLCT($d_{Ru} \rightarrow \pi^*_{bpy}$)
16	2.88	429.7	0.144	MLCT($d_{Ru} \rightarrow \pi^*_{bpy}$)
48	3.63	341.8	0.098	CT($\pi_A \rightarrow \pi^*_{dppn}$) + CT($\pi_A \rightarrow \pi^*_{bpy}$)
59	3.79	326.6	0.340	CT($\pi_G \rightarrow \pi^*_{dppn}$) + IL($\pi_{dppn} \rightarrow \pi^*_{dppn}$)
60	3.81	325.1	0.185	CT($\pi_G \rightarrow \pi^*_{dppn}$) + MLCT($d_{Ru} \rightarrow \pi^*_{bpy}$)

All values were obtained at the B3LYP/de2-TZVP(-f) level of theory.

5.4.2 Dexter Energy Transfer

As stated before, the $[Ru(bpy)2dppn]^{2+}$ complex is able to undergo EnT from the IL T_1 state to generate $^1O_2$ [1, 23, 142, 146]. To investigate the $^3O_2 \rightarrow {}^1O_2$ EnT reaction, it is crucial to set up two major pillars of the DET theory. Firstly, DET reactions occur due to the orbital overlap between the species involved in the transfer [200–202]. In this sense, since the Ru-dppn T_1 state is centered in the dppn ligand, the energy transfer reaction coordinate is likely to be located in the vicinity of this ligand. Figure 5.16 shows the orbitals involved in the transition in terms of the hole-electron pair. The electron orbitals are distributed all over the ligand, while the hole orbitals are concentrated mostly on the last two rings, with a significant overlap between them. Therefore, the reaction coordinate investigation was limited to the sample space of the dppn ligand.

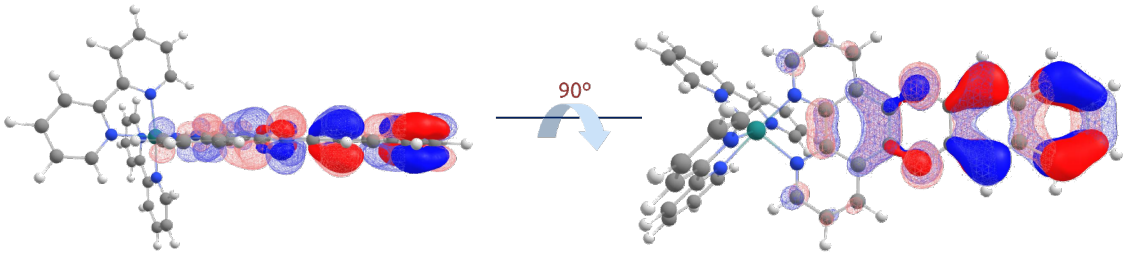

Figure 5.16: Natural Transition Orbitals involved in the T_1 transition of the $[Ru(bpy)_2dppn]^{2+}$ complex. The molecular orbitals in solid color represent the hole, and those in entangled lines represent the electron.

Secondly, DET reactions only occur when total spin is conserved [200]. The scheme presented in Figure 5.17 shows the combination of the spin-multiplicity of both species involved in this reaction and the total spin-multiplicity of the system in each case. Initially, both species are in the ground state, which is singlet (S_0) and triplet ($^3\Sigma_g^-$), for the ^{1}PS and $^3O_2$, respectively. With this combination, the total spin multiplicity of the system is triplet, ^{3}(ST). After the incidence of light with suitable wavelength followed by the excitation of the ^{1}PS, as detailed in the previous section, the intersystem crossing is a highly favored decay channel, populating the triplet manifold. In the triplet excited state, the total spin-multiplicity of the system is either quintet, ^{5}(TT), or singlet, ^{1}(TT). At this point, where the photosensitizer is at the lowest triplet excited state, the EnT reaction takes place. The final state features the PS fully deactivated, meaning its electronic configuration is back to its original ground-state form. On the other hand, the energy excess is concentrated at the molecular oxygen, which is present in its lowest energy excited form, $^1O_2(^1\Delta_g)$. The final state combines two singlet species, thus forming a singlet system, ^{1}(SS). Therefore, two paths are set for the EnT: (*i*) ^{1}(TT) $\rightarrow$ ^{1}(SS) and (*ii*) ^{5}(TT) $\rightarrow$ ^{1}(SS). The first path involves two states with the same total spin multiplicity

and does not violate the spin conservation rule. The second path is spin-forbidden, which breaks the second requirement for DET. Therefore, the DET for this system occurs in the singlet PES. It is important to highlight that the two-electron interaction mechanism is under investigation in this work, and CT states (hole or electron transfers) were not considered. Furthermore, as a supramolecular system, this mechanism is not bridge-mediated.

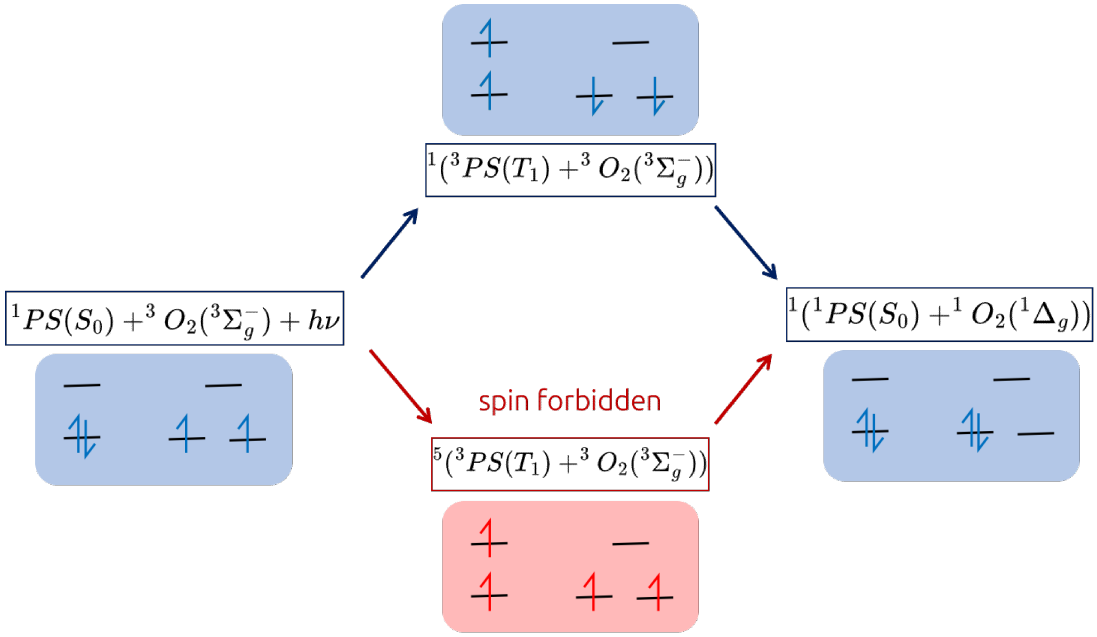

Figure 5.17: Scheme of the spin-allowed and spin-forbidden pathways for EnT between the PS and O_2.

Although the two diabatic states of interest are ^{1}(TT) and ^{1}(SS), the quintet diabat, ^{5}(TT), is quite valuable for determining the non-interaction asymptotic limit between the two molecules. Contrary to the singlet adiabatic state that can arise from different electronic configurations depending on $\mathbf{R}$ (nuclei coordinates) and, in this case, the $\mathbf{D}_{if}$, the quintet state is unambiguous, and both diabatic and adiabatic states will be (mostly) the same. Hence, direct unrestricted DFT calculations can be employed to construct the PES of the ^{5}(TT), avoiding multireference methods and CDFT. Figure 5.18 shows the ^{5}(TT) PES of 10 of the 15 orientations investigated in this work. It is noticeable that the asymptotic limit was achieved at 3.5 Å, and no energy difference is observed for larger distances. This indicates that the relative orientation between the PS and O_2 is no longer an important variable since the two species are not interacting beyond this point. For closer distances, the interaction is highly dependent on the orientation, with a larger repulsion for a perpendicular approach of PS-O_2. This serves as the first evidence that, in fact, different orientations are likely to modulate the rate constants even for small coupling regimes.

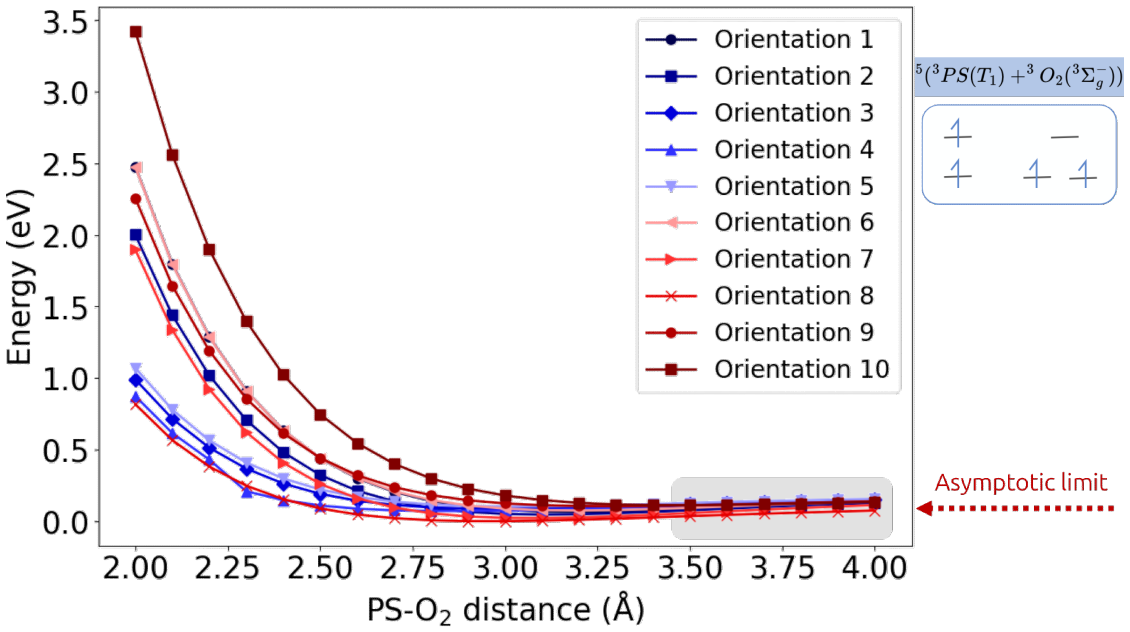

Figure 5.18: Adiabatic PES of the system in the quintet state, ^{5}(TT), of 10 different orientations.

To confirm the transferability of the asymptotic limit from the quintet adiabatic PES to the diabatic states of interest, both ^{1}(TT) and ^{1}(SS) states were constructed for orientation 1 (parallel O_2 towards the center of ring 4) for $\mathbf{D}_{if}$ varying from 2 to 4 Å, as shown in Figure 5.19. Short distances (below 2.5 Å) favor the stability of the ^{1}(SS) state, while larger distances stabilize the ^{1}(TT) state. This indicates that the calculated diabatic states are coherent with the chemical intuition expected from this system. The crossing point between the two diabats occurs between 2.5 and 2.6Å. In fact, the crossing point of all orientations occurs before 3.0 Å. Therefore, because the diabatic couplings are evaluated only at the crossing point, $\mathbf{D}_{ij}$ has been truncated at this distance. Furthermore, the asymptotic limit for the non-interacting system should lead to the same ΔG and does not require to be calculated for the subsequent orientations. Bai and Barbatti investigated the same $\mathbf{D}_{if}$ span for 6-aza-2-thiothymine and reported similar findings using the Divide-to-conquer model [206, 215].

The next 14 pictures display the adiabatic PES of the two singlet states of interest, spanning $\mathbf{D}_{if}$ from 2 to 3 Å. All crossing points are located within this range, corroborating the finding for orientation 1. The pictures also feature graphic representations of the orientation the O_2 molecule approaches the Ru(II) complex. Orientations 1-7 and 11 feature the O_2 molecule approaching the center of one of the aromatic rings of the dppn ligand from above. Among them, orientation 4 is the only one where O_2 is perpendicular to the ligand plane. As a result, no crossing for this set of $\mathbf{D}if$ is observed. Furthermore, perpendicular orientations have been shown to yield much lower EnT rate constants com-

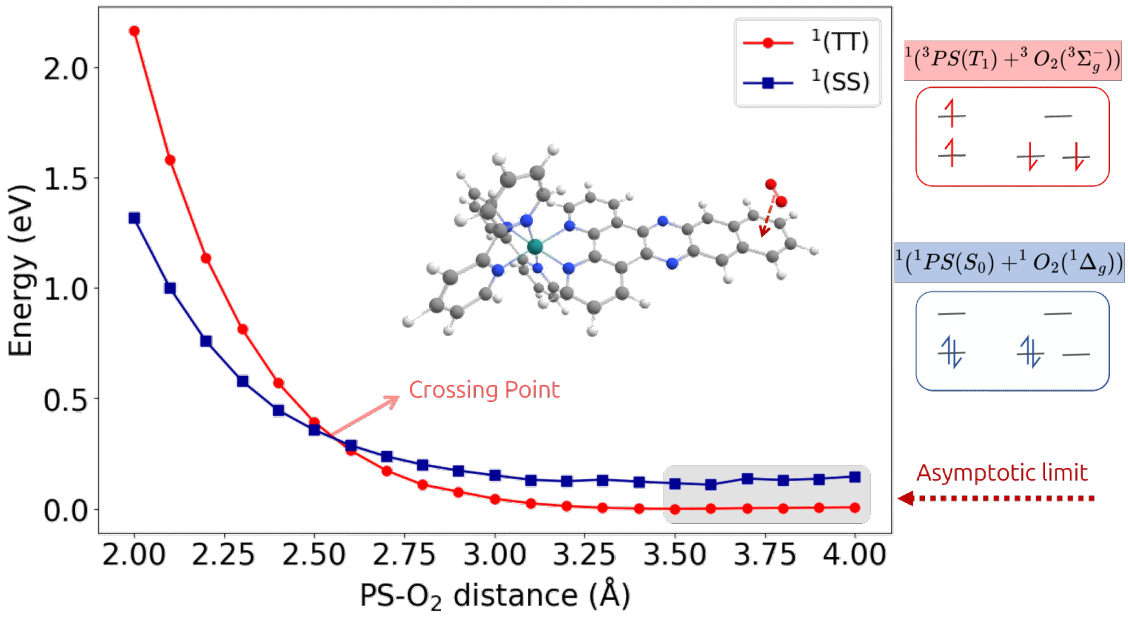

Figure 5.19: Diabatic PES of the system in the initial singlet state (red) formed by the combination of two triplets, ^{1}(TT), and the final singlet state (blue) formed by the combination of two singlets, ^{1}(SS), alongside the PS-O_2 relative orientation **1**.

pared to parallel ones [215]. Orientations 8-10 and 12-15 concentrate on investigating reaction coordinates directly toward specific bonds of dppn. Orientations approaching the plane from the sides of the ligand were not considered.

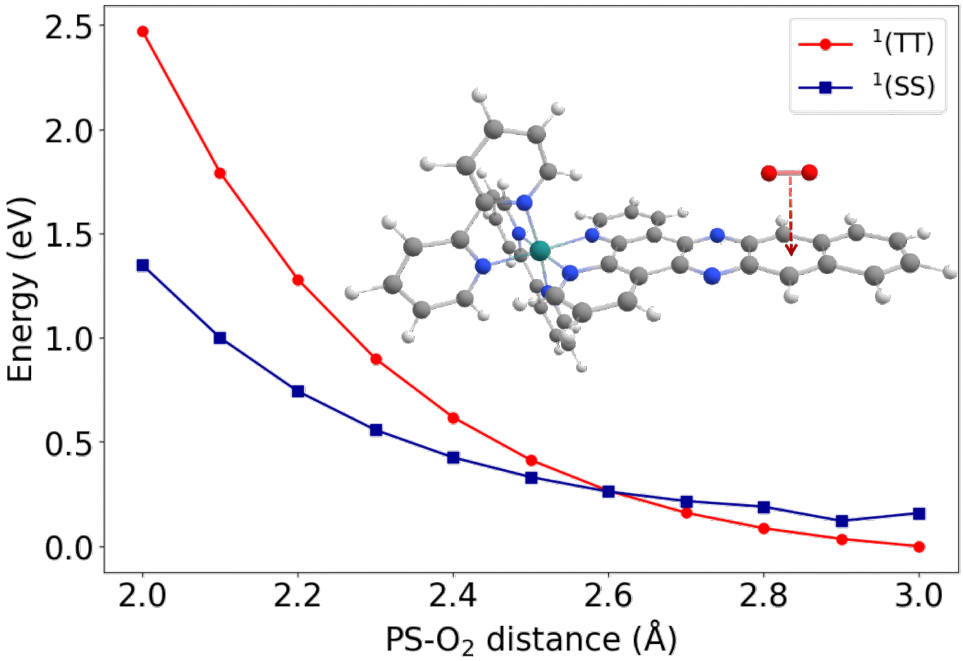

Figure 5.20: Diabatic PES of the system in the initial singlet state (red) formed by the combination of two triplets, ^{1}(TT), and the final singlet state (blue) formed by the combination of two singlets, ^{1}(SS), alongside the PS-O_2 relative orientation **2**.

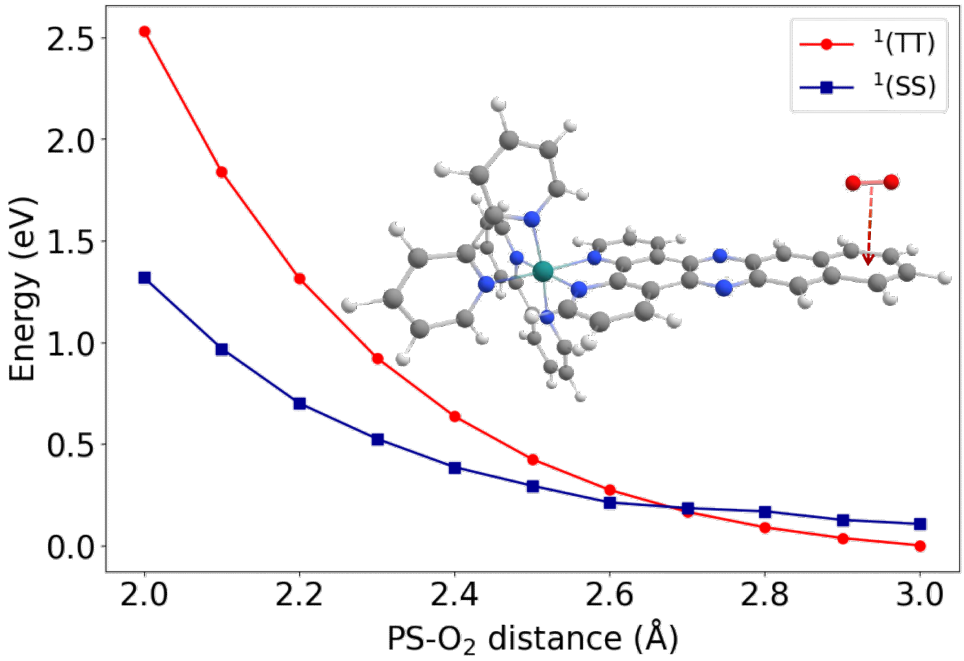

Figure 5.21: Diabatic PES of the system in the initial singlet state (red) formed by the combination of two triplets, ^{1}(TT), and the final singlet state (blue) formed by the combination of two singlets, ^{1}(SS), alongside the PS-O_2 relative orientation **3**.

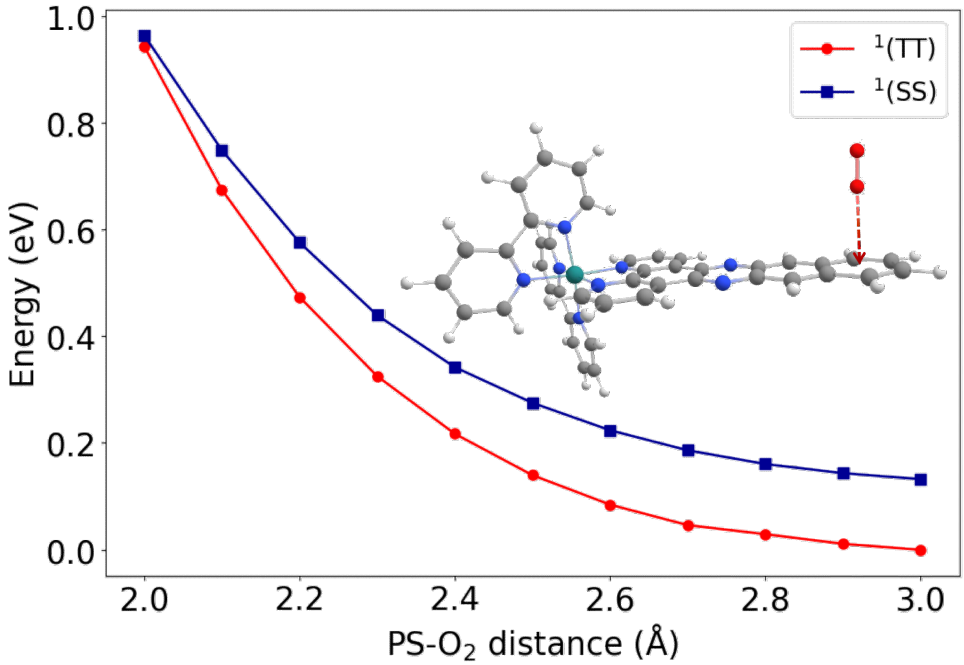

Figure 5.22: Diabatic PES of the system in the initial singlet state (red) formed by the combination of two triplets, ^{1}(TT), and the final singlet state (blue) formed by the combination of two singlets, ^{1}(SS), alongside the PS-O_2 relative orientation **4**.

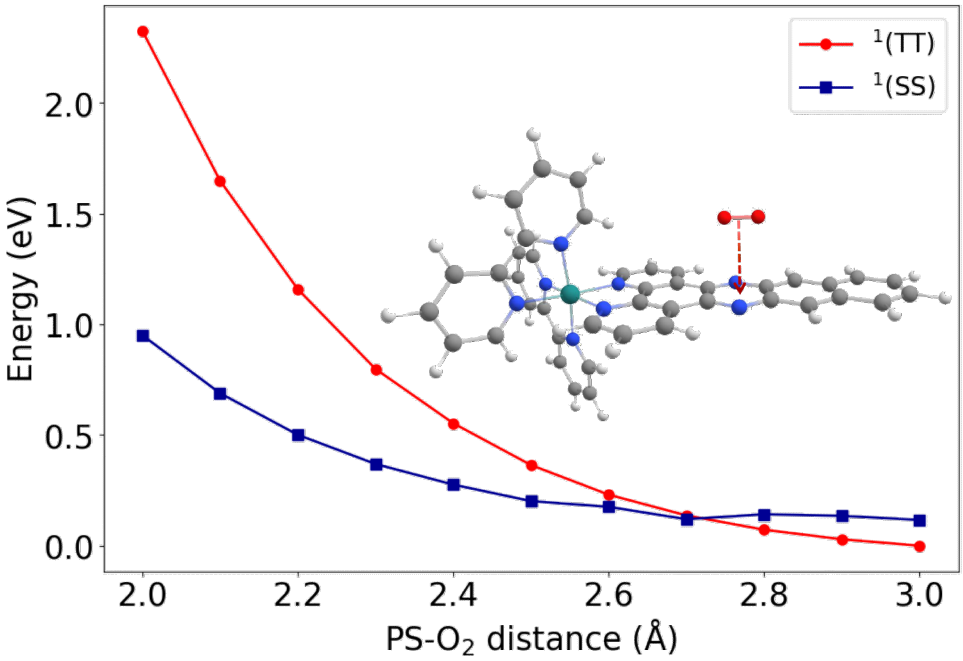

Figure 5.23: Diabatic PES of the system in the initial singlet state (red) formed by the combination of two triplets, ^{1}(TT), and the final singlet state (blue) formed by the combination of two singlets, ^{1}(SS), alongside the PS-O_2 relative orientation **5**.

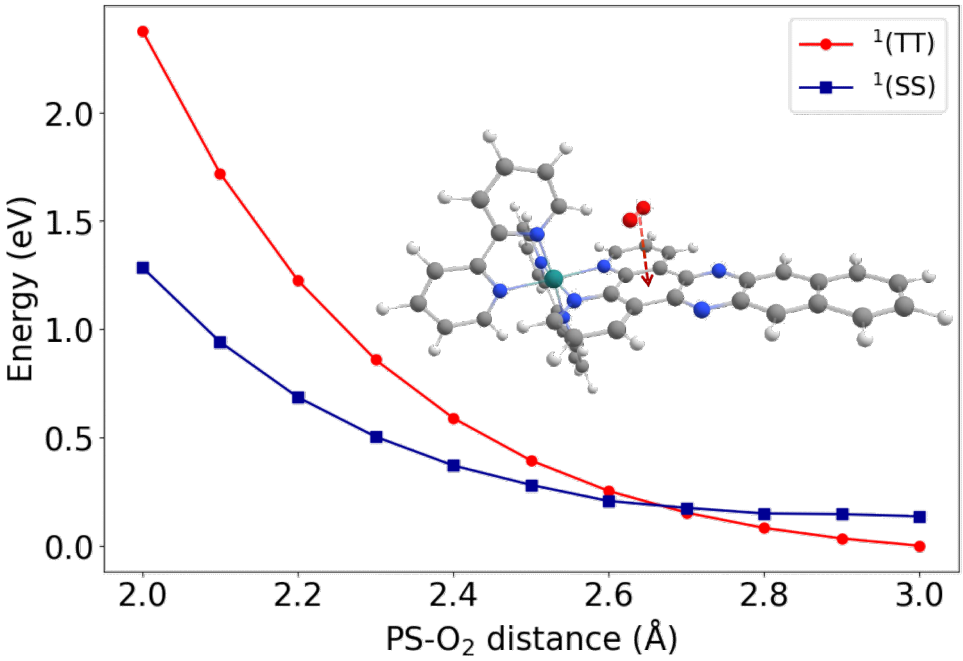

Figure 5.24: Diabatic PES of the system in the initial singlet state (red) formed by the combination of two triplets, ^{1}(TT), and the final singlet state (blue) formed by the combination of two singlets, ^{1}(SS), alongside the PS-O_2 relative orientation **6**.

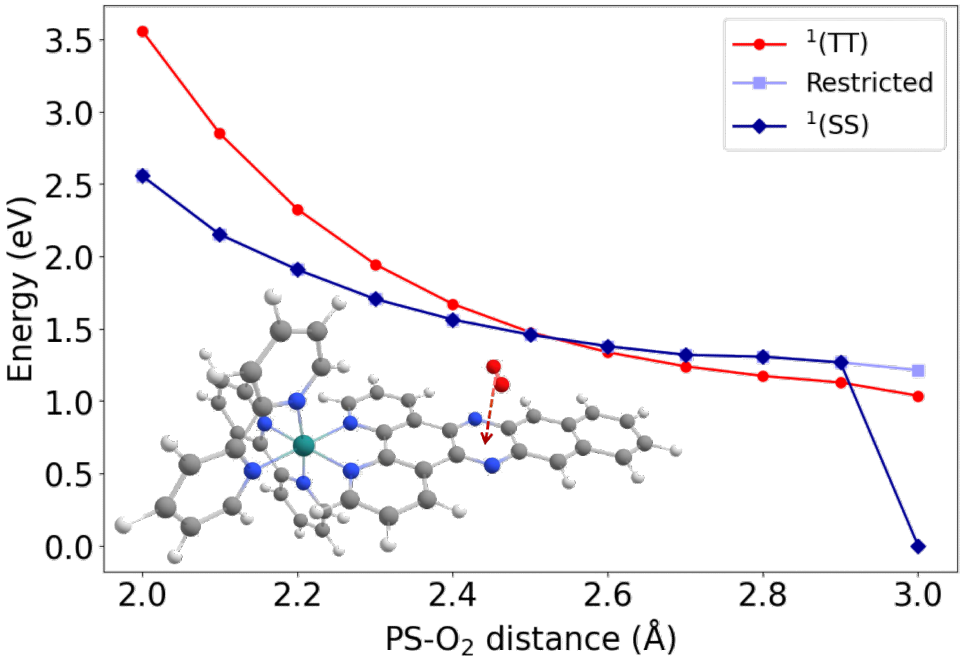

Figure 5.25: Diabatic PES of the system in the initial singlet state (red) formed by the combination of two triplets, ^{1}(TT), and the final singlet state (blue) formed by the combination of two singlets, ^{1}(SS), alongside the PS-O_2 relative orientation **7**.

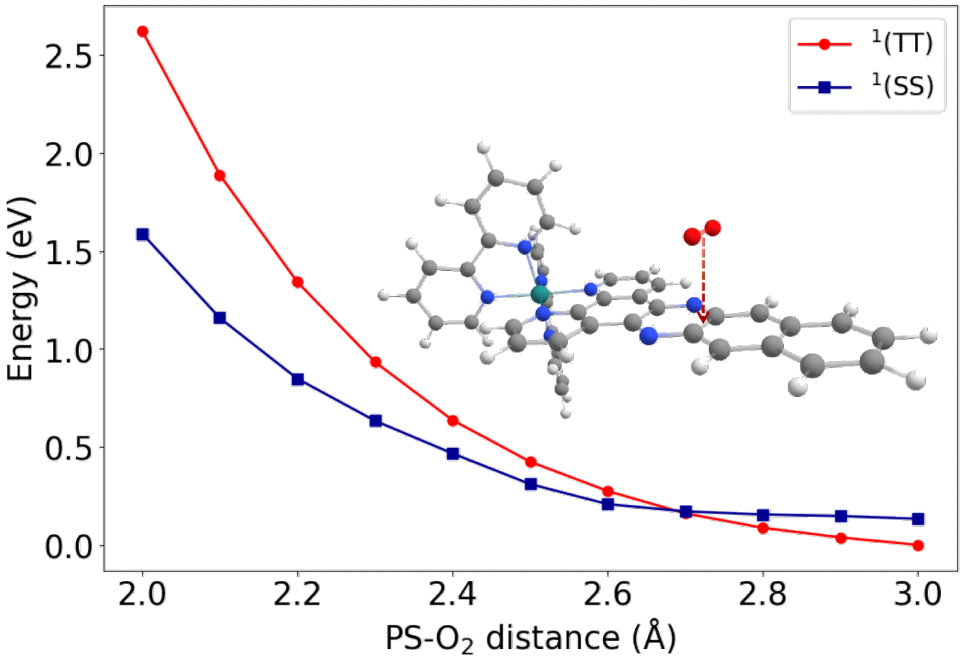

Figure 5.26: Diabatic PES of the system in the initial singlet state (red) formed by the combination of two triplets, ^{1}(TT), and the final singlet state (blue) formed by the combination of two singlets, ^{1}(SS), alongside the PS-O_2 relative orientation **8**.

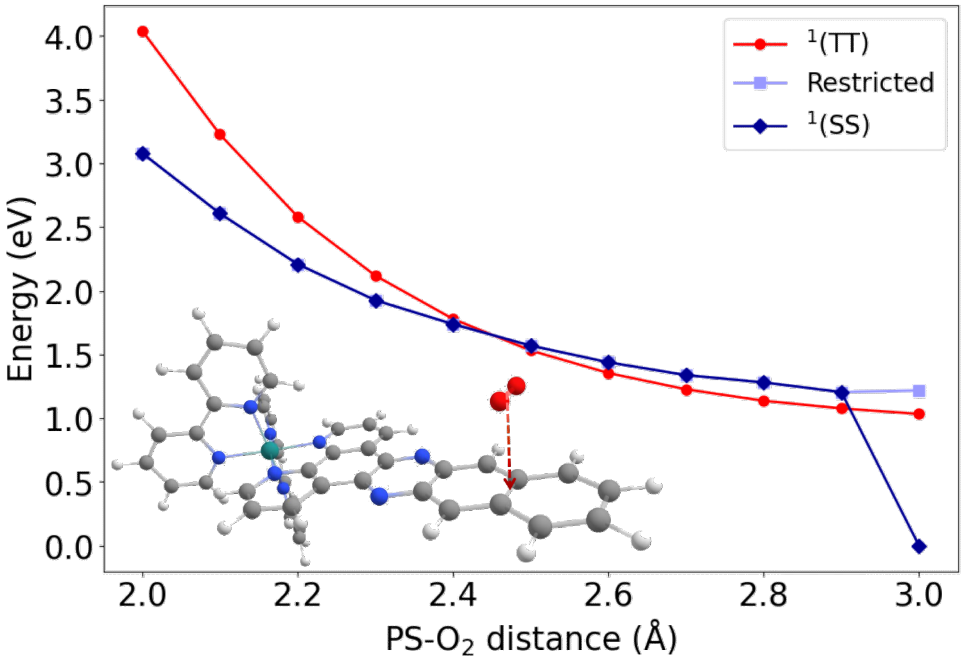

Figure 5.27: Diabatic PES of the system in the initial singlet state (red) formed by the combination of two triplets, ^{1}(TT), and the final singlet state (blue) formed by the combination of two singlets, ^{1}(SS), alongside the PS-O_2 relative orientation **9**.

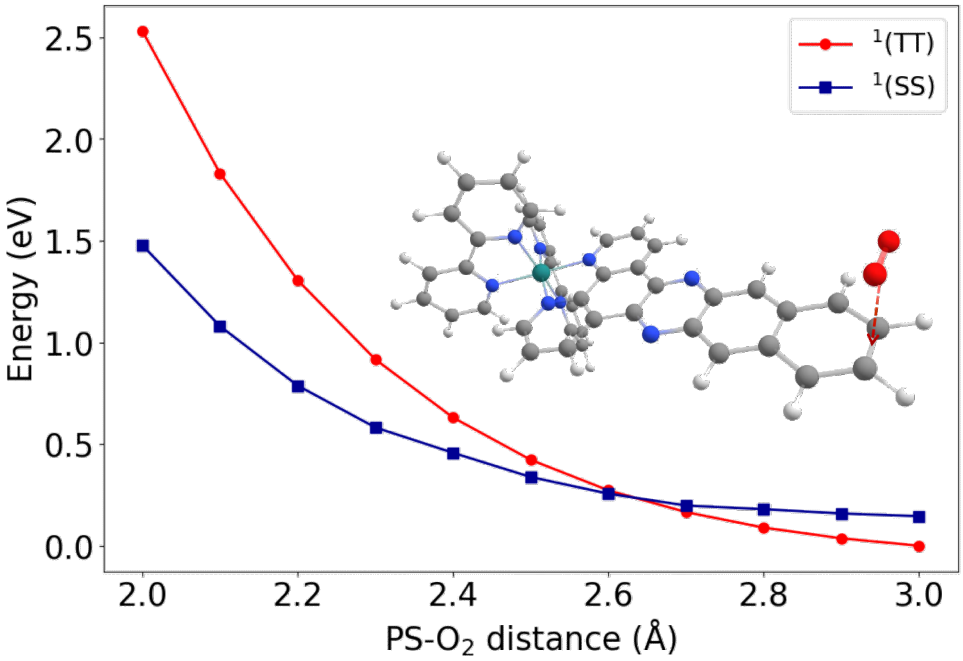

Figure 5.28: Diabatic PES of the system in the initial singlet state (red) formed by the combination of two triplets, ^{1}(TT), and the final singlet state (blue) formed by the combination of two singlets, ^{1}(SS), alongside the PS-O_2 relative orientation **10**.

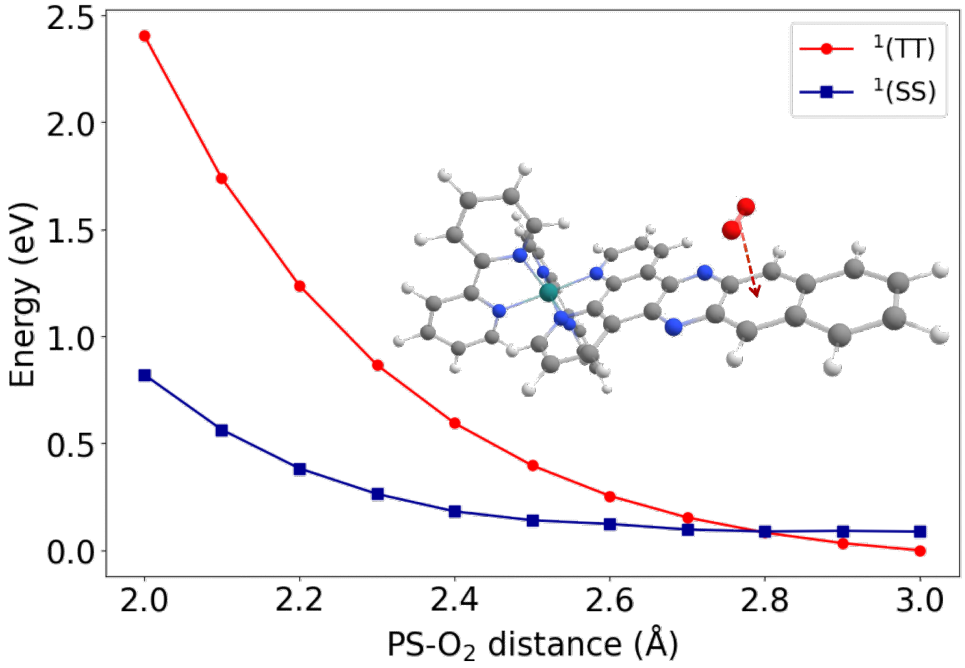

Figure 5.29: Diabatic PES of the system in the initial singlet state (red) formed by the combination of two triplets, ^{1}(TT), and the final singlet state (blue) formed by the combination of two singlets, ^{1}(SS), alongside the PS-O$_2$ relative orientation **11**.

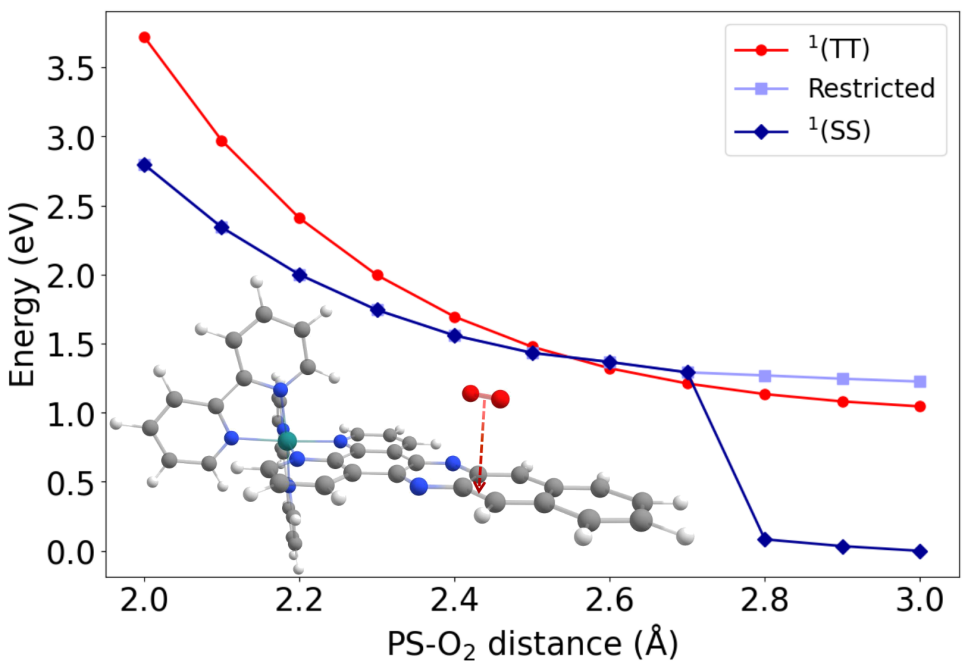

Figure 5.30: Diabatic PES of the system in the initial singlet state (red) formed by the combination of two triplets, ^{1}(TT), and the final singlet state (blue) formed by the combination of two singlets, ^{1}(SS), alongside the PS-O$_2$ relative orientation **12**.

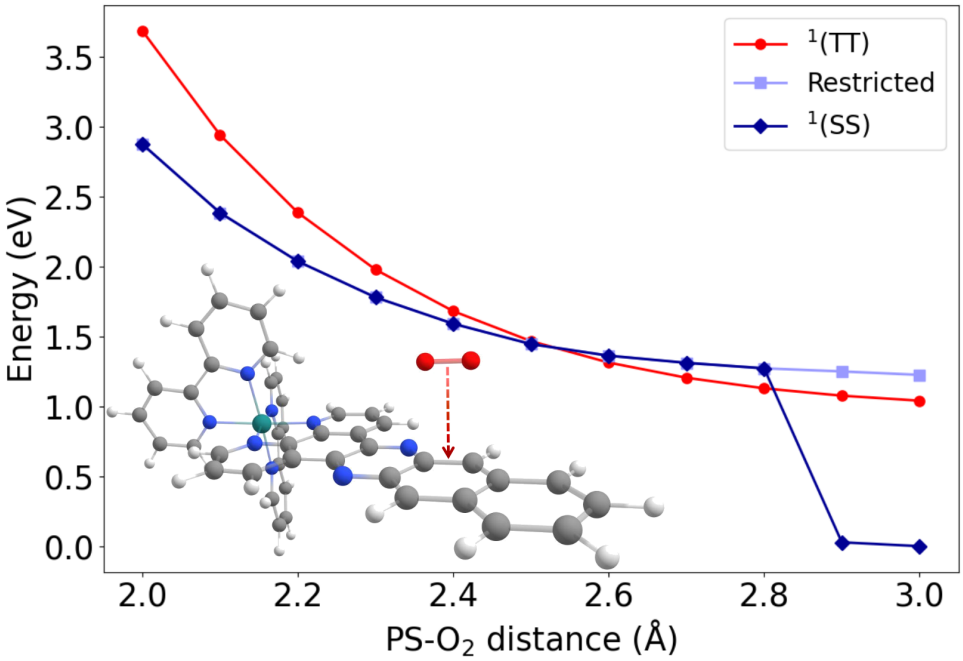

Figure 5.31: Diabatic PES of the system in the initial singlet state (red) formed by the combination of two triplets, ^{1}(TT), and the final singlet state (blue) formed by the combination of two singlets, ^{1}(SS), alongside the PS-O_2 relative orientation **13**.

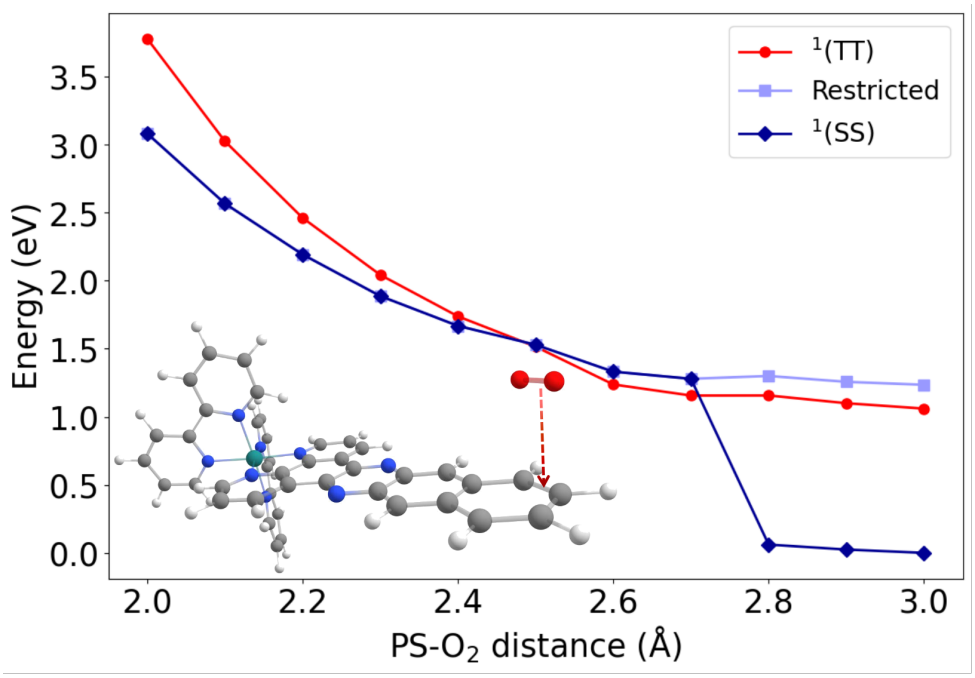

Figure 5.32: Diabatic PES of the system in the initial singlet state (red) formed by the combination of two triplets, ^{1}(TT), and the final singlet state (blue) formed by the combination of two singlets, ^{1}(SS), alongside the PS-O_2 relative orientation **14**.

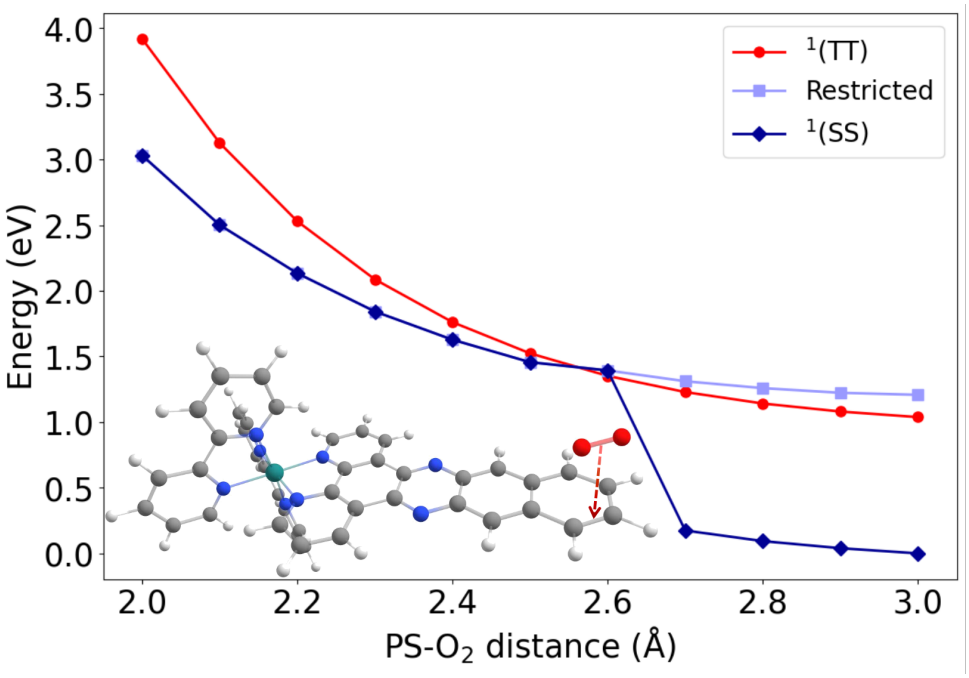

Figure 5.33: Diabatic PES of the system in the initial singlet state (red) formed by the combination of two triplets, ^{1}(TT), and the final singlet state (blue) formed by the combination of two singlets, ^{1}(SS), alongside the PS-O_2 relative orientation **15**.

Orientations 7, 9, and 12-15 present a discontinuity on the final state, ^{1}(SS), passed the crossing point, where this state is no longer the lowest in energy. The points falling off the PES presented spin contamination ($S^2 \approx 1$), indicating a mixing of states, possibly with O_2 triplet (ground) state. To overcome this issue, a second PES was constructed using restricted CDFT, with constraints only on the charge, but enforcing $w_c^\alpha = w_c^\beta$, then converging to a spin pure singlet state. Ideally, the restricted picture describes the exact same state of the singlet unrestricted calculation with no spin contamination (*i.e.*, $S^2 = 0$)) for this system.

Table 5.8 summarizes the distance, $\mathbf{D}_{if}$, where the two diabats cross, the energy difference at the closest point to the crossing, ΔE_{CP}, the coupling at this point, V_{if}^{CP}, and the Dexter energy transfer rate constant, k_{DET}^{CP}, for all 15 orientations. As previously described, in this model, the ΔG and the reorganization energy, λ_M, have negligible changes among the orientations, and the calculated values were 0.14 and 0.29 eV, respectively. Therefore, the rate constant variation among the orientations is completely dependent on the coupling between ^{1}(TT) and ^{1}(SS). This approximation allows an interpretation based solely on the spatial features of the system once the coupling is directly dependent on wavefunction overlap, making a clearer evaluation of the reaction coordinate problem.

Table 5.8: Relative PS-O_2 orientation, PS-O_2 distance at CP ($\mathbf{D}_{ij}^{CP}$), energy difference at CP (ΔE_{CP}), diabatic coupling at CP (V_{if}^{CP}), and DET rate constant at CP (k_{DET}^{CP}).

Orientation	$\mathbf{D}_{ij}^{CP}$ (Å)	ΔE_{CP} (eV)	V_{if}^{CP} ($\times 10^{-4}$ eV)	k_{DET}^{CP} (s^{-1})
1	2.6	0.009	8.89	4.26×10^{7}
2	2.6	0.018	0.30	4.81×10^{4}
3	2.7	0.026	1.01	5.45×10^{5}
4	no crossing	-	-	-
5	2.7	0.072	0.11	6.28×10^{3}
6	2.7	0.022	1.90	1.95×10^{6}
7	2.5	0.017	5	1.35×10^{7}
8	2.7	0.022	14	1.06×10^{8}
9	2.5	0.039	25	3.36×10^{8}
10	2.6	0.133	3.02	4.91×10^{6}
11	2.8	0.005	19	1.94×10^{8}
12	2.6	0.006	132	9.38×10^{9}
13	2.7	0.041	235	2.97×10^{10}
14	2.5	0.011	61	2.00×10^{9}
15	2.6	0.041	47	1.19×10^{9}

$\Delta G = 0.14$ eV; $\lambda_M = 0.29$ eV

As observed in other works [204, 215], the relative orientation significantly affects the diabatic couplings, yielding rate constants spanning from $6.28 \times 10^{3} s^{-1}$ (orientation 5) to $2.97 \times 10^{10} s^{-1}$ (orientation 13). In general, orientations featuring the O_2 going towards the center of one of the aromatic rings of the dppn ligand showed smaller k_{DET}^{CP} values (ranging from 10^{3} to $10^{8} s^{-1}$) compared to orientations where the approach to the PS was towards a bond (ranging from 10^{6} to $10^{10} s^{-1}$). Although the coupling and final rate constant vary significantly among the orientations, the crossing point distances, $\mathbf{D}_{if}^{CP}$, were very consistent, ranging from 2.5 to 2.8 Å. It is important to highlight that even though the kinetic model's ideal crossing point is characterized by $\Delta E_{CP} = 0$, we have considered the threshold of 0.0 eV. The distance incrementation step taken was 0.1Å, and attempts to further refine ΔE_{CP} by decreasing the steps' increments did not lead to a refinement of the energy difference close to the crossing point.

Taking Figure 5.8 as a reference, the orientations targeting the center of the aromatic rings (1-7 and 11) can be further divided into two subgroups: (*i*) along the x-axis (orientations 1, 6, 7, and 11), and (*ii*) along the y-axis (orientations 2, 3, and 5). Orientation 4 is z-axis directed and shows no crossing between the states, as previously discussed. The subgroup (*ii*), along the y-axis, showed the lowest DET rate constant values, indicating these orientations have poor frontier orbital overlap. This result seems reasonable, consid-

ering the O_2 molecule approach towards the center of the rings targets an orbital-lacking region, minimizing the effectiveness of overlap. Within each subgroup, the orientations toward the third and fourth rings also presented better results than those toward rings one and two.

Revisiting Figure 5.16, it is possible to observe that the electron orbitals (LUMO) are spread all over the dppn ligand. On the other hand, the hole orbitals (HOMO) are concentrated on rings 3 and 4. Recalling the two-particle interaction mechanism, both HOMO and LUMO orbitals of the species involved in the energy transfer have to interact to enable the simultaneous electron exchange [90, 201]. In that sense, the third ring shows the major orbital coefficient for both frontier orbitals of dppn at the same site. Interestingly, these sites (bonds) are featured in orientations 12 and 13, which presented the highest V_{if}^{CP} (0.0132 and 0.0235 eV, respectively) and, consequently, the largest k_{DET}^{CP} (9.38×10^9 and $2.97 \times 10^{10} s^{-1}$, respectively). Following the trend, orientations 14 and 15 also feature the O_2 molecule approaching the ligand through the triplet electron density site on ring 4. Consequently, the two orientations also yielded high DET rates (of the order of $10^9 s^{-1}$). The remaining orientations, 8, 9, and 10, also directed to bonds rather than the center of the aromatic rings, presented smaller couplings and rate constants than orientations 12, 13, 14, and 15. When looking at frontier orbitals, it is possible to observe that these sites lack HOMO orbitals contributions, restricting the ideal orbital overlap for two-body interactions.

Besides mapping out the paramount reaction coordinates for EnT and aiming to maximize the DET rate constant, it is also crucial to compare the results to experimental findings. Sun and coworkers determined a quantum yield for singlet oxygen generation through Type II PDT mechanism, Φ_{O_2}, of 0.88 [142]. Following the definition of quantum yields,

$$\Phi_i = \frac{k_i}{k_i + \sum k_r + \sum_{nr}} \tag{5.12}$$

where Φ_i is the quantum yield of event i, k_i is the rate constant of event i, and k_r and k_{nr} are the rate constant of radiative and non-radiative processes [64, 90], the quantum yield of 0.88 for the set of photophysics constants discussed in the previous section corresponds to a DET rate constant of the order of $10^9 s^{-1}$. This result is well-aligned with the collection of DET constants calculated for the orientations directing the oxygen parallel to the highest hole-electron density pair on the dppn ligand, indicating that the optimized set of reaction coordinates for energy transfer following the two-body interaction will rely on the highest hole-electron density pair sites. These findings open up the possibility of extending the kinetic model to more complex systems, narrowing down the sample space of EnT reaction coordinates to a collection of representative orientations.

5.5 Conclusion

In this work, we have performed a theoretical study on the photophysics of the $[Ru(bpy)_2dppn]^{2+}$ (dppn = benzo[*i*]-dipyrido[3,2-*a*:2',3'-*c*]phenazine; bpy = 2,2'-bipyridine) complex. We also investigated the thermodynamics of some electron transfer and energy transfer reactions in the excited states to evaluate the formation of singlet molecular oxygen and the direct interaction with GMP.

The overall structural properties of the complex did not change significantly from the ground states to the excited states due to the rigidity associated with the polypyridyl moiety of the ligands and their bidentate coordinating mode. On the other hand, the electric dipole moment moments increased for the excited states, except for the S_2 and T_1, which decreased compared to the GS. Such change in the electric dipole moment moments is related to a different charge distribution tied to different electronic states. Hence, the change in charge localization can influence the reactivity.

The Ru-dppn photophysical investigations were performed in water, while most of the experimental results available in the literature are reported in acetonitrile. However, the overall photophysics, *i.e.*, the absorption bands, and the nature of the transitions were observed to be the same. The HOMO is reportedly constructed by dppn π orbitals, while the HOMO-1 is metal-centered, which was interchanged in our calculations. However, the energy difference between the HOMO and the HOMO-1 orbital is almost none, making the ordination very subtle. The herein calculated photophysical rate constants showed that the fluorescence constant was approximately 6×10^5 s^{-1}, which is a very low rate constant for this phenomenon, indicating other excited state processes are more likely to happen. The overall ISC rate constant was calculated to be 7.76×10^{12} s^{-1}, agreeing with previous experiments revealing that the triplet states are populated in less than 1 ps.

Also, the first triplet excited state is IL ($^1\pi\pi^*$), while the second is MLCT, which can lead to dual-channel reactivity. Furthermore, the Ru-dppn was found to favorably oxidize the GMP and photosensitize the O_2 to generate $^1O_2$. Hence, the Ru-dppn can interact directly as an intercalator and, therefore, react with DNA nucleobases. Although this complex is more limited regarding the variety of ET and EnT it can undergo, its dual-channel characteristics place it as an efficient PS candidate even in hypoxia environments. Our calculations also demonstrated that, even though the second excited triplet state was observed to react with the guanine, the first excited triplet state is thermodynamically favorable to undergo the same reaction. The investigations with the d(ATGC)2 DNA fragment showed that the guanine orbitals participate in the transitions, reinforcing its role in photochemical reactions.

We have also investigated the DET between the $[Ru(bpy)_2dppn]^{2+}$ complex and O_2 to generate singlet oxygen molecule, which is a highly reactive species that can be key

on Type II PDT mechanism. The kinetic model applied to the investigation of this process has been demonstrated to be effective when allied to the proper set of orientations. Identifying the EnT reaction coordinates has always been challenging, especially when dealing with large and complex systems, such as the Ru-dppn PS. As observed in other works, the parallel orientations approaching the HOMO and LUMO and maximizing the overlap between the frontier orbitals of both species led to the most outstanding SOC and, consequently, the highest k_{DET}^{CP} values. Such results agree with the experimental EnT rate constant, suggesting that the approximations made in the kinetic model are valid. Therefore, the DET modeling allied with a thorough evaluation of the frontier orbitals can be a shortcut to the investigation and estimation of rate constants of newly designed PS.

Chapter 6

Final Considerations and Perspectives

As widely discussed in this work, the light-matter interaction unlocks further chemical possibilities with unique applications. Such applications encompass photocatalysis, light harvesting, solar cells, imaging, artificial photosynthesis, and phototherapies, among others. Photodynamic therapy applied to cancer has been raising great attention in the past years as it approaches one of the most critical health problems of the modern age. It has been formally included as a cancer treatment in the Brazilian public healthcare system, SUS, in 2023 and can potentially revolutionize the field. However, as discussed, it still endures many challenges, such as developing new generations of phototherapeutic agents, aiming for better efficiency, and minimizing side effects. Furthermore, it is paramount to understand the mechanisms of action of such compounds, which can aid in the design and control of desirable photosensitizer (PS) properties. In this sense, computational and theoretical chemistry associated with related fields are powerful allies. The system size and complexity scale up fast when dealing with biological ensembles. This becomes a particular issue when modeling time-dependent phenomena such as photodynamic reactions. Consequently, the main objective of this work was to contribute to the modeling of photoactive real systems, which, more often than not, are very complex, enabling a quantitative understanding of such systems allied to a holistic view of phenomena. Hence, new methods for approaching complex systems in the excited states have been proposed, borrowing from well-established theories. These methods aim to aid the exploration of excited-state dynamics of photoactive species and to facilitate the investigation of their applicability as photosensitizers for diverse endings.

Investigating the photophysics of photosensitizers involves mapping all the competing events of deactivation, which unveils crucial information on the properties of such compounds. A complete description of PS photophysics requires the estimation of the internal conversion (IC) rate constants, which is one of the hardest decay rate constants to calculate. Many PSs present rigid frames and are located in Marcus's inverted region

due to their aromatic groups and long conjugation chains, enabling responsive interaction in the visible region of the electromagnetic spectrum. Applying the Fermi Golden Rule to calculating the IC rate constants of such systems is a laborious task and computationally costly for larger systems. Furthermore, it is not implemented straightforwardly in open-source quantum chemistry packages. On the other hand, the direct use of Marcus's theory for inverted region molecules does not reproduce experimental IC rate constant values. We have identified that this issue arises at the density of states portion of the equation. Hence, we have proposed a correction embedded into the reorganization energy factor by considering the conical intersection between the two states involved in the transition. This correction does not invalidate a well-established theory, such as Marcus's theory, but rather expands it to a broader scope. We also applied this correction to the Marcus-Jortner-Levich theory, a more general theory that accounts for vibronic effects, yielding outstanding IC rate constant results. This method can be used for systems with general purposes that belong to Marcus's inverted region. The method has already been applied in many works, indicating its reliability and impact in the photophysics community.

Focusing on metal complexes as photosensitizers, many compounds show aptitude to undergo several mechanisms. For instance, ruthenium complexes featuring polypyridyl ligands can act simultaneously through energy and electron transfer, while homoleptic complexes also show a propensity to liability, as demonstrated. The diversity of deactivation pathways demonstrates that mapping the photophysics alone is insufficient to account for all the possible photochemical reactions. Instead, it is also relevant to describe the side decay pathways. Therefore, it is critical to observe the time evolution of the exciton. Usually, the description of exciton evolution through time is carried out under nonadiabatic dynamics simulations. Although vastly applied, presenting a handful of different algorithms, such simulations are majorly used for small molecules rather than large systems due to their computational cost. Hence, developing a cost-effective model that accurately describes the time evolution of excited states was also among the objectives of this work. Continuing with the description of the photophysical pathways of photosensitizers, the method for calculating the IC rate constant has also been paired with the kinetic model developed herein to assess the excited-state decay mechanism of complex systems. The kinetic model is based on calculating the rate constant of all decay processes at the Franck-Condon region of key states, mapping not only the main deactivation channel but also unveiling states that are less populated but still play a role as a secondary channel. The secondary channels are paramount to determine if a given photosensitizer is prone to undergo different mechanisms, such as Type I and Type II PDT. The kinetic model was then applied to the $[Ru(bpz)_3]^{2+}$ complex. The results not only agreed with experimental results but also reproduced tendencies reported by nonadiabatic

descriptions for similar compounds. It was demonstrated that besides the population of states participating in the main decay path, it was possible to observe the population of other states responsible for photochemical reactions, such as the triplet metal-centered, achieved by overcoming a thermal activation barrier. Similarly to the IC rate constant calculation method, the kinetic model is expandable to other compound classes for diverse applications, offering an alternative to explore the excitation decay over time and understand the different channels.

To further explore transition-metal complexes as photosensitizers for photodynamic therapy, the $[Ru(bpy)_2dppn]^{2+}$ complex photophysics and potential interaction with DNA and O_2 were investigated. The photophysics results confirmed the propensity of this complex to populate the triplet excited states, culminating in a long lifetime. The photoreactions explored thermodynamically also indicated that electron transfer (ET) to guanosine-monophosphate (GMP) and energy transfer (EnT) to molecular oxygen are two critical deactivation pathways for this PS, confirming the dual-channel reaction scheme proposed experimentally. Furthermore, it was also observed that not only the second triplet state is capable of undergoing electron transfer to GMP, but also the first triplet state.

Types I and II PDT mechanisms are the main two paths of action, culminating in cancer cell death. It is evident that these two mechanisms are vital to the success of a photosensitizer, yet it is still very difficult to control and tune between these two possibilities. Therefore, understanding both processes at a molecular level is a state-of-the-art issue. The problem is even more complicated when working with supramolecular systems. For energy transfer, two major issues arise: (i) which EnT mechanism occurs in PDT and (ii) how to determine the reaction coordinate for EnT in a supramolecular system. In this sense, we focused on combining two kinetic methods tested for small molecules to investigate a large system interacting with O_2 to generate $^1O_2$. Because of the nature of the molecules involved in the reactions, Dexter Energy Transfer (DET) is more likely to dominate the EnT. The first challenge was modeling the energy transfer reaction coordinate and determining the properties that construct an effective interaction between the involved species. Because the PS of the study is large, there is no straightforward way of predetermining the reaction coordinates. As mentioned, the previous works that proposed a kinetic model to calculate the EnT rate constant mainly focused on the calculation itself. Furthermore, the systems used as case studies were small and did not offer the complexity of multiple reaction coordinate possibilities. In this work, we have systematically scanned the relative orientations between the PS and O_2, aiming to identify the interactions that maximized the diabatic coupling between the initial and final states. Our findings led us to conclude that the frontier orbitals overlap of both molecules is responsible for maximizing the coupling. More specifically, the PS regions where the

coefficients of both HOMO and LUMO are present culminated in the most effective interactions, leading to final rate constants that agree with experimental findings. Besides investigating the reaction coordinates for EnT, the kinetic model applied is also extremely important. We combined Constrained Density Functional Theory (CDFT) with Marcus's theory to construct this model. Usually, diabatic system calculations are performed using multireference methods. However, applying such methods to large metal complexes is computationally costly. CDFT is an elegant construction that allows these calculations for complex systems, and we demonstrated that it does not affect the accuracy of the final results. Furthermore, the results revealed that the approximations employed to the kinetic model adapted to large systems, *i.e.*, constraints of internal coordinates, calculation of the reorganization energy taking independent systems, and approaching the adiabatic energy of non-interacting species, do not jeopardize the rate constant estimation for inverted region molecules. This is a valuable contribution to the investigation of EnT in PDT systems and can assist in understanding this phenomenon. Finally, like all the methods presented in this work, the DET kinetic model is also expandable to broader applications.

At this point, we hope the progress in methods applied to excited states and the modeling for complex systems in this work benefit the findings and studies of the next generation of photosensitizers for diverse applications. Furthermore, as perspectives of this work, developing a kinetic model for supramolecular electron transfer (Type I PDT) could complete the set of methods for a full investigation of PDT PSs. Also, implementing an orbital descriptor to quantitatively predict the EnT reaction coordinates would further the study of this phenomenon.

Bibliography

[1] Simon P. Foxon, Mohammed A.H. Alamiry, Mike G. Walker, Anthony J.H.M. Meijer, Igor V. Sazanovich, Julia A. Weinstein, and James A. Thomas. Photophysical properties and singlet oxygen production by ruthenium(ii) complexes of benzo[i]dipyrido[3,2-a:2',3'-c]phenazine: spectroscopic and TD-DFT study. *Journal of Physical Chemistry A*, 113(46):12754–12762, 11 2009.

[2] F. J. Stimson and W. F. Meggers. Dyes for photographic sensitizing. *JOSA, Vol. 4, Issue 3, pp. 91-104*, 4:91–104, 5 1920.

[3] Ronald D. Theys and George Sosnovsky. Chemistry and processes of color photography. *Chemical Reviews*, 97:83–132, 1997.

[4] Frank H. Quina and Gustavo Thalmer Medeiros Silva. The photophysics of photosensitization: A brief overview. *Journal of Photochemistry and Photobiology*, 7:100042, 9 2021.

[5] Davide Vione. Photochemical Transformation Processes of Environmental Significance. *Tomorrow's Chemistry Today*, pages 429–453, 3 2008.

[6] Mohamad Sleiman, Amanda Nienow, and Claire Richard. Environmental photochemistry on plants: recent advances and new opportunities for interdisciplinary research. *Photochemical and Photobiological Sciences*, 21(8):1497–1510, 8 2022.

[7] Kenji Setoura and Syoji Ito. Optical manipulation in conjunction with photochemical/photothermal responses of materials. *Journal of Photochemistry and Photobiology C: Photochemistry Reviews*, 52:100536, 9 2022.

[8] Hiroyuki Takeda, Kazuhide Koike, Tatsuki Morimoto, Hiroki Inumaru, and Osamu Ishitani. Photochemistry and photocatalysis of rhenium(I) diimine complexes. *Advances in Inorganic Chemistry*, 63:137–186, 1 2011.

[9] Archis A. Yawalkar, Dhananjay S. Bhatkhande, Vishwas G. Pangarkar, and Anthony A.C.M. Beenackers. Solar-assisted photochemical and photocatalytic degra-

dation of phenol. *Journal of Chemical Technology & Biotechnology*, 76(4):363–370, 4 2001.

[10] Tehshik P. Yoon, Michael A. Ischay, and Juana Du. Visible light photocatalysis as a greener approach to photochemical synthesis. *Nature Chemistry 2010 2:7*, 2(7):527–532, 6 2010.

[11] Ravindra B. Weerasooriya, Matthew C. Drummer, Brian T. Phelan, Jonathan L. Gesiorski, Emily A. Sprague-Klein, Lin X. Chen, and Ksenija D. Glusac. Toward Metal-free Photocatalysis: Photochemical Regeneration of Organic Hydride Donors Using Phenazine-Based Photosensitizers. *The Journal of Physical Chemistry C*, 126(42):17816–17825, 10 2022.

[12] Yuen Yap Cheng, Burkhard Fückel, Rowan W. MacQueen, Tony Khoury, Raphaël G.C.R. Clady, Tim F. Schulze, N. J. Ekins-Daukes, Maxwell J. Crossley, Bernd Stannowski, Klaus Lips, and Timothy W. Schmidt. Improving the light-harvesting of amorphous silicon solar cells with photochemical upconversion. *Energy & Environmental Science*, 5(5):6953–6959, 4 2012.

[13] Tao Ling, Sergei A. Kulinich, Zi Ling Zhu, Shi Zhang Qiao, and Xi Wen Du. Highly Conductive CdS Inverse Opals for Photochemical Solar Cells. *Advanced Functional Materials*, 24(5):707–715, 2 2014.

[14] Francesco Nastasi, Placido Giuseppe Mineo, Jessica Barichello, Giuseppina La Ganga, Gaetano Di Marco, Giuseppe Calogero, and Massimiliano Cordaro. Synthesis and Photophysics Characterization of Boronic Styril and Distyryl BODIPYs for Water-Based Dye-Sensitized Solar Cells. *Biomimetics 2022, Vol. 7, Page 110*, 7(3):110, 8 2022.

[15] F. Shen, Y. M. Fan, H. Li, S. P. Li, M. Xu, and W. B. Dai. Photophysics and photovoltaic properties of Zn-alloyed Ag-In-S quantum dots sensitized solar cells. *Journal of Alloys and Compounds*, 922:166296, 11 2022.

[16] Amirrasoul Tavakoli and Jung Hyun Min. Photochemical modifications for DNA/RNA oligonucleotides. *RSC Advances*, 12(11):6484–6507, 2 2022.

[17] Brittany P. Rickard, Marta Overchuk, Girgis Obaid, Mustafa Kemal Ruhi, Utkan Demirci, Suzanne E. Fenton, Janine H. Santos, David Kessel, and Imran Rizvi. Photochemical Targeting of Mitochondria to Overcome Chemoresistance in Ovarian Cancer†. *Photochemistry and Photobiology*, 10 2022.

[18] Antonio Tedesco, Jeane Rotta, and Claure Lunardi. Synthesis, Photophysical and Photochemical Aspects of Phthalocyanines for Photodynamic Therapy. *Current Organic Chemistry*, 7(2):187–196, 3 2005.

[19] Carsten Lange and Patrick Bednarski. Photosensitizers for Photodynamic Therapy: Photochemistry in the Service of Oncology. *Current Pharmaceutical Design*, 22(46):6956–6974, 2 2017.

[20] Yuan Yuan Zhao, Ling Zhang, Zixuan Chen, Bi Yuan Zheng, Meirong Ke, Xingshu Li, and Jian Dong Huang. Nanostructured Phthalocyanine Assemblies with Efficient Synergistic Effect of Type i Photoreaction and Photothermal Action to Overcome Tumor Hypoxia in Photodynamic Therapy. *Journal of the American Chemical Society*, 143(34):13980–13989, 9 2021.

[21] Amandeep Arora and Kamaljeet Singh. Click Chemistry Mediated by Photochemical Energy. *ChemistrySelect*, 7(29):e202200541, 8 2022.

[22] Chantal Daniel. Photochemistry and photophysics of transition metal complexes: Quantum chemistry. *Coordination Chemistry Reviews*, 282-283:19–32, 1 2015.

[23] Konrad Szaciłowski, Wojciech Macyk, Agnieszka Drzewiecka-Matuszek, Małgorzata Brindell, and Grazyna Stochel. Bioinorganic photochemistry: Frontiers and mechanisms. *Chemical Reviews*, 105(6):2647–2694, 6 2005.

[24] Aline S. Bozzi and Willian R. Rocha. Calculation of Excited State Internal Conversion Rate Constant Using the One-Effective Mode Marcus-Jortner-Levich Theory. *Journal of Chemical Theory and Computation*, 19(8):2316–2326, 4 2023.

[25] Pavel S. Rukin, Mariagrazia Fortino, Deborah Prezzi, and Carlo Andrea Rozzi. Complementing adiabatic and nonadiabatic methods to understand internal conversion dynamics in porphyrin derivatives. *Journal of Chemical Theory and Computation*, 20:10759–10769, 12 2024.

[26] Kalyani Patrikar, Keval Patadia, Rudranarayan Khatua, and Anirban Mondal. From molecules to devices: A multiscale approach to evaluating organic photovoltaics. *Journal of Chemical Theory and Computation*, 11 2024.

[27] Aniruddha Sarkar, Arun K. Pal, Ankit Kumar, Souradip Dasgupta, Noufal Kandoth, Anindya Datta, Ayan Datta, and Sayam Sen Gupta. Ancillary ligand-promoted charge transfer in bis-indole pyridine ligand-based nickel complexes. *Inorganic Chemistry*, 10 2024.

[28] Zi Kang Zhao, Teng Fei He, Qiang Gao, Ai Min Ren, Tong Shun Wu, Jing Fu Guo, Hui Ying Chu, Zhong Min Su, Hui Li, and Lu Yi Zou. Theoretical investigation and molecular design: A series of tripod-type cu(i) blue light thermally activated delayed fluorescence materials. *Inorganic Chemistry*, 9 2024.

[29] Koen Veys, Manon H.E. Bousquet, Denis Jacquemin, and Daniel Escudero. Modeling the Fluorescence Quantum Yields of Aromatic Compounds: Benchmarking the Machinery to Compute Intersystem Crossing Rates. *Journal of Chemical Theory and Computation*, 19(24):9344–9357, 12 2023.

[30] Pandiyan Sivasakthi and Pralok K. Samanta. Exploring thioxanthone derivatives as singlet oxygen photosensitizers for photodynamic therapy at the near-ir region. *Journal of Physical Chemistry A*, 127:8900–8910, 10 2023.

[31] Jinming Liu, Xinli Song, Jinyou Long, and Song Zhang. Investigations on molecular structures and excited state dynamics of 5-cholorouracil. *Journal of Molecular Structure*, 1336:142115, 8 2025.

[32] Atanu Ghosh, Jonathan T. Yarranton, and James K. McCusker. Establishing the origin of marcus-inverted-region behaviour in the excited-state dynamics of cobalt(iii) polypyridyl complexes. *Nature Chemistry*, 16:1665–1672, 10 2024.

[33] Arun K. Pal and Ayan Datta. First-principles design of heavy-atom-free singlet oxygen photosensitizers for photodynamic therapy. *Journal of Chemical Physics*, 160, 4 2024.

[34] Anjay Manian, Salvy P Russo, Zifei Chen, and Hugh T Sullivan. The up's and down's of internal conversion. *ChemRxiv.*, 2 2025.

[35] Yibo Shi, Lin Liu, Wei-Hai Fang, Qian Wang, Xiao Liu, Kai Feng, Wei Sun, Dongpeng Yan, Xuebo Chen, Y Shi, L Liu, W.-H Fang, Q Wang, X Liu, K Feng, W Sun, D Yan, and X Chen. Excitation-dependent quadruple-level emission from an isolated molecule for dynamic information encryption. *Advanced Science*, page e08987, 7 2025.

[36] Mona E. Arnold, Robert Toews, Lars Schneider, Jonas Schmid, Miftahussurur Hamidi Putra, Michael Busch, Axel Groß, Felix Deschler, Andreas Köhn, and Alexander J.C. Kuehne. The impact of donor-orientation on the emission properties of chlorinated trityl radicals. *Advanced Optical Materials*, 13:2500296, 7 2025.

[37] Zengkui Liu, Zailing Song, and Xiang Sun. All-atom photoinduced charge transfer dynamics in condensed phase via multistate nonlinear-response instantaneous marcus theory. *Journal of Chemical Theory and Computation*, 20:3993–4006, 5 2024.

[38] Aline de Souza Bozzi, Rita de Cássia Oliveira Sebastião, and Willian Ricardo Rocha. Understanding the excited state decay mechanism of complex systems: a general first-order kinetic model. *Physical Chemistry Chemical Physics*, 27:9806–9816, 5 2025.

[39] A. S. Bozzi and W. R. Rocha. Photophysics and Excited State Reactions of [Ru(bpy) ₂ dppn] ²⁺ : A Computational Study. *Chemistry – An Asian Journal*, 19(22), 11 2024.

[40] Douglas B. Kitchen, Hélène Decornez, John R. Furr, and Jürgen Bajorath. Docking and scoring in virtual screening for drug discovery: Methods and applications. *Nature Reviews Drug Discovery*, 3(11):935–949, 11 2004.

[41] Gabriela Bitencourt-Ferreira and Walter Filgueira de Azevedo. *Docking with SwissDock*, volume 2053. Springer Science and Business Media LLC, 2019.

[42] Linus Santana Azevedo, Fernanda Pretto Moraes, Mariana Morrone Xavier, Eduarda Ozorio Pantoja, Bianca Villavicencio, Jana Aline Finck, Audrey Menegaz Proenca, Kelen Beiestorf Rocha, and Walter Filgueira de Azevedo. Recent Progress of Molecular Docking Simulations Applied to Development of Drugs. *Current Bioinformatics*, 7(4):352–365, 11 2013.

[43] Inbal Halperin, Buyong Ma, Haim Wolfson, and Ruth Nussinov. Principles of docking: An overview of search algorithms and a guide to scoring functions. *Proteins: Structure, Function and Genetics*, 47(4):409–443, 6 2002.

[44] R. Norel, H. J. Wolfson, and R. Nussinov. Small molecule recognition: Solid angles surface representation and molecular shape complementarity. *Combinatorial chemistry & high throughput screening*, 2(4):223–22337, 1999.

[45] P. J. Goodford. A Computational Procedure for Determining Energetically Favorable Binding Sites on Biologically Important Macromolecules. *Journal of Medicinal Chemistry*, 28(7):849–857, 1985.

[46] Natasja Brooijmans and Irwin D. Kuntz. Molecular recognition and docking algorithms. *Annual Review of Biophysics and Biomolecular Structure*, 32:335–373, 2003.

[47] Peter Kollman. Free Energy Calculations: Applications to Chemical and Biochemical Phenomena. *Chemical Reviews*, 93(7):2395–2417, 1993.

[48] Thomas Simonson, Georgios Archontis, and Martin Karplus. Free energy simulations come of age: Protein-ligand recognition. *Accounts of Chemical Research*, 35(6):430–437, 2002.

[49] Donald A. McQuarrie. *Quantum Chemistry*. University Science Books, 2nd edition, 2008.

[50] A Szabo and N L Ostlund. *Modern Quantum Chemistry: Introduction to Advanced Electronic Structure Theory*. Dover Publications, Mineola, 1996.

[51] C. J. Cramer. *Essentials of Computational Chemistry: Theories and Models*. Wiley, West Sussex, second edition, 2004.

[52] Robert G. Parr and Weitao Yang. *Density Functional Theory of Atoms and Molecules*. New York: Oxford University Press, 1989.

[53] Klaus Capelle. A Bird ' s-Eye View of Density-Functional Theory. 36(4):1318–1343, 2006.

[54] P. Hohenberg and W. Kohn. Inhomogeneous Electron Gas. *Physical Review*, 136(3B):B864, 11 1964.

[55] W. Kohn and L. J. Sham. Self-Consistent Equations Including Exchange and Correlation Effects. *Physical Review*, 140(4A):A1133, 11 1965.

[56] Carsten A. Ullrich. Time-dependent density-functional theory: Concepts and applications. *Time-Dependent Density-Functional Theory*, 12 2011.

[57] J. Schirmer. Review of the foundations of time-dependent density-functional theory (tddft). *Physical Chemistry Chemical Physics*, 27:4992–5005, 3 2025.

[58] Erich Runge and E. K.U. Gross. Density-functional theory for time-dependent systems. *Physical Review Letters*, 52:997, 3 1984.

[59] Robert van Leeuwen. Mapping from densities to potentials in time-dependent density-functional theory. *Physical Review Letters*, 82:3863, 5 1999.

[60] Michael Kasha. Characterization of electronic transitions in complex molecules. *Discussions of the Faraday Society*, 9(0):14–19, 1 1950.

[61] Gilbert N. Lewis and M. Kasha. Phosphorescence and the Triplet State. *Journal of the American Chemical Society*, 66(12):2100–2116, 12 1944.

[62] Byung Hak Jhun, Dong Yeun Jeong, Sanghee Nah, Soo Young Park, and Youngmin You. Novel anti-Kasha fluorophores exhibiting dual emission with thermally activated delayed fluorescence through detouring triplet manifolds. *Journal of Materials Chemistry C*, 9(22):7083–7093, 6 2021.

[63] Milena Röhrs and Daniel Escudero. Multiple Anti-Kasha Emissions in Transition-Metal Complexes. *Journal of Physical Chemistry Letters*, 10(19):5798–5804, 10 2019.

[64] Nicholas J Turro, V Ramamurthy, and Juan C Scaiano. Quantum Yields for Emission. *Principles of Molecular Photochemistry: an Introduction*, pages 117, 225, 2009.

[65] George C. Schatz and Mark A. Ratner. *Quantum mechanics in chemistry*. Dover Publications, Mineola, New York, 2002.

[66] N. P. Gritsan, A. D. Gudmundsdóttir, D. Tigelaar, Z. Zhu, W. L. Karney, C. M. Hadad, and M. S. Platz. A laser flash photolysis and quantum chemical study of the fluorinated derivatives of singlet phenylnitrene. *Journal of the American Chemical Society*, 123(9):1951–1962, 3 2001.

[67] Richard A. Caldwell. Laser Flash Photolysis Studies of Intersystem Crossing in Biradicals and Alkene Triplets. *Kinetics and Spectroscopy of Carbenes and Biradicals*, pages 77–116, 1990.

[68] Bernard Valeur and Mário Nuno Berberan-Santos. *Molecular Fluorescence: Principles and Applications, Second Edition*. Wiley-VCH GmbH, Weinheim, 2 edition, 5 2012.

[69] José Geraldo M. Castro Júnior and Willian R. Rocha. Theoretical investigation of [Ru(bpy)2(HAT)]2+ (HAT = 1,4,5,8,9,12-hexaazatriphenylene; bpy = 2,2-bipyridine): Photophysics and reactions in excited state. *Spectrochimica Acta Part A: Molecular and Biomolecular Spectroscopy*, 270:120817, 4 2022.

[70] Mariana Yoshinaga and Willian R. Rocha. Theoretical Investigation of the 4,5-Dibromorodamine Methyl Ester (TH9402) Photosensitizer Used in Photodynamic Therapy: Photophysics, Reactions in the Excited State, and Interactions with DNA. *Journal of Physical Chemistry B*, 125(31):8932–8943, 8 2021.

[71] Jörg Tatchen, Natalie Gilka, and Christel M. Marian. Intersystem crossing driven by vibronic spin–orbit coupling: a case study on psoralen. *Physical Chemistry Chemical Physics*, 9(38):5209–5221, 9 2007.

[72] Christel M. Marian, Jelena Föller, Martin Kleinschmidt, and Mihajlo Etinski. *Intersystem Crossing Processes in TADF Emitters*. John Wiley & Sons, Ltd, 7 2018.

[73] Katsuyuki Shizu and Hironori Kaji. Theoretical Determination of Rate Constants from Excited States: Application to Benzophenone. *Journal of Physical Chemistry A*, 125(40):9000–9010, 10 2021.

[74] Tohru Nakajima and Shigeki Kato. An ab initio study of the internal conversion rate from the first singlet excited state to the ground state in formaldehyde. *The Journal of Chemical Physics*, 105(14):5927, 8 1996.

[75] Ken Miyazaki and Nandini Ananth. Singularity-free internal conversion golden-rule rate with application to correlated triplet pair recombination in bipentacenes. *The Journal of Chemical Physics*, 156(4):044111, 1 2022.

[76] Lei Shi, Xiaoyu Xie, and Alessandro Troisi. Rapid calculation of internal conversion and intersystem crossing rate for organic materials discovery. *The Journal of Chemical Physics*, 157(13):134106, 10 2022.

[77] Zhou Lin, Alexander W. Kohn, and Troy Van Voorhis. Toward Prediction of Nonradiative Decay Pathways in Organic Compounds II: Two Internal Conversion Channels in BODIPYs. *The Journal of Physical Chemistry C*, 124(7):3925–3938, 2 2020.

[78] Alexander W. Kohn, Zhou Lin, and Troy Van Voorhis. Toward Prediction of Nonradiative Decay Pathways in Organic Compounds I: The Case of Naphthalene Quantum Yields. *Journal of Physical Chemistry C*, 123(25):15394–15402, 6 2019.

[79] Maria Fumanal, Felix Plasser, Sebastian Mai, Chantal Daniel, and Etienne Gindensperger. Interstate vibronic coupling constants between electronic excited states for complex molecules. *The Journal of Chemical Physics*, 148(12):124119, 3 2018.

[80] J. Patrick Zobel, Thomas Knoll, and Leticia González. Ultrafast and long-time excited state kinetics of an NIR-emissive vanadium(III) complex II. Elucidating triplet-to-singlet excited-state dynamics. *Chemical Science*, 12(32):10791–10801, 8 2021.

[81] Jens Ulstrup and Joshua Jortner. The effect of intramolecular quantum modes on free energy relationships for electron transfer reactions. *The Journal of Chemical Physics*, 63(10):4358–4368, 9 1975.

[82] R. A. Marcus. On the theory of oxidation-reduction reactions involving electron transfer. I. *The Journal of Chemical Physics*, 24(5):966–978, 1956.

[83] R. A. Marcus. Nonadiabatic processes involving quantum-like and classical-like coordinates with applications to nonadiabatic electron transfers. *The Journal of Chemical Physics*, 81(10):4494, 6 1984.

[84] Rudolph A. Marcus. Electron transfer reactions in chemistry. Theory and experiment. *Reviews of Modern Physics*, 65(3):599, 7 1993.

[85] R. A. Marcus. Electrostatic Free Energy and Other Properties of States Having Nonequilibrium Polarization. I. *The Journal of Chemical Physics*, 24(5):979, 12 2004.

[86] Jean Luc Brédas, David Beljonne, Veaceslav Coropceanu, and Jérŏme Cornil. Charge-transfer and energy-transfer processes in π-conjugated oligomers and polymers: A molecular picture. *Chemical Reviews*, 104(11):4971–5003, 11 2004.

[87] Sandy Veríssimo Morais Quintão, Aline de Souza Bozzi, and Willian Ricardo Rocha. Exploring the photophysics and excited state reactivity of [ru(4,4-btfmb)2 (l)]2+ complexes (l = bpy, phen, tap) as photodynamic therapy agents: a theoretical investigation. *Inorganic Chemistry Frontiers*, 2025.

[88] Subhajyoti Chaudhuri, Svante Hedstro, Dalvin D Mendezmendez-Hernandezhernandez, Heidi P Hendrickson, Kenneth A Jung, Junming Ho, and Victor S Batista. Electron Transfer Assisted by Vibronic Coupling from Multiple Modes. *J. Chem. Theory Comput*, 13:38, 2017.

[89] Claudia Turró, Jeffrey M. Zaleski, Yanna M. Karabatsos, and Daniel G. Nocera. Bimolecular electron transfer in the Marcus inverted region. *Journal of the American Chemical Society*, 118(25):6060–6067, 6 1996.

[90] Vincenzo. Balzani, Paola. Ceroni, and Alberto. Juris. Photochemistry and photophysics : concepts, research, applications. page 472, 2014.

[91] Paul Adrien Maurice Dirac. The quantum theory of the emission and absorption of radiation. *Proceedings of the Royal Society of London. Series A, Containing Papers of a Mathematical and Physical Character*, 114(767):243–265, 3 1927.

[92] Kun Huang. Lattice relaxation and multiphonon transitions. *Contemporary Physics*, 22(6):599–612, 1981.

[93] J. R. Reimers. A practical method for the use of curvilinear coordinates in calculations of normal-mode-projected displacements and Duschinsky rotation matrices for large molecules. *The Journal of Chemical Physics*, 115(20):9103, 11 2001.

[94] Rocco P. Fornari, Juan Aragó, and Alessandro Troisi. A very general rate expression for charge hopping in semiconducting polymers. *The Journal of Chemical Physics*, 142(18):184105, 5 2015.

[95] Aritra Das, Nareshbabu Kamatham, A. Mohan Raj, Pratik Sen, and V. Ramamurthy. Marcus Relationship Maintained during Ultrafast Electron Transfer across a Supramolecular Capsular Wall. *Journal of Physical Chemistry A*, 124(26):5297–5305, 7 2020.

[96] J. W. Hershberger, R. J. Klingler, and J. K. Kochi. Electron-Transfer Catalysis. Radical Chain Mechanism for the Ligand Substitution of Metal Carbonyls. *Journal of the American Chemical Society*, 104(11):3034–3043, 1982.

[97] A. R. Holzwarth, M. G. Müller, M. Reus, M. Nowaczyk, J. Sander, and M. Rögner. Kinetics and mechanism of electron transfer in intact photosystem II and in the isolated reaction center: Pheophytin is the primary electron acceptor. *Proceedings of the National Academy of Sciences of the United States of America*, 103(18):6895–6900, 5 2006.

[98] Artur Osyczka, Christopher C. Moser, Fevzl Daldal, and P. Lesile Dutton. Reversible redox energy coupling in electron transfer chains. *Nature 2004 427:6975*, 427(6975):607–612, 2 2004.

[99] G. L. Closs, L. T. Calcaterra, N. J. Green, K. W. Penfield, and J. R. Miller. Distance, stereoelectronic effects, and the marcus inverted region in intramolecular electron transfer in organic radical anions. *Journal of Physical Chemistry*, 90(16):3673–3683, 1986.

[100] J. R. Miller. Intramolecular Long-Distance Electron Transfer in Radical Anions. The Effects of Free Energy and Solvent on the Reaction Rates1. *Journal of the American Chemical Society*, 106(10):3047–3049, 1984.

[101] A. Burquel, V. Lemaur, D. Beljonne, R. Lazzaroni, and J. Cornil. Pathways for photoinduced charge separation and recombination at donor-acceptor heterojunctions: The case of oligophenylenevinylene-perylene bisimide complexes. *Journal of Physical Chemistry A*, 110(10):3447–3453, 3 2006.

[102] Yun Geng, Jianping Wang, Shuixing Wu, Haibin Li, Fei Yu, Guochun Yang, Hongze Gao, and Zhongmin Su. Theoretical discussions on electron transport properties of perylene bisimide derivatives with different molecular packings and intermolecular interactions. *Journal of Materials Chemistry*, 21(1):134–143, 12 2010.

[103] Eugenio Di Donato, Rocco P. Fornari, Simone Di Motta, Yan Li, Zhaohui Wang, and Fabrizia Negri. N-type charge transport and mobility of fluorinated perylene bisimide semiconductors. *Journal of Physical Chemistry B*, 114(16):5327–5334, 4 2010.

[104] A. Beckett and G. Porter. Primary photochemical processes in aromatic molecules. Part 9.—Photochemistry of benzophenone in solution. *Transactions of the Faraday Society*, 59(0):2038–2050, 1 1963.

[105] Gregory D. Gillispie and E. C. Lim. Further results on the triplet-triplet fluorescence of anthracenes. *Chemical Physics Letters*, 63(2):355–359, 5 1979.

[106] R. R. Valiev, V. N. Cherepanov, G. V. Baryshnikov, and D. Sundholm. First-principles method for calculating the rate constants of internal-conversion and intersystem-crossing transitions. *Physical Chemistry Chemical Physics*, 20(9):6121–6133, 2 2018.

[107] Kengo Suzuki, Attila Demeter, Wolfgang Kühnle, Erich Tauer, Klaas A. Zachariasse, Seiji Tobita, and Haruo Shizuka. Internal conversion in 4-substituted 1-naphthylamines. Influence of the electron donor/acceptor substituent character. *Physical Chemistry Chemical Physics*, 2(5):981–991, 1 2000.

[108] Hai Sun and Morton Z. Hoffman. Photophysics of Ru(II)-diimine complexes in H2O-CH3CN mixed solvents. *Journal of Physical Chemistry*, 97(46):11956–11959, 1993.

[109] Frank Neese. The ORCA program system. *Wiley Interdisciplinary Reviews: Computational Molecular Science*, 2(1):73–78, 1 2012.

[110] Frank Neese. Software update: The ORCA program system—Version 5.0. *Wiley Interdisciplinary Reviews: Computational Molecular Science*, 12(5):e1606, 9 2022.

[111] Chengteh Lee, Weitao Yang, and Robert G. Parr. Development of the Colle-Salvetti correlation-energy formula into a functional of the electron density. *Physical Review B*, 37(2):785–789, 1988.

[112] Florian Weigend and Reinhart Ahlrichs. Balanced basis sets of split valence, triple zeta valence and quadruple zeta valence quality for H to Rn: Design and assessment of accuracy. *Physical Chemistry Chemical Physics*, 7(18):3297–3305, 8 2005.

[113] Stefan Grimme, Jens Antony, Stephan Ehrlich, and Helge Krieg. A consistent and accurate ab initio parametrization of density functional dispersion correction (DFT-D) for the 94 elements H-Pu. *Journal of Chemical Physics*, 132(15):154104, 4 2010.

[114] Stefan Grimme, Stephan Ehrlich, and Lars Goerigk. Effect of the damping function in dispersion corrected density functional theory. *Journal of Computational Chemistry*, 32(7):1456–1465, 5 2011.

[115] Frank Neese. An Improvement of the Resolution of the Identity Approximation for the Formation of the Coulomb Matrix. *Journal of Computational Chemistry*, 24(14):1740–1747, 11 2003.

[116] Florian Weigend. Accurate Coulomb-fitting basis sets for H to Rn. *Physical Chemistry Chemical Physics*, 8(9):1057–1065, 2 2006.

[117] So Hirata and Martin Head-Gordon. Time-dependent density functional theory within the Tamm–Dancoff approximation. *Chemical Physics Letters*, 314(3-4):291–299, 12 1999.

[118] Maurizio Cossi, Nadia Rega, Giovanni Scalmani, and Vincenzo Barone. Energies, structures, and electronic properties of molecules in solution with the C-PCM solvation model. *Journal of Computational Chemistry*, 24(6):669–681, 4 2003.

[119] Roberto Cammi, Benedetta Mennucci, and Jacopo Tomasi. Fast Evaluation of Geometries and Properties of Excited Molecules in Solution: A Tamm-Dancoff Model with Application to 4-Dimethylaminobenzonitrile. *Journal of Physical Chemistry A*, 104(23):5631–5637, 6 2000.

[120] G. W. Robinson and R. P. Frosch. Electronic Excitation Transfer and Relaxation. *The Journal of Chemical Physics*, 38(5):1187, 7 2004.

[121] Qin Wu and Troy Van Voorhis. Direct calculation of electron transfer parameters through constrained density functional theory. *Journal of Physical Chemistry A*, 110(29):9212–9218, 7 2006.

[122] Omar López-Estrada, Humberto G. Laguna, Cihuapilli Barrueta-Flores, and Carlos Amador-Bedolla. Reassessment of the Four-Point Approach to the Electron-Transfer Marcus-Hush Theory. *ACS Omega*, 3(2):2130–2140, 2 2018.

[123] V Lawetz, G Orlandi, W Siebrand, Siebrand, and W. Theory of Intersystem Crossing in Aromatic Hydrocarbons. *The Journal of Chemical Physics*, 56(8):4058, 9 2003.

[124] Yihan Shao, Martin Head-Gordon, and Anna I. Krylov. The spin–flip approach within time-dependent density functional theory: Theory and applications to diradicals. *The Journal of Chemical Physics*, 118(11):4807, 2 2003.

[125] Satoshi Maeda, Koichi Ohno, and Keiji Morokuma. Updated branching plane for finding conical intersections without coupling derivative vectors. *Journal of Chemical Theory and Computation*, 6(5):1538–1545, 5 2010.

[126] Robert Send and Filipp Furche. First-order nonadiabatic couplings from time-dependent hybrid density functional response theory: Consistent formalism, implementation, and performance. *The Journal of Chemical Physics*, 132(4):044107, 1 2010.

[127] P. Jeffrey Hay and Willard R. Wadt. Ab initio effective core potentials for molecular calculations. Potentials for K to Au including the outermost core orbitals. *The Journal of Chemical Physics*, 82(1):299, 8 1985.

[128] M J Frisch, G W Trucks, H B Schlegel, G E Scuseria, M A Robb, J R Cheeseman, G Scalmani, V Barone, G A Petersson, H Nakatsuji, X Li, M Caricato, A V Marenich, J Bloino, B G Janesko, R Gomperts, B Mennucci, H P Hratchian, J V Ortiz, A F Izmaylov, J L Sonnenberg, D Williams-Young, F Ding, F Lipparini, F Egidi, J Goings, B Peng, A Petrone, T Henderson, D Ranasinghe, V G Zakrzewski, J Gao, N Rega, G Zheng, W Liang, M Hada, M Ehara, K Toyota, R Fukuda, J Hasegawa, M Ishida, T Nakajima, Y Honda, O Kitao, H Nakai, T Vreven, K Throssell, J A Montgomery Jr., J E Peralta, F Ogliaro, M J Bearpark, J J Heyd, E N Brothers, K N Kudin, V N Staroverov, T A Keith, R Kobayashi, J Normand, K Raghavachari, A P Rendell, J C Burant, S S Iyengar, J Tomasi, M Cossi, J M Millam, M Klene, C Adamo, R Cammi, J W Ochterski, R L Martin, K Morokuma, O Farkas, J B Foresman, and D J Fox. Gaussian-09 Revision E.01, 2009.

[129] Alexander Humeniuk, Margarita Bužančić, Joscha Hoche, Javier Cerezo, Roland Mitrić, Fabrizio Santoro, and Vlasta Bonačić-Koutecký. Predicting fluorescence quantum yields for molecules in solution: A critical assessment of the harmonic approximation and the choice of the lineshape function. *The Journal of Chemical Physics*, 152(5):054107, 2 2020.

[130] Rashid R. Valiev, Victor N. Cherepanov, Rinat T. Nasibullin, Dage Sundholm, and Theo Kurten. Calculating rate constants for intersystem crossing and internal conversion in the Franck–Condon and Herzberg–Teller approximations. *Physical Chemistry Chemical Physics*, 21(34):18495–18500, 8 2019.

[131] R. R. Valiev, R. T. Nasibullin, V. N. Cherepanov, A. Kurtsevich, D. Sundholm, and T. Kurtén. Fast estimation of the internal conversion rate constant in photophysical applications. *Physical Chemistry Chemical Physics*, 23(11):6344–6348, 3 2021.

[132] N. Nijegorodov, V. Ramachandran, and D. P. Winkoun. The dependence of the absorption and fluorescence parameters, the intersystem crossing and internal conversion rate constants on the number of rings in polyacene molecules. *Spectrochimica Acta - Part A: Molecular and Biomolecular Spectroscopy*, 53(11):1813–1824, 10 1997.

[133] Marco Marazzi, Sebastian Mai, Daniel Roca-Sanjuán, Mickaël G. Delcey, Roland Lindh, Leticia González, and Antonio Monari. Benzophenone Ultrafast Triplet Population: Revisiting the Kinetic Model by Surface-Hopping Dynamics. *Journal of Physical Chemistry Letters*, 7(4):622–626, 2 2016.

[134] N. G. Bryantseva, I. V. Sokolova, R. M. Gadirov, V. P. Khilya, and Ya L. Garazd. Luminescence characteristics of new substituted coumarins. *Journal of Applied Spectroscopy 2009 76:6*, 76(6):813–818, 1 2010.

[135] Jianxiong Zhao, Daniel Méndez-Sánchez, Rebecca Roddan, John M. Ward, and Helen C. Hailes. Norcoclaurine Synthase-Mediated Stereoselective Synthesis of 1,1'-Disubstituted, Spiro- And Bis-Tetrahydroisoquinoline Alkaloids. *ACS Catalysis*, 11(1):131–138, 1 2021.

[136] Fortuna Ponte, Daniele Belletto, Roberta Leonetti, Nico Sanna, Stefano Scoditti, Gloria Mazzone, and Emilia Sicilia. DFT Computational Analysis of the Mechanism of Action of Ru(II) Polypyridyl Complexes as Photoactivated Chemotherapy Agents: From Photoinduced Ligand Solvolysis to DNA Binding. *Inorganic Chemistry*, 63(43):20643–20653, 10 2024.

[137] Hiroyuki Takeda, Yu Monma, Haruki Sugiyama, Hidehiro Uekusa, and Osamu Ishitani. Development of Visible-Light Driven Cu(I) Complex Photosensitizers for Photocatalytic CO2 Reduction. *Frontiers in Chemistry*, 0(JUN):418, 2019.

[138] Tammie R. Nelson, Alexander J. White, Josiah A. Bjorgaard, Andrew E. Sifain, Yu Zhang, Benjamin Nebgen, Sebastian Fernandez-Alberti, Dmitry Mozyrsky,

Adrian E. Roitberg, and Sergei Tretiak. Non-adiabatic Excited-State Molecular Dynamics: Theory and Applications for Modeling Photophysics in Extended Molecular Materials. *Chemical Reviews*, 120(4):2215–2287, 2 2020.

[139] James P. Hall, Daniel Cook, Sara Ruiz Morte, Patrick McIntyre, Katrin Buchner, Hanna Beer, David J. Cardin, John A. Brazier, Graeme Winter, John M. Kelly, and Christine J. Cardin. X-ray crystal structure of rac-[Ru(phen)2dppz]2+ with d(ATGCAT)2 shows enantiomer orientations and water ordering. *Journal of the American Chemical Society*, 135(34):12652–12659, 8 2013.

[140] Marta Erminia Alberto, Jenny Pirillo, Nino Russo, and Carlo Adamo. Theoretical Exploration of Type I/Type II Dual Photoreactivity of Promising Ru(II) Dyads for PDT Approach. *Inorganic Chemistry*, 55(21):11185–11192, 11 2016.

[141] Shuang Li, Jian Zhao, Xinyi Wang, Gang Xu, Shaohua Gou, and Qiang Zhao. Design of a Tris-Heteroleptic Ru(II) Complex with Red-Light Excitation and Remarkably Improved Photobiological Activity. *Inorganic Chemistry*, 59(15):11193–11204, 8 2020.

[142] Yujie Sun, Lauren E. Joyce, Nicole M. Dickson, and Claudia Turro. Efficient DNA photocleavage by [Ru(bpy)2(dppn)]2+ with visible light. *Chemical Communications*, 46(14):2426–2428, 3 2010.

[143] Patricia Vicendo, Serge Mouysset, and Nicole Paillous. Comparative Study of Ru(bpz)32+Ru(bipy)32+and Ru(bpz)2CI2 as Photosensitizers of DNA Cleavage and Adduct Formation. *Photochemistry and Photobiology*, 65(4):647–655, 4 1997.

[144] Sofia Kajouj, Lionel Marcélis, Vincent Lemaur, David Beljonne, and Cécile Moucheron. Photochemistry of ruthenium(II) complexes based on 1,4,5,8-tetraazaphenanthrene and 2,2-bipyrazine: a comprehensive experimental and theoretical study. *Dalton Transactions*, 46(20):6623–6633, 5 2017.

[145] Hiwa K Saeed, Paul J Jarman, Stuart Archer, Sreejesh Sreedharan, Ibrahim Q Saeed, Luke K Mckenzie, J A ulia Weinstein, Niklaas J Buurma, Carl G W Smythe, Jim Thomas, A, H KSaeed, DrS Archer, L K Mckenzie, P J rof A Weinstein, J A Thomas, C G W Smythe, DrI QSaeed, and DrN JBuurma. Homo- and Heteroleptic Phototoxic Dinuclear Metallo-Intercalators Based on RuII(dppn) Intercalating Moieties: Synthesis, Optical, and Biological Studies. *Angewandte Chemie International Edition*, 56(41):12628–12633, 10 2017.

[146] Etienne Gicquel, Jean Pierre Souchard, Fay Magnusson, Jad Chemaly, Patrick Calsou, and Patricia Vicendo. Role of intercalation and redox potential in DNA photosensitization by ruthenium(II) polypyridyl complexes: assessment using DNA repair protein tests. *Photochemical & Photobiological Sciences*, 12(8):1517–1526, 8 2013.

[147] R. J. Crutchley and A. B.P. Lever. Ruthenium(II) Tris(bipyrazyl) Dication-A New Photocatalyst. *Journal of the American Chemical Society*, 102(23):7128–7129, 1980.

[148] Robert C. Hilborn. Einstein coefficients, cross sections, f values, dipole moments, and all that. *American Journal of Physics*, 50(11):982–986, 11 1982.

[149] Karin Schmidt, Sergio Brovelli, Veaceslav Coropceanu, David Beljonne, Jérôme Cornil, Cristina Bazzini, Tullio Caronna, Riccardo Tubino, Francesco Meinardi, Zhigang Shuai, and Jean Luc Brédas. Intersystem crossing processes in nonplanar aromatic heterocyclic molecules. *Journal of Physical Chemistry A*, 111(42):10490–10499, 10 2007.

[150] Chengteh Lee, Weitao Yang, and Robert G. Parr. Development of the Colle-Salvetti correlation-energy formula into a functional of the electron density. *Physical Review B*, 37(2):785, 1 1988.

[151] Frank Neese and John Wiley. The ORCA program system. *Wiley Interdisciplinary Reviews: Computational Molecular Science*, 2(1):73–78, 1 2012.

[152] Stefan Grimme, Jens Antony, Stephan Ehrlich, and Helge Krieg. A consistent and accurate ab initio parametrization of density functional dispersion correction (DFT-D) for the 94 elements H-Pu. *The Journal of Chemical Physics*, 132(15):154104, 4 2010.

[153] Stefan Grimme, Stephan Ehrlich, and Lars Goerigk. Effect of the damping function in dispersion corrected density functional theory. *Journal of Computational Chemistry*, 32(7):1456–1465, 5 2011.

[154] Frank Neese. An improvement of the resolution of the identity approximation for the formation of the Coulomb matrix. *Journal of Computational Chemistry*, 24(14):1740–1747, 11 2003.

[155] E. Van Lenthe, E. J. Baerends, and J. G. Snijders. Relativistic regular two-component Hamiltonians. *The Journal of Chemical Physics*, 99(6):4597–4610, 9 1993.

[156] E. Van Lenthe, E. J. Baerends, and J. G. Snijders. Relativistic total energy using regular approximations. *The Journal of Chemical Physics*, 101(11):9783–9792, 12 1994.

[157] K. Suzuki and R. Okamoto. Perturbation Theory for Quasidegenerate System in Quantum Mechanics. *Progress of Theoretical Physics*, 72(3):534–548, 9 1984.

[158] Henry Eyring. The Activated Complex in Chemical Reactions. *The Journal of Chemical Physics*, 3(2):107–115, 2 1935.

[159] David Hernández-Castillo, Roland E. P. Nau, Marie-Ann Schmid, Stefanie Tschierlei, Sven Rau, and Leticia González. Multiple triplet metal-centered jahn-teller isomers determine temperature-dependent luminescence lifetimes in [ru(bpy)3]2+. *Angewandte Chemie International Edition*, 62(48):e202308803, 2023.

[160] F. Plasser. TheoDORE: A toolbox for a detailed and automated analysis of electronic excited state computations. *The Journal of Chemical Physics*, 152(8), 2 2020.

[161] David Hernández-Castillo, Isabel Eder, and Leticia González. Guidelines to calculate non-radiative deactivation mechanisms of ruthenium tris(bipyridine) derivatives. *Coordination Chemistry Reviews*, 510:215819, 2024.

[162] J. Van Houten and R. J. Watts. Temperature dependence of the photophysical and photochemical properties of the tris(2,2'-bipyridyl)ruthenium(II) ion in aqueous solution. *Journal of the American Chemical Society*, 98(16):4853–4858, 8 1976.

[163] Demian van Straten, Vida Mashayekhi, Henriette S. de Bruijn, Sabrina Oliveira, and Dominic J. Robinson. Oncologic Photodynamic Therapy: Basic Principles, Current Clinical Status and Future Directions. *Cancers*, 9(2), 2 2017.

[164] Keith J. Laidler and M. Christine King. The development of transition-state theory. *Journal of Physical Chemistry*, 87(15):2657–2664, 1983.

[165] A. Laubereau and W. Kaiser. Vibrational dynamics of liquids and solids investigated by picosecond light pulses. *Reviews of Modern Physics*, 50(3):607–665, 1978.

[166] Andrew J. Atkins and Leticia González. Trajectory Surface-Hopping Dynamics Including Intersystem Crossing in $[Ru(bpy)_3]^{2+}$. *The Journal of Physical Chemistry Letters*, 8(16):3840–3845, August 2017.

[167] Jonathan P. Celli, Bryan Q. Spring, Imran Rizvi, Conor L. Evans, Kimberley S. Samkoe, Sarika Verma, Brian W. Pogue, and Tayyaba Hasan. Imaging and photo-

dynamic therapy: Mechanisms, monitoring, and optimization. *Chemical Reviews*, 110(5):2795–2838, 5 2010.

[168] Dennis E.J.G.J. Dolmans, Dai Fukumura, and Rakesh K. Jain. Photodynamic therapy for cancer. *Nature Reviews Cancer 2003 3:5*, 3(5):380–387, 5 2003.

[169] Isabel O.L. Bacellar, Tayana M. Tsubone, Christiane Pavani, and Mauricio S. Baptista. Photodynamic Efficiency: From Molecular Photochemistry to Cell Death. *International Journal of Molecular Sciences 2015, Vol. 16, Pages 20523-20559*, 16(9):20523–20559, 8 2015.

[170] Thanh Chung Pham, Van Nghia Nguyen, Yeonghwan Choi, Songyi Lee, and Juyoung Yoon. Recent Strategies to Develop Innovative Photosensitizers for Enhanced Photodynamic Therapy. *Chemical Reviews*, 121(21):13454–13619, 11 2021.

[171] Fortuna Ponte, Stefano Scoditti, Pierraffaele Barretta, and Gloria Mazzone. Computational Assessment of a Dual-Action Ru(II)-Based Complex: Photosensitizer in Photodynamic Therapy and Intercalating Agent for Inducing DNA Damage. *Inorganic Chemistry*, 5 2023.

[172] Yanhong Nie, Zhongming Dai, Fozia, Guangyao Zhao, Jianrong Jiang, Xu Xu, Ming Ying, Yu Wang, Zhangli Hu, and Hong Xu. Comparative Studies on DNA-Binding Mechanisms between Enantiomers of a Polypyridyl Ruthenium(II) Complex. *Journal of Physical Chemistry B*, 126(26):4787–4798, 7 2022.

[173] Stefano Scoditti, Eslam Dabbish, Nino Russo, Gloria Mazzone, and Emilia Sicilia. Anticancer Activity, DNA Binding, and Photodynamic Properties of a N^C^N-Coordinated Pt(II) Complex. *Inorganic Chemistry*, 60(14):10350–10360, 7 2021.

[174] Héctor J. Lozano, Natalia Busto, Gustavo Espino, Arancha Carbayo, José M. Leal, James A. Platts, and Begoña García. Interstrand DNA covalent binding of two dinuclear Ru(II) complexes. Influence of the extra ring of the bridging ligand on the DNA interaction and cytotoxic activity. *Dalton Transactions*, 46(11):3611–3622, 3 2017.

[175] Patrizia Agostinis, Kristian Berg, Keith A. Cengel, Thomas H. Foster, Albert W. Girotti, Sandra O. Gollnick, Stephen M. Hahn, Michael R. Hamblin, Asta Juzeniene, David Kessel, Mladen Korbelik, Johan Moan, Pawel Mroz, Dominika Nowis, Jacques Piette, Brian C. Wilson, and Jakub Golab. Photodynamic therapy of cancer: An update. *CA: A Cancer Journal for Clinicians*, 61(4):250–281, 7 2011.

[176] Ron R. Allison and Claudio H. Sibata. Oncologic photodynamic therapy photosensitizers: A clinical review. *Photodiagnosis and Photodynamic Therapy*, 7(2):61–75, 6 2010.

[177] Jiayuan Kou, Dou Dou, Liming Yang, Jiayuan Kou, Dou Dou, and Liming Yang. Porphyrin photosensitizers in photodynamic therapy and its applications. *Oncotarget*, 8(46):81591–81603, 8 2017.

[178] Susan Monro, Katsuya L. Colón, Huimin Yin, John Roque, Prathyusha Konda, Shashi Gujar, Randolph P. Thummel, Lothar Lilge, Colin G. Cameron, and Sherri A. McFarland. Transition Metal Complexes and Photodynamic Therapy from a Tumor-Centered Approach: Challenges, Opportunities, and Highlights from the Development of TLD1433. *Chemical Reviews*, 119(2):797–828, 1 2019.

[179] Kathryn L. Haas and Katherine J. Franz. Application of metal coordination chemistry to explore and manipulate cell biology. *Chemical Reviews*, 109(10):4921–4960, 10 2009.

[180] Sreekanth Thota, Daniel A. Rodrigues, Debbie C. Crans, and Eliezer J. Barreiro. Ru(II) Compounds: Next-Generation Anticancer Metallotherapeutics? *Journal of Medicinal Chemistry*, 61(14):5805–5821, 7 2018.

[181] Cristina Mari, Vanessa Pierroz, Stefano Ferrari, and Gilles Gasser. Combination of Ru(II) complexes and light: new frontiers in cancer therapy. *Chemical Science*, 6(5):2660–2686, 4 2015.

[182] Yongjie Chen, Lijuan Bai, Pu Zhang, Hua Zhao, and Qianxiong Zhou. The Development of Ru(II)-Based Photoactivated Chemotherapy Agents. *Molecules 2021, Vol. 26, Page 5679*, 26(18):5679, 9 2021.

[183] Yanping Wu, Shumeng Li, Yuncong Chen, Weijiang He, and Zijian Guo. Recent advances in noble metal complex based photodynamic therapy. *Chemical Science*, 13(18):5085–5106, 5 2022.

[184] Jamie Fong, Kamola Kasimova, Yaxal Arenas, Pavel Kaspler, Savo Lazic, Arkady Mandel, and Lothar Lilge. A novel class of ruthenium-based photosensitizers effectively kills in vitro cancer cells and in vivo tumors. *Photochemical and Photobiological Sciences*, 14(11):2014–2023, 11 2015.

[185] Maria Letizia Di Pietro, Giuseppina La Ganga, Francesco Nastasi, and Fausto Puntoriero. Ru(II)-Dppz Derivatives and Their Interactions with DNA: Thirty Years and Counting. *Applied Sciences 2021, Vol. 11, Page 3038*, 11(7):3038, 3 2021.

[186] Aoibhín A. Cullen, Conor Long, and Mary T. Pryce. Explaining the role of water in the "light-switch" probe for DNA intercalation: Modelling water loss from [Ru(phen)2(dppz)]2+•2H2O using DFT and TD-DFT methods. *Journal of Photochemistry and Photobiology A: Chemistry*, 410:113169, 4 2021.

[187] Hui Wang, Xiaohua Liu, and Lifeng Tan. Binding properties of a molecular "light switch" ruthenium(II) polypyridyl complex toward double- and triple-helical forms of RNA. *International Journal of Biological Macromolecules*, 242:124710, 7 2023.

[188] Fuchao Jia, Shuo Wang, Yan Man, Parveen Kumar, and Bo Liu. Recent Developments in the Interactions of Classic Intercalated Ruthenium Compounds: [Ru(bpy)2dppz]2+ and [Ru(phen)2dppz]2+ with a DNA Molecule. *Molecules 2019, Vol. 24, Page 769*, 24(4):769, 2 2019.

[189] Nathan P. Cook, Veronica Torres, Disha Jain, and Angel A. Martí. Sensing amyloid-β aggregation using luminescent dipyridophenazine ruthenium(II) complexes. *Journal of the American Chemical Society*, 133(29):11121–11123, 7 2011.

[190] Hang Song, Jens T. Kaiser, and Jacqueline K. Barton. Crystal structure of Δ-[Ru(bpy)2dppz]2+ bound to mismatched DNA reveals side-by-side metalloinsertion and intercalation. *Nature Chemistry 2012 4:8*, 4(8):615–620, 6 2012.

[191] Jessica D. Knoll and Claudia Turro. Control and utilization of ruthenium and rhodium metal complex excited states for photoactivated cancer therapy. *Coordination Chemistry Reviews*, 282-283:110–126, 1 2015.

[192] Guanying Li, Lingli Sun, Liangnian Ji, and Hui Chao. Ruthenium(II) complexes with dppz: from molecular photoswitch to biological applications. *Dalton Transactions*, 45(34):13261–13276, 8 2016.

[193] Bjørn C. Poulsen, Sandra Estalayo-Adrián, Salvador Blasco, Sandra A. Bright, John M. Kelly, D. Clive Williams, and Thorfinnur Gunnlaugsson. Luminescent ruthenium polypyridyl complexes with extended 'dppz' like ligands as DNA targeting binders and cellular agents. *Dalton Transactions*, 45(45):18208–18220, 11 2016.

[194] Marie Flamme, Emma Clarke, Gilles Gasser, and Marcel Hollenstein. Applications of Ruthenium Complexes Covalently Linked to Nucleic Acid Derivatives. *Molecules 2018, Vol. 23, Page 1515*, 23(7):1515, 6 2018.

[195] Xin Wang, Fu Quan Bai, Yingtao Liu, Yu Wang, Hong Xing Zhang, and Zhenyang Lin. A Computational Way to Achieve More Effective Candidates for Photodynamic Therapy. *Journal of Chemical Information and Modeling*, 57(5):1089–1100, 5 2017.

[196] Bruno Peña, Nicholas A. Leed, Kim R. Dunbar, and Claudia Turro. Excited state dynamics of two new Ru(II) cyclometallated dyes: Relation to cells for solar energy conversion and comparison to conventional systems. *Journal of Physical Chemistry C*, 116(42):22186–22195, 10 2012.

[197] R. A. Marcus. Electrostatic Free Energy and Other Properties of States Having Nonequilibrium Polarization. I. *The Journal of Chemical Physics*, 24(5):979, 12 2004.

[198] Th Förster. Zwischenmolekulare energiewanderung und fluoreszenz. *Annalen der Physik*, 437:55–75, 1 1948.

[199] Igor Medintz and Niko Hildebrandt. Fret - förster resonance energy transfer: From theory to applications. *FRET - Förster Resonance Energy Transfer: From Theory to Applications*, pages 1–791, 10 2013.

[200] D L Dexter and L F H Bovey. A theory of sensitized luminescence in solids. *The Journal of Chemical Physics*, 21:836–850, 5 1953.

[201] Spiros S. Skourtis, Chaoren Liu, Panayiotis Antoniou, Aaron M. Virshup, and David N. Beratan. Dexter energy transfer pathways. *Proceedings of the National Academy of Sciences of the United States of America*, 113:8115–8120, 7 2016.

[202] Shuming Bai, Peng Zhang, and David N. Beratan. Predicting dexter energy transfer interactions from molecular orbital overlaps. *Journal of Physical Chemistry C*, 124:18956–18960, 9 2020.

[203] Shane R. Yost, Jiye Lee, Mark W.B. Wilson, Tony Wu, David P. McMahon, Rebecca R. Parkhurst, Nicholas J. Thompson, Daniel N. Congreve, Akshay Rao, Kerr Johnson, Matthew Y. Sfeir, Moungi G. Bawendi, Timothy M. Swager, Richard H. Friend, Marc A. Baldo, and Troy Van Voorhis. A transferable model for singlet-fission kinetics. *Nature Chemistry 2014 6:6*, 6:492–497, 5 2014.

[204] Sina Yeganeh and Troy Van Voorhis. Triplet excitation energy transfer with constrained density functional theory. *Journal of Physical Chemistry C*, 114:20756–20763, 12 2010.

[205] Troy Van Voorhis, Tim Kowalczyk, Benjamin Kaduk, Lee Ping Wang, Chiao Lun Cheng, and Qin Wu. The diabatic picture of electron transfer, reaction barriers, and molecular dynamics. *Annual Review of Physical Chemistry*, 61:149–170, 5 2010.

[206] Shuming Bai and Mario Barbatti. Divide-to-conquer: A kinetic model for singlet oxygen photosensitization. *Journal of Chemical Theory and Computation*, 13:5528–5538, 11 2017.

[207] Qin Wu and Troy Van Voorhis. Direct optimization method to study constrained systems within density-functional theory. *Physical Review A - Atomic, Molecular, and Optical Physics*, 72:024502, 8 2005.

[208] A D Becke and Appl Phys Lett. A multicenter numerical integration scheme for polyatomic molecules. *The Journal of Chemical Physics*, 88:2547–2553, 2 1988.

[209] Matthijs L.A. Hakkennes, Francesco Buda, and Sylvestre Bonnet. MetalDock: An Open Access Docking Tool for Easy and Reproducible Docking of Metal Complexes. *Journal of Chemical Information and Modeling*, 63(24):7816–7825, 12 2023.

[210] Jorge González-García, Sanja Tomić, Alberto Lopera, Lluís Guijarro, Ivo Piantanida, and Enrique García-España. Aryl-bis-(scorpiand)-aza receptors differentiate between nucleotide monophosphates by a combination of aromatic, hydrogen bond and electrostatic interactions. *Organic & Biomolecular Chemistry*, 13(6):1732–1740, 1 2015.

[211] Marta Erminia Alberto, Jenny Pirillo, Nino Russo, and Carlo Adamo. Theoretical Exploration of Type I/Type II Dual Photoreactivity of Promising Ru(II) Dyads for PDT Approach. *Inorganic Chemistry*, 55(21):11185–11192, 11 2016.

[212] Xue Wei, Wei Bo Cui, Gui Ya Qin, Xiu E. Zhang, Feng Yi Sun, Hui Li, Jing Fu Guo, and Ai Min Ren. Theoretical Investigation of Ru(II) Complexes with Long Lifetime and a Large Two-Photon Absorption Cross-Section in Photodynamic Therapy. *Journal of Medicinal Chemistry*, 66(6):4167–4178, 3 2023.

[213] Claude Schweitzer and Reinhard Schmidt. Physical mechanisms of generation and deactivation of singlet oxygen. *Chemical Reviews*, 103(5):1685–1757, 5 2003.

[214] Grazyna Stochel, Małgorzata Brindell, Wojciech Macyk, Zofia Stasicka, and Konrad Szaciłowski. Bioinorganic Photochemistry. *Bioinorganic Photochemistry*, pages 1–382, 4 2009.

[215] Shuming Bai and Mario Barbatti. Spatial factors for triplet fusion reaction of singlet oxygen photosensitization. *Journal of Physical Chemistry Letters*, 8:5456–5460, 11 2017.

Appendix A

Productions

From this thesis

1. **Bozzi, A. S.**, & Rocha, W. R. (2023). Calculation of excited state internal conversion rate constant using the one-effective mode Marcus-Jortner-Levich theory. *Journal of Chemical Theory and Computation*, 19(8), 2316–2326.

2. **Bozzi, A. S.**, & Rocha, W. R. (2024). Photophysics and Excited State Reactions of [Ru(Bpy)2 dppn]2+: A Computational Study. *Chemistry – An Asian Journal*, 19(22), e202400605.

3. **Bozzi, A. S.**, Sebastião, R. C. O., & Rocha, W. R. (2025). Understanding the excited state decay mechanism of complex systems: A general first-order kinetic model. *Physical Chemistry Chemical Physics*, 27(18), 9806–9816.

From collaborations

1. Salvatti, B. A., Chagas, M. A., Fernandes, P. O., Ladeira, Y. F. X., **Bozzi, A. S.**, Valadares, V. S., Valente, A. P., De Miranda, A. S., Rocha, W. R., Maltarollo, V. G., & Moraes, A. H. (2024). Understanding the enzyme (s)-norcoclaurine synthase promiscuity to aldehydes and ketones. *Journal of Chemical Information and Modeling*, 64(11), 4462–4474.

2. Quintão, S. V. M., **Bozzi, A. S.**, & Rocha, W. R. (2025). Exploring the photophysics and excited state reactivity of $[Ru(4,4'\text{-}BTFMB)_2(L)]^{2+}$ complexes (L = bpy, phen, TAP) as photodynamic therapy agents: A theoretical investigation. *Inorganic Chemistry Frontiers*, 12(14), 4470-4479.

3. Carvalho, L. R.; **Bozzi, A. S.**; Faria, W. M. A.; Venturelli, L. G.; Esteves, T. D.; Duarte, S. S.; De Souza, R. R. M.; Castro, I. O.; Venturini Jr., E.; Sobral, M.

V.; Rocha, W. R. & Tavares, E. C. (2025). In(III) Complexes of Sulfonyldithiocarbimates as Selective Antineoplasic Agents Against Human Colorectal Adenocarcinoma. *Dalton Transactions*. https://doi.org/10.1039/D5DT00868A.

Appendix B

Supporting Information

B.1 Chapter 1

B.1.1 Cartesian Coordinates

All the Cartesian coordinates for the optimized geometries of S_0 and S_1 states and the conical intersection of all molecules are shown below.

Benzophenone

S_0

C -0.533463000 1.212660000 -0.446347000
C 0.108186000 2.440789000 -0.428266000
C 1.357397000 2.565193000 0.173862000
C 1.963317000 1.456406000 0.752408000
C 1.332038000 0.219682000 0.713077000
C 0.078602000 0.088247000 0.112189000
C 1.291913000 -2.625018000 -0.612221000
C 0.077185000 -2.493982000 0.063509000
C -0.500604000 -3.618889000 0.656514000
C 0.138308000 -4.847193000 0.598089000
C 1.348771000 -4.971235000 -0.078619000
C 1.919275000 -3.861857000 -0.691074000
C -0.674341000 -1.202884000 0.110622000
O -1.892583000 -1.202962000 0.146776000
H -1.514376000 1.101918000 -0.888337000
H -0.365005000 3.304987000 -0.876548000
H 1.854431000 3.526757000 0.195925000
H 2.927091000 1.554048000 1.235327000
H 1.802582000 -0.639510000 1.171010000
H 1.734291000 -1.765390000 -1.096618000
H -1.453218000 -3.508513000 1.156685000
H -0.307512000 -5.711862000 1.072733000
H 1.843161000 -5.932947000 -0.131736000
H 2.852253000 -3.959245000 -1.231160000

S_1

C -0.608142000 1.227944000 -0.278031000
C -0.030237000 2.484288000 -0.262431000
C 1.292605000 2.650356000 0.137879000
C 2.029977000 1.537176000 0.544362000
C 1.467541000 0.275678000 0.541015000
C 0.137326000 0.088854000 0.105250000
C 1.437602000 -2.682494000 -0.452120000
C 0.136577000 -2.494817000 0.062917000
C -0.584511000 -3.632370000 0.493228000
C -0.008932000 -4.889125000 0.445157000

C 1.287069000 -5.056223000 -0.034255000
C 1.998837000 -3.944231000 -0.486719000
C -0.497354000 -1.202431000 0.101137000
O -1.811791000 -1.204612000 0.135507000
H -1.628388000 1.106205000 -0.613623000
H -0.614397000 3.342579000 -0.569454000
H 1.742158000 3.634317000 0.145438000
H 3.050096000 1.660099000 0.885748000
H 2.034817000 -0.562879000 0.915337000
H 1.981102000 -1.844630000 -0.861600000
H -1.582456000 -3.509373000 0.889825000
H -0.573569000 -5.746608000 0.788750000
H 1.735166000 -6.040351000 -0.067068000
H 2.996604000 -4.068153000 -0.888447000

Conical Intersection

C -0.587478434 1.077238634 0.165580105
C -0.354072673 2.445249350 0.190224288
C 0.960767987 2.935768012 0.158182259
C 2.030572797 2.027178803 0.101400033
C 1.817719570 0.654262586 0.076448438
C 0.489408100 0.143561222 0.108175160
C 1.818986709 -3.060892034 -0.010721593
C 0.492367264 -2.548455503 0.043067876
C -0.587411482 -3.480079554 0.053683764
C -0.359738022 -4.848589950 0.013101860
C 0.953837164 -5.340976140 -0.039907936
C 2.026785829 -4.434320424 -0.050901393
C 0.135571652 -1.203200287 0.087736560
O -1.490420395 -1.211846442 0.136100480
H -1.639649744 0.745918434 0.192878407
H -1.198041068 3.138151015 0.234820456
H 1.147473653 4.011175350 0.177164360
H 3.056740440 2.403703524 0.075856029
H 2.663671835 -0.033033451 0.031611458
H 2.667324092 -2.375177256 -0.020207418
H -1.639353144 -3.146778275 0.094634295
H -1.206054287 -5.539957858 0.022681061
H 1.137038765 -6.416678944 -0.071783107
H 3.051653391 -4.813020813 -0.092025442

Naphthalene

S_0

C -0.225583000 1.195612000 1.153071000
C 0.351028000 0.008709000 0.783805000
C 1.423872000 -0.006412000 -0.133360000
C 1.897903000 1.165674000 -0.661420000
C 1.324857000 2.408692000 -0.301043000
C 0.239963000 2.424011000 0.626256000
C -0.333084000 3.667029000 0.986632000
C 1.790403000 3.637092000 -0.827857000
C 1.213792000 4.823995000 -0.458591000
C 0.140947000 4.839116000 0.458573000
H -1.049554000 1.209431000 1.856560000
H -0.014918000 -0.923576000 1.194461000
H 1.871797000 -0.950062000 -0.417339000
H 2.721689000 1.156633000 -1.365192000
H -1.156870000 3.676070000 1.690404000
H 2.614375000 3.623272000 -1.531346000
H 1.579739000 5.756279000 -0.869246000
H -0.306978000 5.782765000 0.742552000

S_1

C -0.235909000 1.196964000 1.161904000
C 0.347623000 -0.014129000 0.787919000
C 1.429564000 -0.029102000 -0.134052000
C 1.908391000 1.166859000 -0.670115000
C 1.344940000 2.408399000 -0.318949000
C 0.219881000 2.424305000 0.644165000
C -0.343570000 3.665845000 0.995329000
C 1.800730000 3.635740000 -0.836690000
C 1.217197000 4.846833000 -0.462705000
C 0.135255000 4.861805000 0.459263000
H -1.058617000 1.203922000 1.866474000

H -0.020720000 -0.943128000 1.200089000
H 1.878669000 -0.969619000 -0.421022000
H 2.732053000 1.150652000 -1.373417000
H -1.167234000 3.682052000 1.698630000
H 2.623438000 3.628782000 -1.541260000
H 1.585540000 5.775831000 -0.874875000
H -0.313852000 5.802322000 0.746232000

Conical Intersection

C -0.357602725 1.172677352 1.034269562
C 0.198399447 -0.034358020 0.585703496
C 1.356818825 -0.021490176 -0.173742944
C 1.950777370 1.189868263 -0.522893178
C 1.385649178 2.402640779 -0.121193075
C 0.231231582 2.377985188 0.709977151
C -0.168576310 3.704130068 1.230202341
C 1.874227170 3.678366093 -0.591834777
C 1.071467575 4.845796096 -0.496068028
C -0.045955150 4.838067037 0.281454138
H -1.247084702 1.163069969 1.651795558
H -0.268393604 -0.973576695 0.852410510
H 1.801617465 -0.952338385 -0.502045390
H 2.854311129 1.198395567 -1.121440200
H 0.188454546 3.914792262 2.244867176
H 2.758378829 3.686048307 -1.217305671
H 1.303083203 5.694493665 -1.130045965
H -0.803423827 5.609762631 0.212809295

Dibenzoxalene

S_0

C -1.656104885 -1.062066427 0.064102720
C -2.877836370 -1.723620173 0.064389753
C -2.890336585 -3.117314494 0.065614438
C -1.705553693 -3.852689352 0.066572461
C -0.473884215 -3.201235003 0.066322701
C -0.450106870 -1.816242766 0.065109242
C -1.332322915 0.361338076 0.062873656
C 0.647656545 -0.860610845 0.064691118
C 0.017821480 0.459931262 0.063248564
O 0.761795454 1.597310090 0.062445138
C 1.990559833 -0.963268899 0.065330819
C 2.778603396 0.243640567 0.064557519
C 2.126094771 1.491726547 0.063144123
C 2.844345138 2.679716218 0.062372051
C 4.180616848 0.237448561 0.065219315
C 4.902254637 1.416677244 0.064488234
C 4.229777942 2.639345775 0.063062894
H -3.807810096 -1.168781648 0.063630562
H -3.838902631 -3.639694385 0.065814025
H -1.743657209 -4.934043627 0.067543698
H 0.446617785 -3.772668588 0.067128833
H -2.040635972 1.174304896 0.061868189
H 2.496577565 -1.921343318 0.066319912
H 2.304392048 3.616842182 0.061322776
H 4.692552703 -0.717175008 0.066341661
H 5.983608349 1.391258775 0.064980742
H 4.788736965 3.565903778 0.062499859

S_1

C -15.012796971 0.991729027 -0.001254240
C -16.264062691 0.322266947 -0.001063111
C -16.288359295 -1.047690096 0.000161951
C -15.079625934 -1.791064650 0.001222766
C -13.835516934 -1.175445408 0.001072805
C -13.765495505 0.212993834 -0.000133156
C -14.696985927 2.340956053 -0.002357769
C -12.672326182 1.131730598 -0.000605487
C -13.260391571 2.410197572 -0.001929611
O -12.584327833 3.538879938 -0.002684597
C -11.259987265 1.035346305 0.000061987
C -10.518080744 2.221805075 -0.000681963
C -11.185686153 3.480929772 -0.002087403
C -10.524653049 4.687886283 -0.002904802
C -9.096258366 2.285495208 -0.000129525

C -8.431208878 3.490012863 -0.000942260
C -9.131538638 4.704372554 -0.002344210
H -17.181771832 0.896764299 -0.001882813
H -17.232139314 -1.576233308 0.000328540
H -15.134395644 -2.872253100 0.002164310
H -12.933689828 -1.774167756 0.001891974
H -15.365277673 3.186529586 -0.003351996
H -10.752097441 0.080825440 0.001131919
H -11.101610042 5.603181062 -0.003963563
H -8.543439750 1.354467316 0.000949407
H -7.348520557 3.499253266 -0.000490104
H -8.601054984 5.645867322 -0.002973047

Conical Intersection

C -15.063660501 0.982791568 0.012132441
C -16.317215485 0.303695621 0.014601958
C -16.332243910 -1.062066325 0.000960325
C -15.101194952 -1.769456221 -0.025327217
C -13.853416096 -1.144812057 -0.031029853
C -13.795989567 0.239456027 -0.007994929
C -14.765908382 2.307984613 0.022901027
C -12.666222677 1.154546321 -0.003289294
C -13.192110086 2.368352098 0.026968919
O -12.578996448 3.546839159 -0.005086168
C -11.187673476 0.972948791 -0.090663986
C -10.480892903 2.213262707 -0.041290534
C -11.148683222 3.465687248 -0.029732947
C -10.502284731 4.679140731 -0.022391774
C -9.070917429 2.305278650 -0.011333298
C -8.405114069 3.520447992 -0.002917286
C -9.107140863 4.722090664 -0.016074444
H -17.236019408 0.877223734 0.026692667
H -17.263149542 -1.610807597 0.002436292
H -15.135740022 -2.852759018 -0.043786384
H -12.948601472 -1.736659663 -0.054920953
H -15.425897616 3.162997205 0.008194183
H -10.711288531 0.069987284 0.262571002
H -11.093943147 5.585573908 -0.013394611
H -8.505058610 1.381400362 -0.003029404
H -7.321932002 3.529963472 0.014644014
H -8.590003852 5.671528725 -0.012633746

Psoralene

S_0

C -4.243803314 -0.071466124 0.000000029
C -2.846120046 -0.032222918 0.000000239
C -2.107108306 -1.237945553 0.000000651
C -2.721165681 -2.482436373 0.000000565
C -4.101155966 -2.473475248 0.000001043
C -4.884465129 -1.301673534 0.000000229
C -2.097993319 1.192638608 0.000000686
C -0.752956768 1.188536128 0.000000232
C 0.004472521 -0.052162593 -0.000000836
O -0.743580663 -1.227608125 0.000000122
C -6.253418480 -1.757040231 -0.000000900
O -4.904958264 -3.574152528 0.000000695
C -6.201637777 -3.103989287 -0.000000190
O 1.202027924 -0.151760624 -0.000002773
H -4.803437330 0.855192225 -0.000000431
H -2.137517900 -3.391101984 0.000000655
H -2.643756170 2.129044573 0.000001419
H -0.166227754 2.095043638 0.000000498
H -7.146318837 -1.155225803 -0.000001763
H -6.962968740 -3.863924246 -0.000000167

S_1

C -4.219863472 -0.077290884 -0.000012828
C -2.838884355 -0.008560598 -0.000018364
C -2.104861217 -1.235443707 -0.000008332
C -2.747954471 -2.503239702 0.000001548
C -4.118697033 -2.502188757 0.000002791
C -4.884976914 -1.336310031 -0.000005492
C -2.106611024 1.234074212 -0.000000747
C -0.715017765 1.215371819 -0.000010874

C 0.048665531 0.039679953 -0.000075832
O -0.783081611 -1.262232390 -0.000014880
C -6.234081381 -1.752927589 -0.000001986
O -4.957529425 -3.613690259 0.000012902
C -6.209307462 -3.140873247 0.000008980
O 1.224915511 -0.188398439 0.000050416
H -4.800104125 0.836952572 -0.000012504
H -2.148168546 -3.401650412 0.000006515
H -2.650964581 2.165813674 0.000036852
H -0.141961105 2.131212103 0.000034490
H -7.123439021 -1.144569883 -0.000007488
H -7.000167534 -3.871458434 0.000014835

Conical Intersection

C -4.272775700 -0.027091437 0.061277810
C -2.866446081 0.056122507 0.127144201
C -2.104553892 -1.160209403 0.143071489
C -2.691162955 -2.404985290 0.066658732
C -4.076248030 -2.426472038 -0.019894268
C -4.881398804 -1.272794493 -0.010373314
C -2.121768616 1.253508107 0.261159336
C -0.753669638 1.128043780 -0.282805331
C 0.034086335 -0.039003585 0.126464067
O -0.737157020 -1.154495439 0.390830497
C -6.238452260 -1.756435581 -0.097631211
O -4.851979021 -3.541534852 -0.103160420
C -6.156522506 -3.101724244 -0.150283119
O 1.225852642 -0.124609333 0.204785201
H -4.854197049 0.885562129 0.057415532
H -2.095257784 -3.305042969 0.111218996
H -2.491638345 2.145480195 0.744821154
H -0.537401460 1.480246937 -1.290293787
H -7.143063885 -1.172597391 -0.119548806
H -6.898335929 -3.877697598 -0.220856759

1AN

S_0

C 0.918450140 0.289936016 -1.647306341
C -0.151675435 1.158143668 -1.578816617
C -0.560700763 1.898752181 -2.701323993
C 0.103338378 1.791914541 -3.894094088
C 1.204295862 0.911034570 -4.011344553
C 1.614584771 0.132761203 -2.886716343
C 2.693298761 -0.768883807 -3.043974281
C 1.913348888 0.771259014 -5.228286834
C 2.966274845 -0.098084961 -5.343229103
C 3.355461589 -0.882862887 -4.240148848
N 1.289441881 -0.475564713 -0.540046297
H -0.679627919 1.276184508 -0.639497448
H -1.405078276 2.570018245 -2.607532946
H -0.202341747 2.371909653 -4.755446183
H 2.987488591 -1.406146626 -2.220782296
H 1.601644806 1.368359002 -6.076921770
H 3.494727946 -0.191702469 -6.283438691
H 4.174368856 -1.583621418 -4.340015715
H 0.900882176 -0.144519044 0.329944018
H 2.279516649 -0.645106679 -0.451121671

S_1

C 0.921220374 0.332669321 -1.664448111
C -0.196128399 1.199975201 -1.557147193
C -0.601473454 1.918455548 -2.663249908
C 0.100642710 1.765638064 -3.858318836
C 1.214661341 0.889621426 -4.004280686
C 1.624961453 0.125902629 -2.896582603
C 2.720383007 -0.782027326 -3.008201973
C 1.906407081 0.777153190 -5.246994941
C 2.996919411 -0.113724816 -5.336481604
C 3.389209164 -0.876517672 -4.256629106
N 1.339878497 -0.310003908 -0.554100272
H -0.700797480 1.296697420 -0.603912102
H -1.447137393 2.589095767 -2.605444315
H -0.214644692 2.330007172 -4.727661348
H 2.964660133 -1.481206804 -2.221872819

H 1.591304810 1.370402836 -6.092716183
H 3.534642611 -0.203072763 -6.272404358
H 4.222333228 -1.560315287 -4.358882556
H 0.913646178 -0.121393922 0.337279156
H 2.217011422 -0.803576077 -0.568050241

Conical Intersection

C 0.966646650 0.428607240 -1.665117358
C -0.339863237 1.024001981 -1.690085844
C -0.745544405 1.721121239 -2.773443109
C 0.334893800 2.042429126 -3.739375730
C 1.275302585 0.945269574 -4.047276930
C 1.674257887 0.189967629 -2.912673545
C 2.693530567 -0.755334348 -3.065380203
C 1.838841023 0.698489854 -5.282037034
C 2.845186042 -0.268398163 -5.425008511
C 3.272304878 -0.976938871 -4.316002940
N 1.407828878 -0.187739916 -0.505032299
H -1.012810109 0.819798305 -0.860948156
H -1.773303350 2.020935241 -2.931934149
H 0.754894163 3.048259751 -3.704127231
H 3.028605147 -1.342789525 -2.220371815
H 1.520080940 1.281318639 -6.137551973
H 3.295185031 -0.442226053 -6.393598442
H 4.059349404 -1.714095834 -4.414002970
H 1.000858155 0.151084128 0.352093480
H 2.401455952 -0.339979997 -0.428225240

14DMCN

S_0

C 1.619706058 -1.980569330 0.916043575
C 1.103192285 -0.671343655 0.629207286
C 1.961956983 0.411393516 0.671992947
C 3.297493799 0.265411793 1.066163943
C 3.796764546 -0.964400945 1.435011721
C 2.966147560 -2.124352673 1.358766373
C 3.455510139 -3.412793323 1.670877697
C 2.665144297 -4.521388597 1.512283582
C 1.357773380 -4.390673094 1.008761497
C 0.850019710 -3.150379644 0.717833260
N -0.249365903 -0.538850425 0.276504005
C -0.628558237 0.656123371 -0.457244886
C -1.218580421 -0.851063468 1.329782225
C 5.148484656 -1.080058298 1.872259784
N 6.240560575 -1.181355870 2.230540877
H 1.599948929 1.400987212 0.437111549
H 3.938902030 1.135162802 1.111100754
H 4.473687670 -3.511947401 2.023451784
H 3.056167809 -5.502004503 1.750654671
H 0.755983268 -5.273855596 0.837376282
H -0.139914733 -3.055564562 0.297078912
H -1.634405135 0.513223942 -0.854036759
H 0.052439400 0.813128697 -1.292321172
H -0.641612415 1.562990531 0.166120994
H -1.352616043 0.003940901 2.007604143
H -2.183907161 -1.090273309 0.880435871
H -0.888393046 -1.701008075 1.918809086

S_1

C 1.601271386 -1.891047658 0.949059081
C 1.122298421 -0.556040216 0.907836281
C 1.916392255 0.566077977 1.190754431
C 3.237294247 0.386664727 1.525402060
C 3.790599057 -0.912940917 1.587100465
C 2.982342943 -2.074065426 1.301076114
C 3.488848527 -3.378861041 1.352967950
C 2.691490723 -4.484988504 1.071874976
C 1.358416866 -4.309225792 0.730112516
C 0.817444042 -3.028101763 0.668767633
N -0.258562276 -0.337845344 0.564964829
C -0.617120651 -0.150410672 -0.809777756
C -1.240798468 -0.306191829 1.607840969
C 5.147139944 -1.076017373 1.931569422
N 6.262929920 -1.222235031 2.213976597

H 1.494815587 1.561926589 1.144113879
H 3.862144640 1.240278550 1.743981590
H 4.528506838 -3.516483653 1.619186651
H 3.115337206 -5.479261122 1.121277561
H 0.733231895 -5.165059425 0.509660105
H -0.225894941 -2.922631735 0.399603511
H -1.693523443 -0.085901542 -0.944125019
H -0.193996889 -0.974052195 -1.387957670
H -0.129593126 0.762650117 -1.167449609
H -1.023096028 0.550435731 2.254796578
H -2.250822769 -0.237204473 1.212798075
H -1.114565905 -1.198987981 2.222758781

Conical Intersection

C 1.657429123 -2.053670815 0.871371038
C 1.202343414 -0.679033054 0.608423639
C 2.181707198 0.270719057 0.149044667
C 3.492478295 0.084536153 0.429092762
C 3.690304573 -0.944336079 1.496195822
C 3.005836566 -2.233415767 1.249598314
C 3.563886076 -3.488880882 1.379795270
C 2.773720819 -4.622271140 1.165851551
C 1.441268998 -4.466235676 0.819493663
C 0.882014203 -3.197150811 0.667854189
N -0.161678474 -0.437286870 0.514216024
C -0.625661352 0.740377750 -0.191915949
C -1.007329267 -0.808724504 1.642835480
C 4.099229932 -0.583508689 2.772884984
N 4.523443851 -0.303923220 3.822078729
H 1.871527382 1.101319648 -0.473059801
H 4.317165625 0.596890721 -0.043644994
H 4.602700397 -3.588997647 1.667567083
H 3.197803871 -5.609929245 1.287795622
H 0.821958894 -5.339563584 0.656955338
H -0.151530447 -3.101151895 0.366856211
H -1.706363851 0.669440098 -0.312510500
H -0.179949247 0.791372677 -1.184050669
H -0.402493686 1.673453379 0.344615036
H -1.087129499 0.018047350 2.361565159
H -2.010178841 -1.061066246 1.292261221
H -0.589974552 -1.666530708 2.161000112

$[Ru(bpy)_3]^{2+}$

S_0

C 5.279123000 -1.981887000 -1.682736000
C 4.736975000 -3.234699000 -1.919697000
C 3.405603000 -3.329308000 -2.303971000
C 2.664186000 -2.168864000 -2.433916000
N 3.183002000 -0.954563000 -2.202029000
C 4.484490000 -0.849935000 -1.831138000
C 6.614401000 2.161525000 -1.030640000
C 6.253734000 0.834373000 -1.199270000
C 4.962355000 0.520284000 -1.609691000
N 4.047340000 1.495202000 -1.843251000
C 4.401745000 2.777729000 -1.679829000
C 5.671626000 3.150963000 -1.278031000
C -1.858746000 -0.762079000 -2.825337000
C -0.671589000 -0.283609000 -2.300774000
N 0.374327000 0.045407000 -3.072098000
C 0.272895000 -0.091364000 -4.418604000
C -0.897047000 -0.563943000 -5.004022000
C -1.974747000 -0.903484000 -4.202112000
C 1.471266000 0.288359000 -5.175957000
N 2.499496000 0.763807000 -4.428427000
C 3.636081000 1.130044000 -5.037390000
C 3.802696000 1.048156000 -6.408218000
C 2.755954000 0.566447000 -7.183529000
C 1.580445000 0.182629000 -6.558622000
C 0.596857000 2.398859000 1.259993000
C 0.844588000 1.445994000 2.234889000
C 1.477682000 0.263975000 1.873195000
C 1.843961000 0.079595000 0.551926000
N 1.607111000 0.998255000 -0.395141000
C 0.985161000 2.155410000 -0.053382000

C -0.056981000 5.132505000 -2.125826000
C 0.108196000 4.314112000 -1.020065000
C 0.761186000 3.093830000 -1.159475000
N 1.241722000 2.692548000 -2.363847000
C 1.076696000 3.486815000 -3.431122000
C 0.436139000 4.710524000 -3.353585000
Ru 2.160091000 0.836740000 -2.386017000
H 6.312979000 -1.886299000 -1.387178000
H 5.345623000 -4.121598000 -1.807326000
H 2.940011000 -4.284400000 -2.502098000
H 1.624934000 -2.198793000 -2.724739000
H 7.615768000 2.417543000 -0.712189000
H 6.971169000 0.049775000 -1.012319000
H 3.640540000 3.515813000 -1.883093000
H 5.907277000 4.199416000 -1.162356000
H -2.672186000 -1.014187000 -2.159779000
H -0.541017000 -0.158954000 -1.236472000
H -0.967382000 -0.662809000 -6.076632000
H -2.889594000 -1.271602000 -4.646212000
H 4.423882000 1.502582000 -4.400382000
H 4.738799000 1.358361000 -6.850588000
H 2.852113000 0.489062000 -8.257965000
H 0.756017000 -0.198879000 -7.141822000
H 0.108439000 3.325682000 1.520048000
H 0.548052000 1.625046000 3.259413000
H 1.690941000 -0.509014000 2.597926000
H 2.337776000 -0.825315000 0.231629000
H -0.563685000 6.083067000 -2.029035000
H -0.271231000 4.621617000 -0.057319000
H 1.477445000 3.125103000 -4.365968000
H 0.329769000 5.313759000 -4.244079000

S_1

C 5.295488000 -1.984859000 -1.679576000
C 4.759076000 -3.234492000 -1.951552000
C 3.442222000 -3.329684000 -2.378614000
C 2.701407000 -2.169700000 -2.519846000
N 3.215321000 -0.964170000 -2.247886000
C 4.502123000 -0.855953000 -1.835305000
C 6.574304000 2.167583000 -0.938242000
C 6.245403000 0.837547000 -1.153291000
C 4.964533000 0.514990000 -1.581301000
N 4.040182000 1.484208000 -1.789775000
C 4.353778000 2.767220000 -1.573105000
C 5.615320000 3.147732000 -1.151084000
C -1.883049000 -0.630383000 -2.798154000
C -0.685713000 -0.160312000 -2.289073000
N 0.360022000 0.109144000 -3.079997000
C 0.258502000 -0.060419000 -4.420746000
C -0.920122000 -0.526663000 -4.987916000
C -2.000388000 -0.816415000 -4.168437000
C 1.461869000 0.284062000 -5.187635000
N 2.513329000 0.715601000 -4.448960000
C 3.663156000 1.039011000 -5.052526000
C 3.816773000 0.963103000 -6.425353000
C 2.746197000 0.530051000 -7.194794000
C 1.557808000 0.184795000 -6.569513000
C 0.604959000 2.382536000 1.256082000
C 0.895623000 1.456727000 2.220230000
C 1.590236000 0.272796000 1.870386000
C 1.945691000 0.093027000 0.557675000
N 1.653001000 0.983048000 -0.408057000
C 0.988410000 2.161612000 -0.089664000
C -0.113004000 5.080633000 -2.157280000
C 0.069837000 4.293031000 -1.053913000
C 0.758436000 3.059365000 -1.159224000
N 1.248351000 2.674070000 -2.401547000
C 1.043693000 3.454687000 -3.478302000
C 0.384595000 4.656037000 -3.413761000
Ru 2.173868000 0.831511000 -2.397882000
H 6.319124000 -1.892713000 -1.350401000
H 5.365597000 -4.121890000 -1.832203000
H 2.987104000 -4.283720000 -2.602494000
H 1.672744000 -2.196832000 -2.847084000

H 7.568854000 2.432489000 -0.606096000
H 6.977901000 0.062630000 -0.987702000
H 3.572965000 3.490513000 -1.752160000
H 5.830916000 4.194446000 -0.992088000
H -2.702457000 -0.840901000 -2.126105000
H -0.542843000 0.002421000 -1.231706000
H -0.996613000 -0.662736000 -6.055633000
H -2.923194000 -1.181738000 -4.598072000
H 4.469046000 1.373213000 -4.416484000
H 4.760740000 1.240038000 -6.872184000
H 2.833069000 0.459173000 -8.270434000
H 0.717118000 -0.157698000 -7.153334000
H 0.084555000 3.292961000 1.514976000
H 0.599821000 1.631170000 3.246271000
H 1.838964000 -0.478404000 2.604967000
H 2.472102000 -0.797078000 0.243659000
H -0.639296000 6.021985000 -2.070277000
H -0.314837000 4.604232000 -0.093627000
H 1.444148000 3.091699000 -4.414343000
H 0.257694000 5.250994000 -4.305788000

Conical Intersection

C 5.316504199 -1.971109246 -1.678772973
C 4.797387883 -3.223192145 -1.969470706
C 3.484537587 -3.329106498 -2.408618221
C 2.730927046 -2.176538616 -2.537951280
N 3.228936812 -0.968203575 -2.247565886
C 4.511945976 -0.848152878 -1.826589081
C 6.547212286 2.188267133 -0.891243552
C 6.228766695 0.856899641 -1.109331981
C 4.957703596 0.524168606 -1.560422762
N 4.031578516 1.489421270 -1.784600848
C 4.336375615 2.775695018 -1.568634937
C 5.587518639 3.163822652 -1.125668702
C -1.906357402 -0.595059681 -2.801098248
C -0.695000418 -0.168945034 -2.287953491
N 0.353305805 0.094496167 -3.078884457
C 0.242908935 -0.044860327 -4.423285628
C -0.953449903 -0.460987370 -4.993680568
C -2.037274399 -0.740151286 -4.175743136
C 1.451681880 0.277265961 -5.189312269
N 2.505974602 0.706549214 -4.453209400
C 3.661059029 1.012422628 -5.056633173
C 3.818316042 0.917455004 -6.427585570
C 2.746438815 0.482230852 -7.195059102
C 1.553148214 0.156109214 -6.569622261
C 0.626996253 2.380671785 1.259955150
C 0.925746391 1.456500205 2.221266347
C 1.608921053 0.265736541 1.862688299
C 1.945439348 0.077006336 0.547895722
N 1.640314618 0.966199545 -0.419595567
C 0.990030387 2.154705161 -0.091419685
C -0.104750853 5.069524385 -2.163137210
C 0.085890728 4.291541918 -1.055924239
C 0.764890709 3.051490301 -1.157262416
N 1.250341574 2.655193684 -2.402444079
C 1.031512520 3.427000339 -3.487296724
C 0.376301354 4.628674448 -3.423014844
Ru 2.165830668 0.826185238 -2.393564858
H 6.337142353 -1.871510951 -1.342125453
H 5.413744230 -4.104619426 -1.856195231
H 3.042778108 -4.285377834 -2.649307598
H 1.703889178 -2.211040677 -2.869875524
H 7.534136330 2.458803571 -0.541293058
H 6.962170739 0.085940858 -0.929114308
H 3.556488424 3.495409564 -1.765205376
H 5.795204920 4.212365951 -0.968120417
H -2.726927392 -0.801036065 -2.128983619
H -0.543304228 -0.034535274 -1.227792807
H -1.041008304 -0.561629524 -6.064577674
H -2.973547123 -1.064738607 -4.608987284
H 4.467672039 1.347448891 -4.421594627
H 4.766149039 1.180062492 -6.874981036
H 2.837015238 0.394057277 -8.269130694

H 0.712880898 -0.192259470 -7.150581587
H 0.118352018 3.296659964 1.523472870
H 0.648436394 1.635339192 3.251701110
H 1.862470681 -0.485301045 2.596208891
H 2.461785886 -0.817108989 0.229120168
H -0.625209542 6.014453348 -2.079658276
H -0.286460538 4.612529953 -0.093798526
H 1.422602856 3.056092663 -4.423831207
H 0.240386995 5.216397550 -4.318836402

B.1.2 k_{IC} Fortran Code

```
      !Program to calculate the internal conversion rate constant, kic
      !Aline S. Bozzi - eCsMo Lab - UFMG - Brazil

      program k_ic

      implicit double precision(16) (a-z)
      integer :: i, n
      double precision :: Si, Sf, CI, nac, S, Qi, freqi, isrei, isre,
     lambdaM
      double precision :: delG, omegaeff, roi, ro, kic, logkic, kicf
      double precision, parameter :: kb = 8.61733E-5 ! eV.K^-1
      double precision, parameter :: h = 4.1357E-15 ! eV.s
      double precision, parameter :: hbar = 6.5821E-16 ! eV.s
      double precision, parameter :: Tref = 298.15 ! K
      double precision, parameter :: c = 2.99E10 ! cm.s^-1

      !!!!!!!!!!!!! Reading Parameters !!!!!!!!!!!!!!!!!

      open(1, file='parameters.txt', status='old')
      read(1, FMT= '(A1)') dummy
      read(1,*) Si, Sf, CI, nac, S, n

      !!!!!!! Inner-Sphere Reorganization Energy !!!!!!!!!

      open(3, file='Qi.txt', status='old')
      open(4, file='FREQi.txt', status='old')
      open(5, file='isrei.txt', status='unknown')
6     read(3,*,end=7) Qi
      read(4,*,end=7) freqi ! cm^-1

      if (Qi > 0.1) then
               isrei = Qi**2 * hbar * freqi * c / 2.d0
               isre = isre + isrei  ! eV
               write(5,*) isre
      else
               goto 6
```

```
36          endif
37
38          goto 6
39
40 7        lambdaM = (CI - Sf) * 27.2114 ! eV
41          write(*,'(A, F10.3, A)') 'The reorganization energy MECI is ',
    lambdaM, ' eV'
42
43          delG = (Sf - Si) * 27.2114 ! eV
44          write(*,'(A, F10.3, A)') 'The adiabatic energy difference is ',
    delG, ' eV'
45
46          omegaeff = isre / (S * hbar) ! s^-1
47          omegaeff_cm = omegaeff*3.33E-11 ! cm^-1
48          write(*,'(A, ES13.5, A)') 'The effective frequency is',
    omegaeff_cm, ' cm^-1'
49
50          j = 1
51          ro = 0
52          do i = 0, n, 1
53                  if (i == 0) then
54                     j = 1
55                  else
56                     j = j * i
57                  endif
58                  roi = exp(-S) * (S**i) / j * &
59                        exp(-(delG + lambdaM + i * hbar * omegaeff)**2 / &
60                        (4d0 * lambdaM * kb * Tref))
61                  ro = ro + roi
62          enddo
63
64          open(8, file='FCWD.txt', status='unknown')
65          write(8,*) ro
66
67          !!!!!!!! Internal Conversion Constant !!!!!!!!!!!!
68
69 8        kic = (3.14159d0 * ro * (nac * 1.23981E-4)**2) / &
70                (hbar * sqrt(3.14159d0 * lambdaM * kb * Tref))
71
72          write(*,'(A, ES10.2, A)') 'The IC constant is: ', kic, ' s^-1'
73
74          logkic = log10(kic)
75          kicf = 1 / kic
76
77          write(*,'(A, F10.2)') 'The log of IC constant is: ', logkic
```

```
78          write(*,'(A, ES13.3, A)') 'The decay time is: ', kicf, ' s'
79
80          end program k_ic
```

B.2 Chapter 2

B.2.1 Cartesian Coordinates

All the Cartesian coordinates for the optimized geometries of S_0, S_1, T_1, T_2, ^3MC, TS, and conical intersections for the Ru(bpz)$_3^{2+}$ complex are shown below.

S_0

Ru 0.008301000 0.004407000 0.002074000
N 0.206537000 1.783307000 -1.058066000
N 0.305547000 4.279053000 -2.289470000
C 1.007645000 2.001564000 -2.110012000
C -0.553445000 2.814010000 -0.601647000
C -0.485700000 4.060691000 -1.240995000
C 1.048806000 3.257649000 -2.720666000
H 1.614666000 1.170125000 -2.471218000
H -1.088607000 4.901111000 -0.885498000
H 1.705666000 3.424860000 -3.580653000
N -1.274975000 1.252366000 1.058955000
N -3.011309000 3.087180000 2.230383000
C -1.395871000 2.511219000 0.559766000
C -2.007276000 0.920541000 2.130986000
C -2.873100000 1.850327000 2.712642000
C -2.280931000 3.414621000 1.166287000
H -1.901411000 -0.090158000 2.528076000
H -3.466236000 1.569511000 3.589134000
H -2.397884000 4.427782000 0.771457000
N -1.642502000 -0.708596000 -1.047634000
N -3.884167000 -1.848128000 -2.245384000
C -2.233943000 -0.125564000 -2.099410000
C -2.168089000 -1.870222000 -0.575778000
C -3.295399000 -2.424816000 -1.199693000
C -3.358479000 -0.705515000 -2.692005000
H -1.805757000 0.804399000 -2.476333000
H -3.727808000 -3.361297000 -0.835859000
H -3.833635000 -0.220488000 -3.551057000
N -0.430755000 -1.732517000 1.060856000
N -1.183920000 -4.127251000 2.265228000
C -1.481340000 -2.450230000 0.582484000
C 0.228857000 -2.204437000 2.127455000
C -0.157983000 -3.407228000 2.724139000
C -1.839186000 -3.654152000 1.207139000
H 1.067186000 -1.619813000 2.509207000
H 0.387659000 -3.784492000 3.595240000
H -2.681310000 -4.244173000 0.834893000
N 1.446667000 -1.058814000 -1.060472000
N 3.549184000 -2.421914000 -2.275529000
C 2.713356000 -0.956345000 -0.576651000
C 1.238439000 -1.828473000 -2.137381000
C 2.301155000 -2.506109000 -2.740716000
C 3.753502000 -1.656036000 -1.205537000
H 0.221003000 -1.900363000 -2.524597000
H 2.120210000 -3.130664000 -3.621692000
H 4.777085000 -1.590070000 -0.826106000
N 1.732061000 0.482007000 1.060663000
N 4.179159000 0.992735000 2.286615000
C 1.813630000 1.290503000 2.126257000
C 2.875200000 -0.084649000 0.591451000
C 4.095034000 0.190200000 1.227381000
C 3.046542000 1.538824000 2.734522000
H 0.890767000 1.736724000 2.500012000

H 5.025442000 -0.252835000 0.860862000
H 3.101712000 2.199630000 3.605895000

S_1

Ru 0.032373000 0.043084000 -0.000295000
N 0.230301000 1.867970000 -1.015155000
N 0.265132000 4.355373000 -2.237378000
C 1.067414000 2.115718000 -2.028251000
C -0.597381000 2.855733000 -0.587574000
C -0.559994000 4.105757000 -1.223266000
C 1.072890000 3.374089000 -2.639693000
H 1.727632000 1.311811000 -2.358291000
H -1.215562000 4.917308000 -0.895777000
H 1.754719000 3.573446000 -3.472579000
N -1.327752000 1.246335000 1.018637000
N -3.148688000 2.986430000 2.169499000
C -1.466718000 2.508654000 0.539340000
C -2.080025000 0.853381000 2.052436000
C -2.991392000 1.744559000 2.628774000
C -2.399586000 3.368968000 1.138112000
H -1.951968000 -0.165487000 2.420991000
H -3.603087000 1.425868000 3.478789000
H -2.536275000 4.388359000 0.766734000
N -1.616394000 -0.648527000 -1.049610000
N -3.880880000 -1.798917000 -2.214659000
C -2.249625000 -0.046362000 -2.078747000
C -2.127257000 -1.842834000 -0.563108000
C -3.278801000 -2.382365000 -1.204031000
C -3.365380000 -0.616168000 -2.658516000
H -1.836465000 0.895305000 -2.445982000
H -3.697290000 -3.329256000 -0.846306000
H -3.862933000 -0.127010000 -3.500219000
N -0.375360000 -1.694442000 1.051587000
N -1.108252000 -4.133830000 2.201037000
C -1.450026000 -2.413153000 0.548986000
C 0.313763000 -2.205566000 2.093974000
C -0.051356000 -3.407237000 2.667264000
C -1.775284000 -3.647827000 1.179599000
H 1.156908000 -1.625548000 2.474728000
H 0.504630000 -3.805742000 3.520068000
H -2.620968000 -4.233804000 0.804395000
N 1.441564000 -1.101758000 -1.021141000
N 3.456535000 -2.624230000 -2.158222000
C 2.706162000 -1.041516000 -0.531359000
C 1.181534000 -1.903435000 -2.060041000
C 2.209878000 -2.661526000 -2.629616000
C 3.707063000 -1.827328000 -1.122249000
H 0.158675000 -1.936371000 -2.438125000
H 1.998917000 -3.313138000 -3.483530000
H 4.731464000 -1.805460000 -0.740709000
N 1.800450000 0.538721000 1.015694000
N 4.250080000 0.974244000 2.238028000
C 1.912799000 1.414201000 2.020745000
C 2.907103000 -0.126601000 0.594862000
C 4.134438000 0.110466000 1.232145000
C 3.154039000 1.623861000 2.630984000
H 1.015313000 1.941838000 2.348655000
H 5.039540000 -0.412887000 0.911583000
H 3.243388000 2.336845000 3.456786000

T_1

Ru 0.010694000 -0.029439000 -0.008577000
N 0.234056000 1.713714000 -1.055184000
N 0.390350000 4.279692000 -2.190482000
C 1.068846000 1.970887000 -2.081126000
C -0.531257000 2.771224000 -0.550497000
C -0.412837000 4.051466000 -1.182687000
C 1.143932000 3.231583000 -2.646271000
H 1.668410000 1.143070000 -2.464098000
H -1.012576000 4.888272000 -0.810242000
H 1.813812000 3.419325000 -3.488911000
N -1.262626000 1.164363000 1.051746000
N -3.000684000 3.036396000 2.221480000
C -1.345845000 2.472701000 0.560783000

C -2.059142000 0.823342000 2.084096000
C -2.910602000 1.744428000 2.666845000
C -2.246418000 3.379564000 1.208724000
H -1.992932000 -0.200415000 2.456355000
H -3.537216000 1.457393000 3.514742000
H -2.319348000 4.410034000 0.846280000
N -1.674325000 -0.701620000 -1.038212000
N -3.983804000 -1.726339000 -2.181259000
C -2.253454000 -0.082824000 -2.074119000
C -2.233897000 -1.840539000 -0.554693000
C -3.402593000 -2.337330000 -1.151449000
C -3.416828000 -0.610787000 -2.642594000
H -1.788657000 0.829209000 -2.451819000
H -3.873082000 -3.252027000 -0.779697000
H -3.888768000 -0.103581000 -3.490424000
N -0.441471000 -1.802122000 1.028658000
N -1.261592000 -4.164224000 2.234218000
C -1.540578000 -2.459824000 0.579448000
C 0.239520000 -2.313729000 2.060108000
C -0.184346000 -3.504116000 2.660742000
C -1.933915000 -3.652002000 1.205548000
H 1.119209000 -1.773184000 2.415232000
H 0.373472000 -3.917431000 3.507367000
H -2.816429000 -4.197922000 0.860795000
N 1.487491000 -1.113559000 -1.037706000
N 3.616742000 -2.444546000 -2.218007000
C 2.754228000 -0.920043000 -0.589351000
C 1.283761000 -1.959130000 -2.053683000
C 2.365315000 -2.622925000 -2.642339000
C 3.813322000 -1.604795000 -1.203381000
H 0.260569000 -2.102230000 -2.406342000
H 2.195099000 -3.311607000 -3.476397000
H 4.842004000 -1.468457000 -0.858013000
N 1.734370000 0.527305000 1.020197000
N 4.163794000 1.230296000 2.155595000
C 1.782072000 1.376255000 2.053759000
C 2.893498000 0.010924000 0.535947000
C 4.109249000 0.386504000 1.127312000
C 3.013419000 1.719259000 2.620576000
H 0.840055000 1.776784000 2.431476000
H 5.057360000 -0.007642000 0.750566000
H 3.050574000 2.410397000 3.468963000

T_2

Ru 0.016543000 -0.002601000 -0.000851000
N 0.187961000 1.793337000 -1.101836000
N 0.223515000 4.261871000 -2.373667000
C 0.957866000 1.996443000 -2.176237000
C -0.575958000 2.817919000 -0.643360000
C -0.539748000 4.055298000 -1.301979000
C 0.966148000 3.244663000 -2.809932000
H 1.568943000 1.168516000 -2.539111000
H -1.142782000 4.894963000 -0.944749000
H 1.598720000 3.404680000 -3.689261000
N -1.245004000 1.273929000 1.055228000
N -3.033263000 3.052747000 2.193098000
C -1.400427000 2.516906000 0.530544000
C -1.962730000 0.918804000 2.128600000
C -2.863578000 1.828286000 2.692835000
C -2.313412000 3.398232000 1.127155000
H -1.816560000 -0.083441000 2.534467000
H -3.451544000 1.540263000 3.570362000
H -2.463301000 4.403431000 0.723173000
N -1.599964000 -0.688249000 -1.074698000
N -3.942212000 -1.760398000 -2.169261000
C -2.216711000 -0.096793000 -2.127942000
C -2.164434000 -1.841012000 -0.549292000
C -3.349275000 -2.336959000 -1.141862000
C -3.367303000 -0.630084000 -2.667325000
H -1.762393000 0.805585000 -2.539026000
H -3.816829000 -3.239028000 -0.734522000
H -3.848729000 -0.149737000 -3.522933000
N -0.412907000 -1.703890000 1.072920000
N -1.155725000 -4.147016000 2.215171000

C -1.484336000 -2.423352000 0.567829000
C 0.263873000 -2.217621000 2.128942000
C -0.107825000 -3.419752000 2.692679000
C -1.813496000 -3.653715000 1.183770000
H 1.102192000 -1.639894000 2.520427000
H 0.438913000 -3.818779000 3.550784000
H -2.649380000 -4.242649000 0.793151000
N 1.489663000 -1.024486000 -1.059983000
N 3.556635000 -2.445087000 -2.229601000
C 2.746139000 -0.947951000 -0.550600000
C 1.261522000 -1.792068000 -2.133468000
C 2.315754000 -2.505212000 -2.713677000
C 3.774776000 -1.678474000 -1.162759000
H 0.244990000 -1.833317000 -2.527773000
H 2.131748000 -3.133647000 -3.591133000
H 4.795011000 -1.641286000 -0.770683000
N 1.754827000 0.458303000 1.106240000
N 4.184528000 0.949691000 2.357247000
C 1.817407000 1.231321000 2.195733000
C 2.901150000 -0.089664000 0.627732000

$CI_{T_1\text{-}T_2}$

Ru -1.815938080 -0.004634233 -1.443026484
N -1.584358104 1.756240728 -2.471000221
N -1.409018979 4.271385315 -3.638625617
C -0.764149377 1.978427665 -3.511033693
C -2.325596505 2.803152684 -1.991528474
C -2.206747722 4.057165106 -2.611112600
C -0.686371649 3.225540101 -4.089771345
H -0.182066015 1.147698777 -3.879429953
H -2.781947039 4.898082064 -2.245591695
H -0.030388363 3.393948583 -4.932679152
N -3.116612476 1.220678428 -0.409784987
N -4.790865850 3.088077338 0.786579812
C -3.170301947 2.507885070 -0.869934928
C -3.900872965 0.881255159 0.624576581
C -4.724535791 1.812870137 1.218278217
C -4.029312685 3.420166073 -0.237361987
H -3.854627967 -0.135755410 0.983131040
H -5.344865564 1.533238020 2.058696346
H -4.086986973 4.442708070 -0.587116097
N -3.499915538 -0.702057982 -2.458438157
N -5.765261539 -1.795785570 -3.605412237
C -4.109558129 -0.092435975 -3.476121588
C -4.013215346 -1.864881007 -1.994014434
C -5.156760700 -2.395950092 -2.589092086
C -5.244810224 -0.652756427 -4.046807447
H -3.691652288 0.834091060 -3.839492452
H -5.585787376 -3.323619669 -2.234237104
H -5.734247009 -0.157850576 -4.875845439
N -2.226804913 -1.774667732 -0.423142394
N -2.949576058 -4.167458827 0.757803141
C -3.297698704 -2.467553119 -0.874333857
C -1.526146686 -2.268020612 0.599330641
C -1.901074802 -3.468661830 1.187981442
C -3.639984565 -3.673322982 -0.263449816
H -0.676365549 -1.703684658 0.952421245
H -1.334514003 -3.863000355 2.021777480
H -4.490373138 -4.245734566 -0.608436251
N -0.380915650 -1.083710739 -2.464140992
N 1.743768527 -2.454866746 -3.617143391
C 0.892074230 -0.931692274 -1.985683420
C -0.576897401 -1.917462762 -3.496964111
C 0.481027354 -2.589763273 -4.069305572
C 1.936862147 -1.642825699 -2.596238866
H -1.583567828 -2.030427136 -3.870202371
H 0.314872196 -3.251209849 -4.908459785
H 2.949998073 -1.539989722 -2.229766734
N -0.126813920 0.515933755 -0.403003415
N 2.312412973 1.121950687 0.780128763
C -0.055023865 1.370277652 0.630909485
C 1.033822132 -0.043689449 -0.867904469
C 2.244555722 0.290400233 -0.240497420
C 1.155789043 1.661198466 1.217978541

H -0.975101867 1.805663677 0.989095624
H 3.173913815 -0.136590098 -0.594812098
H 1.204239772 2.342024525 2.056570975

$CI_{S_0\text{-}S_1}$

Ru 0.547494195 0.026457716 -0.085193183
N 0.820274161 1.826955679 -1.089504688
N 0.828556710 4.356384519 -2.195048594
C 1.566583416 2.092549705 -2.163101741
C 0.096886613 2.824414041 -0.527459003
C 0.102073354 4.090966736 -1.119767473
C 1.570674989 3.366978986 -2.705899789
H 2.138649882 1.282064367 -2.591948233
H -0.482078751 4.898393212 -0.696784952
H 2.178358919 3.586611439 -3.573723591
N -0.125704813 1.293179973 1.294887061
N -2.297237305 2.722753600 2.340865001
C -0.595343676 2.447368094 0.685685562
C -0.762802822 0.892417689 2.432949866
C -1.818849059 1.610583697 2.934242126
C -1.685050649 3.120224671 1.235744232
H -0.377637479 0.019188102 2.934914827
H -2.295238273 1.289002988 3.851388454
H -2.067376834 4.006604291 0.744069909
N -0.539134163 -0.915265366 -1.454712742
N -3.132321880 -1.389894207 -2.414572656
C -1.005079067 -0.310663753 -2.587995334
C -1.405263658 -1.791828164 -0.812347335
C -2.688244079 -1.987056728 -1.319763359
C -2.273377833 -0.560264634 -3.043911928
H -0.323041331 0.331697872 -3.122256001
H -3.369100354 -2.650786813 -0.800982540
H -2.615779907 -0.087527828 -3.955417361
N 0.186231775 -1.760818214 0.918883415
N -0.718677248 -4.116328613 2.033130456
C -0.874846557 -2.409184900 0.383798299
C 0.817316149 -2.297394163 1.964670360
C 0.359944240 -3.485142925 2.511882258
C -1.328409539 -3.588702298 0.982241041
H 1.667354189 -1.765207060 2.367818048
H 0.869597510 -3.926883833 3.357874018
H -2.188160951 -4.112603982 0.584108179
N 2.342098054 -1.189807059 -1.036120182
N 4.414023705 -2.703916096 -2.083544327
C 3.602283982 -1.007409687 -0.619514090
C 2.113691887 -2.117822607 -1.959778259
C 3.156815987 -2.873159442 -2.483200184
C 4.634812595 -1.778894512 -1.157071644
H 1.098396140 -2.265089912 -2.289525301
H 2.957837680 -3.624103018 -3.237102751
H 5.655886086 -1.649258742 -0.825393463
N 2.674746068 0.583596299 0.875033651
N 5.158803294 1.327865010 1.850979199
C 2.788944599 1.512941475 1.817048102
C 3.792222324 0.011303067 0.410637747
C 5.037651107 0.399566397 0.909434156
C 4.037858090 1.880800837 2.305908726
H 1.888415745 1.972372141 2.190709663
H 5.950277563 -0.045221384 0.535982969
H 4.119435560 2.636993342 3.076209343

^{3}MC

Ru 0.224907000 0.367292000 0.737449000
N 0.674789000 2.127657000 -0.277598000
N 1.049139000 4.577189000 -1.524362000
C 1.397259000 2.227458000 -1.398749000
C 0.124701000 3.257670000 0.232828000
C 0.330275000 4.476464000 -0.412781000
C 1.577709000 3.455829000 -2.014859000
H 1.829109000 1.324935000 -1.803792000
H -0.101791000 5.387819000 -0.021999000
H 2.163480000 3.526226000 -2.922374000
N -0.798448000 1.792326000 1.860756000
N -1.962969000 3.876950000 3.273298000

C -0.662786000 3.075701000 1.442954000
C -1.507912000 1.561404000 2.970558000
C -2.085926000 2.609778000 3.669474000
C -1.258155000 4.105131000 2.171632000
H -1.610608000 0.538510000 3.299723000
H -2.658778000 2.412611000 4.566484000
H -1.155426000 5.135062000 1.856605000
N -1.965859000 -0.260881000 -0.162535000
N -4.601702000 -0.957669000 -0.576206000
C -2.704962000 0.392082000 -1.050470000
C -2.516809000 -1.260046000 0.537385000
C -3.855681000 -1.597756000 0.318893000
C -4.031510000 0.033274000 -1.261565000
H -2.235132000 1.201882000 -1.593981000
H -4.336882000 -2.387504000 0.879717000
H -4.636639000 0.555852000 -1.991838000
N -0.444789000 -1.374087000 1.780934000
N -1.244552000 -3.681139000 3.097444000
C -1.652012000 -1.926976000 1.524812000
C 0.343958000 -1.965329000 2.684986000
C -0.064524000 -3.114259000 3.343526000
C -2.023877000 -3.093183000 2.197818000
H 1.303765000 -1.510549000 2.882915000
H 0.580387000 -3.579537000 4.077863000
H -2.975813000 -3.564944000 1.994791000
N 1.483828000 -0.956098000 -0.369808000
N 3.071098000 -2.784864000 -1.726160000
C 2.811752000 -1.027909000 -0.125208000
C 0.964531000 -1.781982000 -1.285270000
C 1.764120000 -2.686599000 -1.965114000
C 3.582906000 -1.965830000 -0.815319000
H -0.096382000 -1.712539000 -1.475941000
H 1.331322000 -3.341893000 -2.710102000
H 4.640752000 -2.060688000 -0.610797000
N 2.512898000 0.535823000 1.662496000
N 5.223774000 1.001769000 1.896532000
C 2.976036000 1.398863000 2.558688000
C 3.380840000 -0.103831000 0.868425000
C 4.749836000 0.149035000 0.993241000
C 4.342819000 1.622448000 2.681336000
H 2.253032000 1.911160000 3.180530000
H 5.472120000 -0.330840000 0.346311000
H 4.725733000 2.314259000 3.421163000

TS

Ru 0.015070000 0.042423000 0.021430000
N 0.341292000 1.877334000 -0.918695000
N 0.550521000 4.401612000 -2.073874000
C 1.267883000 2.133209000 -1.855294000
C -0.498834000 2.882419000 -0.551581000
C -0.369493000 4.147013000 -1.147353000
C 1.362393000 3.401827000 -2.428984000
H 1.936927000 1.324537000 -2.151275000
H -1.036413000 4.964367000 -0.860734000
H 2.120738000 3.598150000 -3.192523000
N -1.453542000 1.238664000 0.889062000
N -3.338021000 3.020363000 1.900906000
C -1.492863000 2.528921000 0.458849000
C -2.341397000 0.850539000 1.818067000
C -3.281511000 1.752450000 2.318034000
C -2.454746000 3.405959000 0.984035000
H -2.303588000 -0.182102000 2.166060000
H -4.001377000 1.424676000 3.073623000
H -2.500125000 4.443870000 0.644533000
N -1.852195000 -0.888244000 -1.219976000
N -4.385859000 -1.795591000 -1.878096000
C -2.549600000 -0.304083000 -2.194051000
C -2.397715000 -1.922164000 -0.555369000
C -3.688069000 -2.365135000 -0.896415000
C -3.824125000 -0.773208000 -2.529419000
H -2.088267000 0.541682000 -2.711449000
H -4.165857000 -3.184874000 -0.353567000
H -4.391080000 -0.305688000 -3.340322000
N -0.515139000 -1.798277000 0.962340000

N -1.146713000 -4.249045000 2.119039000
C -1.586985000 -2.507971000 0.529252000
C 0.226906000 -2.305361000 1.958808000
C -0.102744000 -3.530797000 2.539141000
C -1.876159000 -3.747127000 1.125928000
H 1.085512000 -1.723412000 2.297523000
H 0.503013000 -3.926712000 3.359512000
H -2.719032000 -4.346101000 0.771738000
N 1.578318000 -1.058514000 -0.923062000
N 3.604030000 -2.566711000 -2.088733000
C 2.858056000 -0.944788000 -0.487479000
C 1.316512000 -1.909727000 -1.926459000
C 2.340684000 -2.656421000 -2.510447000
C 3.859168000 -1.725041000 -1.090151000
H 0.282766000 -1.988537000 -2.266545000
H 2.116356000 -3.340043000 -3.334437000
H 4.892298000 -1.665133000 -0.739038000
N 2.038628000 0.515464000 1.228458000
N 4.582985000 1.289391000 1.998527000
C 2.208811000 1.395372000 2.214325000
C 3.118779000 0.009674000 0.607049000
C 4.403531000 0.419055000 1.006183000
C 3.497083000 1.775792000 2.605612000
H 1.314025000 1.798388000 2.696533000
H 5.298826000 0.040314000 0.506163000
H 3.640339000 2.487343000 3.424595000

B.2.2 Kinetic Population Decay

The set of figures shown below is a collection of important states populated throughout the simulation but not explicitly shown in the figures of the main manuscript. The graphs are sorted by simulation time. The states not mentioned in the main manuscript or this section had negligible contributions.

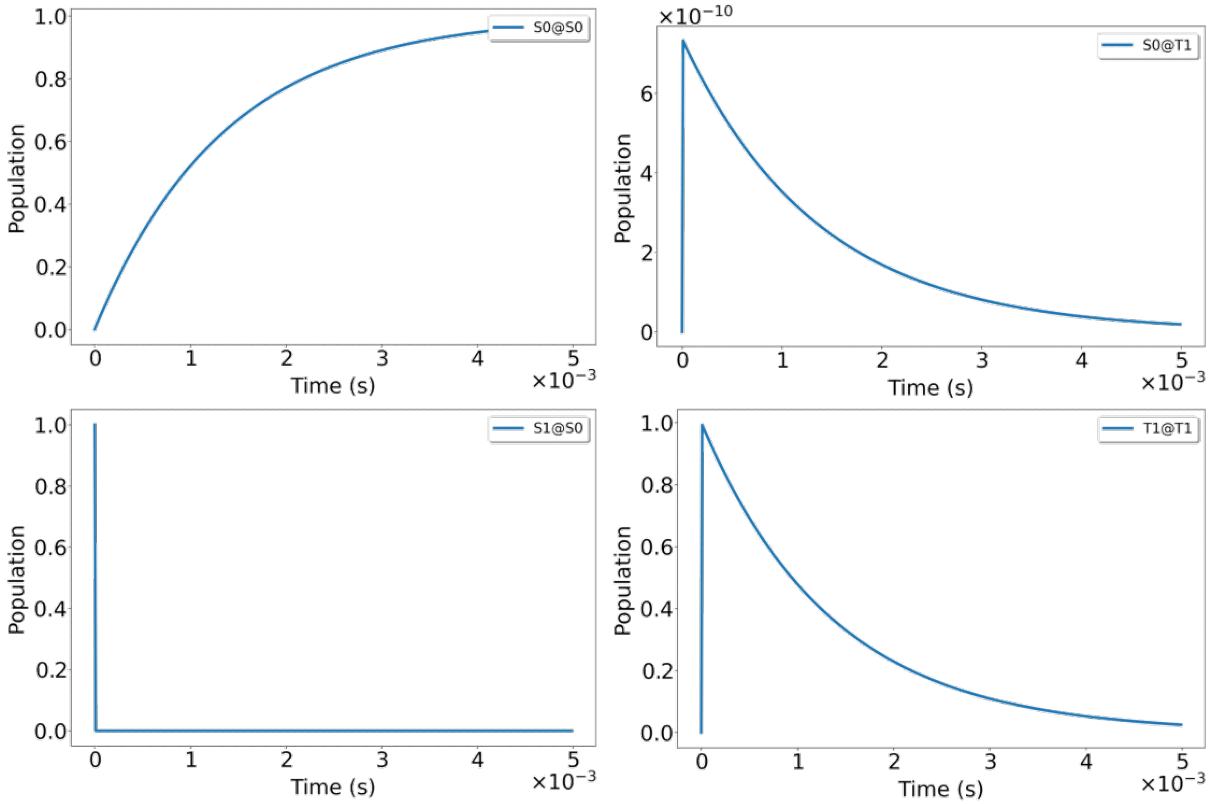

Figure B.1: Evolution of states population over time for a time range from 0 to 5 ms using a propagation step of 10^{-5}.

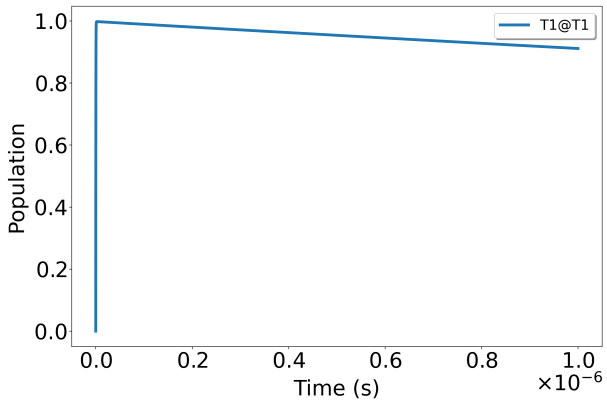

Figure B.2: Evolution of states population over time for a time range from 0 to 1 μs using a propagation step of 10^{-10}.

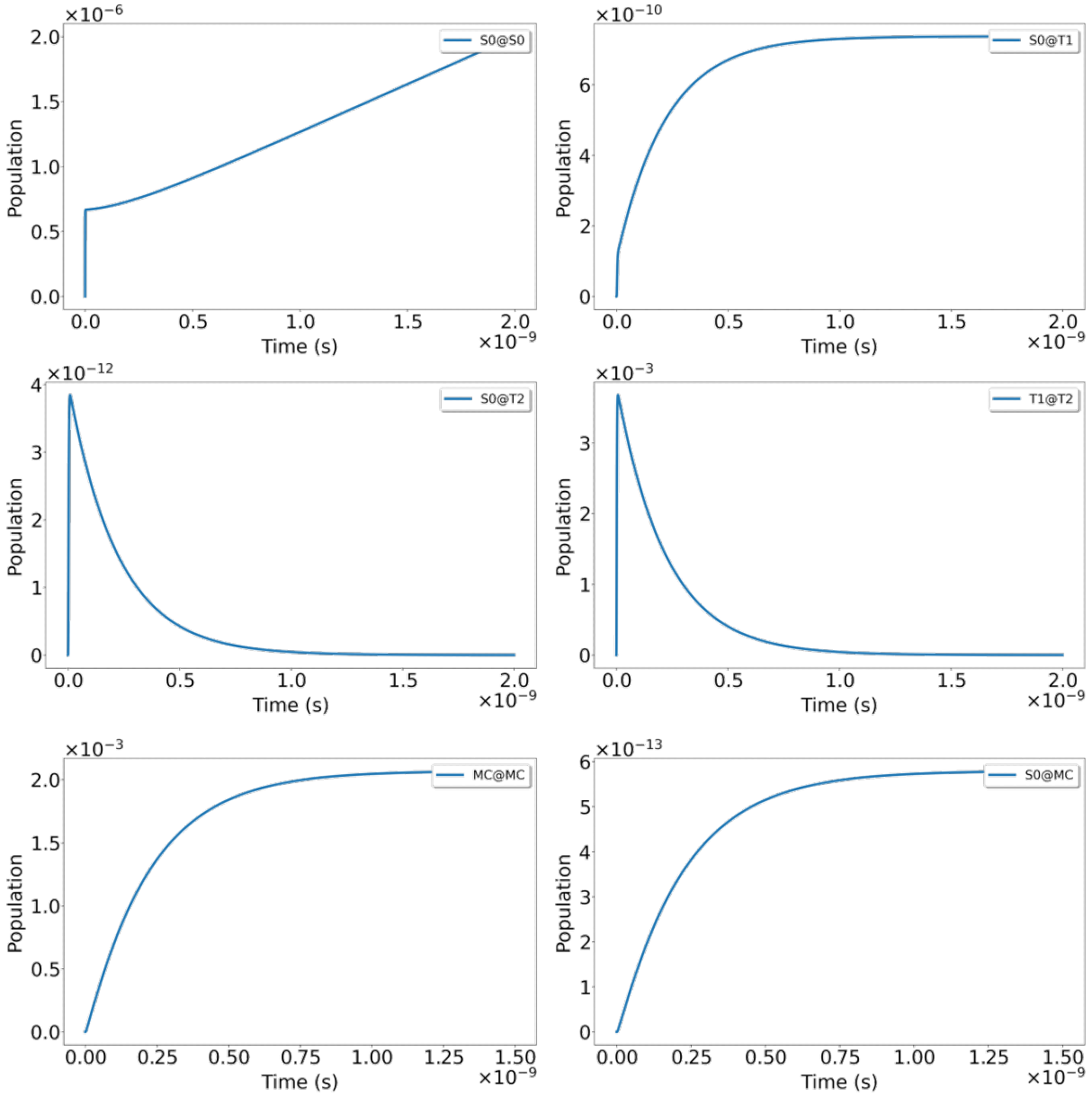

Figure B.3: Evolution of states population over time for a time range from 0 to 2 ns using a propagation step of 10^{-13}.

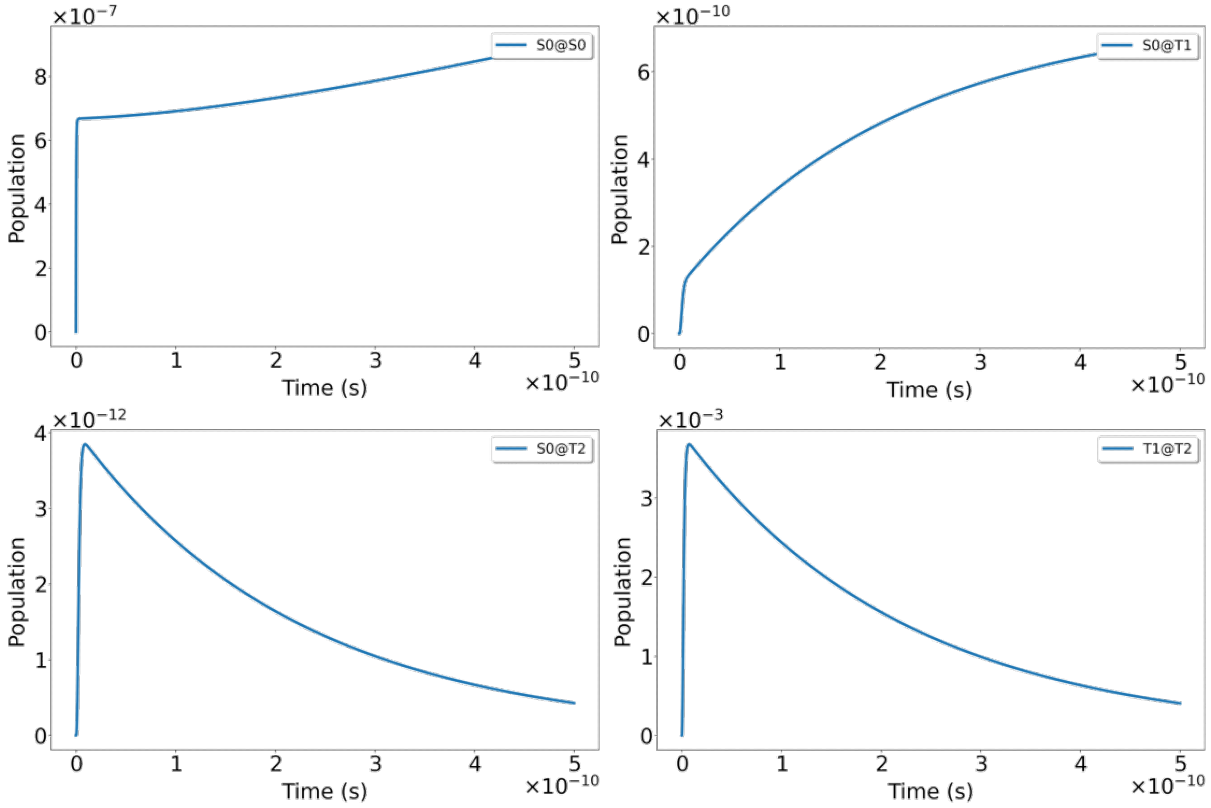

Figure B.4: Evolution of states population over time for a time range from 0 to 5×10^{-10} s using a propagation step of 10^{-13}.

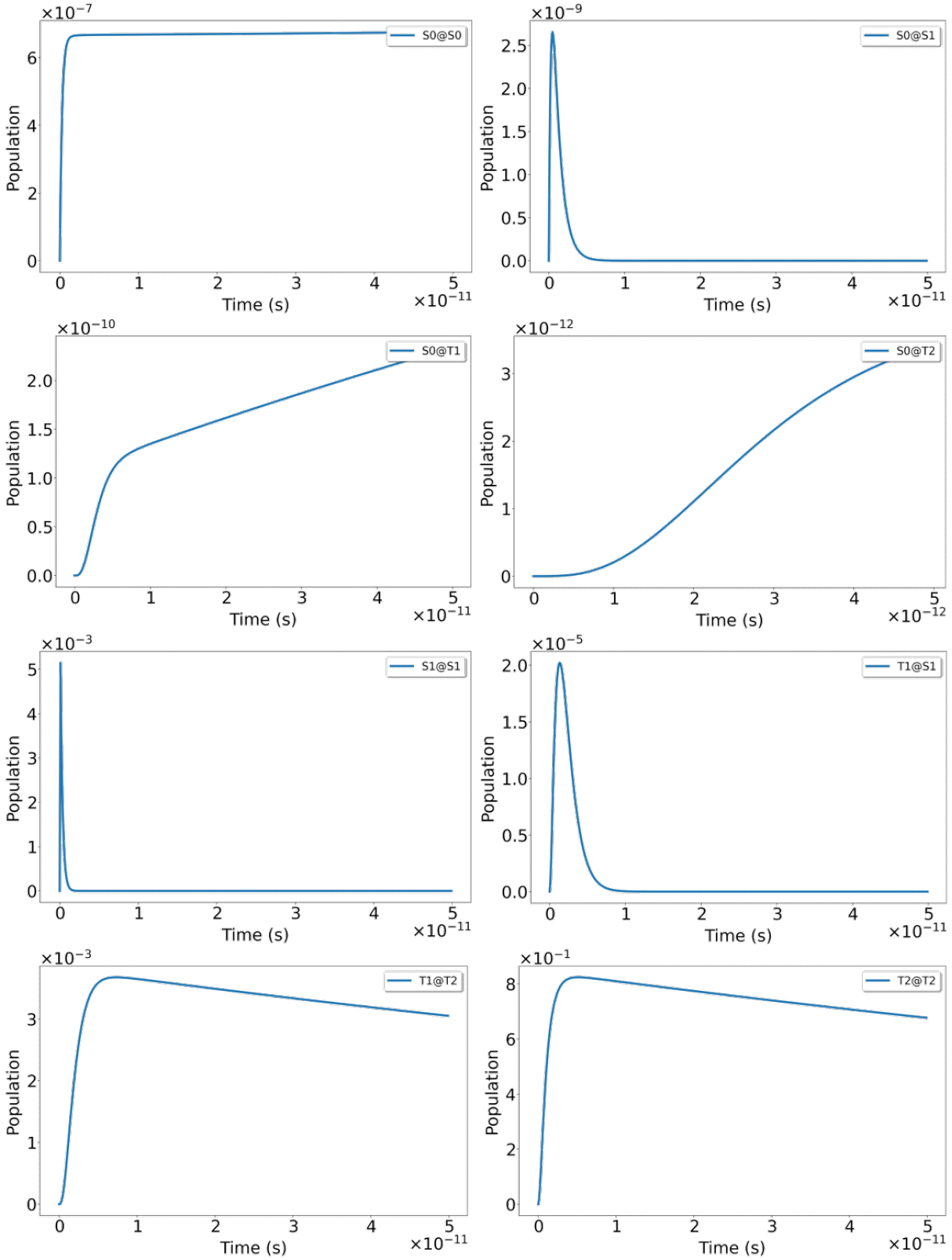

Figure B.5: Evolution of states population over time for a time range from 0 to 5×10^{-11} s using a propagation step of 10^{-13}.

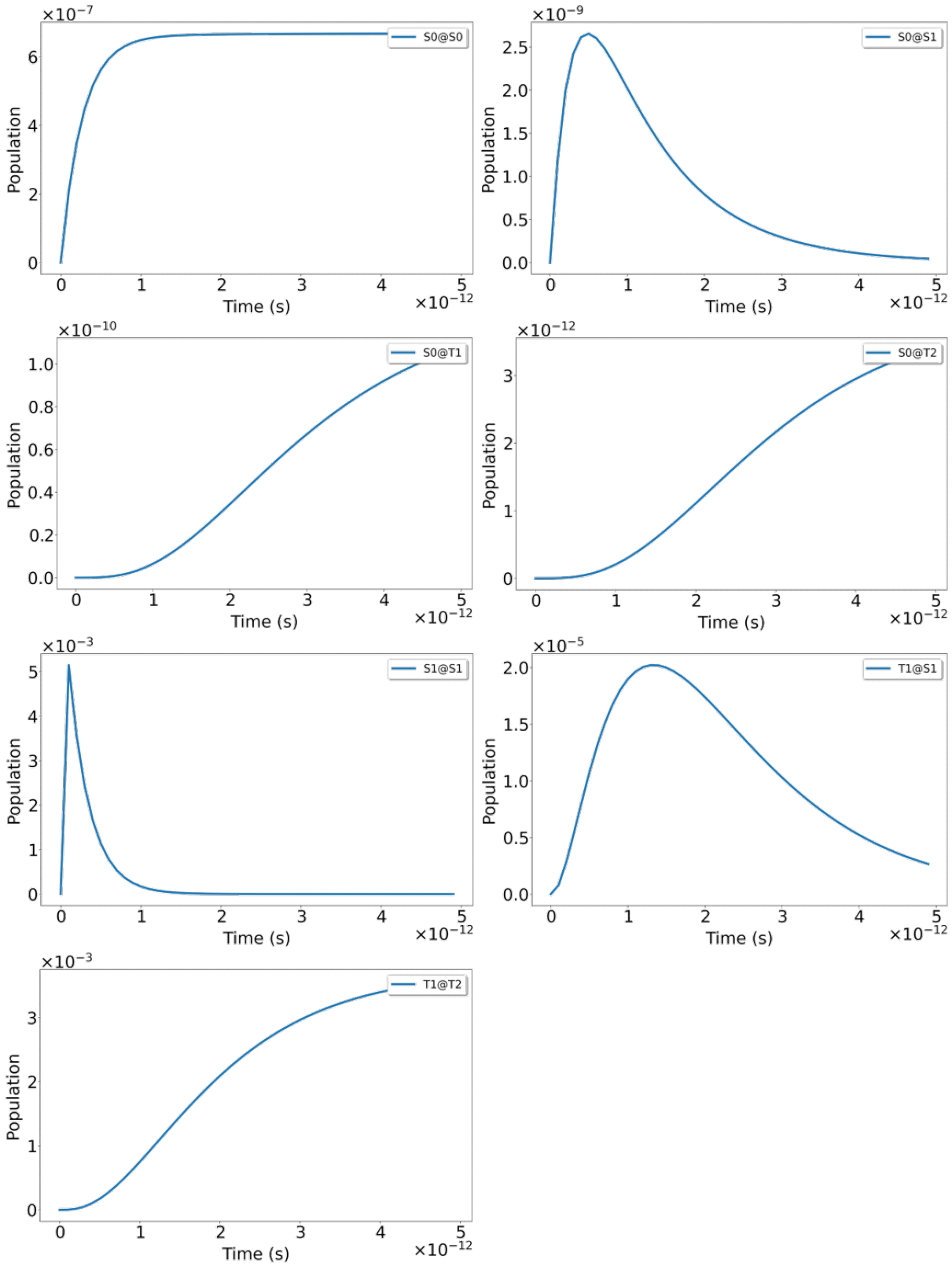

Figure B.6: Evolution of states population over time for a time range from 0 to 5 ps using a propagation step of 10^{-13}.

B.3 Chapter 3

B.3.1 Cartesian Coordinates

All the Cartesian coordinates for the optimized geometries of $\mathbf{S_0}$, $\mathbf{S_1}$, $\mathbf{T_1}$, $\mathbf{T_2}$, $\mathbf{T_3}$ states, and Conical Intersection (CI) between states S_0 and S_1 of the complex $[Ru(bpy)_2dppn]^{2+}$ are shown below.

$\mathbf{S_0}$

Ru 7.643136000 -3.109444000 3.857408000
N 9.204152000 -4.416160000 4.222281000
N 8.784324000 -1.564346000 3.070316000
N 6.003889000 -1.840540000 3.675563000
N 7.722879000 -3.636254000 1.856256000
N 6.628838000 -4.791075000 4.518432000
C 7.407011000 -5.855501000 4.841905000
C 6.844884000 -7.035198000 5.317726000
C 5.470712000 -7.125918000 5.467656000
C 4.684555000 -6.029490000 5.138673000
C 5.299762000 -4.882682000 4.670075000
N 7.523506000 -2.338967000 5.785279000
C 8.409826000 -2.783847000 1.053530000
C 8.534377000 -3.028446000 -0.309733000
C 7.950545000 -4.158558000 -0.858518000
C 7.253836000 -5.025691000 -0.027649000
C 7.163983000 -4.731065000 1.320835000
C 9.281658000 -0.532775000 3.767606000
C 9.998420000 0.489166000 3.171617000
C 10.210530000 0.447665000 1.800101000
C 9.700221000 -0.616607000 1.074659000
C 8.987622000 -1.615504000 1.729428000
C 10.502181000 -4.135570000 4.037275000
C 11.502062000 -5.060894000 4.276039000
C 11.149768000 -6.329400000 4.717549000
C 9.809784000 -6.625493000 4.907720000
C 8.848677000 -5.652213000 4.656132000
C 5.270334000 -1.620551000 2.581880000
C 4.240010000 -0.686221000 2.556344000
C 3.956229000 0.047986000 3.690966000
C 4.712369000 -0.169921000 4.846742000
C 5.729941000 -1.126559000 4.796745000
C 7.164109000 -1.083000000 8.245598000
C 8.143290000 -2.040944000 8.070812000
C 8.297898000 -2.647563000 6.828637000
C 6.547197000 -1.410546000 5.952236000
C 4.482900000 0.559270000 6.092200000
C 5.290758000 0.264052000 7.254100000
C 6.340029000 -0.749802000 7.166405000
N 3.542976000 1.473598000 6.127587000
C 3.343842000 2.144480000 7.289702000
C 4.145215000 1.846720000 8.449321000
N 5.111404000 0.895964000 8.389650000
C 2.359849000 3.130523000 7.365021000
C 2.144800000 3.831847000 8.548392000
C 2.947430000 3.532108000 9.712196000
C 3.928014000 2.546335000 9.636565000
C 1.148492000 4.847643000 8.647825000
C 0.957305000 5.523496000 9.815780000
C 1.747783000 5.227651000 10.962915000
C 2.710538000 4.264177000 10.913122000
H 7.473982000 -7.874888000 5.571840000
H 5.022649000 -8.038019000 5.837688000
H 3.608951000 -6.053081000 5.242110000
H 4.724302000 -4.010057000 4.400055000
H 9.082323000 -2.342797000 -0.937810000
H 8.040083000 -4.358000000 -1.917661000
H 6.783268000 -5.920403000 -0.410029000
H 6.628282000 -5.377836000 1.998885000

H 9.099044000 -0.538465000 4.831346000
H 10.378340000 1.298478000 3.778978000
H 10.764757000 1.230772000 1.300877000
H 9.854281000 -0.667532000 0.007440000
H 10.732051000 -3.138921000 3.692106000
H 12.534237000 -4.783982000 4.114393000
H 11.905552000 -7.078220000 4.911735000
H 9.515752000 -7.606580000 5.248591000
H 5.513598000 -2.208240000 1.709277000
H 3.676053000 -0.547455000 1.644836000
H 3.164653000 0.782899000 3.701908000
H 7.027124000 -0.587422000 9.195539000
H 8.798766000 -2.324860000 8.881904000
H 9.066030000 -3.387660000 6.660524000
H 1.765785000 3.344381000 6.485374000
H 4.537838000 2.312483000 10.500149000
H 0.549204000 5.070166000 7.773683000
H 0.199167000 6.293459000 9.880143000
H 1.576516000 5.777843000 11.879283000
H 3.313863000 4.037100000 11.783337000

S_1

Ru 7.696995000 -3.044753000 3.812025000
N 9.189266000 -4.443884000 4.154522000
N 8.855213000 -1.550288000 2.966992000
N 6.111372000 -1.711274000 3.601538000
N 7.785275000 -3.662028000 1.833640000
N 6.605096000 -4.626903000 4.587614000
C 7.328675000 -5.722792000 4.927007000
C 6.710810000 -6.834726000 5.482557000
C 5.339902000 -6.818177000 5.687373000
C 4.613125000 -5.689335000 5.336848000
C 5.282103000 -4.608170000 4.792740000
N 7.614001000 -2.264197000 5.742668000
C 8.497693000 -2.858767000 1.004863000
C 8.639063000 -3.175869000 -0.339425000
C 8.043348000 -4.326293000 -0.831984000
C 7.320409000 -5.139938000 0.028575000
C 7.217149000 -4.777288000 1.359216000
C 9.337170000 -0.495185000 3.635996000
C 10.090111000 0.482419000 3.011696000
C 10.340940000 0.366952000 1.651888000
C 9.834604000 -0.720581000 0.957304000
C 9.089808000 -1.674765000 1.636726000
C 10.485588000 -4.257511000 3.877314000
C 11.431960000 -5.236944000 4.118040000
C 11.018574000 -6.449480000 4.651144000
C 9.675264000 -6.645947000 4.930420000
C 8.770590000 -5.624109000 4.675510000
C 5.404374000 -1.468039000 2.506802000
C 4.355638000 -0.542060000 2.505371000
C 4.052525000 0.140758000 3.662151000
C 4.789457000 -0.092214000 4.834777000
C 5.828603000 -1.042822000 4.757001000
C 7.226467000 -1.035247000 8.194548000
C 8.214911000 -1.978790000 8.024598000
C 8.382184000 -2.584501000 6.774452000
C 6.626571000 -1.334189000 5.891621000
C 4.524270000 0.592726000 6.082942000
C 5.332837000 0.298982000 7.232068000
C 6.392930000 -0.681873000 7.120747000
N 3.533450000 1.479429000 6.128672000
C 3.308864000 2.112688000 7.318561000
C 4.127702000 1.821468000 8.475485000
N 5.136882000 0.902801000 8.401607000
C 2.288029000 3.046547000 7.427547000
C 2.029862000 3.721918000 8.634859000
C 2.844980000 3.436352000 9.781791000
C 3.877399000 2.486634000 9.667650000
C 0.990448000 4.678666000 8.759147000
C 0.762005000 5.324972000 9.948500000
C 1.565123000 5.044708000 11.077442000
C 2.579717000 4.123772000 10.993543000
H 7.290910000 -7.702900000 5.754786000

H 4.847144000 -7.678503000 6.119200000
H 3.543853000 -5.636247000 5.481562000
H 4.758058000 -3.709776000 4.505229000
H 9.208415000 -2.534742000 -0.994463000
H 8.145649000 -4.583515000 -1.877357000
H 6.841964000 -6.045259000 -0.315820000
H 6.663484000 -5.379045000 2.063711000
H 9.117361000 -0.446236000 4.691314000
H 10.465408000 1.315208000 3.588514000
H 10.922970000 1.116468000 1.133330000
H 10.016497000 -0.822628000 -0.101433000
H 10.762963000 -3.299603000 3.464295000
H 12.469321000 -5.043781000 3.886455000
H 11.732948000 -7.237348000 4.847090000
H 9.336449000 -7.585096000 5.340053000
H 5.664482000 -2.020780000 1.616150000
H 3.800323000 -0.377666000 1.593325000
H 3.248375000 0.862350000 3.685955000
H 7.077632000 -0.555796000 9.151486000
H 8.866271000 -2.263177000 8.838274000
H 9.149834000 -3.326181000 6.609753000
H 1.680719000 3.255780000 6.554892000
H 4.497132000 2.262002000 10.527645000
H 0.376261000 4.892286000 7.892157000
H -0.035679000 6.053052000 10.026091000
H 1.375936000 5.560497000 12.010491000
H 3.196288000 3.906883000 11.858025000

T_1

Ru 7.694441000 -3.043620000 3.813079000
N 9.195969000 -4.411118000 4.204931000
N 8.896135000 -1.584128000 2.963965000
N 6.093325000 -1.727837000 3.620125000
N 7.730318000 -3.641697000 1.831606000
N 6.607648000 -4.648394000 4.544907000
C 7.339040000 -5.731968000 4.910498000
C 6.728195000 -6.860553000 5.446393000
C 5.352853000 -6.880141000 5.611918000
C 4.614601000 -5.765180000 5.237418000
C 5.277197000 -4.671445000 4.710188000
N 7.626395000 -2.230183000 5.727609000
C 8.467362000 -2.864462000 0.997543000
C 8.588347000 -3.177062000 -0.352249000
C 7.948566000 -4.298391000 -0.854696000
C 7.198721000 -5.087382000 0.007527000
C 7.115853000 -4.727649000 1.340524000
C 9.436834000 -0.548160000 3.621335000
C 10.205290000 0.411962000 2.988227000
C 10.423467000 0.301958000 1.621214000
C 9.864928000 -0.764976000 0.936501000
C 9.101777000 -1.700176000 1.627430000
C 10.502521000 -4.207780000 3.982639000
C 11.457667000 -5.174034000 4.241949000
C 11.049735000 -6.401833000 4.746439000
C 9.700596000 -6.618401000 4.975183000
C 8.786246000 -5.607776000 4.697996000
C 5.358712000 -1.493026000 2.535386000
C 4.313616000 -0.566696000 2.531482000
C 4.017413000 0.135856000 3.677952000
C 4.778873000 -0.091959000 4.836323000
C 5.816696000 -1.035157000 4.758142000
C 7.246516000 -0.987092000 8.196624000
C 8.243802000 -1.918517000 8.012636000
C 8.408078000 -2.522859000 6.764351000
C 6.632962000 -1.315642000 5.896673000
C 4.538333000 0.589417000 6.087431000
C 5.337125000 0.306500000 7.212880000
C 6.406316000 -0.661130000 7.118873000
N 3.533372000 1.496793000 6.139978000
C 3.324239000 2.110843000 7.309681000
C 4.135979000 1.814384000 8.465041000
N 5.129951000 0.921320000 8.402793000
C 2.293793000 3.066893000 7.425989000
C 2.027774000 3.737203000 8.644316000

C 2.829380000 3.438877000 9.792447000
C 3.868194000 2.483797000 9.677466000
C 0.999930000 4.680207000 8.758950000
C 0.754830000 5.328773000 9.974223000
C 1.533501000 5.041973000 11.085961000
C 2.565825000 4.101831000 10.996607000
H 7.320656000 -7.715474000 5.734959000
H 4.867066000 -7.751975000 6.028457000
H 3.540088000 -5.734263000 5.349806000
H 4.740112000 -3.786639000 4.403693000
H 9.178758000 -2.552135000 -1.004857000
H 8.035877000 -4.551297000 -1.902564000
H 6.683386000 -5.971991000 -0.338953000
H 6.542453000 -5.313326000 2.042912000
H 9.244819000 -0.500656000 4.682549000
H 10.619758000 1.227722000 3.563466000
H 11.018245000 1.035467000 1.094165000
H 10.019779000 -0.867113000 -0.126884000
H 10.777237000 -3.240429000 3.590008000
H 12.499010000 -4.960100000 4.047129000
H 11.769720000 -7.180488000 4.958419000
H 9.362733000 -7.567304000 5.363447000
H 5.603965000 -2.060016000 1.649605000
H 3.748912000 -0.416776000 1.622194000
H 3.212506000 0.855162000 3.704281000
H 7.099619000 -0.503402000 9.150731000
H 8.908165000 -2.192768000 8.819820000
H 9.187339000 -3.251262000 6.595526000
H 1.693271000 3.283382000 6.551059000
H 4.482630000 2.251229000 10.538463000
H 0.391105000 4.905675000 7.892022000
H -0.044878000 6.054583000 10.041327000
H 1.346185000 5.542785000 12.026679000
H 3.172550000 3.878346000 11.865548000

T_2

Ru 7.694451000 -3.048793000 3.810169000
N 9.189422000 -4.446950000 4.162206000
N 8.850759000 -1.549523000 2.965431000
N 6.111831000 -1.722769000 3.597134000
N 7.782249000 -3.661749000 1.826973000
N 6.602934000 -4.631978000 4.584748000
C 7.327150000 -5.725069000 4.933541000
C 6.707874000 -6.836437000 5.489887000
C 5.335506000 -6.822385000 5.687507000
C 4.608321000 -5.696185000 5.327957000
C 5.278078000 -4.615949000 4.782307000
N 7.620791000 -2.270096000 5.734480000
C 8.488264000 -2.852212000 0.998699000
C 8.624051000 -3.161498000 -0.348557000
C 8.029105000 -4.310917000 -0.845203000
C 7.312726000 -5.131363000 0.014978000
C 7.214937000 -4.776143000 1.348435000
C 9.332273000 -0.494223000 3.635724000
C 10.075193000 0.490758000 3.010451000
C 10.317577000 0.382906000 1.648106000
C 9.813063000 -0.705348000 0.952695000
C 9.077809000 -1.667134000 1.633001000
C 10.487740000 -4.258050000 3.894627000
C 11.436593000 -5.230702000 4.154827000
C 11.024069000 -6.439461000 4.697968000
C 9.678604000 -6.639146000 4.966048000
C 8.771333000 -5.624204000 4.690753000
C 5.403719000 -1.475786000 2.503727000
C 4.359458000 -0.547147000 2.501152000
C 4.058773000 0.139061000 3.659623000
C 4.793503000 -0.094090000 4.829038000
C 5.833247000 -1.048686000 4.754864000
C 7.230102000 -1.039964000 8.188252000
C 8.220320000 -1.985336000 8.017704000
C 8.386837000 -2.589351000 6.768479000
C 6.629773000 -1.338123000 5.884215000
C 4.529848000 0.592389000 6.077499000
C 5.338893000 0.295215000 7.229744000

C 6.398855000 -0.686764000 7.117566000
N 3.544916000 1.480121000 6.125914000
C 3.319396000 2.112314000 7.315235000
C 4.133558000 1.816878000 8.471136000
N 5.140517000 0.897144000 8.395736000
C 2.300680000 3.048522000 7.422916000
C 2.042135000 3.719749000 8.630458000
C 2.853178000 3.428686000 9.778464000
C 3.882777000 2.478351000 9.665151000
C 1.004405000 4.678647000 8.754689000
C 0.774839000 5.320476000 9.944656000
C 1.574313000 5.034575000 11.075276000
C 2.586223000 4.112673000 10.992034000
H 7.288066000 -7.702833000 5.768907000
H 4.842144000 -7.682283000 6.120451000
H 3.537834000 -5.644228000 5.466878000
H 4.752883000 -3.719974000 4.488118000
H 9.187971000 -2.514630000 -1.003244000
H 8.126498000 -4.561633000 -1.892984000
H 6.834572000 -6.036312000 -0.331943000
H 6.665651000 -5.383771000 2.052069000
H 9.119541000 -0.450312000 4.693033000
H 10.449268000 1.323584000 3.588743000
H 10.891506000 1.138507000 1.128540000
H 9.988902000 -0.801770000 -0.107951000
H 10.764911000 -3.303122000 3.473305000
H 12.475505000 -5.034882000 3.930823000
H 11.740519000 -7.221553000 4.910699000
H 9.340649000 -7.575529000 5.383607000
H 5.659679000 -2.030450000 1.612856000
H 3.803632000 -0.382205000 1.589811000
H 3.256591000 0.862849000 3.682350000
H 7.082070000 -0.561349000 9.145704000
H 8.871790000 -2.269527000 8.831019000
H 9.155433000 -3.330627000 6.605413000
H 1.696460000 3.260992000 6.549911000
H 4.499719000 2.249922000 10.525118000
H 0.393622000 4.896135000 7.886898000
H -0.020889000 6.049923000 10.023154000
H 1.383071000 5.547856000 12.008764000
H 3.199737000 3.891386000 11.856932000

T_3

Ru 7.688059000 -3.022842000 3.823690000
N 9.219478000 -4.388786000 4.241894000
N 8.936892000 -1.620146000 2.956613000
N 6.086744000 -1.726349000 3.612039000
N 7.683231000 -3.626811000 1.819683000
N 6.619169000 -4.656266000 4.503716000
C 7.354676000 -5.727261000 4.894717000
C 6.736428000 -6.855481000 5.415281000
C 5.355294000 -6.878412000 5.543778000
C 4.616740000 -5.773301000 5.144777000
C 5.283193000 -4.679980000 4.622955000
N 7.648048000 -2.215606000 5.730369000
C 8.442950000 -2.873648000 0.987012000
C 8.534165000 -3.175669000 -0.365459000
C 7.833071000 -4.260251000 -0.869721000
C 7.054859000 -5.019500000 -0.008986000
C 7.006852000 -4.673337000 1.330620000
C 9.507344000 -0.608654000 3.628350000
C 10.288968000 0.339114000 2.993791000
C 10.494183000 0.229749000 1.625546000
C 9.907403000 -0.818399000 0.932028000
C 9.123354000 -1.735878000 1.617863000
C 10.527049000 -4.164290000 4.064987000
C 11.484749000 -5.119325000 4.361322000
C 11.074444000 -6.349940000 4.850946000
C 9.720261000 -6.585939000 5.032547000
C 8.806262000 -5.587354000 4.722606000
C 5.348732000 -1.508956000 2.527436000
C 4.295233000 -0.591648000 2.529367000
C 4.007151000 0.105323000 3.682232000
C 4.770572000 -0.103859000 4.844799000

C 5.820517000 -1.040016000 4.760476000
C 7.274646000 -0.966385000 8.177206000
C 8.282816000 -1.889078000 8.001886000
C 8.445397000 -2.499828000 6.756405000
C 6.642161000 -1.306626000 5.886978000
C 4.515328000 0.591764000 6.086466000
C 5.343260000 0.317984000 7.229166000
C 6.416742000 -0.644054000 7.110378000
N 3.515664000 1.466707000 6.137525000
C 3.297576000 2.104707000 7.324875000
C 4.131254000 1.830323000 8.474633000
N 5.151889000 0.926397000 8.395895000
C 2.267464000 3.027281000 7.438522000
C 2.013159000 3.704416000 8.644063000
C 2.841378000 3.433399000 9.784820000
C 3.883747000 2.497297000 9.665978000
C 0.963798000 4.649293000 8.773069000
C 0.738460000 5.296684000 9.961109000
C 1.554317000 5.030032000 11.084648000
C 2.578392000 4.121812000 10.996261000
H 7.323167000 -7.707862000 5.722146000
H 4.864374000 -7.752236000 5.950873000
H 3.539619000 -5.749436000 5.229547000
H 4.749284000 -3.803108000 4.290259000
H 9.145949000 -2.572474000 -1.018811000
H 7.895693000 -4.505705000 -1.921326000
H 6.491114000 -5.873165000 -0.357479000
H 6.413420000 -5.241924000 2.029995000
H 9.327616000 -0.568234000 4.691722000
H 10.725565000 1.141860000 3.570772000
H 11.104991000 0.951427000 1.099872000
H 10.055914000 -0.915096000 -0.132762000
H 10.809973000 -3.197153000 3.679145000
H 12.529137000 -4.891261000 4.202560000
H 11.796263000 -7.119566000 5.089040000
H 9.381815000 -7.539081000 5.409758000
H 5.594678000 -2.076848000 1.642704000
H 3.721519000 -0.446130000 1.625650000
H 3.195233000 0.817769000 3.712785000
H 7.129311000 -0.478194000 9.130156000
H 8.952923000 -2.149755000 8.808105000
H 9.230255000 -3.221337000 6.585954000
H 1.650019000 3.224305000 6.571184000
H 4.513989000 2.284403000 10.520244000
H 0.340464000 4.851695000 7.910572000
H -0.066479000 6.015483000 10.043442000
H 1.366183000 5.547149000 12.016618000
H 3.204798000 3.915167000 11.855520000

Conical Intersection

Ru 7.624883000 -3.182869000 3.852959000
N 9.220342000 -4.447814000 4.228947000
N 8.713888000 -1.580115000 3.109007000
N 5.946721000 -1.945600000 3.672873000
N 7.726793000 -3.654192000 1.835687000
N 6.654961000 -4.905682000 4.468809000
C 7.457744000 -5.957242000 4.778241000
C 6.919574000 -7.168871000 5.200088000
C 5.545894000 -7.306901000 5.314654000
C 4.734949000 -6.221801000 5.007532000
C 5.326039000 -5.041858000 4.592749000
N 7.492658000 -2.436098000 5.799540000
C 8.386676000 -2.756679000 1.057877000
C 8.522718000 -2.960769000 -0.311692000
C 7.975566000 -4.090621000 -0.897078000
C 7.304119000 -5.002274000 -0.092849000
C 7.204626000 -4.749328000 1.263219000
C 9.171829000 -0.546906000 3.832463000
C 9.853163000 0.515712000 3.266643000
C 10.071450000 0.518325000 1.895264000
C 9.600295000 -0.544872000 1.142462000
C 8.922584000 -1.587316000 1.767204000
C 10.515249000 -4.120394000 4.097342000
C 11.540705000 -5.007418000 4.368695000

C 11.220980000 -6.292851000 4.786728000
C 9.886326000 -6.638858000 4.920407000
C 8.897045000 -5.701009000 4.639905000
C 5.196542000 -1.709791000 2.605504000
C 4.169097000 -0.753381000 2.601541000
C 3.917930000 -0.013223000 3.730998000
C 4.697095000 -0.237555000 4.886753000
C 5.704696000 -1.225115000 4.809874000
C 7.135405000 -1.092007000 8.231847000
C 8.098070000 -2.060430000 8.084620000
C 8.252146000 -2.711715000 6.850866000
C 6.511597000 -1.492892000 5.934814000
C 4.515214000 0.487852000 6.102455000
C 5.288515000 0.223680000 7.190068000
C 6.303358000 -0.778145000 7.135477000
N 3.503913000 1.494315000 6.120793000
C 3.387143000 2.140383000 7.256458000
C 4.197543000 1.852079000 8.411728000
N 5.131460000 0.930845000 8.419326000
C 2.412653000 3.199306000 7.372982000
C 2.172607000 3.983267000 8.589524000
C 2.951521000 3.688552000 9.723927000
C 3.948351000 2.618147000 9.609439000
C 1.237111000 4.964672000 8.647517000
C 1.023465000 5.729214000 9.876550000
C 1.763007000 5.449962000 10.952698000
C 2.766598000 4.388428000 10.871653000
H 7.567010000 -7.998821000 5.439657000
H 5.116586000 -8.244183000 5.640888000
H 3.658926000 -6.282196000 5.088593000
H 4.736196000 -4.171750000 4.345230000
H 9.051985000 -2.242577000 -0.919386000
H 8.074040000 -4.257112000 -1.960991000
H 6.862123000 -5.898460000 -0.504610000
H 6.690648000 -5.431403000 1.923905000
H 8.981954000 -0.587859000 4.894215000
H 10.202314000 1.323084000 3.894689000
H 10.599057000 1.333596000 1.419522000
H 9.757735000 -0.559970000 0.074707000
H 10.718639000 -3.112047000 3.768913000
H 12.567758000 -4.691767000 4.251481000
H 11.997035000 -7.013253000 5.006104000
H 9.617878000 -7.632639000 5.245410000
H 5.415505000 -2.292442000 1.721625000
H 3.590697000 -0.610592000 1.699574000
H 3.142669000 0.738445000 3.765062000
H 6.993508000 -0.559071000 9.160849000
H 8.750344000 -2.329568000 8.903547000
H 9.017127000 -3.462657000 6.712299000
H 1.827659000 3.416014000 6.486554000
H 4.551162000 2.368670000 10.475026000
H 0.633007000 5.195241000 7.778210000
H 0.270775000 6.504860000 9.888734000
H 1.640885000 5.987433000 11.882539000
H 3.364268000 4.167977000 11.747976000